ABSTRACT

O'BRIEN, ELLEN MARGARET. Application and Validation of Multi-Physics Coupling to Model Los Alamos National Laboratory's Routine Production RbCl-RbCl-Ga Target Stack. (Under the direction of Joseph Doster.)

The goal of this work is to successfully couple particle physics and computational fluid dynamics for the purposes of accurately modeling behavior exhibited by a multiphase molten salt target during radioisotope production. The specific geometry of interest is a routine production target stack containing two multiphase molten salt targets at Los Alamos National Laboratory's Isotope Production Facility. In target fluids where density varies as a function of temperature, heat deposition will cause the fluid in the path of the particle beam to decrease in density, thus changing particle beam penetration. The goal of this coupling is to reach a steady state solution that accurately depicts both particle beam interaction and fluid distribution behavior within a target under nominal operating conditions. MCNP is used to model particle energy deposition as a function of position. This energy deposition profile is imported into ANSYS CFX and utilized to simulate the thermal behavior of the target and fluid motion of molten target regions. Validation metrics were chosen to quantify the accuracy of multi-physics coupling for multiphase domains. Comparison of experimental and computationally predicted yields were used as an initial benchmark. To provide an additional benchmark, experimental data providing information about the spatial energy distribution in downstream targets was compared to model predictions. Uncertainty quantification was performed where possible for specific system response quantities of interest and for experimentally obtained data.

Application and Validation of Multi-Physics Coupling to Model Los Alamos National Laboratory's Routine Production RbCl-RbCl-Ga Target Stack

by
Ellen Margaret O'Brien

A dissertation submitted to the Graduate Faculty of
North Carolina State University
in partial fulfillment of the
requirements for the degree of
Doctor of Philosophy

Nuclear Engineering

Raleigh, North Carolina

2018

APPROVED BY:

_____	_____
Dr. J.M. Doster Committee Chair	Dr. R.C. Smith
_____	_____
Dr. I.A. Bolotnov	Dr. M.H. Stokely

DEDICATION

I'd like to dedicate this dissertation to my parents and to my boyfriend Antonio. Your love and support is unwavering and always appreciated.

BIOGRAPHY

Ellen Margaret O'Brien was born on November 13, 1991 to Daniel and Ann O'Brien. She attended school in her hometown of Apex, NC before attending the North Carolina School of Science and Math (NCSSM) in Durham, NC for the final two years of her high school education. In 2010 she enrolled in the nuclear engineering undergraduate program at North Carolina State University on a full academic state scholarship provided to attendees of NCSSM. After graduating Summa Cum Laude with a Bachelor of Science degree in nuclear engineering in spring of 2014, she accepted a three-year Nuclear Energy University Program (NEUP) Fellowship to pursue her Ph.D. in nuclear engineering at North Carolina State University. She completed her final year of Ph.D. research at Los Alamos National Laboratory, and in spring of 2018 she received her Ph.D.

ACKNOWLEDGMENTS

I would like to acknowledge the Department of Energy's Nuclear Energy University Program (NEUP) Fellowship, which supported me during my first three years of graduate school. I would also like to thank the Isotope Program in the Department of Energy, Office of Science, Office of Nuclear Physics for their support both financially and in the form of mentorship during the final year of my graduate studies. Without the isotope group at Los Alamos National Laboratory, the bulk of the work done in this dissertation would not have been possible. In particular I would like to thank Dr. Doster, Dr. Stokely, Dr. Nortier, and Eric Olivas for the significant mentorship roles they played and from whom I have learned a great deal in terms of how to conduct myself as a critical thinker and researcher.

TABLE OF CONTENTS

LIST OF TABLES

LIST OF FIGURES

CHAPTER 1. INTRODUCTION

Section 1.1. Background

Radionuclide production for applications in nuclear medicine allows for noninvasive diagnostic procedures to be performed via the use of either single-photon emission computed tomography (SPECT) imaging or positron emission tomography (PET) imaging. Clinical PET and SPECT imaging enables diagnosis and management in areas such as cancer diagnosis, cardiology, and neuropsychiatry by providing quantitative information about biochemical and physiologic processes in the body [1,2]. SPECT utilizes radioisotopes decaying by individual photon emissions, while PET uses radioisotopes that decay by positron emission. Both of these imaging techniques have the same end goal – to develop a three-dimensional image of an organ or organ system of interest via detection of photons.

Gamma emitting isotopes used for SPECT have a known half-life and distinct photon energies. ^{99m}Tc is a commonly used SPECT radioisotope and has a mono-energetic decay via a 140 keV photon. For other isotopes with more than one characteristic gamma, one or two additional photon energies are used for imaging as well [3]. This is a random process, with isotropic photon emissions from the decaying nucleus.

SPECT is based on determining the trajectory and origin of the detected photons. This requires the use of a collimator to minimize the number of detected photons not emitted within a small solid angle subtended by the detector. A single detector is rotated around the patient in order to collect photon intensities at a number of emission angles that can then be used to construct an image [2,3]. This method results in more than 99% of the emitted gammas being absorbed or scattered by the collimator, making much less efficient use of the injected radiopharmaceutical.

Positron emitting radioisotopes are used for PET. Positrons are positively charged electrons that emit two 511 keV photons in equal and opposite directions when they annihilate after collision with an electron. Depending on the energy of the positron, it can be assumed that the positron annihilates at the same time and location it was emitted, allowing the PET scanner to find this position. Generally, modern detectors are ring-shaped, allowing

annihilation photons to be detected simultaneously and in many directions. Coincident detection allows for tomographic (or slice) images to be reconstructed into a picture of the activity within the patient's body [2]. This coincident counting of photons removes the need for collimators to ascertain the photon location and significantly increases the resolution of the scan. Modern PET and SPECT scanners have been combined with CT scanners to further improve resolution.

While SPECT is significantly less expensive than PET, detection sensitivity and increased spatial and temporal resolution make PET scans more desirable [2,4]. Another substantial advantage of PET over SPECT is the total radiation dose to the patient. The collimators present in SPECT machines mean that a large portion of the radiation dose received by the patient is not actually used for imaging.

Since the development of the first PET and SPECT devices in the 1950s and 60s, there has been a rapid increase in both PET and SPECT technology and associated radiopharmaceutical demand [2]. Following WWII there was a slow shift from the use of reactors to the use of accelerators as the primary source of a variety of desired medical radioisotopes due to their wide range of charged particle energies and beam currents [5]. Both low energy accelerators, generally in the form of cyclotrons, and high energy linear accelerators may be used for the generation of some of these radioisotopes.

Reactor and accelerator produced radioisotopes and parent/daughter generator pairs can provide both positron and photon emitting sources. In facilities without an on-site accelerator or reactor, a radionuclide generator is favorable as it allows for on demand access of daughter radionuclides. A typical generator pair consists of a parent with a relatively long half-life and a short-lived positron or gamma emitting daughter. The long half-life of the parent radionuclide allows for ease of both large-scale production and transport. In addition, the secular equilibrium occurring between the long-lived parent and short-lived daughter permits repeated daughter/parent separations while the concentration of the daughter activity remains almost constant [6]. By developing an appropriate generator separation technique, relatively pure concentrations of the daughter radioisotope can be obtained. This is generally done by passing a liquid (e.g., saline) over the parent/daughter generator, thereby removing the

daughter radioisotope and leaving the parent behind. The strontium-82/rubidium-82 (^{82}Sr/^{82}Rb) and germanium-68/gallium-68 (^{68}Ge/^{68}Ga) pairs are examples of radionuclide generator pairs with a positron emitting daughter. The molybdenum-99/technechium-99m (^{99}Mo/^{99m}Tc) pair is another generator system with a photon emitting daughter.

^{82}Rb is the positron emitting radionuclide daughter of ^{82}Sr. ^{82}Sr is produced via proton bombardment of ^{nat}Rb and has a relatively long half-life of 25.36 days. ^{82}Rb has a half-life of approximately 1.3 minutes [7,8]. Rubidium is a potassium analogue, and thus its biological activity is comparable to that of potassium. It requires no labelling, meaning that it does not need to be attached to a carrier molecule, but independently follows pathways taken by potassium within the body with a myocardial muscle uptake proportional to myocardial blood flow. Because of this it has been utilized to observe myocardial perfusion and blood flow [1,6,7,9].

^{99m}Tc ($t_{1/2}$ = 6.0067 hr) is a photon emitting radionuclide daughter of ^{99}Mo ($t_{1/2}$ = 65.976 hr), which is produced via fission of ^{235}U targets in reactors. It can then be labelled and used with SPECT for the same myocardial perfusion studies as ^{82}Sr in PET, but it has poorer diagnostic accuracy and administers a higher radiation dose to the patient given its significantly longer half-life [9]. In addition, disruptions in availability of ^{99m}Tc supply has caused many facilities to invest in and switch to the use of ^{82}Sr in PET machines.

As ^{82}Sr can only be produced via bombardment with higher energy protons, this has historically only been possible at higher energy linear accelerator facilities. However, in the past several years there has been development of cyclotrons capable of operating at proton energies up to 70 MeV, making the cyclotron production of ^{82}Sr possible.

Similarly, the ^{68}Ge/^{68}Ga pair also produces a positron emitting daughter (^{68}Ga). While ^{68}Ge was initially of interest only as a long-lived positron source ($t_{1/2}$ = 270.8 days) for calibration of PET scanners, its role as a parent of the ^{68}Ga radionuclide ($t_{1/2}$ = 68 min) is now gaining recognition. ^{68}Ga provides 89% positron branching along with low photon emission, creating more recent interest in ^{68}Ga as a radiopharmaceutical label for PET scans [6].

Section 1.2. Purpose

As PET imaging technology improves, the demand for $^{82}Sr/^{82}Rb$ generators continues to grow. Despite this, the thermal performance of RbCl targets used to produce ^{82}Sr remains a limiting factor for large scale production. Operation at beam currents above 230 μA in the proton energy range of interest occasionally leads to target failure though many of the existing facilities producing ^{82}Sr are capable of operating at beam currents much higher than this.

Los Alamos National Laboratory's (LANL) Isotope Production Facility (IPF) has access to 100 MeV protons through the linear accelerator located at the Los Alamos Neutron Science Center (LANSCE). IPF is able to produce multiple radionuclides simultaneously due to a three stacked target configuration, including ^{82}Sr via proton bombardment of RbCl targets. Nonetheless, the thermal performance of these targets continues to limit the maximum allowable beam current. Understanding target behavior is then essential to understanding target thermal performance. Computational modeling of these targets can help determine what factors contribute to this limiting thermal behavior and provide ways to optimize target thermal performance and radioisotope production.

Historically LANL has assumed average target material densities to perform predicted yield and transmitted energy calculations. However, it became apparent when examining experimentally measured transmitted energies and yields at LANL that RbCl targets partially melt during irradiation, creating substantial density gradients. In target fluids where density varies as a function of temperature, heat deposition will cause fluid in the path of the particle beam to decrease in density, thus changing particle beam penetration. Cumulative effects of upstream density gradients significantly impact downstream transmitted energies, making any average density assumption invalid [10].

It is clear then that these targets are influenced by two tightly coupled physics problems – radiation transport and thermal hydraulic fluid motion. Modeling these targets via multi-physics coupling allows for analysis of the closely coupled nature of particle transport and thermal hydraulic behavior and a more accurate prediction of target behavior. In addition, this multi-physics coupling can help to understand and predict the simultaneous production of other

isotopes in the downstream low-energy targets by accurately determining the incident proton energy distribution.

The purpose of this dissertation is to establish and attempt to validate a multi-physics coupling methodology capturing the effects of a proton beam impinging upon a RbCl target stack. Attempts at model validation through comparison with measured observables, or validation metrics, will provide a measure of confidence in nominal target behavior predictions as well as predicted behavior for optimized or varying target configurations and beam shapes. More importantly, this model will allow for an in depth analysis of the various physical system drivers and could provide avenues by which to improve overall target performance and ^{82}Sr production.

Section 1.3. Problem of Interest

The focus of this dissertation is a specific radioisotope target configuration in use at LANL's IPF, with the intention of successfully developing a computational model to provide useful information applicable to real-world target behavior. This routine production target configuration consists of two inconel-encapsulated rubidium chloride (RbCl) salt targets and one niobium-encapsulated gallium (Ga) target separated by water cooling channels. RbCl is hygroscopic, so to minimize the presence of water molecules that could lead to target capsule over pressurization, they are cast into target pucks at temperatures significantly above the melting point and then encapsulated in inconel under vacuum. Images of this process are shown in 0. The targets will be referred to as the A, B, and C slot targets according to their position in the target stack. To illustrate this stacked geometry, an image of the target stack is shown below in Figure 1-1.

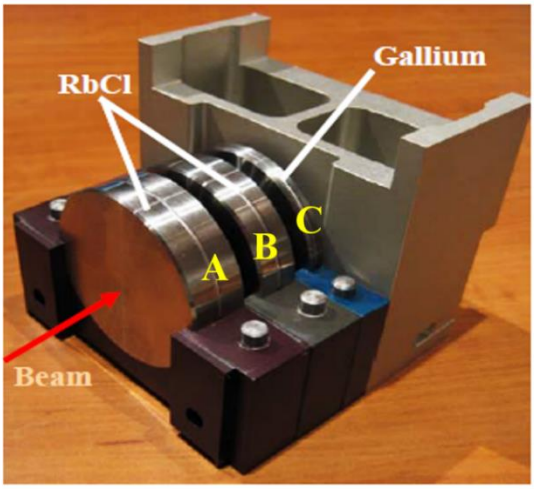

Figure 1-1: RbCl-RbCl-Ga target stack used for ^{82}Sr and ^{68}Ge production at Los Alamos National Laboratory.

These three target pucks are bombarded with 100 MeV incident protons in a pulsed ring-shaped beam with a nominal operating current of 230 µA. It is important to note that this 230 µA is the effective continuous beam current, not the instantaneous beam current during the pulse. The accelerator facility operates at 120 Hz, that is, it is capable of providing 120 macro pulses per second. However, only 100 of these are sent to IPF, with every sixth pulse sent to a downstream target station. Each macro pulse is 625 µs, and so there is a space of 7.708 ms between each pulse. As the sixth pulse is skipped, after each fifth pulse there is a 16.041 ms gap before the next pulse. The figure below illustrates this cyclic process.

Figure 1-2: Diagram indicating gate length times and pulses.

The beam is swept in a circle at a rate of 5 kHz to produce a ring-shaped profile. This reduces the peak power density on the target as the beam is swept a total of three times during

the duration of a single macro pulse. The beam profile and approximations made in order to model it will be explained in detail in Section 2.2.2.

The first two RbCl targets are subject to the (p,xn) reaction, producing ^{82}Sr. The first A slot target experiences incident proton energies averaging 93 MeV and average exiting proton energies of 70 MeV. The second B slot target experiences average incident proton energies of 65 MeV and average exiting proton energies of 40 MeV. The C slot Ga target is subject to the (p,2n) and (p,4n) reactions and average energies ranging from 31 to 0 MeV, producing ^{68}Ge.

All targets have a radius of 2.54 cm, and all capsules have a radius of 2.875 cm. The thickness of each target is given in Table 1-1.

Table 1-1: Target thicknesses.

Target Dimensions	
Domain	**Thickness Δz [cm]**
RbCl Target A	1.641
RbCl Target B	1.268
Ga Target C	0.508
In718 Beam Window	0.064

For this target stack, all capsules were designed to be 0.0305 cm thick on both faces and 0.335 cm thick along the radial edge. There is a distance of 0.5 cm between each of the target capsules, and a 0.63 cm gap between the vacuum beam window and the first target capsule. Cooling water flows within each of these channels. General target characteristics are illustrated below in Figure 1-3.

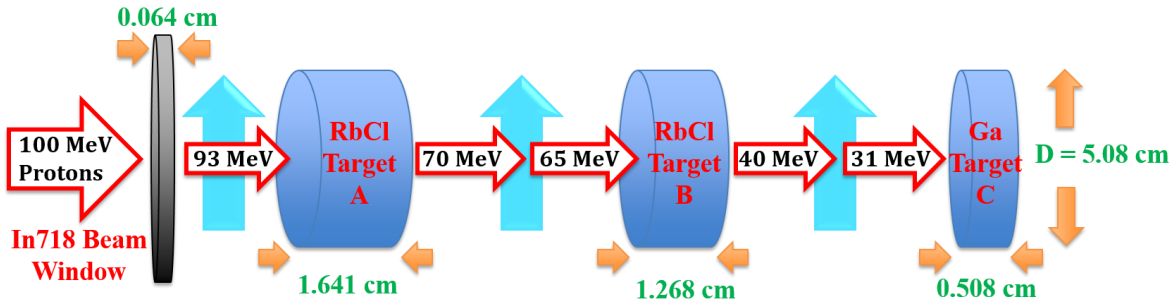

Figure 1-3: Target cut-away with dimensions and average beam energies.

During target development, yield data indicated that the RbCl and Ga targets were melting during operation, causing a shift in both energy distribution and net yield [10,11]. This indicates that not accounting for the physical processes occurring during target operation has a significant impact on target design and radioisotope production.

Section 1.4. Related Work

Relevant work performed in target design and production will be discussed to lay a foundation for the investigation of physical processes at play in RbCl-RbCl-Ga stack targets. The focus of the prior relevant work emphasizes gas targets as they are commonly used in the production of commercially available radioisotopes and represent a compressible target material that experiences a large shift in thermal behavior and particle beam penetration during operation.

While research relevant to isotope production in RbCl-RbCl-Ga targets includes work done on boiling water targets for ^{18}F production [12,13], this work has been referenced but not discussed for the sake of conciseness. Previous work involving experimental results and simulation benchmarking done with gas targets are thoroughly discussed as they have more significance for the research topic of interest.

Tárkányi et al. observed thermal hydraulic behavior in compressible radioisotope target materials and describe a phenomenological model to explain physical phenomenon driving target behavior based on optical observations, experimental results, and measurements [14].

In gas targets the range of incident particles has a strong dependency on the beam current density and thus the incoming diameter of a charged-particle beam expands as it passes through a gaseous medium. Tárkányi et al. posited that this effect is explained by a local reduction in the target gas density. The density distribution of the target gas is influenced by multiple factors, including the temperature gradient caused by an incident beam, convective heat transfer, the specific target material, the dimensions of the target chamber, and the effectiveness of target cooling mechanisms.

Prior to the work performed by Tárkányi et al., all existing model calculations were based purely on simple application of general gas laws using average values, neglecting the dynamic

change in the stopping power as a function of energy, heat deposition, target density, and heat transfer. Focus was also concentrated solely on equilibrium behavior, prompting investigation of transient beam oscillations [15,16]. Tárkányi et al. observed beam shape during irradiation using a combination of photography and video, allowing for transient effects of beam penetration to be studied in addition to equilibrium beam behavior. Images of emitted light during irradiation are shown in Figure 1-4.

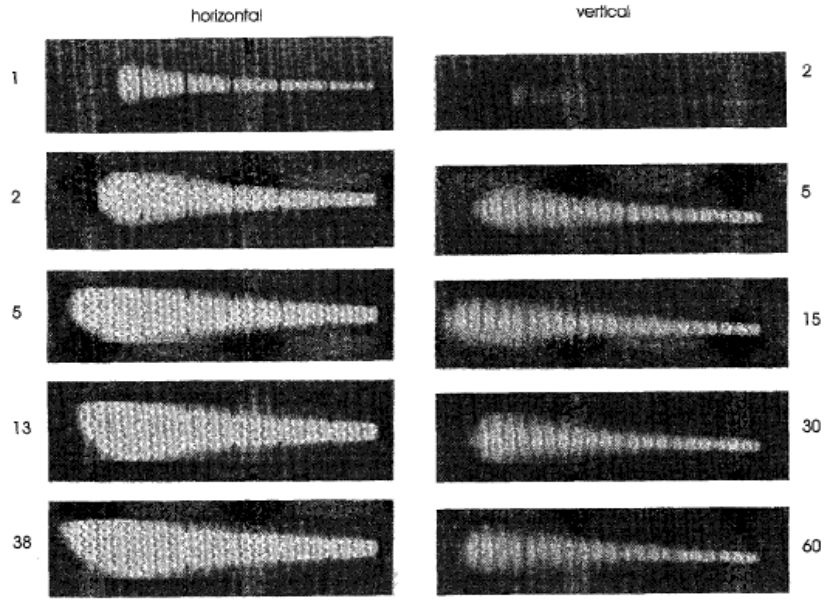

Figure 1-4: Frames of recorded light during bombardment with horizontal and vertical beams (Ar, 6.8 bar, 5.8 μA) with 40 ms/frame [14].

Initially the beam holds its predicted symmetric shape. Given the beam's theoretical range, there is no time for buildup of a density gradient across or along the target or for mass transport. This range can be described via the appropriate charged particle stopping power formula and this initial penetration into the target is at a minimum.

The range of the incident beam quickly increases, reaching a maximum size and length after a few tenths of a second. The density along the charged particle path is significantly reduced as a result of heat deposition, and the impact of mass transport becomes significant due to buoyancy effects. After this initial maximum penetration, the beam shape and length slowly change as the thermal upward mass transport, density profile, heat transfer, and gas and

wall temperature reach equilibrium. The top edge of a horizontal beam penetrates further due to the upward thermal and downward density gradient. Upward mass transport is symmetric for a vertical irradiation, causing a peaked but symmetric beam shape. The equilibrium beam range reaches some length that is between its maximum and minimum penetration.

Experimental observations indicate there is a significant impact on beam penetration and shape resulting from mass transport and density reduction. While this provides compelling evidence that the observed beam behavior is dictated by the density variation of the target gas resulting from heat deposition and mass transport, the authors state that this phenomenological model must be confirmed by further experiments and via computer simulation. The observed behavior has a significant impact on applications of radioisotope gas targetry, and knowledge of these observed beam shapes will influence the construction of higher-yield targets for isotope production and the appropriate choice of beam current, gas pressure, and target geometry. The authors used their preliminary findings of optically observed beam penetration from the observed light emission to increase yield production in target designs.

Prior work performed by Heselius et al. involved bulk models for net target behavior, but Tárkányi et al. outlined the significance of quantifying the target material properties as a function of position due to their impact on beam penetration and yield. The observed beam shape has implications for radioisotope gas targetry. Fluid redistribution due to density variation influences conduction, convective heat transfer, and radiative heat transfer. Given thermal conductivities of gases are quite low, quantifying the impact of natural convection in the system becomes significant. Accurately modeling the temperature and density distribution within the system facilitates accurate transmitted energy and yield predictions when selecting target parameters. The authors developed a physics driven theory for the behavior seen in gas targetry to offer as possible explanation of the observed effect, e.g. the density variation of the target gas under non-uniform heat production and mass transport as a function of time.

Lenz developed a computational model to couple stopping power and density using computational fluid dynamics (CFD) software for a gas target [17]. In this work, stopping power calculations were performed and the coupled nature of the target density distribution

and heat deposition were accounted for, but it is unclear to what extent. It appears as though the author took into account only the axial density variation and not the angular variation.

Multi-physics coupling of the energy deposition and density distribution within the target medium is necessary to accurately capture the effects of a particle beam impinging upon a target to generate a radioisotope, particularly for a highly compressible target material. In the early stages of our work, a multi-physics coupling methodology was established using ANSYS Fluent and MCNPX to model thermal hydraulic behavior and particle transport [18] in gas targets.

Previous research demonstrated the success of this approach for a water target operating at a very low beam current [12,13]. Since water is a relatively incompressible fluid, the density distribution that developed within the target as a result of energy deposition did not vary strongly with successive iterations. Our earlier work established a methodology based on a convergent set of stable solutions for a gas target [18] in order to examine the same coupling for highly compressible fluids, where density varies significantly due to energy deposition. Accurate predictions of beam penetration and internal fluid conditions are required for optimization and improved performance of the target design. This coupling was done to model incident deuterons on a conical Ne target for the $^{nat}Ne(p,n)^{18}F$ reaction.

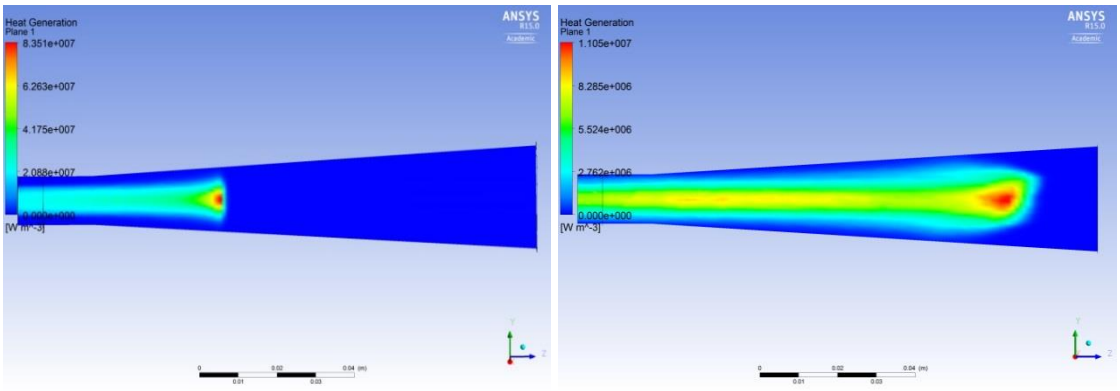

Figure 1-5: Uniform density beam energy deposition distribution (L) and beam energy deposition distribution of steady state solution (R) [18].

The significant change in the beam penetration illustrated in Figure 1-5 demonstrates the need to treat beam transport and thermal hydraulic behavior in a coupled manner. This

elongation in beam shape was also seen in [14–16] in optically observed images of beam shape during operation in gas targets. The first frame of the horizontal irradiation in Figure 1-4 is very similar to the first image in Figure 1-5, while the fifth frame bears a close resemblance to the second image. This clearly demonstrates that the iteration process employed mimics the time dependent evolution of the beam shape and density distribution. Thus the body of this work provides proof of concept for using this coupling methodology and its significance for both beam penetration and mass transport as a result of convective currents and density variation.

Peeples et al. applied this methodology [12,13,18] to design and optimize a high current conical ^{11}C gas target with a well characterized production yield for the $^{14}N(p,\alpha)^{11}C$ reaction [19].

Two different prototype geometries were designed and benchmarked for the production of ^{11}C. To employ the multi-physics technique, explicit coupling of radiation transport in MCNPX to a computational fluid dynamics model of the gas target in ANSYS Fluent was performed as demonstrated in [18]. Both prototypes were conical in shape with a length of 25 cm and a window diameter of 1.2 cm. The taper angle for prototype 2 was increased so that the back wall diameter was 2.72 cm versus the 2.24 cm back wall diameter of prototype 1. The aluminum body walls of both prototypes were cooled using four 6.1 mm water channels, and both the principal 38 μm Havar and vacuum 25 μm Havar windows were cooled with helium.

Axial plots of yield and temperature profiles determined after iterating to reach a convergent solution for the prototype 1 design are shown in Figure 1-6 and Figure 1-7.

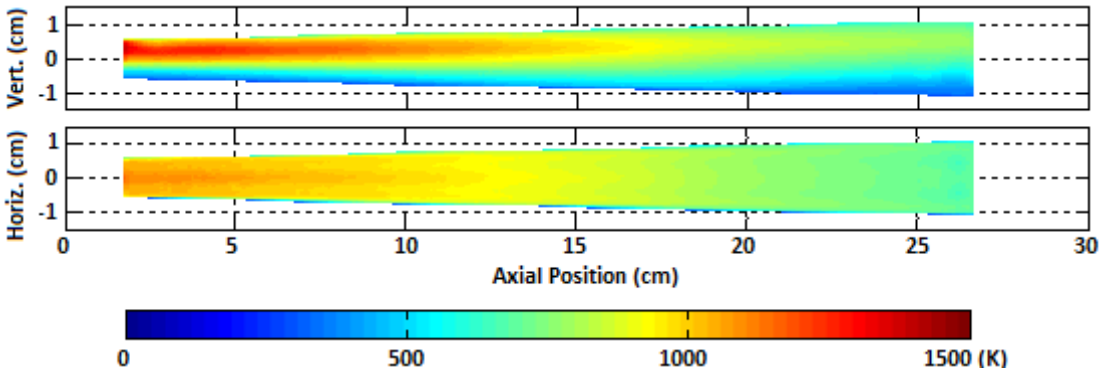

Figure 1-6: Nitrogen temperature along vertical and horizontal mid-planes for case A1 (80 μA and 16 bar) [19].

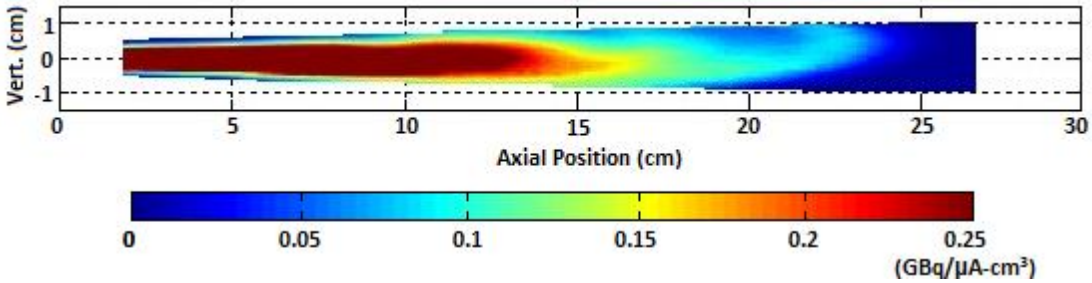

Figure 1-7: Yield density distribution along vertical mid-plane for case A1 (80 μA and 16 bar) [19].

The temperature profile and yield density distribution shown in Figure 1-6 and Figure 1-7, respectively, illustrate the active region of the target and demonstrate a shape that correlates well with experimentally observed light emission from gas targets [14–16]. The temperature distribution seen is a result of convective currents and buoyancy forces within the target. The yield density distribution is useful for determination of the optimum target depth and diameter for maximum yield production. Based on the production rate distribution in Figure 1-7 it is clear that a significant portion of the target is not being utilized for production of ^{11}C.

Two copper foils each 25 μm thick were stacked in the back of the target chamber (with an energy degrader) to measure the transmitted energy spectrum. The measurement was performed by observing the ratio of ^{63}Zn activity produced in each copper foil and from this the average proton energy striking the back face of the target was estimated [20]. The two copper foils were included in the MCNPX geometry, and the foil activation ratio was used as an additional benchmark for the computational model.

Due to the 3.22 MeV threshold energy for the $^{14}N(p,\alpha)^{11}C$ reaction, protons of energies below 6 MeV contribute one third of the total heat input to the target, but less than 2% of the total production yield. Given the desire to optimize total target yield production implies an ideal target design is yield thick and range thin due to the proton threshold energy and location of the highest yield regions. The ideal target design would increase its volume only in regions of high yield production. Increasing target volume in a low yield region would detract from total net activity recovered due to decay.

Prototype 1 was tested by measuring target density and saturation yield to benchmark the multi-physics simulation as a predictive tool. Based on the yield density distribution in Figure 1-7 it is apparent that in prototype 1, activity is being lost to the radial walls, prompting the increase in taper angle for the design of prototype 2. As predicted by the model, prototype 2 produces a higher saturation yield than prototype 1, primarily due to less proton escape through the radial walls. Peeples et al. successfully proved that this multi-physics coupling technique is a valuable tool for gas target design and optimization. This computational methodology [18,19] will be directly adapted to perform modeling of RbCl-RbCl-Ga target stacks.

CHAPTER 2. MODELING

This dissertation focuses on the simulation set-up and multi-physics coupling process. To achieve accurate results, it is important to ensure that the appropriate simulation tools are chosen and employed in a manner reflecting real world system behavior. The multi-physics coupling technique chosen is also significant, as effectiveness and frequency of communication between two different computational tools can impact the behavior of the simulation. MCNP [21] was used to model radiation transport and particle interactions, while ANSYS CFX [22] was used as the computational fluid dynamics package. These codes are extremely robust tools for modeling particle transport and thermal hydraulic behavior.

Several iterations of models were created in both MCNP and ANSYS CFX. The first two iterations of the ANSYS CFX model were utilized as learning tools, and modifications were made as necessary to more closely match real-world system conditions. Assistance in ANSYS CFX model set-up was provided by Eric Olivas, a LANL employee who has modeled RbCl targets in ANSYS CFX in the past.

In order to gain first order knowledge about the system, the problem geometry in ANSYS CFX was simplified and an average heat transfer coefficient boundary condition was applied between the target capsules and the cooling water. This significantly reduced the problem size and complexity in order to recognize and address issues with model set up quickly. This simpler model was able to quickly generate an initial guess at the equilibrium beam distribution and thermal hydraulic conditions. It may also be employed for scoping studies in a preliminary design phase.

Once this initial set up yielded results, the cooling water domain was added into the system to more accurately model heat removal. Based on the results provided by this model, several corrections were made to the MCNP geometry and the multi-physics coupling process.

These changes were applied to the final model, which was created to capture heat removal from the targets via the four cooling water channels with an increased level of accuracy. This refined model was then utilized for validation, as discussed in Chapter 4. Model iterations

ensure that errors in the coupling process or model set up have been addressed and that heat removal from the system is being represented with the highest degree of accuracy possible.

Section 2.1. ANSYS CFX

Computational fluid dynamics codes solve mass, energy, and momentum conservation equations describing fluid flow over a region of interest given a set of known boundary conditions. This is accomplished by dividing all regions of interest into small sub-regions called control volumes, or cells. The fluid conservation equations are then discretized to generate a linearized system of equations for all these cells. This matrix system is solved computationally to provide information regarding heat and mass transfer and fluid motion. ANSYS CFX utilizes these techniques to simulate the behavior of thermal fluid systems. When modeling anything using computational fluid dynamics software, it is essential to ascertain what aspects of the system geometry are required for capturing relevant physics and what boundary conditions are necessary to enclose the system.

ANSYS CFX consists of five components, or modules, each with specific roles in the modeling process. The tasks performed by each component are listed below in Table 2-1.

Table 2-1: Component modules comprising ANSYS CFX model set-up.

Component	Task
Geometry	Edit geometry
Meshing	Divide geometry into mesh elements
Setup	Material definition
	Initial Conditions
	Boundary Conditions
	Physics models
	Simulation Type
	Convergence criteria
Solver	Solves linearized system of equations on mesh
	Monitors solution progress
Results	Post-process results
	Visualize thermal hydraulic behavior

The problem-specific tasks performed by the meshing, setup, and solver modules will be detailed in the following sections of this chapter. All CFX results may be post-processed in the results module, and these results will be presented in Chapter 3.

The geometry module in ANSYS is capable of importing computer-aided design (CAD) geometries. A labelled SolidWorks [23] image of the full CAD representation of the target stack geometry is given below in Figure 2-1.

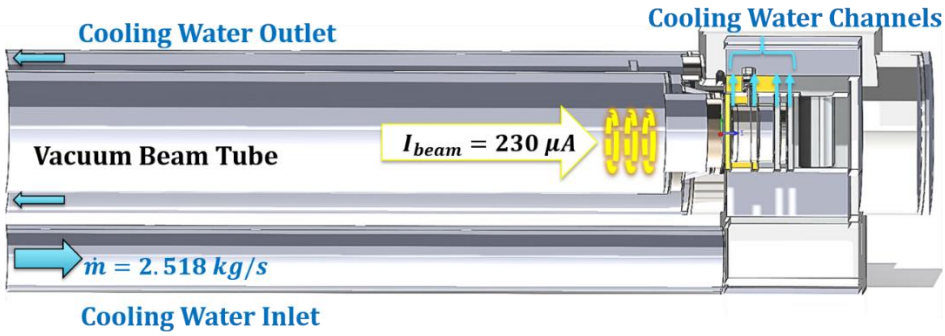

Figure 2-1: Labelled SolidWorks [23] geometry with problem parameters.

Some of the components shown in the above geometry were removed to simplify the model and minimize unnecessary computational expense. All components removed, such as the aluminum housing bodies, were considered non-essential physical components whose removal would not detract from the completeness of the model. The model as viewed in the geometry editor of ANSYS is described for each model set-up to illustrate which bodies were suppressed.

Section 2.1.1. Boundary Conditions

As all aspects of the flow are symmetric about the YZ plane, a symmetry plane was created for all models. Within ANSYS CFX the symmetry plane boundary condition imposes constraints that assume the flow is 'mirrored', or symmetric, about the specified plane.

A fluid-solid interface was created between the targets and their capsules. These interfaces generate boundaries that account for heat transfer via conservative interface flux along a smooth, no-slip wall. Other additional boundary conditions required for each model iteration are described in separate sections below.

Section 2.1.1.1. Average Heat Transfer Coefficient Model

In order to speed up the iterative process, the geometry was temporarily simplified by omitting the cooling water. Only the RbCl targets A and B and their capsules were included in this initial simulation.

An average heat transfer coefficient (htc) of 10742 [W m^{-2} K^{-1}] was applied as a boundary condition along the cooling water faces. This value was determined using the process outlined here. The Prandtl, Reynolds, and Nusselt numbers are dimensionless parameters given below in Eq. (2-1) – Eq. (2-3).

$$Pr = \frac{C_p \cdot \mu}{k} \tag{2-1}$$

$$Re = \frac{G \cdot D_e}{\mu} \tag{2-2}$$

$$Nu = \frac{h_c \cdot D_e}{k} \tag{2-3}$$

For this calculation all water properties were taken at atmospheric pressure with an average temperature of 300 K. Here C_p is the specific heat of water, μ is the dynamic viscosity, k is the thermal conductivity, G is the mass flux, and h_c is the convective heat transfer coefficient.

The Nusselt number for flow inside a channel may be determined using the empirical Dittus-Boelter [24] correlation given in Eq. (2-4). Since the fluid is being heated, $n = 0.4$.

$$Nu = 0.023 Re^{0.8} Pr^n \tag{2-4}$$

The equivalent diameter D_e for a rectangular channel can be determined using Eq. (2-5).

$$D_e = \frac{4wl}{2(w+l)} \tag{2-5}$$

In the above equation w and l are the cross-sectional dimensions. Given the relationships provided in Eq. (2-3) and Eq. (2-4) for the Nusselt number, the heat transfer coefficient may be solved for as shown in Eq. (2-6).

$$h_c = \frac{k \cdot 0.023 Re^{0.8} Pr^n}{D_e} \tag{2-6}$$

All other boundaries were considered insulated and assigned a smooth, no-slip adiabatic wall boundary condition.

Section 2.1.1.2. Full Cooling Water Domain Model

For the second model iteration the cooling water, beam window, and C-slot gallium target and capsule were added to the problem geometry. The cooling water is considered an essential system component as it is important to incorporate the impact of modeling heat removal via

the cooling water channels on the system. A fluid-solid interface was created between the cooling water flow and the target capsules and beam window as well as between the targets and their capsules. These interfaces generate boundaries that account for heat transfer via conservative interface flux along a smooth, no-slip wall. The RbCl and Ga targets are encapsulated by materials (Inconel 625 and Nb) that remain solid during nominal operation conditions.

The Inconel 718 beam window face exposed to the vacuum beam tube and impinging beam was insulated by defining the surface with a smooth, no-slip adiabatic wall boundary condition. All surfaces of the water domain not serving as an interface with the solid target capsules or the beam window or as a symmetry boundary condition were also assigned this insulating boundary condition. The geometry as visualized in the CFX setup module is shown below in Figure 2-2. The axes shown with the geometry in the lower right hand corner give a feel for the orientation of the problem.

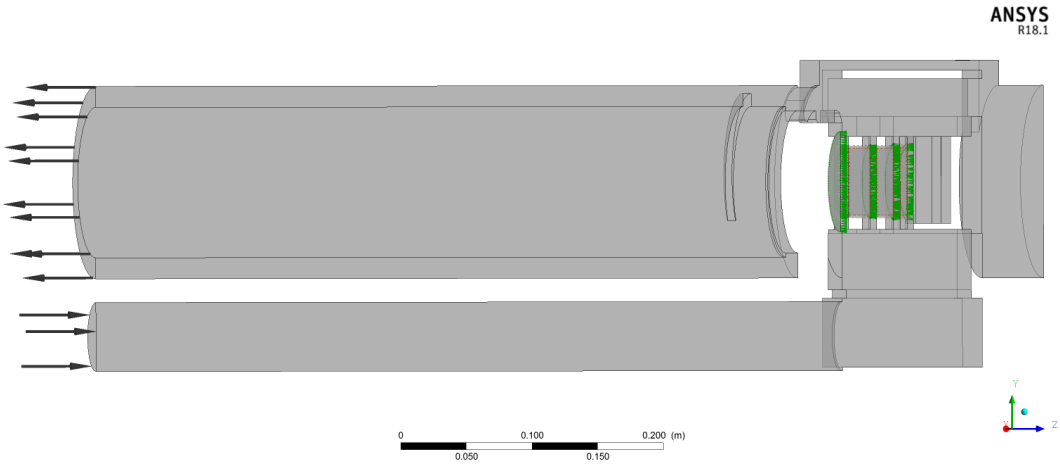

Figure 2-2: Full cooling water geometry in ANSYS CFX Pre with assigned boundary conditions.

A total pressure of 0.117 MPa was specified as a boundary condition normal to the cooling water inlet with a static inlet temperature of 298.15 K. The total pressure is the sum of the static and dynamic pressures for incompressible flows, as shown in Eq. (2-7). A zero boundary gradient was specified at the inlet as recommended for turbulent flow systems.

$$P_{total} = P_{static} + \frac{1}{2}\rho(U \cdot U) \tag{2-7}$$

In Eq. (2-7) U is the fluid velocity and ρ is the fluid density, and with these values the CFX solver is able to compute the static pressure needed to properly close the boundary condition. The cooling mass flow rate outlet boundary condition was specified as 2.518 kg/s. However, as a symmetry boundary condition is used for this model, the domain is half the size, and therefore the cooling mass flow rate must be divided by two. Thus, $\frac{\dot{m}}{2}$ = 1.259 kg/s.

Section 2.1.1.3. Refined Cooling Water Domain Model

In order to ensure the solution for this system is complete and heat transfer out of the system is accurate, it is necessary to incorporate the cooling water into the model while also fully resolving the boundary layers in the four cooling water channels adjacent to the target pucks. This allows for a complete and accurate representation of heat removal from the system during operation. For this refined cooling water model, the cooling water domain size was significantly reduced to increase resolution in the cooling water channels without compromising run time. The problem geometry as visualized in the CFX setup module is shown in Figure 2-3.

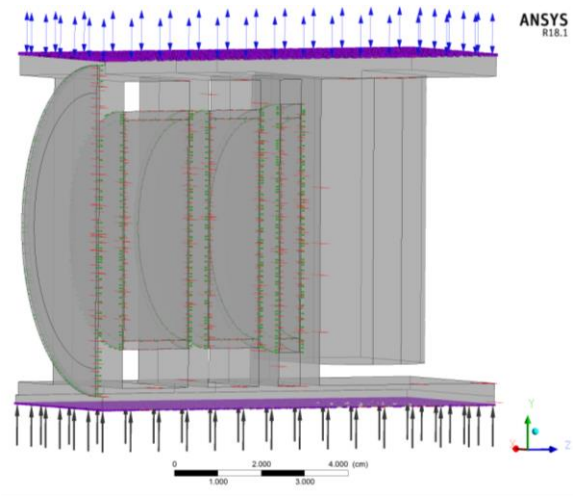

Figure 2-3: Simplified cooling water geometry in ANSYS CFX-Pre with assigned boundary conditions.

In order to obtain boundary conditions for the refined cooling water geometry, a steady state ANSYS solve of the full cooling water geometry illustrated in Figure 2-2 with no heat

transfer was used. All heat input was suppressed, and the model was run with only the cooling water present and the appropriate inlet and outlet boundary conditions discussed in Section 2.1.1.2.

Once a full solution was obtained for the cooling water problem, a plane was taken 5 mm above and below the inlet and outlet of the cooling channels. Flow data exported from these planes may be imposed as boundary conditions in the refined cooling water geometry to simulate velocity and pressure profiles seen when modeling the full cooling water problem.

The (u,v,w) velocity components and the static pressure were exported at the planes where the boundary condition was to be applied in the refined cooling water model. The static pressure was supplied as the inlet boundary condition and the velocity components were supplied as the outlet boundary condition.

An opening boundary condition was applied at the outlet instead of a fixed outlet boundary condition. This is to allow for inflow into the system as a result of recirculating fluid currents at the exit of the cooling channels. These recirculating fluid currents are a product of the manifold-type geometry.

Section 2.1.2. Material Definition

Section 2.1.2.1. Cooling Water

Water was defined using the IAPWS-IF97 database within ANSYS. This database spans temperatures from 273.15 K to 1073.15 K and pressures from 611 Pa to 100 MPa. For this simulation the water domain should not exceed the lower single phase range of this database given its flow conditions. The analytical equation of state is used to create a tabular set of values that can be utilized efficiently in a CFD calculation.

Section 2.1.2.2. User-Defined Materials

Material definition in ANSYS CFX for this type of problem requires significant user input regarding material thermal properties. A tabulated set of material properties as a function of temperature must be imported and defined as user functions and expressions. All imported material properties used for this model are listed in Appendix B.

ANSYS supports user-defined equations of state, and any temperature-dependent equations of state (such as density and specific heat) can be written as below.

$$\rho = \rho(P,T) \tag{2-8}$$

$$C_p = C_p(T,P) \tag{2-9}$$

Density and specific heat are both a function of pressure and temperature. For this problem the materials are relatively independent of pressure, or the pressure is known and assumed to be constant. This allows the user to pull data as a function of only temperature at the known pressure [22].

The enthalpy may be calculated given a known pressure, temperature, and specific heat.

$$dh = \frac{\partial h}{\partial T}\bigg|_P dT + \frac{\partial h}{\partial P}\bigg|_T dP \tag{2-10}$$

$$dh = C_p dT + \frac{\partial h}{\partial P}\bigg|_T dP \tag{2-11}$$

But since:

$$\frac{\partial h}{\partial P}\bigg|_T = v - T\frac{\partial v}{\partial T}\bigg|_P \tag{2-12}$$

The equation of state for enthalpy can be written as shown in Eq. (2-13), where the specific volume $v = \frac{1}{\rho}$.

$$dh = C_p dT + \left(v - T\frac{\partial v}{\partial T}\bigg|_P\right)_T dP \tag{2-13}$$

To calculate change in enthalpy, Eq. (2-13) is integrated to construct a table of enthalpies based on supplied data for specific heat and density.

$$h_2 - h_1 = \int_{T_1}^{T_2} C_p dT + \int_{P_1}^{P} \frac{1}{\rho}\left[1 + \frac{T}{\rho}\left(\frac{\partial \rho}{\partial T}\right)_P\right] dP \tag{2-14}$$

When material properties are supplied only as a function of temperature at a known pressure, then the change in enthalpy is only dependent upon the change in temperature and specific heat in the system and may be written as shown in Eq. (2-15).

$$h_2 - h_1 = \int_{T_1}^{T_2} C_p dT \tag{2-15}$$

As stated above, for this analysis material properties were assigned only as a function of temperature. This is valid for the definition of a general equation of state, but requires

specification of both density and specific volume at a constant pressure (C_p), not at a constant volume (C_v). This is because it is impossible to heat fluids at a constant volume when density is only a function of temperature. When this is the case, thermal expansion cannot be adjusted by changes in system pressure. In this case, the value for C_v would be extremely large – essentially infinite.

The melting point of gallium is only slightly above room temperature (302.9 K/85.6 °F), so it will be in a liquid state almost immediately during operation. Therefore gallium was treated as being solely in the liquid phase and only liquid-state thermal properties were imported and used.

RbCl is a mixture consisting of one atom of natural rubidium and one atom of chlorine, with 70.681 mass percent rubidium and 29.319 mass percent chlorine. As the RbCl target is heated during operation, some of the target will melt and there will be both liquid and solid RbCl present. ANSYS CFX does not presently have the capability to explicitly model phase change from solid to liquid.

A process for defining RbCl to account for phase change from solid to liquid was established by Eric Olivas in conjunction with ANSYS corporate [25]. RbCl data was provided across a range of temperatures for dynamic viscosity, thermal conductivity, density, and specific heat. In order to account for the two-phase solid-liquid behavior of the RbCl targets, a homogeneous phase change model was defined in ANSYS CFX. This model facilitates a transition from solid to liquid RbCl material properties at the material melting temperature of 990 K (~717 °C). Homogeneous binary mixtures can be used to define the phase boundary between two different thermodynamic states of the same material existing simultaneously in a domain. The phase change model will be described in further detail in Section 2.1.4.2.

Section 2.1.3. Physics Models

While the full three-dimensional time-dependent Navier-Stokes equations are able to resolve turbulent flows completely, they lack an analytic solution and numerical approaches to solving them are computationally prohibitive for problems of this nature and scale [26]. The full conservative form of the continuity and momentum equations are shown below for a compressible system.

$$\frac{\partial \rho}{\partial t}+\nabla\cdot(\rho\vec{u})=0 \tag{2-16}$$

$$\frac{\partial(\rho\vec{u})}{\partial t}+\nabla\cdot\left(\rho\vec{u}\left(\vec{u}^{\,T}\right)\right)=-\nabla p\vec{I}+\nabla\cdot\bar{\bar{\tau}}+\bar{\rho}\vec{g} \tag{2-17}$$

In Eq. (2-17) $\bar{\rho}$ is the average system density, $\vec{u}$ is the velocity, p is the system pressure, $\vec{I}$ is the identity vector, $\vec{g}$ is gravity, and $\bar{\bar{\tau}}$ is the stress tensor describing the shear and normal stresses for the system. This stress tensor is of the form shown below.

$$\bar{\bar{\tau}}=\begin{bmatrix}\tau_{xx} & \tau_{xy} & \tau_{xz}\\ \tau_{yx} & \tau_{yy} & \tau_{yz}\\ \tau_{zx} & \tau_{zy} & \tau_{zz}\end{bmatrix}=\begin{bmatrix}\sigma_{x} & \tau_{xy} & \tau_{xz}\\ \tau_{yx} & \sigma_{y} & \tau_{yz}\\ \tau_{zx} & \tau_{zy} & \sigma_{z}\end{bmatrix}$$

The conservative form of the energy equation is given in Eq. (2-18).

$$\frac{\partial}{\partial t}\left[\rho\left(h+\frac{u^2}{2}\right)\right]+\nabla\cdot\left[\rho\left(h+\frac{u^2}{2}\right)\vec{u}\right]=\nabla\cdot(\lambda\nabla T)+\nabla\cdot(\vec{u}\cdot\tau)+\vec{u}\cdot\vec{S}_M+\vec{S}_E \tag{2-18}$$

Here the static enthalpy h is a function of temperature and pressure $h(T,P)$. Eq. (2-18) may also be written using total enthalpy, where $h_{total}=h+\frac{u^2}{2}$.

$$\frac{\partial}{\partial t}(\rho h_{total})+\nabla\cdot(\rho h_{total}\vec{u})==\nabla\cdot(\lambda\nabla T)+\nabla\cdot(\vec{u}\cdot\tau)+\vec{u}\cdot\vec{S}_M+\vec{S}_E \tag{2-19}$$

In Eq. (2-19) the $\nabla\cdot(\vec{u}\cdot\tau)$ term represents the work due to viscous stresses and is generally very small, $\vec{S}_E$ encompasses all external energy sources, and λ is the thermal conductivity. In order to define these equations in a form which may be more easily solved, instantaneous quantities are decomposed into both a time-averaged and a fluctuating quantity.

$$U_i=\bar{u}_i+u_i'$$

This is applicable when working with time scales much larger than the time scale corresponding to turbulent fluctuations. The resulting equations are called the Reynolds-averaged Navier-Stokes (RANS) equations. The unknown quantity now becomes the fluctuating time-dependent component of these equations, also known as the Reynolds stresses and fluxes. These unknown Reynolds stresses and fluxes require closure equations in the form of turbulence models [22]. The conservative form of the RANS continuity and momentum equations are shown in Eq. (2-20) and Eq. (2-21).

$$\frac{\partial \rho}{\partial t} + \frac{\partial}{\partial x_j}\left(\rho U_j\right) = 0 \tag{2-20}$$

$$\frac{\partial \rho U_i}{\partial t} - \frac{\partial \rho}{\partial t} + \frac{\partial}{\partial x_j}\left(\rho U_i U_j\right) = - \frac{\partial p}{\partial x_i} + \frac{\partial}{\partial x_j}\left(\tau_{ij} - \rho\overline{u_i u_j}\right) + S_M \tag{2-21}$$

In Eq. (2-21), gravity is folded into the momentum source term, S_M, which includes all work due to external momentum sources. τ_{ij} represents the normal and shear viscous forces and $-\rho\overline{u_i u_j}$ is the Reynolds stress due to the fluctuating velocity field. The conservative form of the RANS energy equation is shown below in Eq. (2-22).

$$\frac{\partial \rho h_{total}}{\partial t} - \frac{\partial \rho}{\partial t} + \frac{\partial}{\partial x_j}\left(\rho u_j h_{total}\right) = \frac{\partial}{\partial x_j}\left(\lambda \frac{\partial T}{\partial x_j} - \rho\overline{u_j h}\right) + \frac{\partial}{\partial x_j}\left[u_i\left(\tau_{ij} - \rho\overline{u_i u_j}\right)\right] + S_E \tag{2-22}$$

Two-equation eddy viscosity turbulence models are frequently employed to provide closure for the RANS equations. These eddy viscosity turbulence models use the Boussinesq approximation, assuming that the Reynolds stresses are proportional to the mean velocity gradients. This relationship is shown below [22].

$$-\rho\overline{u_i u_j} = \mu_t\left(\frac{\partial U_i}{\partial x_j} + \frac{\partial U_j}{\partial x_i}\right) - \frac{2}{3}\delta_{ij}\left(\rho k + \mu_t \frac{\partial U_k}{\partial x_k}\right) \tag{2-23}$$

In Eq. (2-23) U is the velocity, μ_t is the eddy viscosity, δ_{ij} is the Kronecker delta, ρ is the density, and k is the turbulent kinetic energy given below.

$$k = \frac{1}{2}\overline{u_i' u_i'} \tag{2-24}$$

While zero, one, and two-equation eddy viscosity turbulence models may be used, two-equation turbulence models are most frequently employed. Two-equation models utilize both the velocity and length scales [26], and the number of equations corresponds to the number of differential equations that must be solved in addition to the mean flow equations.

Several two-equation models exist, each appropriate for specific flow conditions. The k - ϵ model is a frequently used two-equation turbulence model. In this model k is the turbulent kinetic energy in [m^2/s^2] and ϵ is the turbulent eddy dissipation rate, or the rate at which fluctuations in velocity dissipate, with units of [m^2/s^3] [22]. This dissipation rate may be calculated as shown in Eq. (2-25) [26] where ν is the kinematic viscosity in [m^2/s].

$$\epsilon = \nu\frac{\overline{\partial u_i \partial u_i}}{\partial x_k \partial x_k} \tag{2-25}$$

This model requires damping functions or higher order correlations near the wall in order to capture boundary layer effects, reducing the numerical robustness. It also does not supply natural boundary conditions for turbulent dissipation near the wall [27].

Capturing the effects of near wall turbulence is essential to accurately modeling wall heat transfer as the velocity profile near the wall dictates how quickly heat is removed. With turbulent near wall flows, the removal rate of heat rapidly increases, not allowing for the development of an insulating layer.

For this reason the k - ω model is desirable in the boundary layer near the wall as it does not require damping functions or correlations and is therefore more numerically robust [28]. In this model ω is the turbulent frequency, or the rate of dissipation of turbulence per unit energy [29], with units of [s^{-2}]. This turbulent frequency, ω, is determined in terms of ϵ and k as shown below [26], where C_D is a constant.

$$\omega = \epsilon^2/(C_D k)^2 \tag{2-26}$$

The k - ω model has also been shown to be superior to the k - ϵ model when dealing with adverse pressure gradients and compressible flows. However the k - ω model is limited due to its extreme sensitivity in freestream flows due to the freestream value of ω – a problem not shared by the k - ϵ model. To combine the beneficial aspects of these two models, Menter [28] utilized a blending function to take advantage of the k - ϵ model in the wake and freestream region and utilize the k - ω model in the sublayer and boundary layer regions. This yields coefficients for the combined models of the form:

$$\phi_{BSL} = F_1\phi_{k\text{-}\omega} + (1\text{-}F_1)\phi_{k\text{-}\epsilon} \tag{2-27}$$

The blending function F_1 is equal to one near the wall and approaches zero as it enters the freestream region. This is called the baseline (BSL) model, and the summation of the k - ω and k - ϵ models with these blending functions is shown below.

$$\frac{\partial(\rho k)}{\partial t} + \frac{\partial}{\partial x_j}\left(\rho u_j k\right) = \tau_{ij}\frac{\partial u_i}{\partial x_j} - \beta^*\rho\omega k + \frac{\partial}{\partial x_j}\left[\left(\mu + \sigma_k\mu_t\right)\frac{\partial k}{\partial x_j}\right] \tag{2-28}$$

$$\frac{D\rho\omega}{Dt} = \frac{\gamma}{\nu_t}\tau_{ij}\frac{\partial u_i}{\partial x_j} - \beta\rho\omega^2 + \frac{\partial}{\partial x_j}\left[\left(\mu + \sigma_\omega\mu_t\right)\frac{\partial\omega}{\partial x_j}\right] + 2\rho(1\text{-}F_1)\sigma_{\omega 2}\frac{1}{\omega}\frac{\partial k}{\partial x_j}\frac{\partial\omega}{\partial x_j} \tag{2-29}$$

In this new formulation β^*, β, $\sigma_{\omega 2}$, γ, σ_ω, and σ_k are prescribed constants provided by Menter's formulation [28]. μ_t is the dynamic turbulent eddy viscosity, μ is the molecular dynamic viscosity, and v_t is the kinematic turbulent eddy viscosity, $v_t = \mu_t/\rho$. τ_{ij} is the turbulent shear or Reynold's stress, $\tau_{ij}=-\rho\overline{u_i u_j}$.

In order to improve the robustness of this model in adverse pressure gradients, i.e. where $\frac{dP}{dz}$ is very large for flows travelling in the positive z direction, Menter also developed the shear stress transport (SST) model [28]. In addition to the modifications made for the BSL model, this model modifies the eddy viscosity term in order to account for the transportation of turbulent shear stress. It is known that the turbulent shear stress is proportional to the turbulent kinetic energy in the wake region of the boundary layer, but traditional eddy viscosity definitions fail to recognize this. The Johnson-King (JK) model [30] accounts for this proportionality via the relationship shown in Eq. (2-30).

$$\tau = \rho a_1 k \tag{2-30}$$

In Eq. (2-30), τ is the turbulent shear stress, k is the turbulent kinetic energy, and a_1 is a constant.

However, for both the k - ω and k - ϵ two-equation models, this shear stress is expressed in the form shown below.

$$\tau = -\rho\overline{u'v'} = \mu_t \frac{\partial u}{\partial y} \tag{2-31}$$

The formulation of the dynamic eddy viscosity for the k - ϵ model is given below [26].

$$\mu_t = \rho C_\mu \frac{k^2}{\epsilon} \tag{2-32}$$

While the dynamic eddy viscosity for the $k - \omega$ model is of the form [29]:

$$\mu_t = \rho \frac{k}{\omega} \tag{2-33}$$

According to Menter [31] the following relationship for turbulent shear stress is valid for boundary-layer flows outside of the viscous sublayer.

$$-\overline{u'v'} = C_\mu \frac{k^2}{\epsilon}\frac{\partial u}{\partial y} = \frac{k}{\omega}\frac{\partial u}{\partial y} \tag{2-34}$$

And therefore Eq. (2-34) may be rewritten as given in Eq. (2-35).

$$-\overline{u'v'} = \sqrt{\frac{Production_k}{Dissipation_k}} a_1 k \tag{2-35}$$

To prevent over-prediction of experimental values of τ as is commonly done in adverse pressure gradient flows where the ratio of production to dissipation is over predicted [28,31], a new eddy viscosity may be defined.

$$\mu_t = \frac{a_1 k}{\max\left(a_1 \omega \; ; \; \frac{\partial u}{\partial y} F_2\right)} \tag{2-36}$$

In Eq. (2-36), F_2 is a function equal to one in the boundary layer and zero in free shear layer flows. Thus, in the adverse pressure gradient boundary layers Eq. (2-30) is satisfied but $\mu_t = k/\omega$ is still applied for free shear flow outside the boundary layer. This SST model is thus capable of capturing both the onset and amount of flow separation. This is depicted in Figure 2-4.

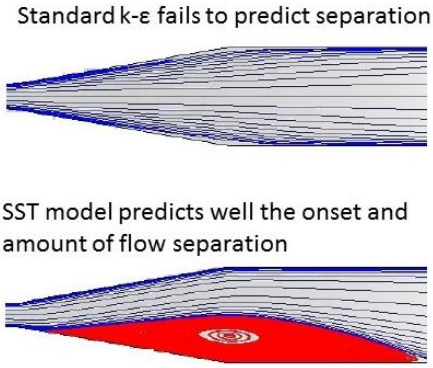

Figure 2-4: Flow separation prediction using the standard k-ε and the SST turbulence models [25].

The SST model was chosen for this work, particularly in the cooling water domain as the manifolds create recirculating flows, indicating that flow reversal and separation is occurring.

In the target domains a modification to the SST model called the two equation gamma theta transition model was employed. It is also known as the Langtry-Menter transitional shear stress transport turbulence model [32,33]. This model allows for the transition from laminar to turbulent flow in fluid domains via calculation of a transitional Reynolds number. This is useful for the target domains where laminar flow regions may exist.

Section 2.1.4. Source Terms

Source terms were defined to model heat input to the system in the form of volumetric heat generation rates. Source terms were also used to allow for phase change in the RbCl target material.

Section 2.1.4.1. Volumetric Heat Generation

The incident proton beam deposits a significant amount of heat in each target body and this must be accounted for in the model. In each domain a heat transfer option of thermal energy for both solids and fluids was chosen. An additional heat generation variable was assigned to all domains, with heat generation data being divided into each domain based on coordinate location. This is to prevent interpolation or smearing between the regions, which would lead to an inaccurate prediction of beam energy deposition.

Heat generation information was imported as a three-dimensional set of cylindrical coordinate data with units of [cm,cm,rad,W cm^{-3}]. The argument units correspond to the (r,z,θ) coordinates over the domain volume and the volumetric heat generation rate at each corresponding location. The domains in which volumetric heat generation was incorporated for each model is shown below in Table 2-2.

Table 2-2: Domains incorporating volumetric heat generation for each model.

Domains with Volumetric Heat Generation			
Domain	**Average Heat Transfer Coefficient Model**	**Full Cooling Water Domain Model**	**Refined Cooling Water Domain Model**
In718 Window	–	×	×
In625 Capsule A	×	×	×
RbCl Target A	×	×	×
In625 Capsule B	×	×	×
RbCl Target B	×	×	×
Nb Capsule C	–	×	×
Ga Target C	–	×	×
Cooling Water	–	–	×

Section 2.1.4.2. RbCl Momentum Source Term

As ANSYS CFX is not capable of modeling solid-liquid phase change independently, both a momentum source and porous loss term are required to capture the behavior of the partially

molten RbCl targets. The set-up described in this section was developed by Eric Olivas from LANL in conjunction with designers from ANSYS corporate [25].

Darcy's law describes the resistance to flow in porous mediums, e.g. in regions of phase change. A general formulation of Darcy's law is shown below in Eq. (2-37) [34] and is used to calculate the pressure drop of a fluid flowing through a packed bed of solids or flow through partially molten porous regions.

$$\frac{\Delta P}{L} = \frac{Q}{K_{perm} \cdot A}\mu = \frac{v}{K_{perm}}\mu \tag{2-37}$$

In Eq. (2-37) Q is the volumetric flow rate, determined by $Q = v \cdot A$ where v is the fluid velocity and A is the cross-sectional flow area, μ is the fluid dynamic viscosity, and K_{perm} is the permeability coefficient. A common form of Darcy's law is the Kozeny-Carman permeability model [35], which is applied to capture the resistance to flow and momentum loss in partially solid – or mushy – regions. This model is only valid for laminar flows when the Reynolds number is less than one, and one formulation is given below [36].

$$\frac{\Delta P}{L} = - \frac{180\mu}{\varphi_s^2 D_p^2} \frac{(1-\epsilon)^2}{\epsilon^3} v_s \tag{2-38}$$

In Eq. (2-38) ΔP is the pressure drop, L is the total height of the bed, v_s is the superficial velocity, μ is the fluid viscosity, ϵ is the porosity (or liquid fraction) of the bed, φ_s is the sphericity of the particles in the packed bed, and D_p is the diameter of the related spherical particle.

This model may also be written as a function of the porosity (or liquid fraction), the surface area of the solid, and a Kozeny-Carman constant [34,35]. This is shown below in Eq. (2-39).

$$\frac{\Delta P}{L} = \frac{v}{K_{perm}}\mu = \frac{C_{kc} \cdot S_v^2 \cdot (1-\epsilon)^2}{\epsilon^3} = \frac{C_{kc} \cdot S_v^2 \cdot (1-\alpha_l)^2}{\alpha_l^3} \tag{2-39}$$

However, this permeability relationship is only applicable on the microscale, and to employ it in the present macroscale ANSYS model would require sub-grid modeling. Therefore this equation was reformulated as a function of only RbCl average liquid mass fraction, $\alpha_{l_{RbCl}}$, which is desirable in numerical simulations. With these alterations the permeability coefficient

given below in Eq. (2-40) was obtained [34]. In ANSYS CFX a minimum bound was placed upon the liquid fraction in order to prevent permeability coefficients of zero.

$$K_{perm} = \frac{\alpha_{l_{RbCl}}^3}{C_{KC}^{*}\left(1-\alpha_{l_{RbCl}}\right)^2} \tag{2-40}$$

The above permeability coefficient is then applied to Darcy's law from Eq. (2-37) to obtain the force per unit volume or pressure drop per unit length.

$$S = \frac{\Delta P}{L} = \frac{\mu \cdot C_{KC}^{*}\left(1-\alpha_{l_{RbCl}}\right)^2}{\alpha_{l_{RbCl}}^3} v \tag{2-41}$$

In ANSYS CFX this method treats the RbCl phase change region as an isotropically porous medium, where the porosity in a specific cell is defined as the RbCl liquid fraction present. If the RbCl liquid mass fraction is zero then the cell region of interest is solid and its porosity zero, thereby eliminating any fluid motion.

The result obtained depends heavily on the permeability constant chosen for this highly empirical model. The permeability constant C_{KC}^{*} was given a value of 1×10^{10} m^2. Typical microscale values of this constant are significantly smaller (approximately 1-5) for the Kozeny-Carman permeability model [34], but as this is a macroscale model, significantly larger constants are required. The greater this constant value the steeper the damping curve becomes and the faster the velocity drops to zero as the material solidifies. In any CFD calculation this value is chosen with care, for if this constant is too large the solution may oscillate, as mesh cells alternately solidify and melt with minor perturbations in the liquid volume fraction [22]. These oscillations are not desirable as they create numerical instabilities.

A momentum source term was applied as a force per unit volume acting on the fluid domain. Two directional sources were applied to account for buoyancy forces due to temperature gradients and phase change. Since the RbCl mixture is being modeled with the morphology of a continuous fluid, these terms form a momentum sink, ensuring that the fluid remains at a zero velocity condition if it is made up of a significant fraction of solid RbCl. These momentum source terms are given below in Eq. (2-42) and Eq. (2-43).

$$Buoy_{SRC1} = -\left(\left(\alpha_l \rho_l + (1 - \alpha_l)\rho_s\right) - \rho_s\right) g \tag{2-42}$$

In Eq. (2-42) α_l is the liquid-phase mass fraction, ρ_l is the liquid-phase density at the melting temperature, ρ_s is the solid-phase density, and g is the gravitational constant.

$$Buoy_{SRC2} = \beta_l \rho_l (T-T_{ref})\alpha_l g \tag{2-43}$$

In Eq. (2-43) T_{ref} is a reference temperature set to 293 K and β_l is the coefficient of thermal expansion, or thermal expansivity, described by $\beta = -\frac{1}{\rho}\frac{\partial \rho}{\partial T}$. The coefficient of thermal expansion describes a material's increase in volume as a function of temperature. Both of these buoyancy terms act in the vertical direction and will be zero if a significant fraction of the cell is solid RbCl.

The Rhie-Chow model was utilized in this momentum source term. The Rhie-Chow model is a discretization approach that allows pressure-velocity coupling. At each integration point (per cell), an equation similar to a momentum equation is applied, ensuring that the mass redistribution is consistent with the specified material velocity. Thus, velocity components at the cell faces are calculated from cell center values using the Rhie-Chow interpolation algorithm [22].

One of the limitations of this implementation is that in its current definition it cannot model the free body motion of the solid, forcing the solid RbCl to a zero velocity condition. In order to model any free body motion, the velocity of the solid in relation to the fluid domain would need to be known, and the momentum source terms and melting model would need to be significantly altered.

This melting model and momentum source term have not previously been validated and do not capture all physics present in real-world targets. However, it is the only known available method to date for modeling solid-liquid phase change in ANSYS CFX. Validation metrics and techniques used in this work will indicate if this is indeed a sufficiently valid approach for modeling melting in partially molten salt targets.

Section 2.1.5. Meshing

Meshing in ANSYS CFX provides a way to subdivide a geometry so that a discrete set of linearized equations describing momentum, mass, and heat transfer in a system may be solved. This is done by dividing a domain into many subdomains, creating a mesh of computational

cells. The number of cells in this mesh should be sufficiently large that it adequately represents the system behavior while not comprising memory usage. Mesh statistics are used to indicate how accurate a solution using the given mesh will be. Thus, poorly meshed elements are indicative that even if a solution converges, the answer will most likely not be correct. Each separately defined domain for the model may have a different prescribed meshing scheme. However, ensuring that the boundaries between each domain have aligning meshes is essential for conjugate heat transfer.

Several types of three-dimensional mesh elements exist – tetrahedron, pyramid, triangular prism (wedge), and hexahedron. These mesh element types are shown below in Figure 2-5.

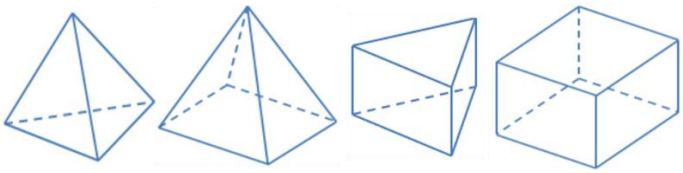

Figure 2-5: Types of mesh elements: tetrahedron, pyramid, triangular prism (wedge), and hexahedron.

Hexahedral meshes on structured grids are the most accurate mesh element type, displaying better convergence and higher resolution than their unstructured grid counterparts. However, these structured meshes are not often achievable for complex geometries. Complex geometries are often more easily meshed with unstructured tetrahedral grids, but these tetrahedron mesh elements are not recommended in thin boundary layers or in critical regions where high gradients or large changes exist. In these regions a more rectangular, i.e., hexahedral mesh is desirable.

Mesh elements orthogonal to the flow direction are advantageous, particularly in boundary layers, as numerical diffusion is high when non-orthogonal mesh elements are present. Both hexahedral or wedge (prismatic) mesh elements are able to resolve boundary layers efficiently, while pyramidal elements can be used as a transition element between square and triangular faced mesh elements.

Given these guidelines, the targets were meshed with hexahedral mesh elements to capture any essential target behaviors or gradients. The bulk cooling water flow was meshed with

tetrahedral elements, while the boundary layers of the four cooling water channels were assigned more rectangular mesh elements.

Skew and orthogonal quality are two measures of mesh quality, and are always values between zero and one. Orthogonality describes how close the angles between adjacent element faces or edges are to the optimal angle for a specific mesh element. This desired angle is 90º for quadrilateral-faced elements and 60º for triangular-faced elements. Orthogonality values should be as close to one as possible. Skewness is a measure of how close a face or cell is to ideal (quadrilateral or equiangular) [22]. This value should be as close to zero as possible. Values of skewness close to one indicate that the mesh is of extremely poor quality and solutions obtained from that mesh may not be valid. Aspect ratio describes the degree to which mesh elements are stretched via surface area relations. Acceptable values for the aspect ratio are below 100. Mesh quality should always be closely examined to ensure that mesh elements in critical regions are of a quality that will ensure an accurate solution.

For all models, initial meshing was performed using a global setting size function of proximity and curvature with a CFD physics preference and CFX solver preference. This ensures optimized mesh settings for CFD calculations. Face curvature is based on the normal angle variation between adjacent mesh elements. Face proximity is based on the number of element layers created in the gaps between faces. Symmetry was used to reduce the total number of nodes and elements, as discussed in Section 2.1.1.

Section 2.1.5.1. Average Heat Transfer Coefficient Model

Body sizing was specified for the two RbCl targets with an element size of 0.75 mm. Behavior was set to hard so that the sizing would override the global settings. Edge sizing was selected with a bias for both the RbCl targets as an alternative to inflation layers within the domain. The edge size was set to 0.75 mm for the RbCl targets.

Mesh statistics for this model are given in Table 2-3, with associated standard deviations presented for all mesh metrics. The type and number of each mesh element used are also provided in Table 2-4.

Table 2-3: Mesh statistics for the average heat transfer coefficient model.

Mesh Statistics	
Number of Nodes	148234
Number of Elements	219107
Average Skew	0.2351 ± 0.17047
Average Orthogonal Quality	0.7673 ± 0.17401
Average Aspect Ratio	6.9569 ± 15.068

Table 2-4: Number of each mesh element type for the average heat transfer coefficient model.

Mesh Elements	
Mesh Element Type	**Number**
Pyramidal	10330
Tetrahedral	107761
Hexahedral	100860
Prismatic (Wedge)	156

Section 2.1.5.2. Full Cooling Water Domain Model

As boundary layer heat transfer from the capsule walls to the cooling water is extremely important, inflation layers were utilized in the cooling water channels. Inflation layers allow for significant mesh refinement near walls in order to capture wall and boundary layer effects. This near-wall heat transfer is significantly increased by turbulence, and thus an extremely fine mesh must be used to capture any near-wall turbulence. These inflation layers were given a first layer height of 0.05 mm with a maximum of eight layers and a growth rate factor of 1.2.

Body and edge sizing was specified for the two RbCl targets as described above in Section 2.1.5.1. Body and edge sizing was also specified for the gallium target with a smaller element size of 0.25 mm and the behavior again set to hard. Cross-sectional images of the cooling water domain and targets are shown in Figure 2-6 and Figure 2-7, and mesh statistics are given in Table 2-5. The type and number of each mesh element used are also provided in Table 2-6.

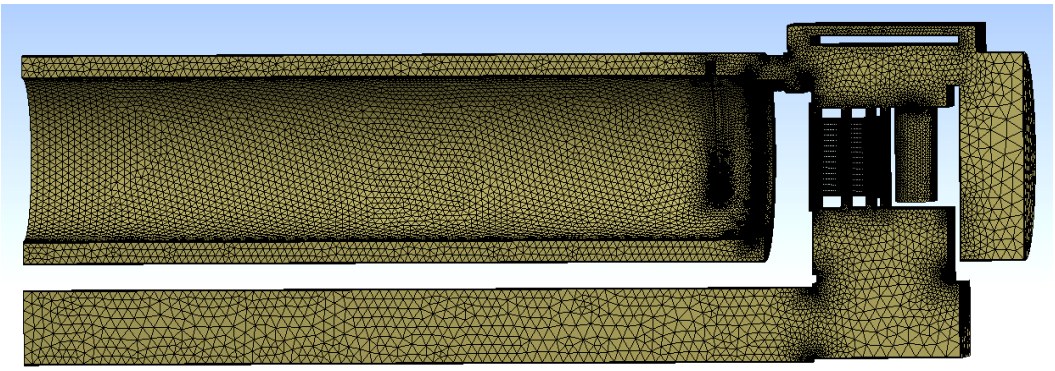

Figure 2-6: Cross-sectional image of full cooling water domain model mesh.

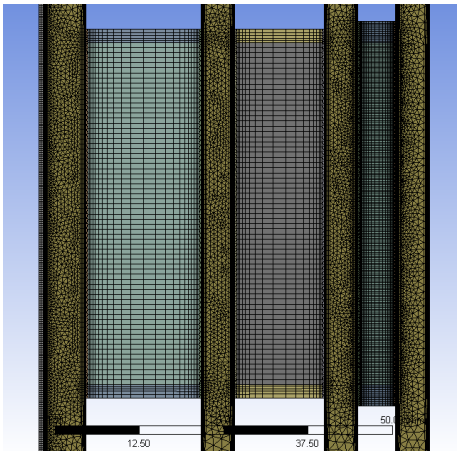

Figure 2-7: Cross-sectional image of full cooling water domain model mesh, magnified to show mesh for target pucks and capsules.

Table 2-5: Mesh statistics for the full cooling water domain model.

Mesh Statistics	
Number of Nodes	2470341
Number of Elements	5706001
Average Skew	0.2351 ± 0.17047
Average Orthogonal Quality	0.7673 ± 0.17401
Average Aspect Ratio	6.9569 ± 15.068

Table 2-6: Number of each mesh element type for the full cooling water domain model.

Mesh Elements	
Mesh Element Type	**Number**
Pyramidal	79852
Tetrahedral	2917873
Hexahedral	783915
Prismatic (Wedge)	1924361

Section 2.1.5.3. Refined Cooling Water Domain Model

In order to ensure the solution for this system is complete and heat transfer out of the system is accurate, it is necessary to incorporate the cooling water channels into the model while fully resolving the boundary layers in each channel. Resolving these boundary layers allows for a smooth transition region between the bulk fluid velocity in the channel and the zero wall velocity and captures any near-wall turbulence. This is essential to accurately modeling heat transfer into the cooling water, as near-wall velocity profiles dictate how quickly heat is removed from the target capsules. To accomplish this, the appropriate first layer thickness for the boundary layers in the cooling channels as well as the appropriate number of inflation layers was determined. This process is outlined below.

The cooling water channels in the system geometry are extremely narrow, with a width of only 5 mm. The cooling water mass flow rate through the system runs at approximately $\dot{m}$ = 2.518 kg/s. The appropriate first layer thickness was calculated using average system properties and the cooling water channel geometry. For determination of average water properties, an average temperature was determined between an estimated inlet and outlet temperature value.

$$T_{in} = 293 \text{ K} \quad ; \quad T_{out} = 308 \text{ K}$$

$$T_{avg} = \frac{T_{in} + T_{out}}{2} = 300.5 \text{ K} \tag{2-44}$$

If the pressure is assumed to be atmospheric with an average temperature T_{avg} = 300.5 K, then the corresponding water properties used are given in Table 2-7.

Table 2-7: Water Properties at T_{avg} = 300.5 K, $P_{atmosphere}$.

Water Properties	
C_p	$4.179 \frac{\text{kJ}}{\text{kg·K}}$
k_{H_2O}	$0.602 \frac{\text{W}}{\text{m·K}}$
μ_{H_2O}	$957 \cdot 10^{-6}$ Pa·s
ρ_{H_2O}	$997.76 \frac{\text{kg}}{\text{m}^3}$

The channel dimensions are specified with a width *w* and length *l*.

$$w = 5.038 \text{ mm} \quad ; \quad l = 51.054 \text{ mm}$$

The volumetric flow rate may be used to determine the mass flow rate.

$$\dot{Q} = 40 \text{ gpm}$$

$$\dot{m} = \dot{Q} \cdot \rho_{H_2O} \tag{2-45}$$

The average channel velocities can be determined using Eq. (2-46). As there are four channels in the system, the channel velocity must be corrected by a factor of four.

$$v_{H2O} = \frac{\dot{Q}}{4 \cdot A_x} \tag{2-46}$$

The cross-sectional channel area is given in Eq. (2-47).

$$A_x = w \cdot l \tag{2-47}$$

The hydraulic diameter for a rectangular channel can be calculated as shown in Eq. (2-48).

$$D_e = \frac{4(w \cdot l)}{2(w+l)} = \frac{2 \cdot w \cdot l}{w+l} \tag{2-48}$$

The Reynolds number may then be determined as shown in Eq. (2-49) using the water properties provided in Table 2-7.

$$Re_L = \frac{\rho_{H_2O} v_{H_2O} D_h}{\mu_{H_2O}} = 2.345 \times 10^4 \tag{2-49}$$

Using boundary layer theory [37], the skin friction coefficient correlation for internal flows may then be determined using the Reynolds number.

$$C_f = 0.058 Re_L^{-0.2} = 7.752 \times 10^{-3} \tag{2-50}$$

The wall shear stress is calculated using this skin friction coefficient as shown below in Eq. (2-51).

$$\tau_w = 0.5 \cdot C_f \rho_{H_2O} \cdot v_{H_2O}^2 = 23.255 \frac{\text{kg}}{\text{m} \cdot \text{s}^2} \quad (2\text{-}51)$$

The wall frictional velocity is calculated using the equation given in Eq. (2-52).

$$U_\tau = \sqrt{\frac{\tau_w}{\rho_{H_2O}}} \quad (2\text{-}52)$$

The desired y^+ value for viscous sublayers is one. Therefore the appropriate first layer thickness Δy for each channel is determined as shown in Eq. (2-53).

$$\Delta y = \frac{y^+ \cdot \mu_{H_2O}}{\rho_{H_2O} \cdot U_\tau} = 6.281 \times 10^{-3} \text{ mm} \quad (2\text{-}53)$$

y^+ is a dimensionless quantity and is the distance from the wall measured in terms of viscous lengths. When applied to the boundary layer of the liquid region mesh, it dictates the first layer thickness, or the necessary distance from the boundary to the center of the first computational node [22].

Refinement in the boundary layer via specification of first layer thickness is essential to ensuring that the desired y^+ value is achieved. While this calculation provides an approximation of the average first layer thickness necessary for achieving a y^+ value of one, it is still necessary to determine the actual y^+ value along the walls after running any flow simulation. If the y^+ value is not approximately one at the wall, the first layer thickness should be decreased.

As decreasing the first layer thickness and increasing the number of inflation layers significantly increases the number of mesh elements, it was necessary to look at reducing the size of the cooling water domain in order to minimize run time. This reduction in cooling water domain size is discussed in Section 2.1.1.3.

A study was done on the necessary number of inflation layers to capture the behavior of the cooling water. A steady state ANSYS solve was utilized with only the cooling water domain present and no heat transfer. Boundary conditions were specified for the full cooling water model as previously described in Section 2.1.1.2. This hydraulic problem was run with 8, 12, 15, and 20 inflation layers, all with a first layer thickness equal to the Δy value of 6.281e-3 mm. The pressure drop across the domain and velocity in the middle of channels one, two,

three, and four were compared to see what mesh resolution was sufficient to resolve fluid behavior. The results from this study are given in Table 2-8.

Table 2-8: ANSYS CFX mesh inflation layer study.

Case		8 inflation layers	12 inflation layers	15 inflation layers	20 inflation layers
Pressure Drop: $\Delta P = P_{in} - P_{out}$ [kPa]		-9.3200	-9.3328	-9.2962	-9.1544
Velocity [m/s]	**Channel 1: (0, 0, 0.004) m**	2.9560	2.82234	2.8936	2.9094
	Channel 2: (0, 0, 0.02635) m	2.8439	2.7940	2.7175	2.7283
	Channel 3: (0, 0, 0.04475) m	2.5463	2.6457	2.7013	2.7214
	Channel 4: (0, 0, 0.0553) m	2.4696	2.5809	2.6534	2.6145
Maximum % Change		-	4.522%	2.809%	1.525%

Based on the cases presented in Table 2-8, it was decided that 15 inflation layers would be sufficient to capture channel wall effects. The cooling water domain was sliced so that the only regions remaining were the four cooling channels and a 5 mm distance above and below. This was done to decrease the necessary number of boundary conditions. Images of the final mesh and cooling water channel inflation layers are given in Figure 2-8 and Figure 2-9. In addition to increased resolution in the cooling water channels, the resolution was also increased slightly in the target capsules.

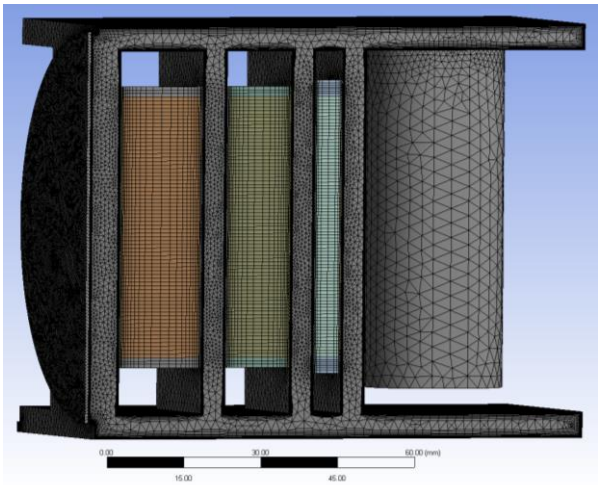

Figure 2-8: Refined cooling water domain model mesh.

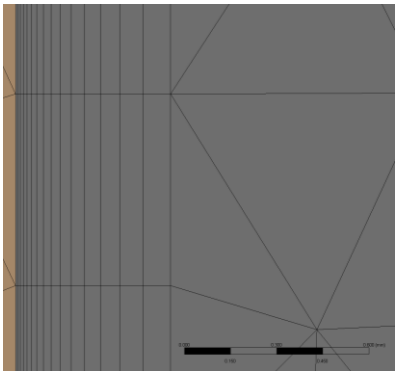

Figure 2-9: Inflation layers in cooling channels.

The global mesh statistics of the refined cooling water domain model are given in Table 2-9. All are well within the prescribed mesh statistic standards discussed in the introduction of Section 2.1.5.

Table 2-9: Mesh statistics for the refined cooling water domain model.

Mesh Statistics	
Number of Nodes	1351366
Number of Elements	3206388
Average Skew	0.25257 ± 0.17236
Average Orthogonal Quality	0.74281 ± 0.17961
Average Aspect Ratio	18.125 ± 31.117

The type and number of each mesh element used are provided in Table 2-10. Hexahedral elements were predominantly used in the targets and their capsules, while wedge elements were used to resolve the boundary layers of the cooling water domain. Tetrahedral elements were generally used in the bulk cooling water flow outside of the boundary layers.

Table 2-10: Number of each mesh element type for the refined cooling water domain model.

Mesh Elements	
Mesh Element Type	**Number**
Pyramidal	23658
Tetrahedral	1233547
Hexahedral	135562
Prismatic (Wedge)	1813621

To illustrate the mesh quality in each domain, the mesh statistics for each individual domain are provided below in Table 2-11.

Table 2-11: Mesh statistics for each domain.

Domain	Number of Mesh Elements	Average Skew	Average Orthogonal Quality	Average Aspect Ratio
In718 Window	60855	0.3382 ± 0.1353	0.6612 ± 0.1343	2.1231 ± 0.6300
RbCl Target A	46266	0.0662 ± 0.0967	0.9891 ± 0.0247	2.2388 ± 0.9089
RbCl Target B	46436	0.0631 ± 0.0972	0.9892 ± 0.0294	2.1822 ± 0.8810
Ga Target C	21856	0.0632 ± 0.0969	0.9883 ± 0.0309	2.6174 ± 1.2753
Cooling Water	2776532	0.2391 ± 0.1548	0.7534 ± 0.1615	20.5388 ± 32.7801

Body sizing was specified with an element size of 0.75 mm for RbCl target A and 0.7 mm for RbCl target B. A body element size of 0.65 mm was specified for Ga target C. The behavior was set to hard for all domains so that the sizing specification would override global settings. Edge sizing was selected with a bias for both the RbCl targets and the Ga target as an alternative to inflation layers within the domain. The edge size was set to 0.75 mm for RbCl target A, 0.7 mm for RbCl target B, and 0.65 mm for the Gallium target. Body sizing was also used for the beam window, with an element size of 0.6 mm.

The cooling water channels were given a first layer thickness of $\Delta y = 7 \times 10^{-3}$ mm and 15 inflation layers. The first layer thickness outside of the cooling channels was set to $\Delta y = 4 \times 10^{-2}$ mm.

Section 2.1.6. Transient Solve

In an attempt to capture the time-dependent behavior of the system, a transient model in ANSYS CFX was developed. Information was communicated between ANSYS CFX and MCNP in order to mimic the coupled nature of the density distribution, beam penetration, and heat deposition as a function of time.

The solver was set to run in parallel, dividing the computation into more than one process. A total of ten processors were used. This is the maximum allowable number of processors when running in local parallel with a high-performance computing (HPC) license on one user machine. Double precision for this solve was selected. For all models, information was communicated between ANSYS CFX and MCNP after a specified number of seconds of simulation time in ANSYS.

Transient terms at a time step $t = n$ can be expressed as shown below using a discretization in time.

$$\frac{\partial}{\partial t}\int_V \rho\varphi dV \approx V\frac{(\rho\varphi)^{n+\frac{1}{2}}-(\rho\varphi)^{n-\frac{1}{2}}}{\Delta t} \tag{2-54}$$

In the above equation $n + \frac{1}{2}$ and $n - \frac{1}{2}$ represent the beginning and the end of the time step. The time dependent terms in Eq. (2-54) may be approximated as shown below.

$$(\rho\varphi)^{n-\frac{1}{2}}=(\rho\varphi)^{n-1}+\frac{1}{2}\left((\rho\varphi)^{n-1}-(\rho\varphi)^{n-2}\right)$$

$$(\rho\varphi)^{n+\frac{1}{2}}=(\rho\varphi)^{n}+\frac{1}{2}\left((\rho\varphi)^{n}-(\rho\varphi)^{n-1}\right)$$

If these two time step values are substituted into Eq. (2-54), the form below is obtained. This is known as the second order backward Euler scheme.

$$\frac{\partial}{\partial t}\int_V \rho\varphi dV \approx V\frac{1}{\Delta t}\left(\frac{3}{2}(\rho\varphi)^{n}-2(\rho\varphi)^{n-1}+\frac{1}{2}(\rho\varphi)^{n-2}\right) \tag{2-55}$$

This second order backward Euler scheme is implicit, conservative in time, does not have a time step size limitation, and is second-order accurate in time with the exception of the turbulence equations and other bounded quantities, which remain first order accurate. The

implicit second order backward Euler transient scheme was used for this this model, applying the solution of the previous time step for each term [22].

Choosing an appropriate time step size is extremely important for any transient simulation, as it must be sufficiently small such that time-dependent features are resolved. Figure 2-10 illustrates this by comparing the solution of a time-dependent variable over time using two different time step sizes. In the top scheme the time step is too large and unable to resolve the true system behavior. In the bottom scheme the smaller time step size is able to fully resolve the true solution at each time step.

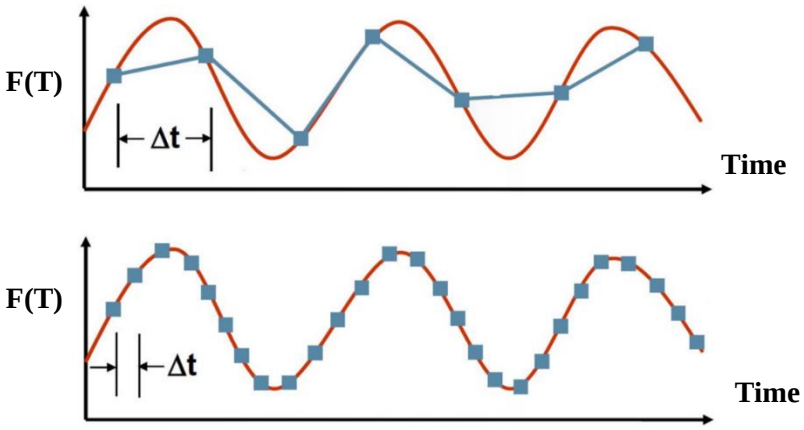

Figure 2-10: Time-dependent variable resolution as a function of time step size [25].

The courant number for each time step is given during a transient simulation. In a one-dimensional case the courant number can be calculated as shown in Eq. (2-56).

$$C = \frac{v\Delta t}{\Delta x} \tag{2-56}$$

However in a multidimensional case, this number is based on the mass flow into the control volume and the dimensions of the control volume. For an explicit numerical scheme, a sufficiently small time step is required such that the courant number is below some upper limit. However, for implicit numerical schemes used by ANSYS CFX, the courant number does not need to be small for the solution to be stable, but it is required to get an accurate picture of the transient.

For the first two models created in ANSYS CFX, information was communicated between ANSYS CFX and MCNP every 3 seconds of simulation time with an average time step size of

0.001 seconds. For the refined cooling water domain model, an average time step size of 0.00025 seconds was used, coupling between CFX and MCNP every 1.5 seconds of simulation time.

Section 2.1.6.1. Determination of Convergence in ANSYS CFX Solver

A multigrid (MG) accelerated incomplete lower upper (ILU) factorization technique is used to solve the discrete system of linearized equations describing the system. The solver approaches the exact solution as it iterates. The general form of the matrix used to describe the linearized system of discrete equations is given below in Eq. (2-57).

$$Ax = b \tag{2-57}$$

In Eq. (2-57) A is the coefficient matrix, x is the solution vector, and b contains constant parameters.

This equation is solved by beginning with an approximate solution of x^n that is improved by some correction x', to yield a better solution, x^{n+1}.

$$x^{n+1} = x' + x^n \tag{2-58}$$

Where x' is the solution of Eq. (2-59).

$$Ax' = r^n \tag{2-59}$$

And r^n is the residual as calculated in Eq. (2-60).

$$r^n = b - Ax^n \tag{2-60}$$

Residuals are one of the standards by which the CFX solver determines convergence. This iterative process is repeated until the residual becomes sufficiently small that the exact solution has been 'found'.

This iterative solver will be less efficient as the number of computational elements increases or if there are large element aspect ratios present. Convergence speed can be increased by the use of a method called algebraic multigrid. This multigrid method initially iterates upon a fine mesh, and then generates virtual coarser meshes to iterate upon. The solution solved with the coarser mesh is then applied to the original fine mesh.

A Root Mean Square (RMS) residual was chosen to ascertain when convergence was reached, with a default target value of 1×10^{-4}. This value is the root mean square normalized

residual taken over the entire domain. If a solution is converging, the residuals should decrease with successive iterations.

Transient simulations are solved by computing a solution for many discrete points in time, iterating to the solution at each point. To do this, the ANSYS CFX solver iterates on a single time step using coefficient loops until it either converges or reaches the user-specified maximum number of coefficient loops before progressing to the next time step. Given the implicit nature of a transient with the unknown φ^{n+1} term, inner iterations, or coefficient loops, are introduced to satisfy this implicit dependency with more accuracy. The role of coefficient loops at each time step is illustrated below in Figure 2-11.

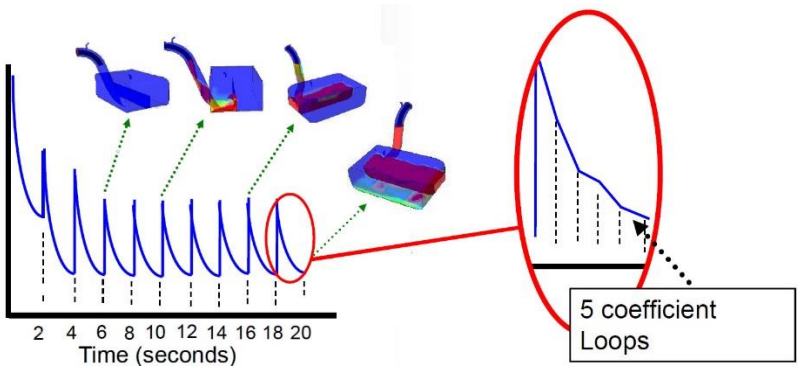

Figure 2-11: Demonstration of transient simulation convergence with the use of coefficient loops [25].

For transient runs in CFX the values of the maximum and RMS courant numbers are given at every time step as well as the rate and the linear solver residual. The rate is a comparison of the residuals between iterations, and is calculated as shown below in Eq. (2-61).

$$Rate = \frac{R_n}{R_{n-1}} \tag{2-61}$$

The rate is an indication of whether or not the residual is being reduced between successive iterations. A rate of less than one indicates that the solution is converging. In a transient simulation such as the one used here, the rate is calculated for each coefficient loop iteration.

How close the final solution is to the real flow solution will depend on the size and shape of the control volumes, as well as the final residuals. Turbulence models rely heavily on empirical relationships and therefore the approximations used by the turbulence model chosen

will also lead to differences between the real solution and the solution predicted by CFX. These numerical and model errors and ways to reduce them will be discussed in Section 2.1.7.

Section 2.1.7. Error Types

A variety of errors can impact a CFD simulation, and reduction of these errors is essential for achieving results reflecting the true physical nature of the system of interest. Numerical and model errors are the two main error types which impact the solution of any CFD simulation.

Types of numerical errors are solution errors, time or spatial discretization errors, iteration errors, and round-off errors.

Solution errors quantify the difference between the model's numerical solution and exact solution. The goal of any CFD simulation is to reduce this error to some limit which has been deemed sufficiently small. However, this is not necessarily straightforward, as oftentimes the exact solution is not known (thus the numerical approach). When this is the case, comparison of the exact and the discretized solutions is not possible. These solution errors can be minimized by reducing the time and spatial discretization errors. Spatial discretization replaces the analytical derivatives and integrals with numerical approximations. These approximations have a corresponding truncation error corresponding to the grid (mesh) resolution. For a first order accurate spatial discretization method $\left(o(\Delta x)\right)$, doubling the grid refinement will lead to a 50% reduction in the error, while for a second order method $\left(o(\Delta x^2)\right)$, this same doubling will lead to a 75% reduction in error. Time discretization errors are similar in definition to spatial discretization errors, and the order of the scheme dictates the reduction in error due to the time step size.

Round-off errors occur because computers can only solve equations with a finite number of digits. For example, for single precision calculations in ANSYS CFX the computer only calculates equations out to eight digits, and out to 16 digits for double precision. Double precision was chosen for these models to minimize the round-off error.

Model errors in this simulation would be due to the choice of turbulence model, as well as any user applied models – in this case the melting model. As turbulence models provide

closure in the RANS equations, once a model has been selected the accuracy cannot be increased beyond the capabilities of the selected model. Application of an incorrect turbulence model for the flow type will lead to extremely large model errors, so knowing general flow characteristics can assist in choosing an appropriate model for the system. The accuracy of any user applied models cannot be determined until a validation study is performed.

It should be noted that when experimentally measured values with unknown uncertainties are used, as they are for this model, significant and unknown errors are introduced to the system. This is unavoidable when limited existing data is required to model a system.

Knowledge of error types and approaches to minimize different error sources are essential for accurately modeling any thermal hydraulic system.

Section 2.2. MCNP

MCNP was used to model proton interactions within the target material. Material and geometry definitions may be used to outline the scope of a problem and built-in physics models are used to predict proton interactions and heat deposition. A MCNP input deck describes a specific problem of interest and is made up of input cards. Each input card delineates a specific component of the problem, whether it be material specification, geometry definition, or source definition. Within MCNP, general units are length – [cm], energy – [MeV], and mass density – [g cm^{-3}].

For the first two system models considered in ANSYS CFX, a single MCNP input deck was utilized. However, for the final model, inconsistencies between MCNP, the real world system, and the ANSYS model were addressed. The initial assumptions made in the MCNP model are discussed as are the modifications made for the final model.

Section 2.2.1. Geometry

The CAD geometry was defined in such a way that its geometric orientation aligned exactly with the MCNP geometry definition. This eliminated any beam translation between the MCNP and ANSYS meshes. The beam travels in the negative z direction in MCNP and in the positive z direction in ANSYS, requiring only the change in z-coordinates to positive values when importing the volumetric beam data and corresponding coordinates into ANSYS CFX. An

image of the MCNP geometry as depicted using the MCNP Visual Editor [38] is shown below in Figure 2-12.

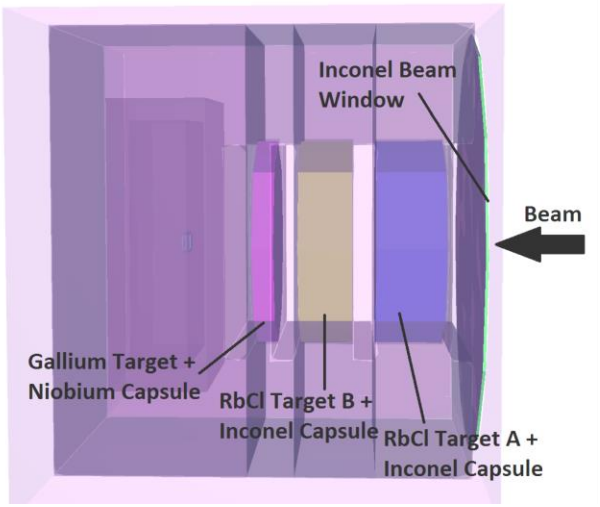

Figure 2-12: Target geometry and housing components in MCNP's Visual Editor [38].

Geometry specification was performed using macrobody surface cards. The two macrobodies used were the rectangular parallelepiped (RPP) and right circular cylinder (RCC) macrobodies. Surface planes were also employed later to divide the three target regions into small cells. This division of target domains to capture density variation will be discussed in Section 2.2.3.

Section 2.2.1.1. Changes to MCNP Geometry for Refined Cooling Water Domain Model

An existing MCNP model of the target stack was used in the initial development of the average heat transfer coefficient and full fluid domain models. Several discrepancies were found between the real-world target dimensions and the supplied MCNP geometry. For example, the MCNP geometry in the provided input file did not match the physical target radii. These differences are shown in Table 2-12, and were corrected in the final MCNP input deck.

Table 2-12: MCNP and physical target dimensions.

Dimension	MCNP	Physical Geometry
R_{target}	2.4892 cm	2.54 cm
$R_{capsule}$	2.54 cm	2.875 cm

A discrepancy was noted between the MCNP geometry and the CAD model geometry used in the ANSYS model. The C-slot niobium capsule encapsulating the gallium target was approximately 0.005 cm thinner on each flat face in the ANSYS model than in the MCNP model. Calculations were performed using the Stopping Range of Ions in Matter (SRIM) software [39] to see the impact of this geometry change on incident beam energy. The results shown in Table 2-13 indicate that the impact of this change in geometry is not significant, allowing the MCNP geometry to be altered to match the ANSYS target dimensions.

Table 2-13: Stopping power and energy loss in Nb and Ga.

Material	**Density** ρ **[g/cm^3]**	**Stopping Power at** $E = 30$ **MeV** $\frac{dE}{dx}$ **[MeV/mm]**	**Energy Loss in** $\Delta z = 0.005$ **cm** ΔE **[MeV]**
Niobium	8.57	9.359	0.468
Gallium	5.91	6.825	0.341

This will not impact any behavior in the A and B slot targets, whose dimensions in the CAD model used by ANSYS are consistent with that given in the MCNP input deck. Any experiments performed in the C slot will also not be affected by this geometry alteration, as they are only influenced by upstream behavior.

Section 2.2.2. Beam Distribution

A source term was used to specify the 100 MeV incident proton beam in MCNP. The beam is normally distributed in both the x and y directions, and a series of transformations were used in MCNP to alter the beam shape from a single spot to a ring shape. The center of the ring-shaped beam is located at 1.27 cm, and the distribution is symmetric in both the x and y directions. An illustration of the physical beam profile is shown in Figure 2-13.

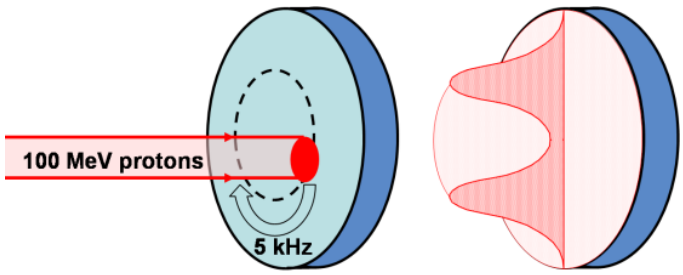

Figure 2-13: Beam shape and distribution [40].

A Gaussian (normal) distribution may be described by the following probability density function.

$$\rho(x) = \frac{1}{\sqrt{2\pi}\sigma} e^{\frac{(x-\mu)^2}{2\sigma^2}} \tag{2-62}$$

Here μ is the mean of the distribution and σ is the standard deviation of the distribution. The full-width half-maximum (FWHM) value of a Gaussian distribution is given by:

$$\mathrm{F}WHM = \sqrt{8\,ln(2)}\,\sigma = 2\sqrt{2\,ln(2)}\,\sigma \tag{2-63}$$

The centroid of the Gaussian distribution in both the x and y directions was set at $(0,0)$ and was specified using equations describing FWHM as per the MCNP User's Manual [21]. These are provided below in Eq. (2-64) and Eq. (2-65).

$$f_x = (8\,ln(2))^{1/2} a \tag{2-64}$$

$$f_y = (8\,ln(2))^{1/2} b \tag{2-65}$$

In the above equations *a* and *b* are the standard deviations of the Gaussian distribution in the x and y directions.

As described in Section 1.3, the beam operates at 120 Hz, or 120 pulses per second. Only 100 of these pulses are sent to the target, with a gate length of 625 μs each. However, the MCNP input deck models the incident source term as constant - that is, it models the average heat input into each target per second of pulse time. Given the thermal time response of the system in relation to the pulse length this should be a valid assumption.

However, in order to justify this simplification, the calculations below were performed to quantify the magnitude of the oscillations around mean predicted target temperature as a result of the beam pulses.

The total work done during a one second cycle is:

$$Q\,[J] = Q_{rate}[W] \cdot 1s \tag{2-66}$$

This may also be expressed in terms of energy input per unit volume.

$$Q\left[\frac{J}{cm^3}\right] = Q_{rate}\left[\frac{W}{cm^3}\right] \cdot 1s \tag{2-67}$$

As there are 100 pulses incident on the target per second, the energy deposited per unit volume for each pulse is as shown below.

$$Q_{pulse}\left[\frac{\frac{J}{cm^3}}{pulse}\right] = \frac{Q\left[\frac{J}{cm^3}\right]}{100\ pulses} \tag{2-68}$$

The energy deposited per pulse may be related to an associated temperature rise by the following relationship.

$$Q\left[\frac{J}{cm^3}\right] = \rho\left[\frac{g}{cm^3}\right] \cdot C_p\left[\frac{J}{g \cdot K}\right] \cdot \Delta T\,[K] \tag{2-69}$$

In Eq. (2-69) ρ is the density and C_p is the material's specific heat capacity, both of which are functions of temperature. Given a prescribed average operating temperature the density and specific heat capacity are known and the change in temperature per pulse may be ascertained.

Using average heat deposition data obtained from MCNP for a preliminary calculation, temperature oscillations of $\Delta T \sim 5 - 8$ K were seen when using average temperatures ranging from T = 293 – 1450 K.

The average operating temperature of these targets ranges from ~ 1100 – 1250 K. Given this range, the corresponding temperature oscillation on the order of less than ~ 0.5% per beam pulse will not impact the pseudo steady state thermal target behavior. This confirms that the MCNP input deck simplification to model the incident beam source term as constant will not significantly impact predicted target behavior.

Section 2.2.2.1. Average HTC and Full Cooling Water Domain Model

For both the average heat transfer coefficient boundary condition model and the full cooling water domain model, an initial idealized Gaussian beam distribution was used. This idealized distribution has a beam center of 1.27 cm, a standard deviation of σ = 0.539 cm, and a full width half-maximum value of *FWHM* = 1.27 cm. This beam distribution profile was historically used in all MCNP models of this target. When more accurate beam distribution information was provided, the MCNP beam distribution was corrected accordingly for the refined cooling water domain model.

Section 2.2.2.2. Refined Cooling Water Domain Model

When creating the MCNP input deck for the refined cooling water domain model, a more realistic beam distribution was utilized. This realistic beam distribution has a beam center of

1.27 cm, a standard deviation σ = 0.24 cm, and a *FWHM* = 0.565 cm. This is approximately half of the standard deviation for the previous beam distribution, indicating that this beam distribution will be much narrower than the previous idealized distribution. Updating the beam to match the operating beam distribution allows for more accurate comparison of results between physical and model values. It should be noted that this is a fairly significant alteration to the beam distribution.

Section 2.2.3. Density Mesh

To account for density variation due to phase change in the RbCl targets, the cell cards in MCNP were divided into regions using a series of planes in cylindrical coordinates. In MCNP, each cell can only be assigned one density, so this splitting of the regions of interest into many smaller cells allows for the density variation over the target volume to be captured.

A number of radial, axial, and angular planes were employed for this sectioning. Six angular planes were defined to create 12 'wedges', dividing the volume at 30° intervals. Figure 2-14 depicts an example of a simplified target geometry with six angular planes and five cylindrical planes.

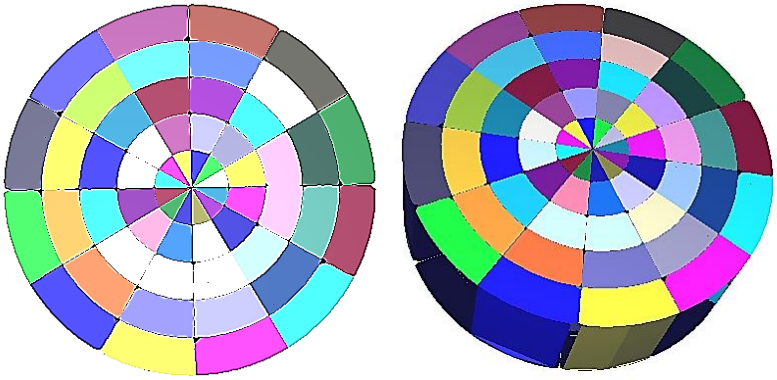

Figure 2-14: Cross-sectional plane of target geometry in Vised for RbCl target A with angular and radial discretization [38].

This mesh was created only for RbCl targets A and B as validation metrics of interest were calculated using information obtained solely from these two targets. As information obtained in the Ga C slot target was considered non-essential other than overall heat input to the cooling water channel, this target was assigned an average uniform density.

Section 2.2.3.1. Average Heat Transfer Coefficient and Full Cooling Water Domain Model

For these models a uniformly spaced radial and axial mesh was utilized, with 30 radial and 30 axial planes defined within each RbCl target volume and 12 angular wedges.

Section 2.2.3.2. Refined Cooling Water Domain Model

Non-uniform mesh sizes were applied to both radial and axial plane spacing to more accurately capture the phase transition regions in the target as well as areas of beam strike. Several iterations of mesh resolution were performed to find the optimum value for each target region. The goal was to capture the maximum amount of information possible with as few mesh elements as possible.

The radial planes were divided into four regions, starting at the center of the target and oriented around the center of the beam ring. This division is shown in Figure 2-15.

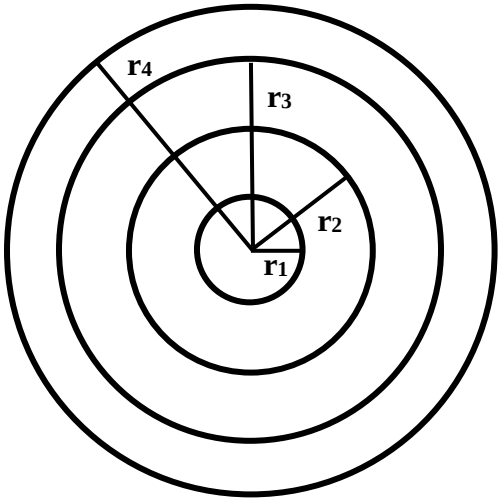

Figure 2-15: Radial regions defined in MCNP for non-uniform mesh resolution.

The center of the beam is located at 1.27 cm, and the Gaussian beam distribution has a standard deviation of $\sigma = 0.24$ cm in both the x and y directions. Thus, 99.7% of the beam distribution is encompassed by $3\sigma = 0.72$ cm on either side of the beam center. The beam strike region was given the highest resolution as this is where the majority of the proton interactions modeled in MCNP occur. The resolution of each radial region – i.e., the number of planes taken in each radial region – is given below in Table 2-14.

Table 2-14: MCNP density mesh radial region definition.

Radial Region	Symbolic Representation	Position [cm]	Radial Resolution
r_1	r_{center}-3σ	0.55	5
r_2	r_{center}	1.27	10
r_3	r_{center}+3σ	1.99	10
r_4	r_{target}	2.54	2

The axial planes were divided into five regions, starting at the front face of the target and oriented based on the phase transition regions near the front and back target faces. This is illustrated in Figure 2-16, and the axial location of each plane is provided in Table 2-15.

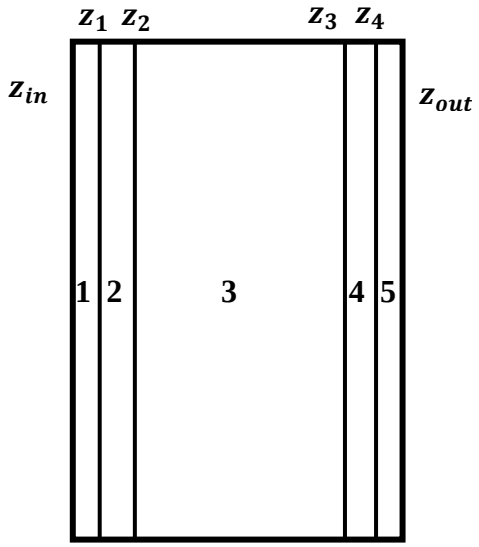

Figure 2-16: Axial region spacing for MCNP density mesh.

Table 2-15: MCNP density mesh axial location specification.

Target Domain	Position [cm]					
	z_{in}	z_1	z_2	z_3	z_4	z_{out}
RbCl Target A	0.7245	0.7655	0.7955	2.294	2.325	2.3655
RbCl Target B	2.9265	2.945	3.009	4.112	4.178	4.1945

Non-uniform resolution was utilized in order to capture the large density gradient present in regions of phase change. The axial resolution of each region – i.e. the number of planes taken in each axial region – is given in Table 2-16.

Table 2-16: MCNP mesh tally axial region resolutions.

Region	Axial Resolution
1	3
2	3
3	14
4	3
5	3

Section 2.2.4. Mesh Tally Generation

It was important to ascertain a method by which to capture the volumetric heat generation profile as a function of position. To do this, a mesh tally was used to divide the domains into a collection of cells. Each cell could then be individually assigned information. The mesh tally was defined using cylindrical coordinates. In order to generate a volumetric heat distribution for each target domain, a type one mesh tally with a PEDEP specification was used to score the average energy deposition per unit volume for the particle type. This generated a tally value per cell with units of $\left[\frac{\text{MeV}}{\text{cm}^3}\right]$. When the mesh tally is multiplied by the beam current in [μA], the tally is converted to units of heat deposition in $\left[\frac{\text{W}}{\text{cm}^3}\right]$. For all MCNP calculations of heat generation, 20 million particle histories were run. Based on observation of MCNP determined relative errors, this number of particles was sufficiently small to give confidence in the volumetric heat generation profiles.

Section 2.2.4.1. Average HTC and Full Cooling Water Domain Model

For the first two models, heat deposition data was generated with uniform resolution in the axial and angular directions, as described in Section 2.2.3.1. The angular resolution was uniform as well, with a total of 24 angular wedges. Heat was only supplied to the target bodies, windows, and capsules and heat deposition in the cooling water was not exported.

Section 2.2.4.2. Refined Cooling Water Domain Model

Heat input to the cooling water domain will impact the peak temperatures seen in the cooling water channels. Thus, for this model heat deposited in the cooling water channels was exported. In addition, heat generation data was supplied with a non-uniform resolution. In the

radial region the target was divided as shown in Figure 2-15. The number of planes specified for the exported mesh tally in each region is listed in Table 2-17.

Table 2-17: MCNP mesh tally radial region definition.

Radial Region	Symbolic Representation	Position [cm]	Radial Resolution
r_1	$r_{center} - 3\sigma$	0.55	5
r_2	r_{center}	1.27	15
r_3	$r_{center}+3\sigma$	1.99	15
r_4	r_{target}	2.54	5

A uniform axial resolution was assumed to be sufficient in each target domain. The resolutions for each domain are given in Table 2-18. The capsule and beam window axial resolution is very coarse as the number of mesh elements in ANSYS is limited to approximately two per layer of capsule or window material. Therefore higher resolution when generating the mesh tally in MCNP was not required.

Table 2-18: MCNP mesh tally axial region definition.

Domain	Axial Resolution
Cooling Water Channel	10
Target	30
Capsule	2
Beam Window	2

The number of axial planes taken in the Ga target was increased to 40 as interpolation errors resulting from the absence of heat generation at the back of the target were leading to a slight over prediction of heat input.

Section 2.3. Multiphysics Coupling

The inconsistent input/output formats used by MCNP and ANSYS requires the use of a data translation algorithm. Routines were written in FORTRAN and MATLAB to perform this operation. A diagram of the process used for the LANL target stack is shown in Figure 2-17. The first iteration of this coupling process was initially developed and employed by Tim Faugl when modeling water targets [12]. The codes used were significantly altered, adapted, or rewritten to model gas targets [18,19]. The framework of this process was then

applied to the LANL target stack discussed in this dissertation, with alterations made and additional codes added to facilitate the coupling process as needed.

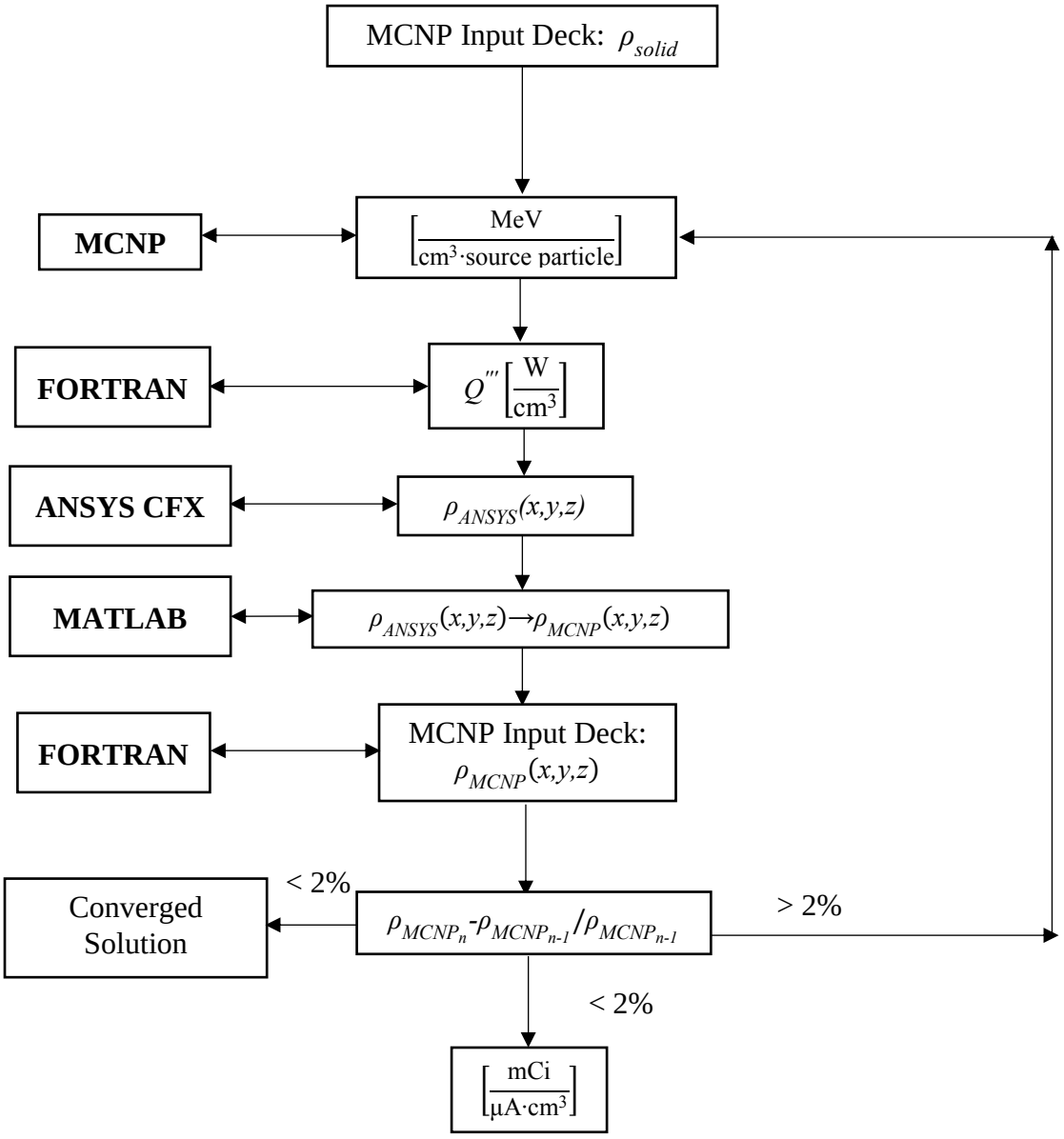

Figure 2-17: Flow diagram of iterative process to couple MCNP and ANSYS CFX.

A FORTRAN code is used to read the mesh tally data from MCNP and convert it from energy deposited per unit volume to heat deposited per unit volume using the specified beam current. The FORTRAN code reads the data and reformats it, accounting for any axis

translation or coordinate shift disparities between the MCNP geometry and the ANSYS geometry.

Once the beam data for each domain has been imported into CFX-Pre, ANSYS is run until some thermal solution has been established. This thermal solution provides a density distribution which may be utilized by MCNP in its radiation transport calculations. To account for density variation in the MCNP run, it is necessary to translate these ANSYS provided density distributions into a format which may be used by MCNP.

A FORTRAN code was written to find the cell centers for a MCNP mesh based on user specified radial, axial, and angular mesh resolutions discussed in Section 2.2.3. MATLAB's [41] built-in interpolation function is utilized to translate density information between the cell centers of the unstructured ANSYS mesh to the cell centers of the structured MCNP mesh. Another FORTRAN code generates a MCNP input deck with this density mesh.

This process is repeated until the variation in density between successive iterations is sufficiently small. The inputs, outputs, and tasks performed are outlined for each code in Table 2-19.

Table 2-19: Codes tasks for iterating between MCNP and ANSYS CFX.

Code	Input	Output	Tasks
FORTRAN	MCNP generated mesh tally $\left[\frac{\text{MeV}}{\text{cm}^3}, \text{cm}, \text{cm}, \text{rad}\right]$	Text files of heat deposition for each domain $Q'''_{domain}\left[\frac{\text{W}}{\text{cm}^3}, \text{cm}, \text{cm}, \text{rad}\right]$	Read in unsorted mesh tally sum heat deposited in each target body
			Multiply energy deposition by beam current [μA]
			Sort heat deposition data into each domain
		Total heat deposition in each target domain Q_{domain}[W]	Write volumetric heat deposition to text file for each domain
			Multiply sorted volumetric heat generation by cell volume
			Sum heat deposited in each target body

Table 2-19 (continued)

Code	Input	Output	Tasks
FORTRAN	Axial and radial mesh resolution	Text file of MCNP cell centers for RbCl A and B	Generate text file of cell center positions given specified mesh resolution for cell definition in MCNP
MATLAB	ANSYS generated temperature solution $[T,x,y,z]_{ANSYS}$ for $\theta \in \left[\frac{3\pi}{2}, \frac{\pi}{2}\right]$	Density information at MCNP cell centers $[\rho,x,y,z]_{MCNP}$ for $\theta \in \left[\frac{3\pi}{2}, \frac{\pi}{2}\right]$	Read in ANSYS mesh cell centers and corresponding temperatures
	MCNP cell centers		Read in MCNP mesh cell centers
			Generate densities as a function of temperature $\rho(T)$
			Interpolate ANSYS densities $[\rho,x,y,z]_{ANSYS}$ onto MCNP mesh
			Write densities at MCNP cell centers to text file $[\rho,x,y,z]_{MCNP}$
FORTRAN	Density information at MCNP cell centers $[\rho,x,y,z]_{MCNP}$ for $\theta \in \left[\frac{3\pi}{2}, \frac{\pi}{2}\right]$	MCNP input deck	Read in densities at MCNP cell centers $[\rho,x,y,z]_{MCNP}$ for $\theta \in \left[\frac{3\pi}{2}, \frac{\pi}{2}\right]$
		Density at MCNP cell centers for $\theta \in [0, 2\pi]$	Reflect the densities over the y-axis, generating densities for $\theta \in [0, 2\pi]$
			Create cells in each target with assigned densities
			Write input deck to a text file

CHAPTER 3. THERMAL-HYDRAULIC MODEL RESULTS

The results from the initial two models are presented briefly in the first section of this chapter. The results for the final model will be discussed in more detail as they more accurately represent the true system and were utilized for the validation study discussed in Chapter 4.

Section 3.1. Average Heat Transfer Coefficient and Full Cooling Water Domain Models

For this section the average heat transfer coefficient model will be referred to as the simplified model and the full cooling water domain model will be referred to as the full model. As discussed in Section 2.1, for the simplified model all housing components not of interest were suppressed in ANSYS CFX to minimize mesh size and total run time. Only the RbCl targets A and B and their capsules were included for this initial simulation. For the second (full) model, the third target (Ga metal), its capsule, the beam window, and the cooling water were included in the ANSYS CFX model.

For both models a transient simulation was utilized, as discussed in Section 2.1.6, in an attempt to capture the time-dependent behavior of the targets. Information was communicated between ANSYS CFX and MCNP every 3 seconds of simulation time in ANSYS to mimic the coupled nature of the density distribution on beam penetration and heat deposition. These targets reach some quasi-steady state solution after approximately 30 seconds of operating time. A quasi or pseudo steady state solution refers to a final ‘solution’ in which there is some stable oscillation about a mean value, causing a true steady state solution to be unattainable. In this simulation, progressive phase change (melting and re-solidification) and convective patterns prevent the establishment of a true steady state solution.

Section 3.1.1. Initial Multi-Physics Coupling Test

An initial test employing multi-physics coupling was performed with the simplified average heat transfer coefficient model. This initial iteration was to ascertain to what degree

the coupled nature of the target impacted heat deposition and to gain an idea of the pseudo steady state behavior of the target. These initial results are shown below. For all midplane distributions, a plane was taken at the center of each target. This midplane has a z-position of 1.545 cm in RbCl target A and 3.5605 cm in RbCl target B. For all YZ distributions, the midplane is located at the position x = 0 cm.

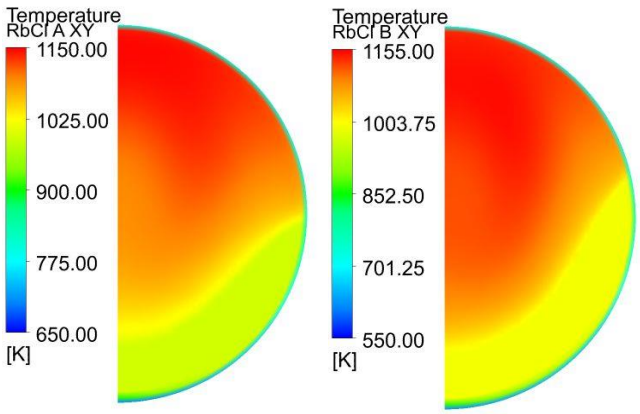

Figure 3-1: Equilibrium solution for the midplane temperature distribution in RbCl Targets A and B for the average heat transfer coefficient model.

Table 3-1: Comparison of heat deposition [kW] in MCNP.

Case	Iteration 0 – Uniform 2.8 g/cm^3 density	Iteration 17
Inconel 718 Window	0.3531	0.3530
RbCl Target A	5.9807	4.6545
Inconel 625 Capsule A	0.7226	0.7012
RbCl Target B	7.3768	4.8292
Inconel 625 Capsule B	1.3577	0.9503
Gallium Target C	7.89E-04	5.2792
Niobium Capsule C	0.2795	0.7120
Water	5.6899	4.2522
Total	21.7611	21.7316

As illustrated in Table 3-1, when a solid density is assumed for the RbCl targets, the majority of the incident protons are stopped before reaching the gallium target. Once density changes due to melting of the RbCl are taken into account, a significantly greater amount of heat is deposited in the gallium. This clearly highlights the significance of employing multi-physics coupling. Additionally, the temperature gradients presented in Figure 3-1 demonstrate

that assuming an average target temperature and density is not valid, particularly for production calculations.

Section 3.1.2. Comparative Study between Full and Simplified Models

A comparative study was done to determine the validity of using a simplified model with a suppressed cooling water domain and applied average heat transfer coefficient boundary condition to model a RbCl target stack. A full model, including all target bodies and the flowing cooling water domain, was run with ANSYS CFX and MCNPX until convergence was reached. The C-slot Ga target was assumed to be liquid at all time steps due to its low melting point of ~30 °C (303 K). Natural gallium (60% ^{69}Ga, 40% ^{71}Ga) was used with an assumed average density.

The full model's converged solution was compared to that of the simplified model. Parameters presented here include heat deposition, peak and average temperatures and velocities, and average liquid fraction. For a more qualitative comparison, velocity, temperature, and liquid fraction profiles are shown side by side for the two models.

Table 3-2: Comparison of heat deposition [kW] for the simplified and full model target solutions.

Heat Deposition [kW]			
Target Domain	**Full Model [Iteration 14]**	**Simplified Model [Iteration 17]**	**Relative Difference |Full-Simplified|/Full**
Inconel 718 Window	0.353	0.353	0.00%
RbCl Target A	4.7256	4.6545	1.50%
Inconel 625 Capsule A	0.7019	0.7012	0.10%
RbCl Target B	4.9137	4.8292	1.72%
Inconel 625 Capsule B	0.9582	0.9503	0.82%
Gallium Target C	5.0648	5.2792	4.23%
Niobium Capsule C	0.7240	0.712	1.66%
Water	4.2944	4.2522	0.98%
Total (sans water)	17.4412	17.4794	0.22%
Total	21.7356	21.7316	0.02%

Given the data presented in Table 3-2, it can be concluded that using a simplified model (via suppression of the cooling water) with an average heat transfer coefficient boundary condition predicts heat deposition to within ~4% of the full model. As the relative error between the two models is small, using a simplified model for approximation of heat deposition

in the target domains provides a reasonably accurate first-order picture of target behavior without the added computational expense. Due to the mesh resolution required in the cooling water channels, the cooling water domain is often the limiting factor on the allowable time step size. The simplified model is able to run at least 18 times faster than the full model, but this factor increases the smaller the required time step for convergence in the cooling water domain.

Thermal hydraulic parameters for both models are presented in the tables below.

Table 3-3: Thermal hydraulic data for simplified and full model target solutions.

Target Domain	Temperature Data [K]					
	Maximum		Average		Minimum	
	Full	Simple	Full	Simple	Full	Simple
Inconel 718 Window	322.521	-	301.002	-	298.177	-
RbCl Target A	1113.61	1147.81	987.068	1012.7	344.149	364.203
Inconel 625 Capsule A	824.978	823.62	590.484	618.793	310.024	325.291
RbCl Target B	1133.5	1151.64	981.144	1007.32	344.938	371.373
Inconel 625 Capsule B	737.705	772.774	529.031	567.096	309.964	328.071
Gallium Target C	364.39	-	333.39	-	-	-
Niobium Capsule C	338.496	-	312.624	-	301.674	-
Water	326.106	-	298.552	-	298.147	-

Table 3-4: Velocity data for simplified and full model target solutions.

Target Domain	Velocity Data [m/s]			
	Maximum		Average	
	Full	Simple	Full	Simple
Inconel 718 Window	-	-	-	-
RbCl Target A	0.06407	0.05685	0.01106	0.01238
Inconel 625 Capsule A	-	-	-	-
RbCl Target B	0.06322	0.06641	0.01023	0.01332
Inconel 625 Capsule B	-	-	-	-
Gallium Target C	0.04833	-	0.02291	-
Niobium Capsule C	-	-	-	-
Water	7.3663	-	1.3364	-

Table 3-5: Average liquid fractions for RbCl targets A and B.

Liquid Fraction [%]		
Target Domain	**Full Model**	**Simplified Model**
RbCl Target A	71.7561%	76.0596%
RbCl Target B	67.17%	73.2916%

Overall the temperatures for each target body are lower in the full model, but this is expected due to the lower overall heat deposition. It appears that heat removal is more non-uniform between the target bodies of the full model than the simplified model based on the peak target temperatures for RbCl targets A and B. The overall average liquid fractions for both targets are greater in the simplified model.

Figure 3-2 – Figure 3-10 compare the converged temperature, velocity, and liquid fraction distributions in RbCl targets A and B for the full and simplified models. The distributions appear very similar, though there is a slight difference between the two models in the RbCl target B XY midplane temperature, liquid fraction, and velocity distributions. All images were scaled to the same temperature or velocity range scale for ease of comparison.

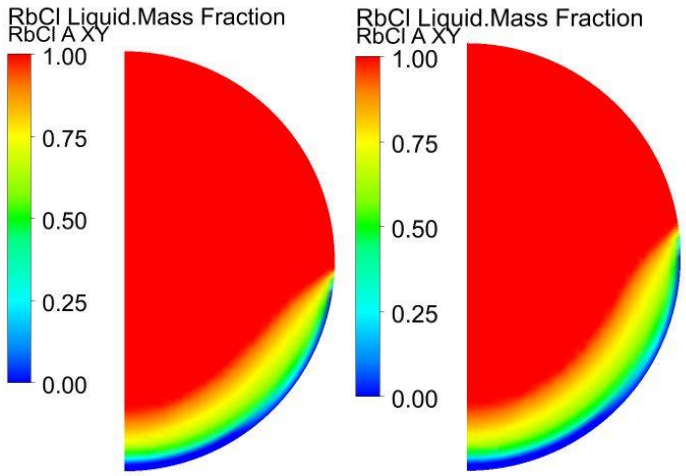

Figure 3-2: Comparison of RbCl target A's XY midplane liquid fraction profiles for the simplified model (L) and the full model (R).

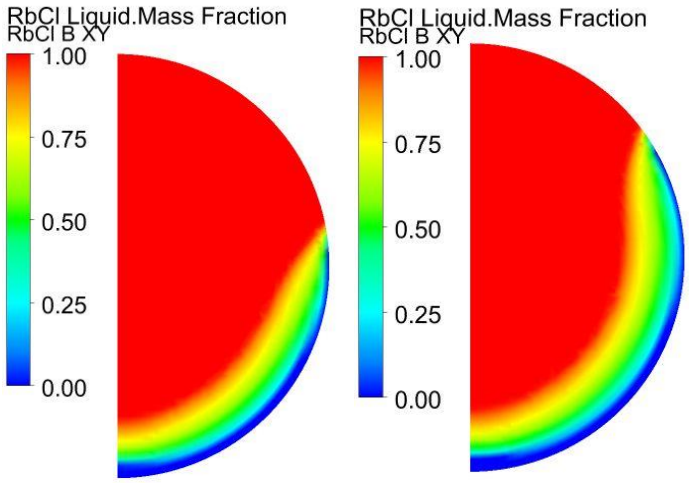

Figure 3-3: Comparison of RbCl target B's XY midplane liquid fraction profiles for the simplified model (L) and the full model (R).

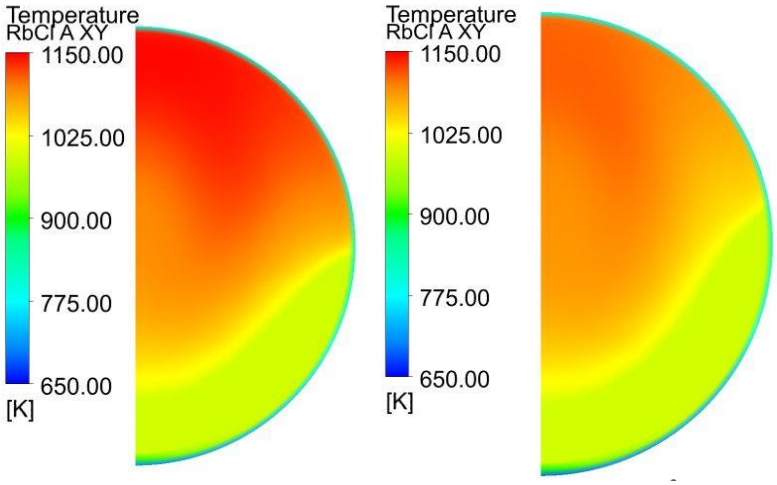

Figure 3-4: Comparison of RbCl target A's XY midplane temperature distribution profiles for the simplified model (L) and the full model (R).

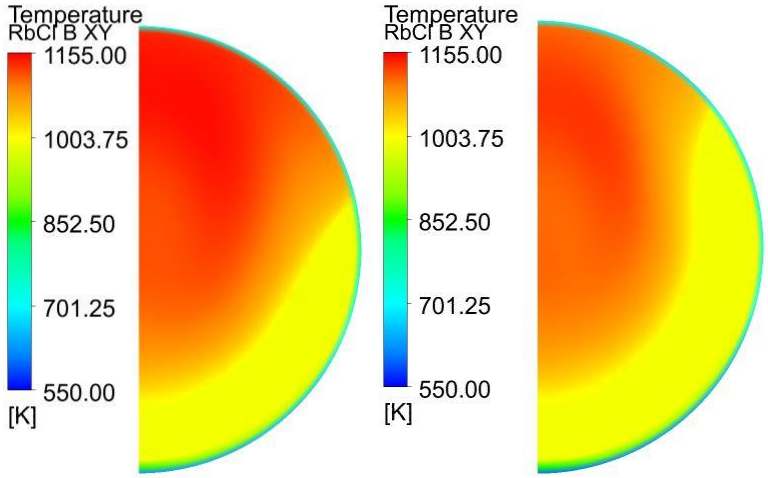

Figure 3-5: Comparison of RbCl target B's XY midplane temperature distribution profiles for the simplified model (L) and the full model (R).

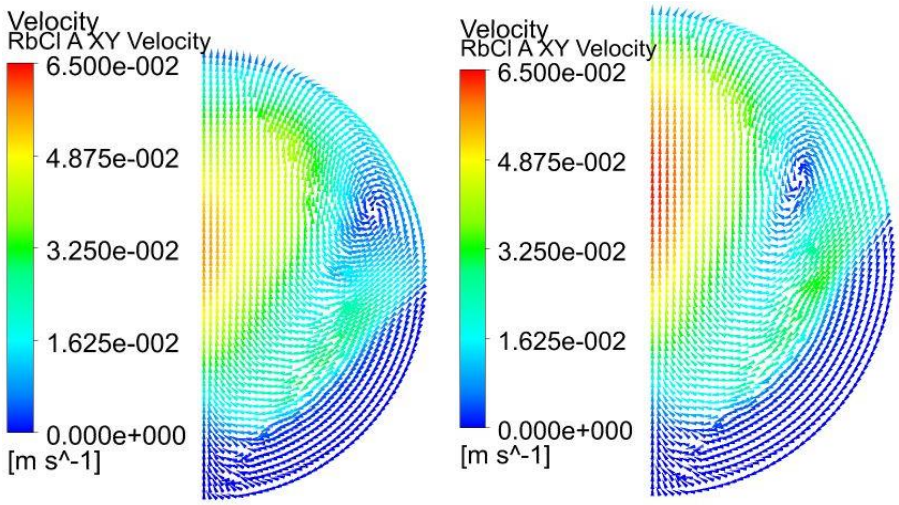

Figure 3-6: Comparison of RbCl target A's XY midplane velocity distribution profiles for the simplified model (L) and the full model (R).

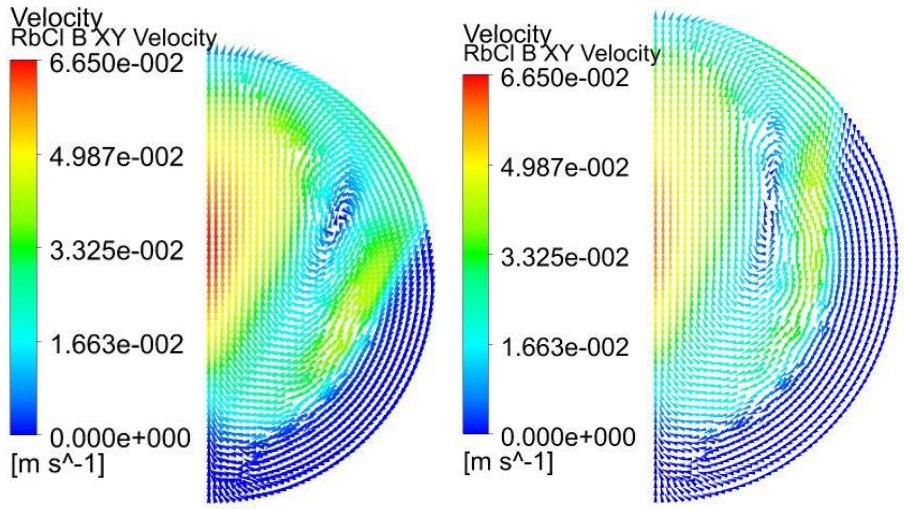

Figure 3-7: Comparison of RbCl Target B's XY midplane velocity distribution profiles for the simplified model (L) and the full model (R).

Recirculating convective patterns are clearly evident in the liquid phase region in all models for RbCl targets A and B.

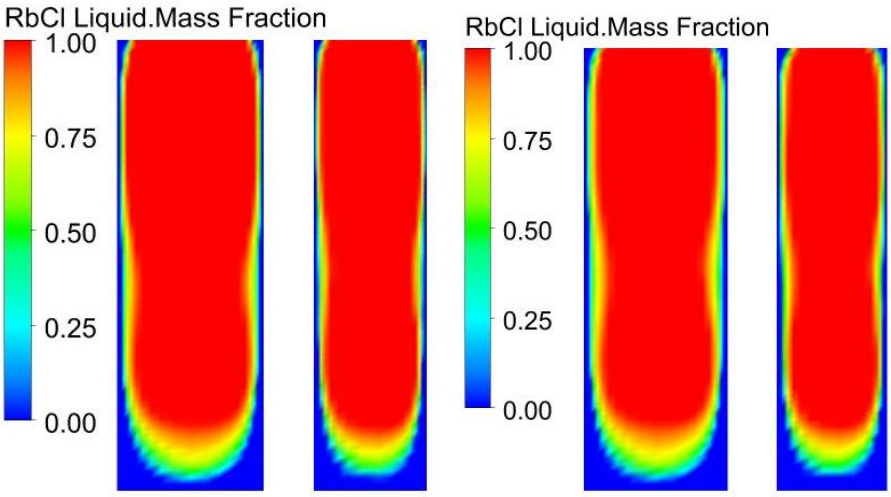

Figure 3-8: Comparison of RbCl targets YZ midplane liquid fraction profiles for the simplified model (L) and the full model (R).

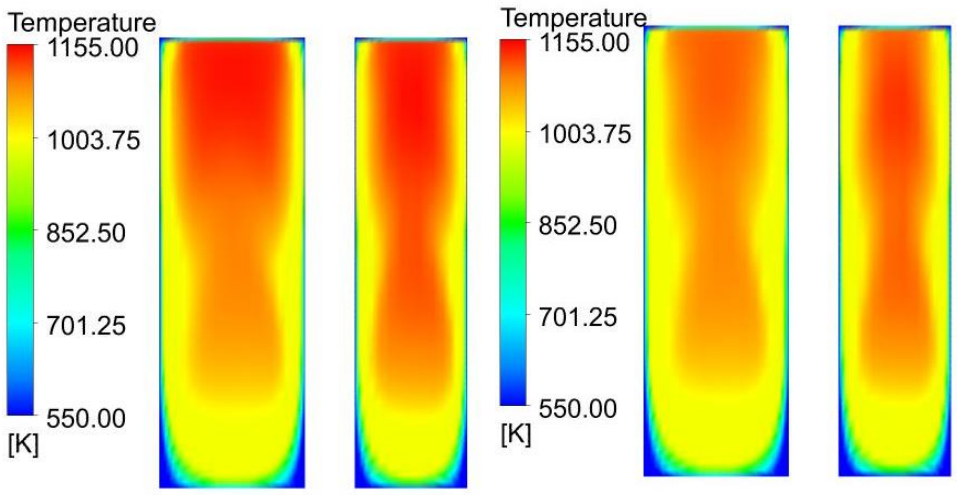

Figure 3-9: Comparison of RbCl targets YZ midplane temperature profiles for the simplified model (L) and the full model (R).

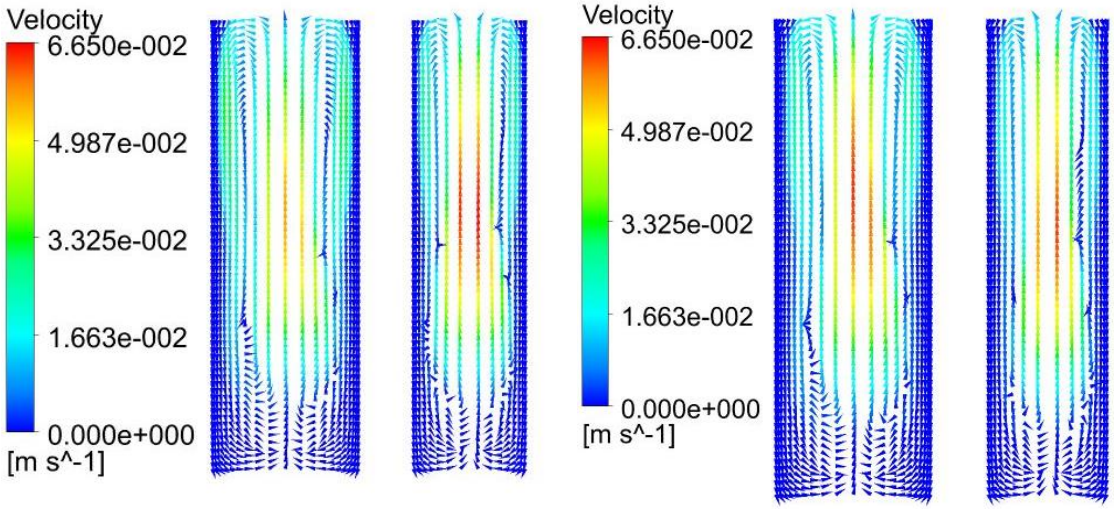

Figure 3-10: Comparison of RbCl targets YZ midplane velocity profiles for the simplified model (L) and the full model (R).

Limitations with the full model include memory issues when saving transient time steps and total run time. Given the relatively low error between the simplified and full models, the simplified average heat transfer coefficient model is adequate for performing scoping and parametric studies with the full model reserved for final calculations requiring higher accuracy. Using a simplified model with suppressed geometry and an assumed average heat transfer

coefficient boundary condition yields results that demonstrate the same behavior and trends seen when using a full model. However, while a first order solution may be adequate for scoping parametric studies, a highly accurate solution is desirable for benchmarking and validation.

Section 3.2. Refined Cooling Water Domain Results

Ensuring heat transfer from the target bodies is modeled as accurately as possible requires more detailed modeling of the cooling water channels. In addition, a significant correction in the beam distribution was made to this model. These results were used in Chapter 4 for quantitative comparison with measured observables, or validation metrics.

This model was run for a total of 61.5 seconds of transient simulation time in ANSYS CFX. As described in Section 2.1.6, iterative coupling between ANSYS and MCNP was performed every 1.5 seconds of transient simulation time. The MCNP input decks providing heat generation data were run with 20 million particle histories. Several thermal hydraulic metrics were tracked as a function of iteration number and time and are recorded in the tables below. These parameters include heat deposition, maximum and average temperatures, and RbCl liquid fraction. Also recorded were the average incident and exiting proton energies at the front and back face of all three targets. Cumulatively, these values provide an idea of how each domain behaves before reaching pseudo steady state. The heat deposition for all domains as a function of iteration number is provided in Table 3-6 and Table 3-7, and the heat deposition in RbCl targets A and B and Ga target C is graphed as a function iteration number in Figure 3-11. The beam profile for the first iteration is compared to the beam profile for the last iteration in Figure 3-12 to illustrate the drastic change in beam shape and heat deposition.

Table 3-6: Heat deposition at each iteration for each domain.

Heat Deposition [kW] – MCNP Predicted							
Iteration	**In Window**	**RbCl Target A**	**In Capsule A**	**RbCl Target B**	**In Capsule B**	**Ga Target C**	**Nb Capsule C**
1	0.3586	6.1111	0.7389	7.6107	1.4189	9.0886e-4	0.0104
2	0.3587	5.8994	0.7313	6.2622	1.2080	1.6747	0.4388
3	0.3587	5.0707	0.7186	5.0564	1.0297	4.8360	0.3805
4	0.3587	4.7247	0.7122	4.8654	0.9829	5.6689	0.3689
5	0.3587	4.7421	0.7143	4.8499	0.9812	5.6867	0.3693
6	0.3587	4.7045	0.7140	4.8164	0.9770	5.7897	0.3660
7	0.3587	4.6849	0.7137	4.8049	0.9754	5.8344	0.3649
8	0.3587	4.6768	0.7137	4.8029	0.9748	5.8490	0.3649
9	0.3587	4.6808	0.7141	4.8034	0.9752	5.8427	0.3654
10	0.3587	4.6797	0.7142	4.8021	0.9752	5.8460	0.3654
11	0.3587	4.6802	0.7144	4.8021	0.9753	5.8449	0.3657
12	0.3587	4.6804	0.7145	4.8056	0.9756	5.8402	0.3659
13	0.3587	4.6826	0.7147	4.8049	0.9758	5.8376	0.3661
14	0.3587	4.6827	0.7147	4.8048	0.9758	5.8374	0.3661
15	0.3587	4.6836	0.7148	4.8038	0.9759	5.8380	0.3662
16	0.3587	4.6835	0.7149	4.8024	0.9758	5.8398	0.3661
17	0.3587	4.6834	0.7149	4.8017	0.9759	5.8409	0.3661
18	0.3587	4.6830	0.7149	4.8025	0.9758	5.8407	0.3661
19	0.3587	4.6819	0.7149	4.8032	0.9758	5.8412	0.3661
20	0.3587	4.6804	0.7148	4.8024	0.9757	5.8442	0.3660
21	0.3587	4.6793	0.7148	4.8032	0.9756	5.8450	0.3660
22	0.3587	4.6779	0.7148	4.8029	0.9755	5.8473	0.3660
23	0.3587	4.6768	0.7147	4.8029	0.9754	5.8491	0.3659
24	0.3587	4.6758	0.7148	4.8027	0.9754	5.8507	0.3659
25	0.3587	4.6751	0.7147	4.8024	0.9754	5.8519	0.3658
26	0.3587	4.6747	0.7147	4.8024	0.9753	5.8525	0.3658
27	0.3587	4.6743	0.7147	4.8025	0.9753	5.8529	0.3657
28	0.3587	4.6739	0.7147	4.8024	0.9753	5.8535	0.3657
29	0.3587	4.6736	0.7147	4.8022	0.9753	5.8544	0.3657
30	0.3587	4.6732	0.7147	4.8023	0.9753	5.8548	0.3657
31	0.3587	4.6732	0.7147	4.8019	0.9753	5.8553	0.3656
32	0.3587	4.6728	0.7147	4.8022	0.9753	5.8556	0.3657
33	0.3587	4.6727	0.7146	4.8017	0.9752	5.8564	0.3656
34	0.3587	4.6726	0.7147	4.8022	0.9753	5.8558	0.3656
35	0.3587	4.6724	0.7147	4.8017	0.9752	5.8565	0.3656
36	0.3587	4.6722	0.7147	4.8019	0.9752	5.8566	0.3656
37	0.3587	4.6722	0.7146	4.8019	0.9752	5.8566	0.3656
38	0.3587	4.6720	0.7147	4.8020	0.9752	5.8567	0.3656
39	0.3587	4.6722	0.7147	4.8019	0.9752	5.8566	0.3656
40	0.3587	4.6717	0.7147	4.8019	0.9751	5.8572	0.3655
41	0.3587	4.6721	0.7147	4.8019	0.9752	5.8567	0.3655

Table 3-7: Heat deposition in cooling water and individual channels for each iteration.

	Heat Deposition [kW] – MCNP Predicted				
Iteration	**Cooling Water**	**Channel 1**	**Channel 2**	**Channel 3**	**Channel 4**
1	5.6693	1.1169	1.2269	3.3254	0
2	5.2064	1.1298	1.2173	2.8592	0
3	4.3928	1.1298	1.1671	2.0959	0
4	4.1786	1.1298	1.1479	1.9009	0
5	4.1603	1.1298	1.1478	1.8827	0
6	4.1370	1.1298	1.1457	1.8615	0
7	4.1270	1.1298	1.1447	1.8524	0
8	4.1232	1.1298	1.1443	1.8491	0
9	4.1240	1.1298	1.1445	1.8497	0
10	4.1230	1.1298	1.1444	1.8488	0
11	4.1228	1.1298	1.1444	1.8485	0
12	4.1232	1.1298	1.1444	1.8490	0
13	4.1235	1.1298	1.1445	1.8492	0
14	4.1235	1.1298	1.1445	1.8492	0
15	4.1299	1.1299	1.1445	1.8487	0
16	4.1225	1.1299	1.1444	1.8482	0
17	4.1222	1.1299	1.1444	1.8479	0
18	4.1222	1.2999	1.1444	1.8480	0
19	4.1221	1.1299	1.1444	1.8479	0
20	4.1215	1.1299	1.1443	1.8473	0
21	4.1212	1.1299	1.1442	1.8471	0
22	4.1208	1.1299	1.1442	1.8467	0
23	4.1205	1.1299	1.1441	1.8465	0
24	4.1202	1.1299	1.1441	1.8462	0
25	4.1198	1.1299	1.1440	1.8459	0
26	4.1197	1.1299	1.1440	1.8458	0
27	4.1197	1.1299	1.1440	1.8458	0
28	4.1194	1.1299	1.1440	1.8456	0
29	4.1193	1.1299	1.1440	1.8455	0
30	4.1193	1.1299	1.1440	1.8455	0
31	4.1192	1.1299	1.1439	1.8454	0
32	4.1192	1.1299	1.1439	1.8454	0
33	4.1189	1.1299	1.1439	1.8451	0
34	4.1191	1.1299	1.1440	1.8453	0
35	4.1189	1.1299	1.1439	1.8451	0
36	4.1189	1.1299	1.1439	1.8451	0
37	4.1189	1.1298	1.1440	1.8451	0
38	4.1189	1.1299	1.1439	1.8451	0
39	4.1188	1.1299	1.1439	1.8450	0
40	4.1187	1.1299	1.1439	1.8449	0
41	4.1188	1.1299	1.1439	1.8450	0

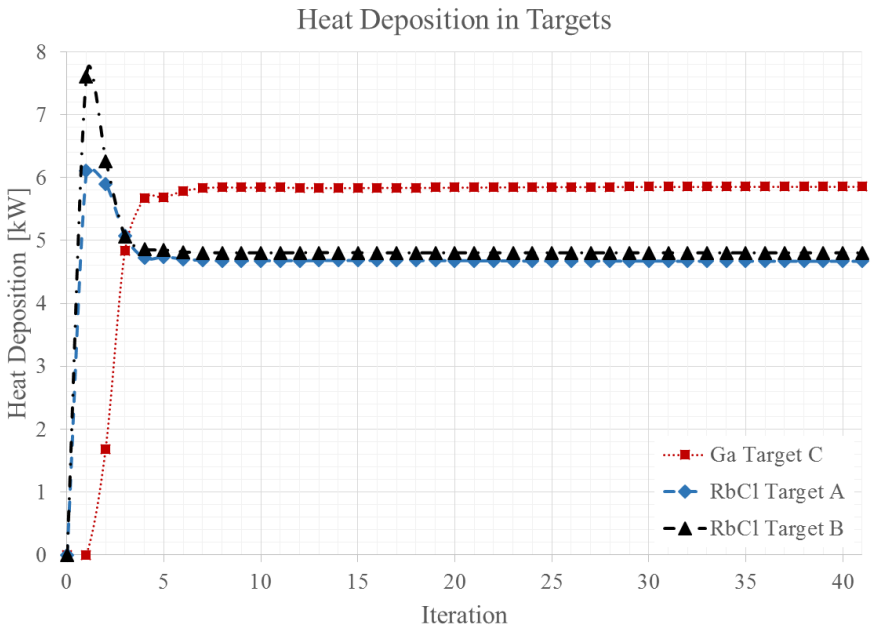

Figure 3-11: Heat deposition in targets as a function of iteration number.

Figure 3-11 illustrates the heat deposition in RbCl targets A and B and the C slot Ga target as a function of iteration number. Initially almost no heat is deposited in the Ga target as the solid RbCl upstream stops the majority of the incident protons. In addition, Table 3-6 and Table 3-7 indicate that there is a large amount of heat deposition in RbCl target B and cooling water channel three due to the location of the Bragg peak as the proton energies approach zero. As the A and B slot RbCl targets begin to melt, the heat deposition in these targets decreases and the heat deposition in the Ga C slot target increases. This is also illustrated in the images of volumetric heat deposition for the initial iteration and the final iteration, shown in Figure 3-12. These figures have been provided to give a sense of beam penetration and behavior when assuming solid RbCl targets versus accounting for the impact of density variation. As a result of significantly different mesh sizes in all target domains and smaller mesh elements at domain interfaces, the volumetric heat generation rates do not scale as the total heat produced in a particular cell volume, and must be plotted on different scales in each target domain to visualize the beam behavior.

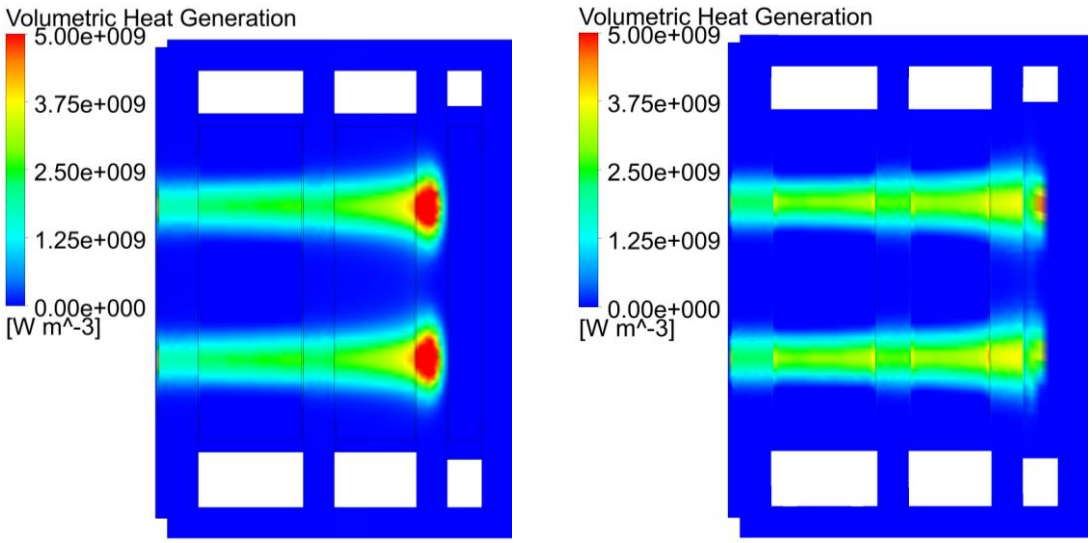

Figure 3-12: Volumetric heat generation profiles at the YZ midplane in all domains for the initial iteration (L) and final iteration at 61.5 s (R).

To provide a visualization of the ring-shaped beam profile in the A, B, and C slot targets, their volumetric heat generation profile for the final iteration is shown below in Figure 3-13. This figure presents RbCl targets A and B on the same scale, but presents Ga target C on a different scale to fully resolve the considerably higher heat deposition in the domain.

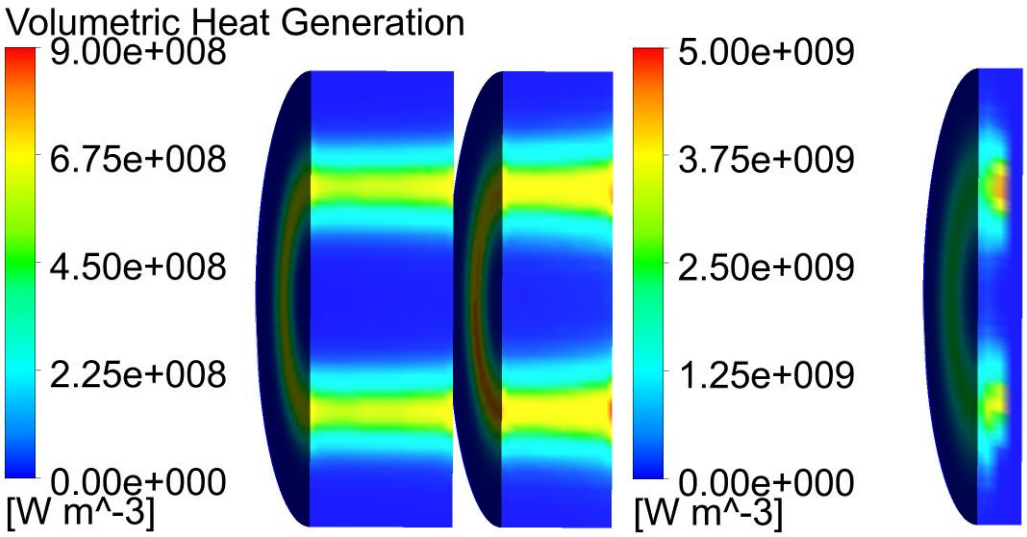

Figure 3-13: Volumetric heat generation profiles for RbCl targets A and B (L) and the C-slot Ga (R) target for the final iteration at 61.5 s.

Table 3-8 shows the impact of the melting RbCl A and B targets on the incident and exiting energy. As the RbCl targets begin to melt, the average energy of the protons exiting RbCl target A significantly increases, as does the resulting incident energy into RbCl target B. This is also seen in the average proton energy exiting RbCl target B and the average proton energy entering Ga target C. This average energy increase seen exiting RbCl target B and entering Ga target C is more significant with successive iterations due to the cumulative effects of the incident proton beam passing through two upstream targets.

Table 3-8: Average energy incident and exiting each target.

Average Incident and Exiting Energies [MeV]					
Iteration	**RbCl Target A**		**RbCl Target B**		**Ga Target C**
	E_{in}	E_{out}	E_{in}	E_{out}	E_{in}
1	90.8512	64.6185	55.5736	20.8722	~ 0
2	90.8479	65.4619	56.5184	28.1088	13.3843
3	90.8479	69.0838	60.5337	37.9322	25.9960
4	90.8478	70.5829	62.1860	40.5114	28.0283
5	90.8478	70.4981	62.0901	40.4749	27.7378
6	90.8478	70.6571	62.2638	40.8047	28.1218
7	90.8478	70.7387	62.3544	40.9480	28.2734
8	90.8478	70.7714	62.3909	40.9926	28.3154
9	90.8478	70.7519	62.3693	40.9674	28.2744
10	90.8478	70.7556	62.3733	40.9767	28.2833
11	90.8478	70.7525	62.3696	40.9717	28.2714
12	90.8478	70.7509	62.3669	40.9532	28.2444
13	90.8478	70.7405	62.3557	40.9436	28.2326
14	90.8478	70.7405	62.3555	40.9435	28.2325
15	90.8478	70.7360	62.3511	40.9412	28.2243
16	90.8478	70.7362	62.3516	40.9483	28.2345
17	90.8478	70.7363	62.3518	40.9508	28.2374
18	90.8478	70.7380	62.3539	40.9495	28.2354
19	90.8478	70.7428	62.3589	40.9513	28.2380
20	90.8478	70.7489	62.3662	40.9622	28.2529
21	90.8478	70.7534	62.3704	40.9643	28.2554
22	90.8478	70.7595	62.3777	40.9723	28.2665
23	90.8478	70.7640	62.3828	40.9779	28.2737
24	90.8478	70.7681	62.3874	40.9837	28.2814
25	90.8478	70.7712	62.3905	40.9879	28.2876
26	90.8478	70.7731	62.3924	40.9903	28.2902
27	90.8478	70.7744	62.3943	40.9918	28.2922
28	90.8478	70.7759	62.3961	40.9940	28.2955
29	90.8478	70.7775	62.3980	40.9970	28.2992
30	90.8478	70.7795	62.3998	40.9985	28.3014
31	90.8478	70.7796	62.4003	41.0003	28.3042
32	90.8478	70.7808	62.4016	41.0007	28.3042
33	90.8478	70.7815	62.4028	41.0039	28.3087
34	90.8478	70.7816	62.4028	41.0020	28.3060
35	90.8478	70.7826	62.4034	41.0049	28.3101
36	90.8478	70.7838	62.4048	41.0052	28.3104
37	90.8478	70.7832	62.4045	41.0050	28.3103
38	90.8478	70.7842	62.4052	41.0055	28.3111
39	90.8478	70.7838	62.4039	41.0054	28.3108
40	90.8478	70.7854	62.4064	41.0077	28.3137
41	90.8478	70.7839	62.4047	41.0055	28.3111

The progressive melting of RbCl targets A and B is shown as a function of iteration number in Table 3-9 and as a function of time in Figure 3-14. The maximum and average temperatures in all domains are given for each iteration in Table 3-10 and Table 3-11. As the behavior of RbCl targets A and B are of most interest, the maximum and average temperatures of these targets are shown graphically as a function of time in Figure 3-15.

Table 3-9: Liquid fraction for RbCl targets A and B at each iteration.

Iteration	α_l [%]	
	RbCl Target A	**RbCl Target B**
0 (0 s)	0	0
1 (1.5 s)	0.546094	10.626
2 (3.0 s)	15.8482	26.9731
3 (4.5 s)	26.6954	37.1191
4 (6.0 s)	32.6521	42.4735
5 (7.5 s)	38.1722	47.0698
6 (9.0 s)	43.0558	50.4908
7 (10.5 s)	46.5636	52.8118
8 (12.0 s)	49.4231	54.5797
9 (13.5 s)	51.5444	55.9872
10 (15.0 s)	53.5306	57.0690
11 (16.5 s)	55.3333	57.8557
12 (18.0 s)	56.8602	58.4535
13 (19.5 s)	58.1749	58.8856
14 (21.0 s)	59.2864	59.2759
15 (22.5 s)	60.1985	59.6315
16 (24.0 s)	60.9603	59.9274
17 (25.5 s)	61.5968	60.1604
18 (27.0 s)	62.1447	60.3350
19 (28.5 s)	62.6251	60.4700
20 (30.0 s)	63.0364	60.5784
21 (31.5 s)	63.3857	60.6697
22 (33.0 s)	63.6816	60.7440
23 (34.5 s)	63.9326	60.8051
24 (36.0 s)	64.1424	60.8548
25 (37.5 s)	64.3157	60.8943
26 (39.0 s)	64.4600	60.9217
27 (40.5 s)	64.5758	60.9441
28 (42.0 s)	64.6782	60.9690
29 (43.5 s)	64.7602	60.9854
30 (45.0 s)	64.8268	61.0015
31 (46.5 s)	64.8820	61.0105
32 (48.0 s)	64.9276	61.0224
33 (49.5 s)	64.9661	61.0279
34 (51.0 s)	64.9977	61.0340
35 (52.5 s)	65.0242	61.0393
36 (54.0 s)	65.0445	61.0420
37 (55.5 s)	65.0610	61.0431
38 (57.0 s)	65.0733	61.0433
39 (58.5 s)	65.0838	61.0427
40 (60.0 s)	65.0911	61.0426
41 (61.5 s)	65.0981	61.0420

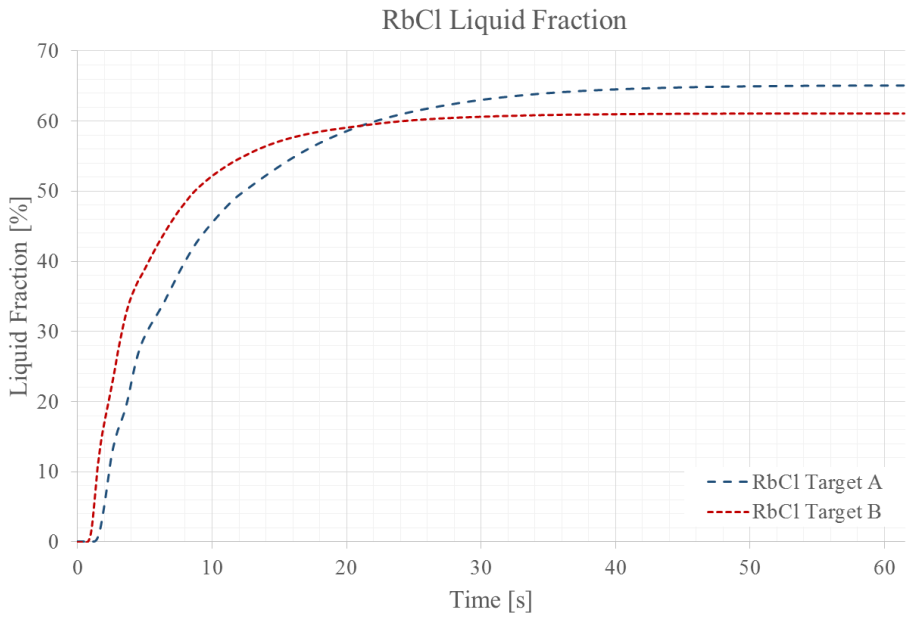

Figure 3-14: Average liquid fraction in RbCl targets A and B as a function of time.

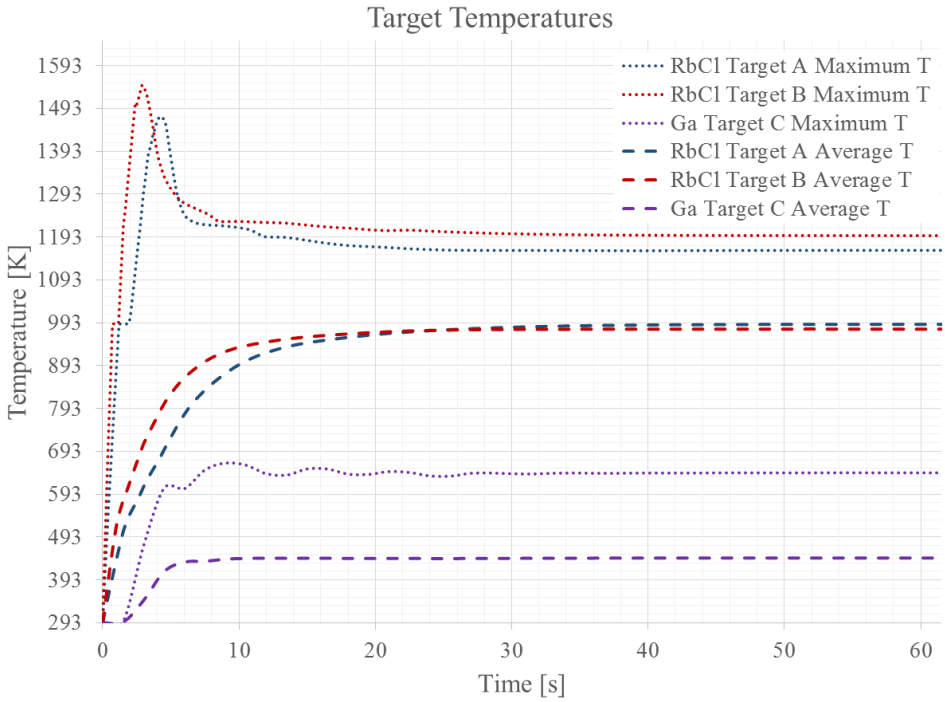

Figure 3-15: Maximum and average temperatures in RbCl targets A and B and Ga target C as a function of time.

As RbCl targets A and B experience a large amount of heat deposition while still in the solid phase, they both reach a peak temperature before enough of the target has melted to allow convective heat transfer to dominate. Poor thermal conductivity of RbCl means that convective heat transfer is a much more efficient heat transfer mechanism. This is evident when comparing the plot of liquid fraction as a function of time in Figure 3-14 and maximum temperatures presented as a function of time in Figure 3-15. For both RbCl targets A and B, once approximately ~25% of the target has melted the peak temperatures begin to decrease. This peak temperature excursion is not seen in Ga target C and the pseudo steady state average and peak temperatures are significantly lower. This is due to an entirely liquid Ga target, where convective heat transfer is immediately possible and because Ga has much better thermal conductivities.

One of the key reasons to model transient target behavior is to capture temperature excursions as the target is approaching its quasi-steady state solution. This maximum temperature seen early on when operating at high beam currents could lead to peak target temperatures above the RbCl boiling temperature of 1660 K. This causes vapor development and could lead to target overpressurization and failure. This behavior has been witnessed at LANL when operating above the nominal beam current. A slight fluctuation of ~0.4% is seen in the plot of RbCl target B maximum temperature in Figure 3-15 but is not considered significant to the transient behavior of the system. The maximum and average temperatures for all domains for each iteration are shown below in Table 3-10 – Table 3-12.

Table 3-10: Maximum temperature in target domains per iteration.

Iteration	Max T [K]					
	RbCl Target A	**RbCl Target B**	**Ga Target C**	**In Cap A**	**In Cap B**	**Nb Cap C**
0 (0 s)	293	293	293	293	293	293
1 (1.5 s)	990.000	1216.300	295.503	446.168	561.222	295.182
2 (3.0 s)	1301.300	1544.580	472.525	463.322	545.352	454.093
3 (4.5 s)	1466.720	1334.070	606.813	495.122	568.604	515.328
4 (6.0 s)	1243.630	1271.070	605.624	505.894	569.290	536.574
5 (7.50 s)	1221.410	1249.420	649.683	517.147	572.008	539.790
6 (9.0 s)	1218.310	1228.640	665.581	526.729	574.970	554.347
7 (10.5 s)	1212.020	1228.590	660.570	535.355	581.205	543.194
8 (12.0 s)	1192.660	1226.600	640.602	539.439	621.143	538.928
9 (13.5 s)	1191.770	1224.980	637.572	612.725	641.674	542.494
10 (15.0 s)	1184.800	1220.290	651.854	654.912	656.097	543.812
11 (16.5 s)	1177.930	1216.070	651.550	679.093	674.751	543.068
12 (18.0 s)	1172.860	1213.560	639.547	696.870	688.492	539.775
13 (19.5 s)	1170.480	1209.610	638.994	709.381	698.133	539.513
14 (21.0 s)	1168.240	1207.630	645.718	723.472	703.742	541.101
15 (22.5 s)	1165.290	1208.780	643.496	733.352	707.502	540.248
16 (24.0 s)	1163.370	1206.440	635.399	739.706	709.310	537.458
17 (25.5 s)	1162.130	1204.510	635.013	743.534	709.373	537.191
18 (27.0 s)	1161.720	1202.840	641.751	745.982	708.367	539.623
19 (28.5 s)	1161.600	1201.420	642.281	749.096	706.699	539.768
20 (30.0 s)	1161.430	1200.310	640.600	751.955	704.793	539.389
21 (31.5 s)	1161.390	1199.370	639.972	754.533	702.933	539.152
22 (33.0 s)	1161.370	1198.670	641.755	756.899	701.477	539.741
23 (34.5 s)	1161.190	1198.060	642.309	758.966	700.382	539.925
24 (36.0 s)	1161.020	1197.600	641.659	760.696	699.574	539.785
25 (37.5 s)	1160.840	1197.260	641.618	762.191	698.972	539.798
26 (39.0 s)	1160.750	1197.060	642.093	763.398	698.549	539.948
27 (40.5 s)	1160.750	1196.820	642.271	764.399	698.214	539.991
28 (42.0 s)	1160.930	1196.600	642.223	765.257	697.960	540.020
29 (43.5 s)	1161.090	1196.500	642.182	765.961	697.717	540.075
30 (45.0 s)	1161.210	1196.380	642.550	766.544	697.513	540.247
31 (46.5 s)	1161.320	1196.300	642.607	767.014	697.343	540.298
32 (48.0 s)	1161.390	1196.160	642.575	767.387	697.177	540.279
33 (49.5 s)	1161.450	1196.130	642.591	767.691	697.051	540.268
34 (51.0 s)	1161.530	1196.080	642.592	767.942	696.920	540.302
35 (52.5 s)	1161.600	1196.030	642.701	768.169	696.820	540.344
36 (54.0 s)	1161.630	1196.040	642.775	768.372	696.747	540.388
37 (55.5 s)	1161.660	1196.000	642.747	768.530	696.705	540.379
38 (57.0 s)	1161.660	1195.960	642.663	768.654	696.652	540.276
39 (58.5 s)	1161.690	1195.940	642.682	768.759	696.610	540.263
40 (60.0 s)	1161.700	1195.930	642.692	768.843	696.579	540.273
41 (61.5 s)	1161.720	1195.920	642.635	768.912	696.560	540.266

Table 3-11: Average temperature in each target domain per iteration.

Iteration	Average T [K]					
	RbCl Target A	**RbCl Target B**	**Ga Target C**	**In Cap A**	**In Cap B**	**Nb Cap C**
0 (0 s)	293	293	293	293	293	293
1 (1.5 s)	505.496	578.319	294.611	299.920	308.364	294.193
2 (3.0 s)	610.775	710.495	344.908	302.450	311.555	310.738
3 (4.5 s)	696.945	803.184	411.607	306.006	319.590	340.852
4 (6.0 s)	780.143	863.937	433.807	312.947	332.584	352.304
5 (7.5 s)	836.397	901.580	435.569	326.151	352.731	352.432
6 (9.0 s)	875.236	924.997	440.660	345.103	375.298	354.937
7 (10.5 s)	904.199	938.583	442.389	367.297	397.768	356.444
8 (12.0 s)	923.865	947.272	442.918	391.545	417.082	356.829
9 (13.5 s)	937.676	954.237	442.537	416.484	432.004	356.270
10 (15.0 s)	946.754	959.267	442.861	439.923	444.246	355.637
11 (16.5 s)	953.596	963.039	442.683	459.786	453.971	355.717
12 (18.0 s)	959.478	966.11	442.057	476.039	461.379	355.761
13 (19.5 s)	964.530	968.801	442.072	489.400	466.852	355.641
14 (21.0 s)	968.673	971.229	442.317	500.425	470.836	355.487
15 (22.5 s)	972.154	973.015	442.319	509.492	473.892	355.540
16 (24.0 s)	975.082	974.255	441.940	516.723	476.186	355.482
17 (25.5 s)	977.574	975.134	441.902	522.424	477.881	355.443
18 (27.0 s)	979.706	975.749	442.277	526.848	479.142	355.508
19 (28.5 s)	981.526	976.158	442.298	530.254	480.045	355.529
20 (30.0 s)	983.038	976.440	442.477	532.881	480.647	355.678
21 (31.5 s)	984.317	976.666	442.517	534.920	481.038	355.706
22 (33.0 s)	985.384	976.847	442.741	536.507	481.280	355.744
23 (34.5 s)	986.279	977.007	442.892	537.754	481.430	355.809
24 (36.0 s)	987.006	977.117	442.967	538.742	481.506	355.874
25 (37.5 s)	987.585	977.186	443.021	539.520	481.535	355.903
26 (39.0 s)	988.056	977.222	443.085	540.141	481.530	355.909
27 (40.5 s)	988.445	977.240	443.081	540.637	481.500	355.905
28 (42.0 s)	988.763	977.287	443.177	541.031	481.463	355.952
29 (43.5 s)	989.017	977.307	443.221	541.344	481.411	355.973
30 (45.0 s)	989.221	977.326	443.255	541.588	481.357	355.987
31 (46.5 s)	989.389	977.336	443.296	541.778	481.301	356.002
32 (48.0 s)	989.526	977.360	443.296	541.928	481.254	356.008
33 (49.5 s)	989.628	977.353	443.341	542.042	481.205	356.026
34 (51.0 s)	989.724	977.368	443.331	542.133	481.173	356.029
35 (52.5 s)	989.795	977.368	443.370	542.201	481.143	356.034
36 (54.0 s)	989.848	977.364	443.366	542.249	481.115	356.040
37 (55.5 s)	989.894	977.360	443.355	542.283	481.092	356.038
38 (57.0 s)	989.921	977.342	443.340	542.306	481.066	356.030
39 (58.5 s)	989.946	977.334	443.341	542.322	481.041	356.029
40 (60.0 s)	989.962	977.323	443.379	542.332	481.020	356.046
41 (61.5 s)	989.980	977.320	443.347	542.339	481.001	356.036

Table 3-12: Average and maximum temperatures in cooling water and beam window per iteration.

Iteration	Max T [K]		Average T [K]	
	Cooling Water	**In Window**	**Cooling Water**	**In Window**
0 (0 s)	293	293	293	293
1 (1.5 s)	492.463	363.429	293.180	301.231
2 (3.0 s)	476.366	363.612	293.238	301.266
3 (4.5 s)	495.224	363.631	293.307	301.274
4 (6.0 s)	495.844	363.598	293.356	301.288
5 (7.5 s)	498.815	363.613	293.376	301.313
6 (9.0 s)	501.176	363.606	293.399	301.331
7 (10.5 s)	505.053	363.608	293.415	301.348
8 (12.0 s)	505.483	363.618	293.428	301.366
9 (13.5 s)	506.003	363.631	293.436	301.384
10 (15.0 s)	505.450	363.637	293.443	301.400
11 (16.5 s)	504.526	363.635	293.449	301.413
12 (18.0 s)	503.737	363.627	293.454	301.423
13 (19.5 s)	502.632	363.618	293.458	301.432
14 (21.0 s)	501.360	363.610	293.462	301.437
15 (22.5 s)	501.025	363.555	293.465	301.435
16 (24.0 s)	500.653	363.550	293.468	301.441
17 (25.5 s)	500.065	363.564	293.469	301.445
18 (27.0 s)	499.585	363.553	293.471	301.446
19 (28.5 s)	499.069	363.547	293.473	301.449
20 (30.0 s)	498.654	363.566	293.473	301.451
21 (31.5 s)	498.417	363.561	293.474	301.450
22 (33.0 s)	498.250	363.552	293.475	301.451
23 (34.5 s)	498.050	363.570	293.475	301.452
24 (36.0 s)	498.001	363.570	293.476	301.451
25 (37.5 s)	497.987	363.557	293.476	301.451
26 (39.0 s)	497.873	363.563	293.476	301.453
27 (40.5 s)	497.780	363.569	293.476	301.453
28 (42.0 s)	497.840	363.554	293.477	301.452
29 (43.5 s)	497.756	363.551	293.477	301.453
30 (45.0 s)	497.705	363.565	293.477	301.454
31 (46.5 s)	497.667	363.553	293.477	301.452
32 (48.0 s)	497.686	363.547	293.478	301.453
33 (49.5 s)	497.647	363.568	293.477	301.452
34 (51.0 s)	497.706	363.558	293.478	301.452
35 (52.5 s)	497.693	363.563	293.478	301.452
36 (54.0 s)	497.668	363.567	293.478	301.453
37 (55.5 s)	497.698	363.560	293.478	301.452
38 (57.0 s)	497.657	363.557	293.478	301.453
39 (58.5 s)	497.639	363.572	293.478	301.454
40 (60.0 s)	497.637	363.565	293.478	301.453
41 (61.5 s)	497.614	363.553	293.478	301.453

Figures of the pseudo steady state thermal behavior obtained using ANSYS CFD-Post are shown below to further illustrate target behavior. Also given is a more detailed table of the pseudo steady state target temperatures and velocities.

Table 3-13: Pseudo steady state thermal hydraulic temperatures and velocities for the refined cooling water domain model.

Thermal Hydraulic Parameters					
Domain	**Temperature [K]**			**Velocity [m/s]**	
	Minimum	**Average**	**Maximum**	**Average**	**Maximum**
In718 Window	293.000	301.453	363.553	-	-
RbCl Target A	323.880	989.980	1161.720	1.2155×10^{-2}	5.5849×10^{-2}
Inconel Capsule A	303.733	542.339	768.912	-	-
RbCl Target B	317.832	977.320	1195.920	1.1182×10^{-2}	5.9005×10^{-2}
Inconel Capsule B	300.638	481.001	696.560	-	-
Ga Target C	303.511	443.347	642.635	2.9404×10^{-2}	8.1860×10^{-2}
Nb Capsule C	297.873	356.036	540.266	-	-
Cooling Water	292.908	293.478	497.614	1.0552	5.2863

Table 3-14: Pseudo steady state RbCl liquid fractions in RbCl targets A and B for the refined cooling water domain model.

RbCl Liquid Fraction	
Target Domain	**Liquid Fraction [%]**
RbCl Target A	65.0981
RbCl Target B	61.0420

Various midplane plots of temperature, density, liquid fraction, and velocities in RbCl targets A and B at the final quasi-steady state solution are shown below. For all XY distributions, the plane was taken at the center of the target. This midplane has a z-position of 1.545 cm in RbCl target A and 3.5605 cm in RbCl target B. For all YZ distributions, the midplane is located at the position x = 0 cm. All temperature, density, and velocity distributions are presented on the same scale for each target for ease of comparison.

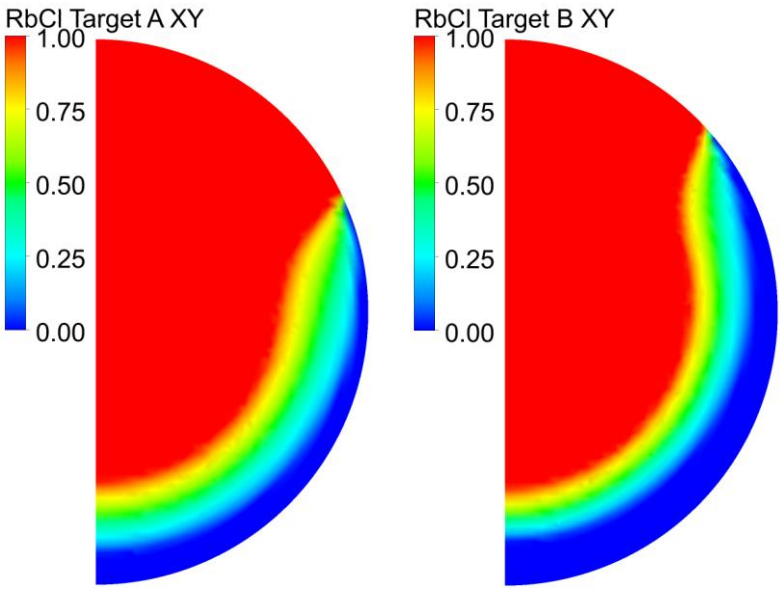

Figure 3-16: XY plane midplane liquid fraction distribution profiles in RbCl targets A (L) and B (R) at 61.5 s.

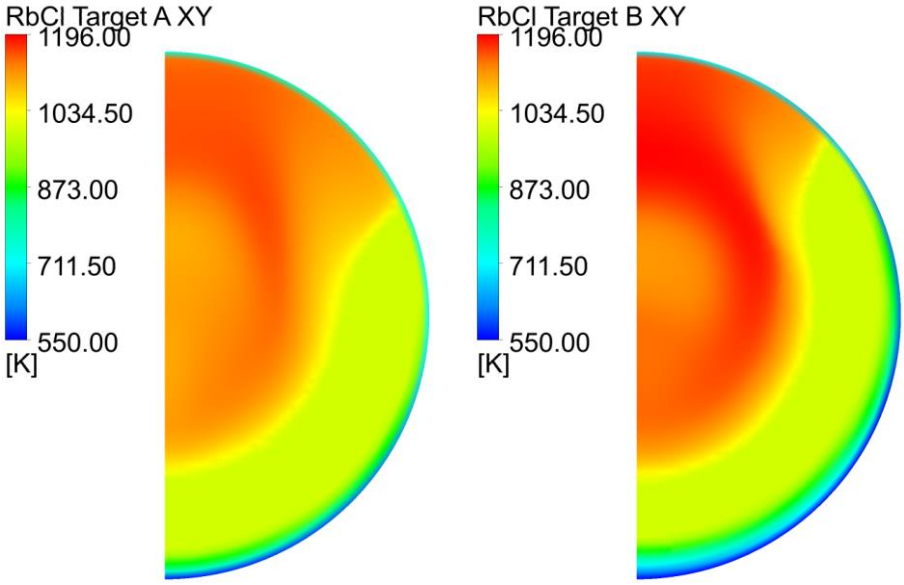

Figure 3-17: XY plane midplane temperature distribution profiles in RbCl targets A (L) and B (R) at 61.5 s.

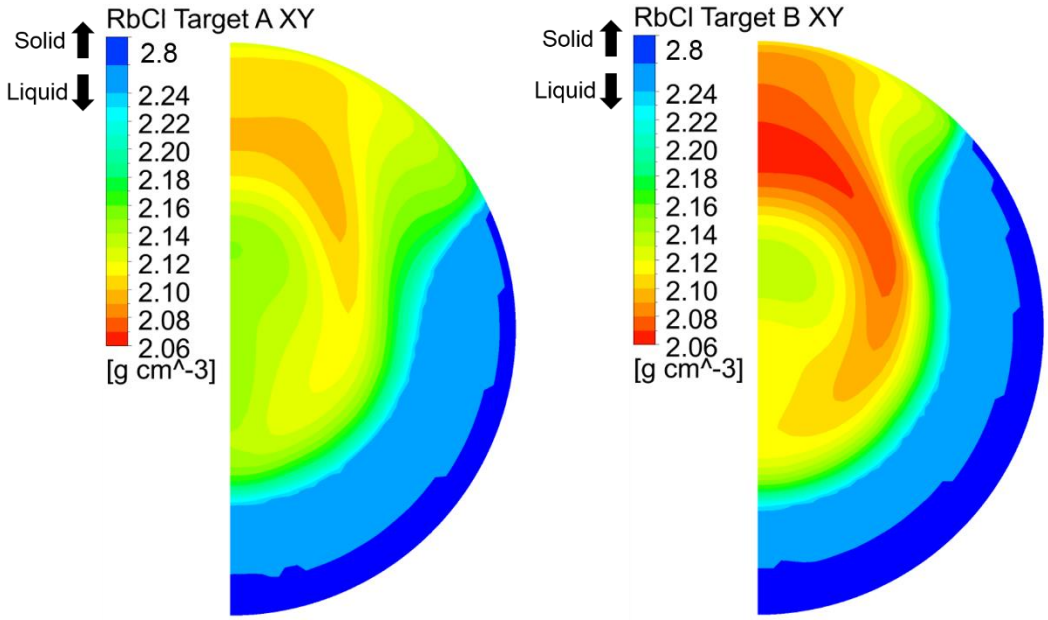

Figure 3-18: XY plane midplane density distribution profiles in RbCl targets A (L) and B (R) at 61.5 s.

Again Figure 3-17 and Figure 3-18 show that the less dense, molten RbCl material migrates to the top of the target and recirculates, following the convective patterns shown in Figure 3-19. In this midplane RbCl target A shows larger regions of peak velocities than RbCl target B. However, overall RbCl target B has higher peak velocities, provided in Table 3-13.

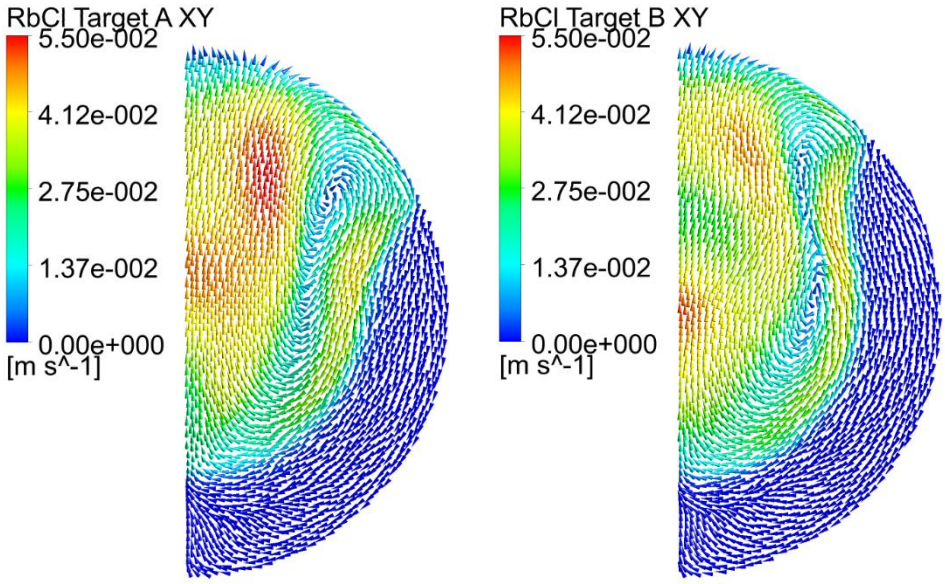

Figure 3-19: Midplane velocity profiles in RbCl targets A (L) and B (R) at 61.5 s.

To give an idea of the orientation of these planes, for all YZ plane images presented below the beam enters from the left and exits to the right.

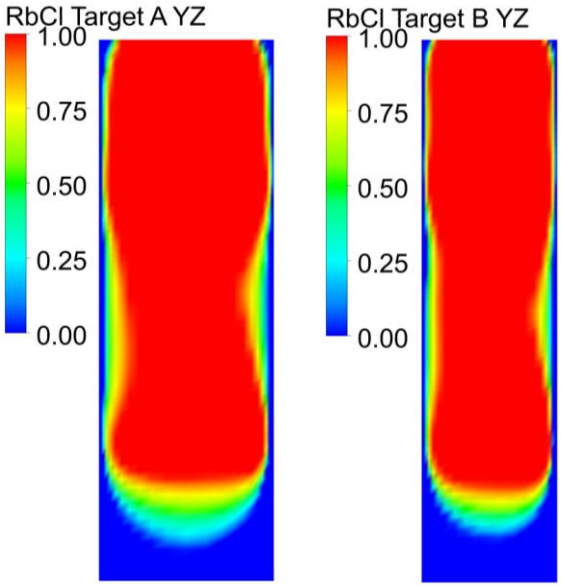

Figure 3-20: YZ plane midplane liquid fraction distribution profiles in RbCl targets A (L) and B (R) at 61.5 s.

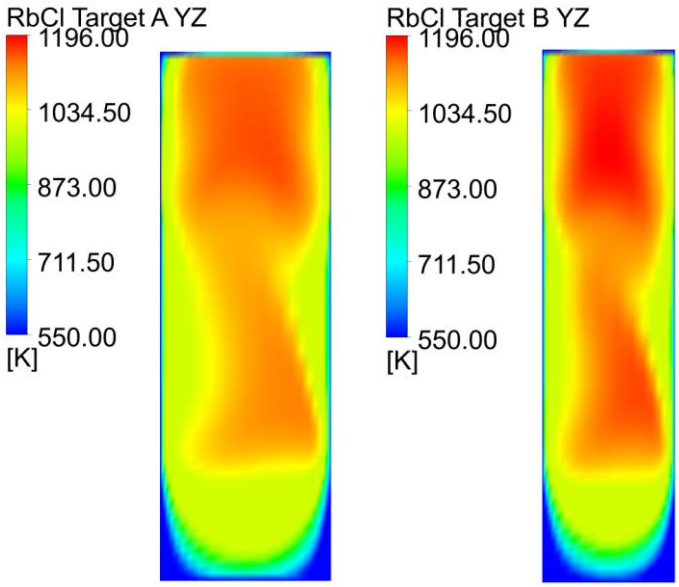

Figure 3-21: YZ plane midplane temperature distribution profiles in RbCl targets A (L) and B (R) at 61.5 s.

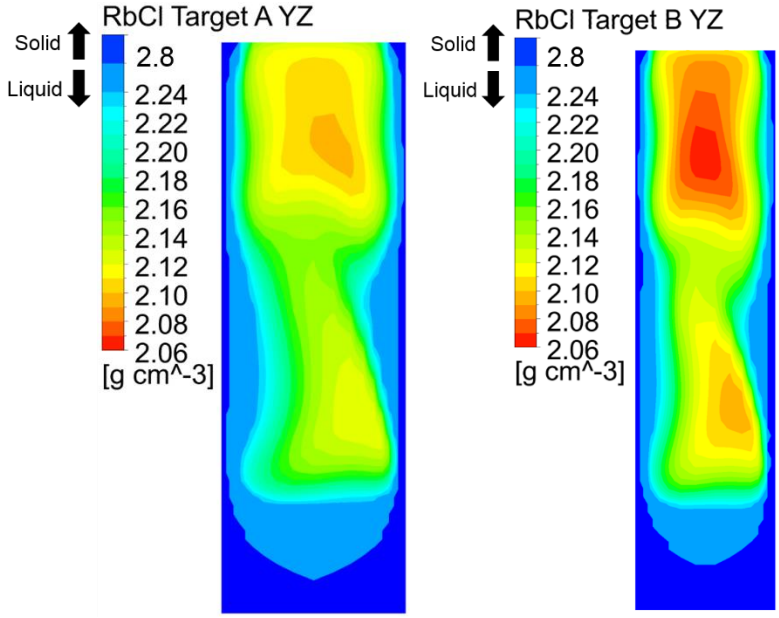

Figure 3-22: YZ plane midplane density distribution profiles in RbCl targets A (L) and B (R) at 61.5 s.

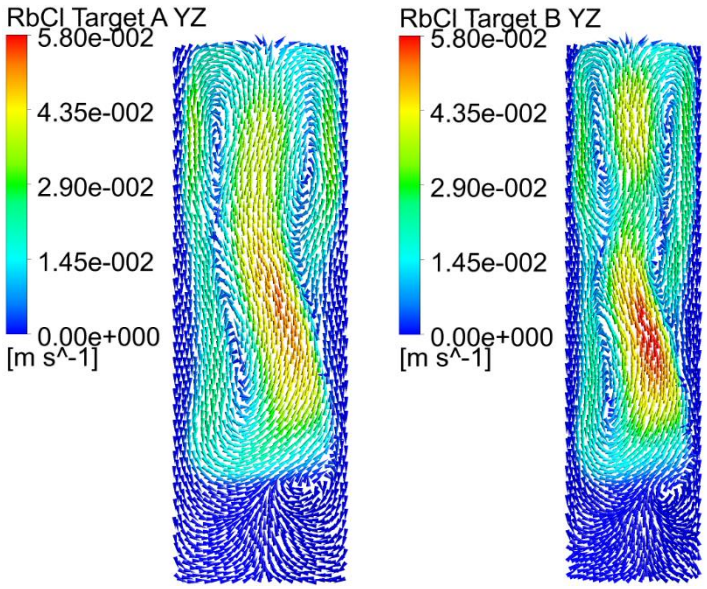

Figure 3-23: YZ plane midplane velocity profiles in RbCl targets A (L) and B (R) at 61.5 s.

The same recirculating behavior and molten RbCl relocation is again shown in these YZ plane midline images of temperature, density, and velocity. Convective patterns are clearly visible near the target centerline in Figure 3-23.

The final cooling water velocities in the YZ plane are shown below in Figure 3-24. Some recirculation can be seen at the exit of the cooling water channels due to the manifold type geometry.

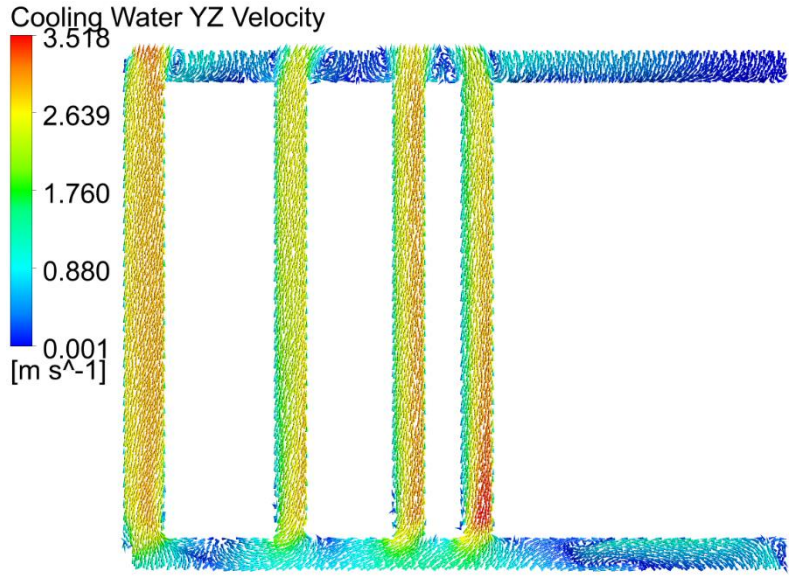

Figure 3-24: Cooling water velocity profile in the YZ midplane at 61.5 s.

A YZ plane slice depicting the temperature distribution in the cooling water domain is shown below in Figure 3-25.

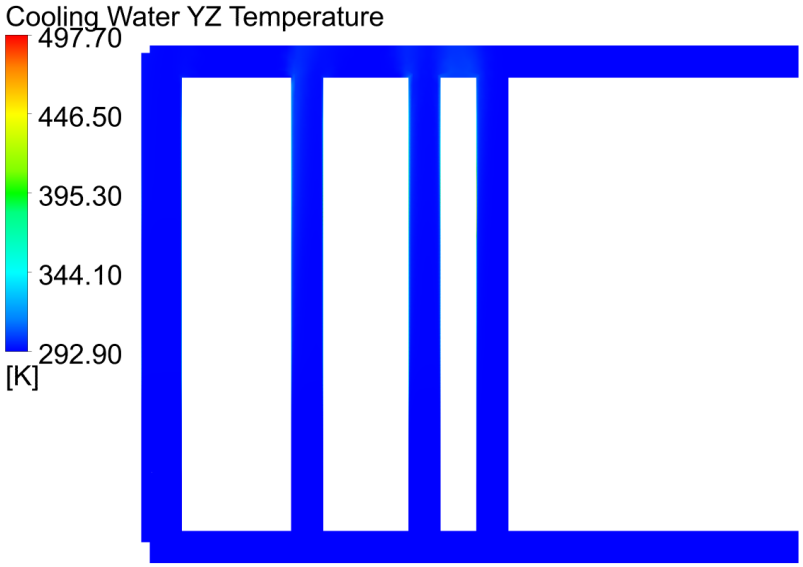

Figure 3-25: Cooling water temperature profile in the YZ midplane at 61.5 s.

While the bulk fluid cooling water temperature remains at around 293 K, near wall temperatures are significantly above this. Figure 3-26 gives the near wall temperature

distribution if Figure 3-25 is magnified in the area of one of the cooling water channel walls in channel 3. This figure illustrates the steep near-wall temperature gradient experienced by the cooling water.

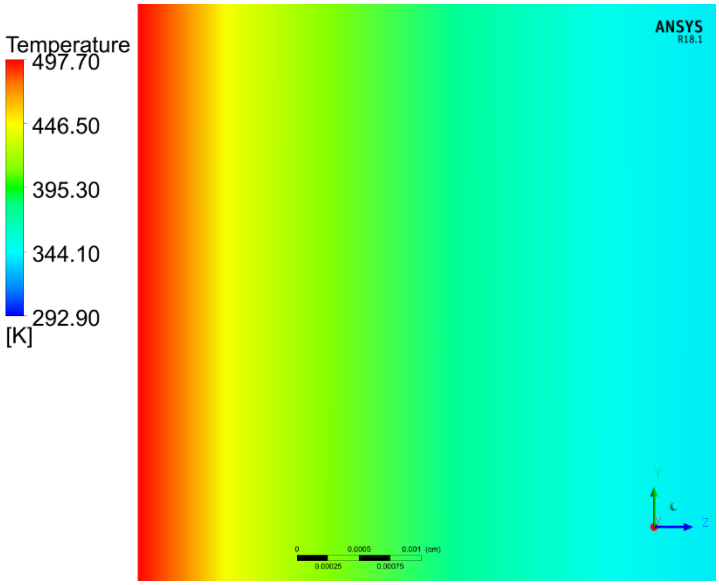

Figure 3-26: Magnified image of the near-wall temperature gradient in the cooling water channels.

The peak near wall temperatures seen above in Figure 3-26 are significantly above the saturation temperature of the cooling water. This would indicate that near-wall void development is occurring. To further illustrate these peak near-wall temperatures, a cooling water temperature distribution was taken at the face of each target capsule for all channels. These are shown on the same scale below in Figure 3-27 – Figure 3-30. These temperature distributions are similar to the target temperature distributions seen above, which is to be expected. Peak temperature excursions are seen most predominantly in Channel 3.

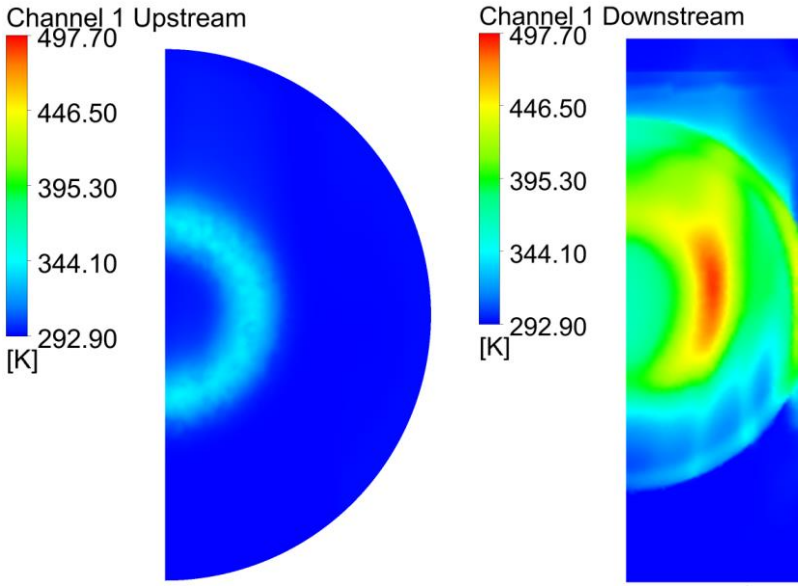

Figure 3-27: Channel 1 near-wall cooling water temperatures at the water-capsule interface at 61.5 s.

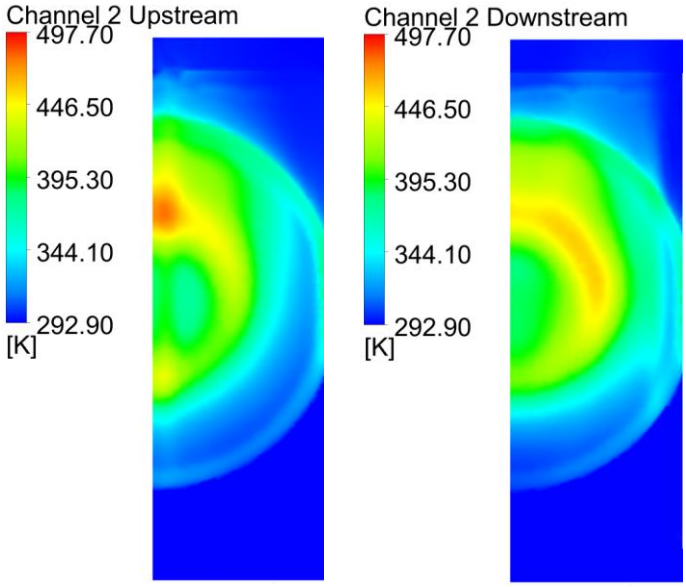

Figure 3-28: Channel 2 near-wall cooling water temperatures at the water-capsule interface at 61.5 s.

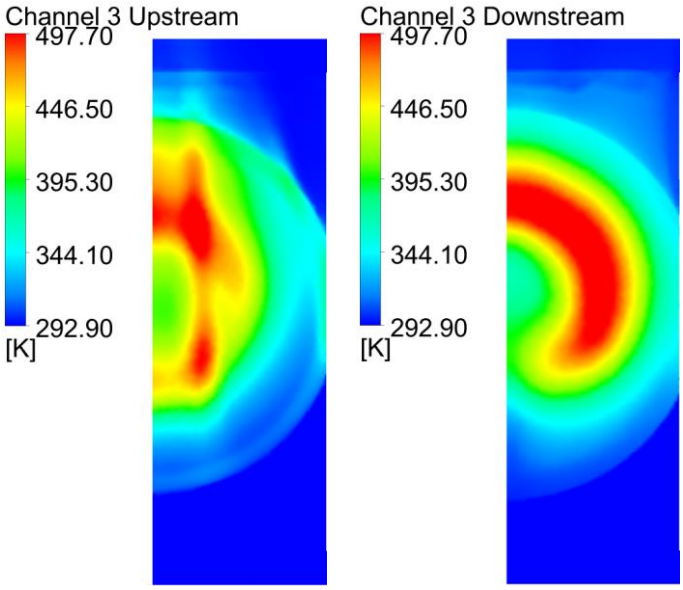

Figure 3-29: Channel 3 near-wall cooling water temperatures at the water-capsule interface at 61.5 s.

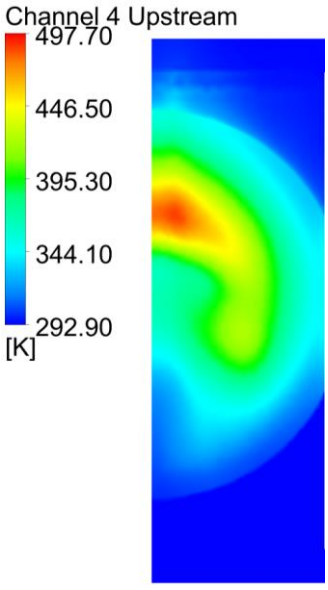

Figure 3-30: Channel 4 near-wall cooling water temperatures at the water-capsule interface at 61.5 s.

These images clearly display peak temperatures significantly above the boiling point of atmospheric pressure water at the cooling water-capsule interface. In addition, the peak near-wall temperature distributions resemble scorch mark patterns seen on physical targets, suggesting that critical heat flux may be occurring at these locations. This similarity is shown

in Figure 3-31 – Figure 3-34 by comparing the pseudo steady state near-wall temperature distributions obtained using ANSYS CFX and images taken from physical targets.

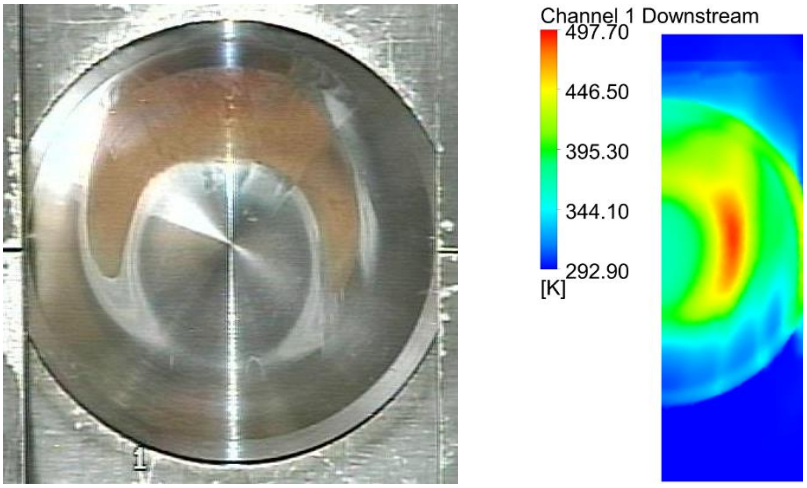

Figure 3-31: Scorch marks present on the front of the RbCl target A capsule after irradiation compared with the near-wall cooling water temperatures (back of cooling water channel 1).

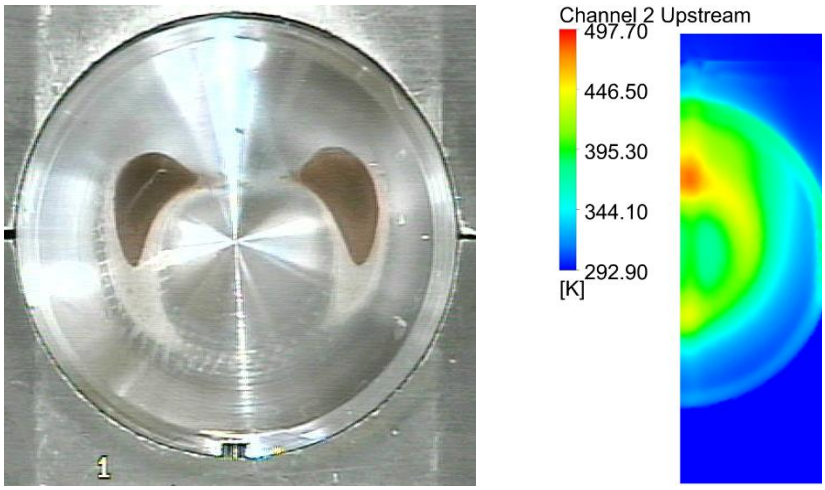

Figure 3-32: Scorch marks present on the back of the RbCl target A capsule after irradiation compared with the near-wall cooling water temperatures (front of cooling water channel 2).

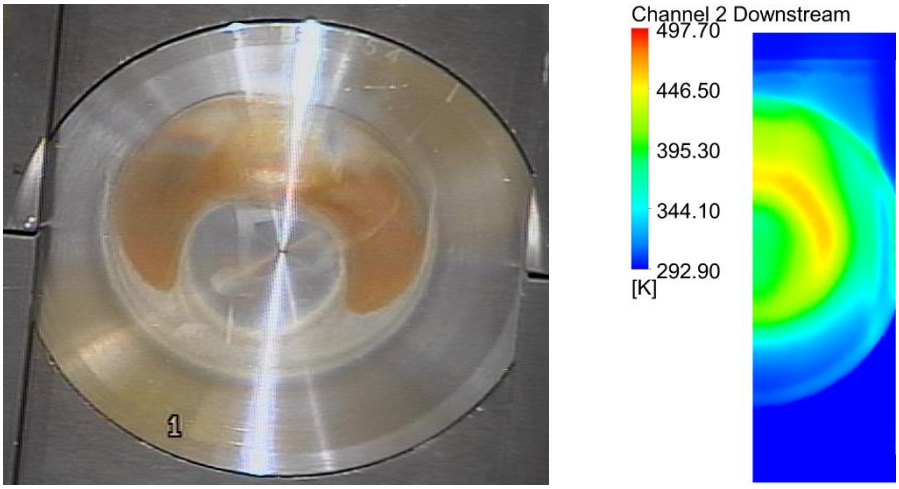

Figure 3-33: Scorch marks present on the front of the RbCl target B capsule after irradiation compared with the near-wall cooling water temperatures (back of cooling water channel 2).

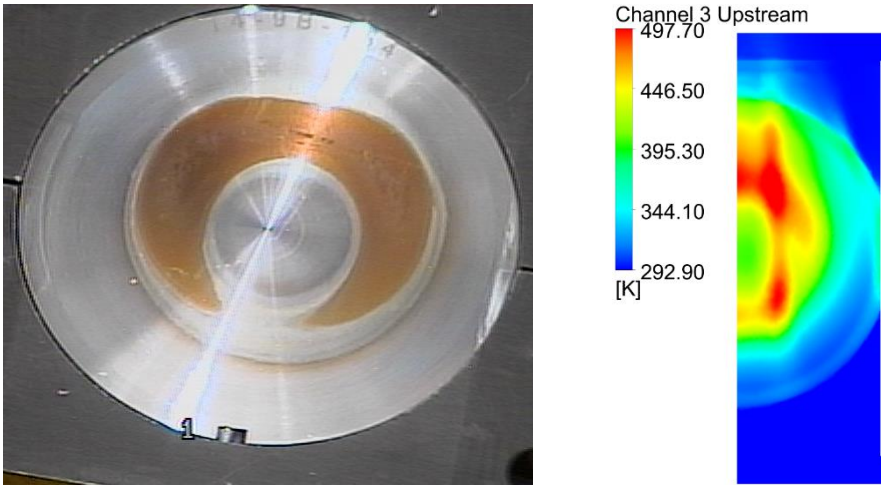

Figure 3-34: Scorch marks present on the back of the RbCl target B capsule after irradiation compared with the near-wall cooling water temperatures (front of cooling water channel 3).

The similarity between the physical images and near wall behavior seen in the model highlights a potential limitation in the modeling performed here – that there is void development occurring at the wall that is not presently being captured. If void development is present this limits the utility of the average heat transfer coefficient model as it cannot capture the influence of void development on heat transfer.

While these thermal hydraulic model results are useful for getting some 'picture' of target behavior, there needs to be some means by which to prove that this is indeed the correct 'picture'. By choosing experimentally measured values and using them as validation metrics, the physical meaning of these temperature and density gradients and convective patterns can be shown. The next chapter will discuss the chosen validation metrics and techniques used to obtain them.

Section 3.2.1. Comparison with Average Heat Transfer Coefficient Model

To determine the usefulness of the average heat transfer coefficient model for scoping and parametric studies, this model was re-run to a quasi-steady state solution with the same beam distribution and coupling time as used for the refined cooling water domain model. This means that the corrected beam distribution described in Section 2.2.2.2 was used for this comparison. This average heat transfer coefficient model's pseudo steady state solution will be used in the next chapter as a point of comparison against the validation metrics calculated for the final refined cooling water domain model.

In the tables below the refined cooling water domain model's pseudo steady state solution was compared to that of the average heat transfer coefficient model. Parameters presented here for comparison in Table 3-15 – Table 3-18 include heat deposition, peak and average temperatures and velocities, and average liquid fractions. For a more qualitative comparison, velocity, temperature, and liquid fraction distribution profiles are shown side by side for the two models.

Table 3-15: Comparison of heat deposition [kW] in the average heat transfer coefficient and refined cooling water domain model solutions.

Heat Deposition [kW]			
Target Domain	**Refined Cooling Water Domain**	**Average HTC**	**Relative Difference**
Inconel 718 Window	0.3587	0.3587	0.00%
RbCl Target A	4.6721	4.6551	0.36%
Inconel 625 Capsule A	0.7147	0.7141	0.08%
RbCl Target B	4.8019	4.7673	0.72%
Inconel 625 Capsule B	0.9752	0.9729	0.24%
Gallium Target C	5.8567	5.9261	1.19%
Niobium Capsule C	0.3655	0.3631	0.66%
Water	4.1188	4.1067	0.29%
Total (sans water)	17.7448	17.7573	0.07%
Total	21.8636	21.8640	1.8×10^{-3} %

Given the data presented in Table 3-15, it can be concluded that using a simplified model (via suppression of the cooling water) with an average heat transfer coefficient boundary condition predicts heat deposition to within ~1.2% of the refined cooling water domain model. Thermal hydraulic parameters for both models are presented in the tables below.

Table 3-16: Thermal hydraulic data for the average heat transfer coefficient and refined cooling water domain model solutions.

Target Domain	Temperature Data [K]					
	Maximum		**Average**		**Minimum**	
	Refined Cooling Water	**Average HTC**	**Refined Cooling Water**	**Average HTC**	**Refined Cooling Water**	**Average HTC**
RbCl Target A	1161.720	1170.700	989.980	997.506	323.880	335.497
4Inconel 625 Capsule A	768.912	777.825	542.339	549.016	303.733	312.696
RbCl Target B	1195.920	1203.390	977.320	991.205	317.832	330.181
Inconel 625 Capsule B	696.560	700.434	481.001	494.720	300.638	310.774

Table 3-17: Velocity data for the average heat transfer coefficient and refined cooling water domain model solutions.

Target Domain	Velocity Data [m/s]			
	Maximum		Average	
	Refined Cooling Water	Average HTC	Refined Cooling Water	Average HTC
RbCl Target A	5.5849×10^{-2}	5.8032×10^{-2}	1.2155×10^{-2}	1.2988×10^{-2}
RbCl Target B	5.9005×10^{-2}	6.0317×10^{-2}	1.1182×10^{-2}	1.2013×10^{-2}

Table 3-18: Comparison of average liquid fractions for RbCl targets A and B for the average heat transfer coefficient and refined cooling water domain models.

Liquid Fraction [%]		
Target Domain	Refined Cooling Water	Average HTC
RbCl Target A	65.0981%	66.2909%
RbCl Target B	61.0420%	63.2637%

The data provided in Table 3-16 shows that the temperatures for each target body are lower in the refined cooling water domain model. The overall average liquid fractions presented for both targets in Table 3-18 are slightly higher in the average heat transfer coefficient model.

Figure 3-35 – Figure 3-43 compare the converged temperature, velocity, and liquid fraction distributions in RbCl targets A and B for both models. The distributions appear very similar, and all images were scaled to the same temperature or velocity range scale for ease of comparison.

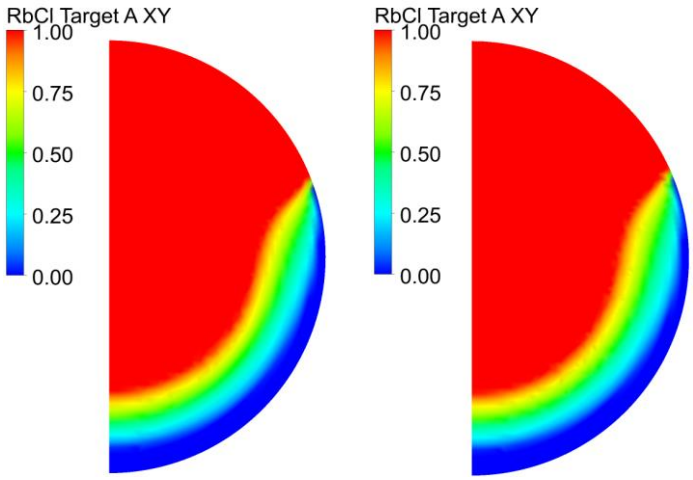

Figure 3-35: Comparison of RbCl target A's XY midplane liquid fraction distribution profiles for the average heat transfer coefficient model (L) and the refined cooling water domain model (R).

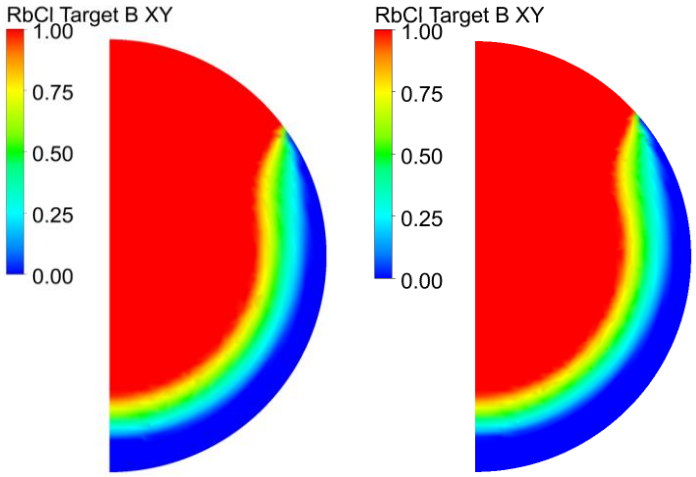

Figure 3-36: Comparison of RbCl target B's XY midplane liquid fraction distribution profiles for the average heat transfer coefficient model (L) and the refined cooling water domain model (R).

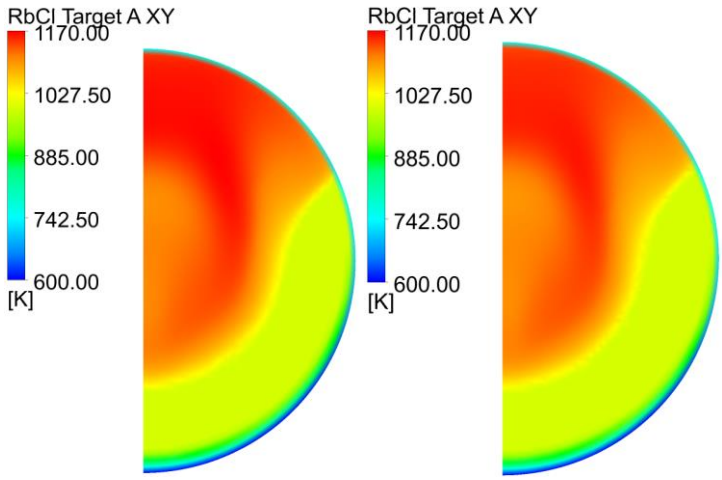

Figure 3-37: Comparison of RbCl target A's XY midplane temperature distribution profiles for the average heat transfer coefficient model (L) and the refined cooling water domain model (R).

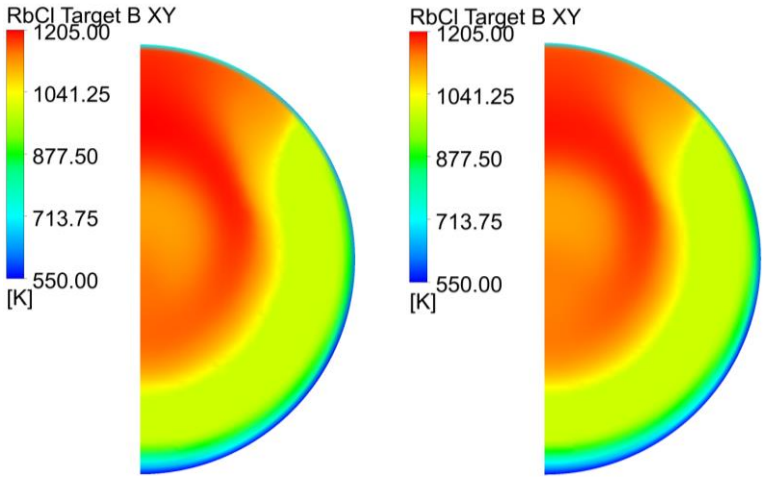

Figure 3-38: Comparison of RbCl target B's XY midplane temperature distribution profiles for the average heat transfer coefficient model (L) and the refined cooling water domain model (R).

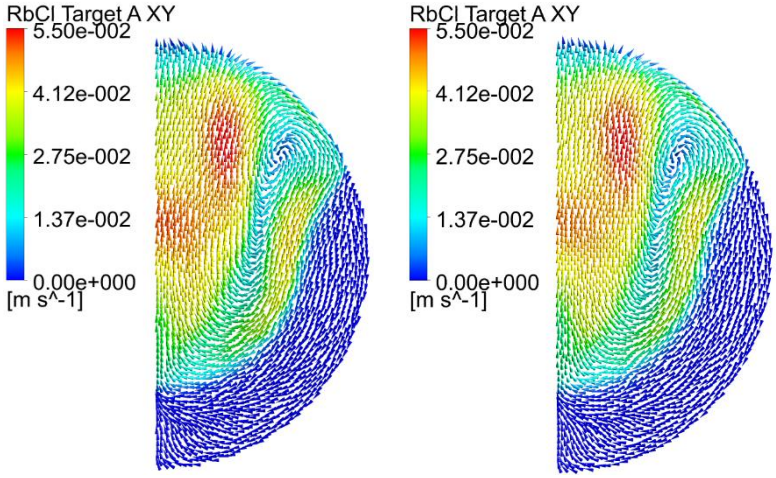

Figure 3-39: Comparison of RbCl target A's XY midplane velocity distribution profiles for the average heat transfer coefficient model (L) and the refined cooling water domain model (R).

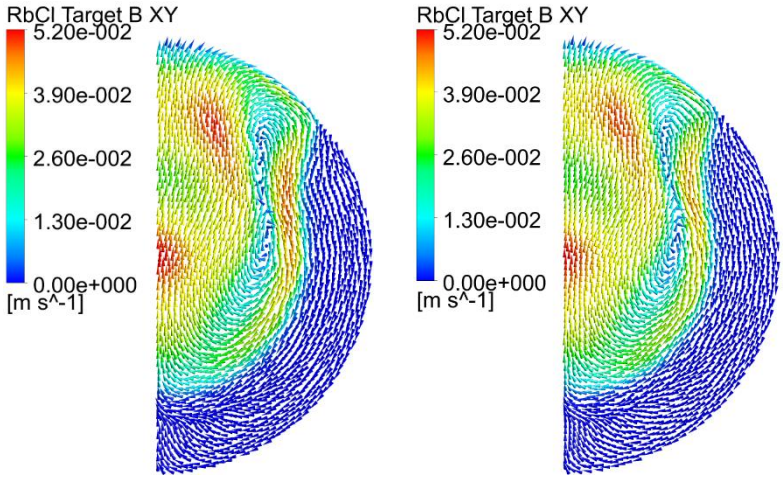

Figure 3-40: Comparison of RbCl Target B's XY midplane velocity distribution profiles for the average heat transfer coefficient model (L) and the refined cooling water domain model (R).

Similar recirculating convective patterns are clearly evident in the liquid phase region in all models for RbCl targets A and B.

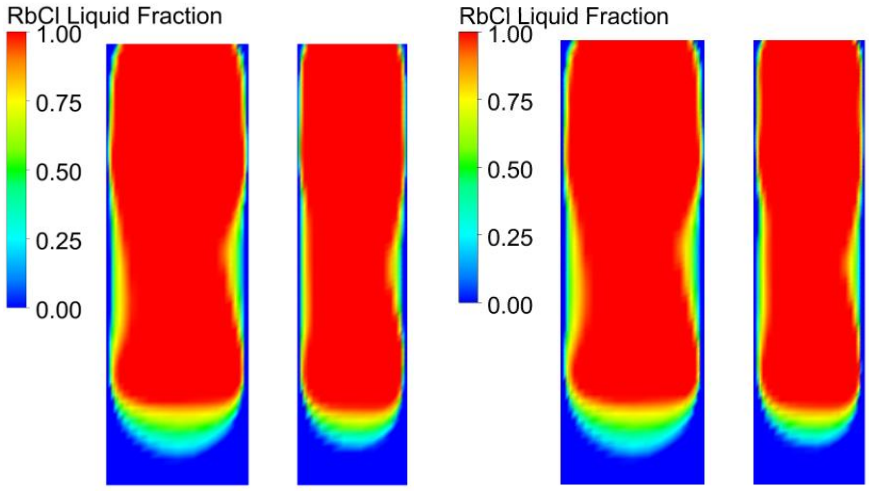

Figure 3-41: Comparison of RbCl targets YZ midplane liquid fraction distribution profiles for the average heat transfer coefficient model (L) and the refined cooling water domain model (R).

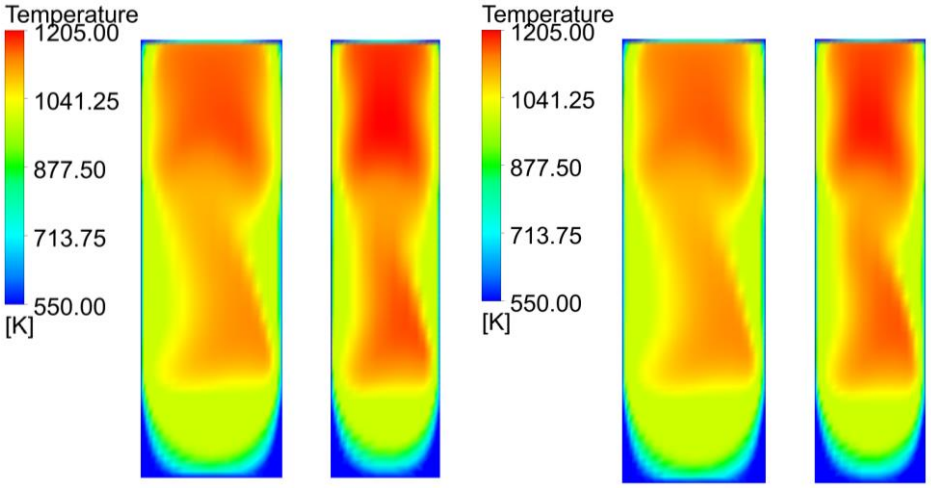

Figure 3-42: Comparison of RbCl targets YZ midplane temperature distribution profiles for the average heat transfer coefficient model (L) and the refined cooling water domain model (R).

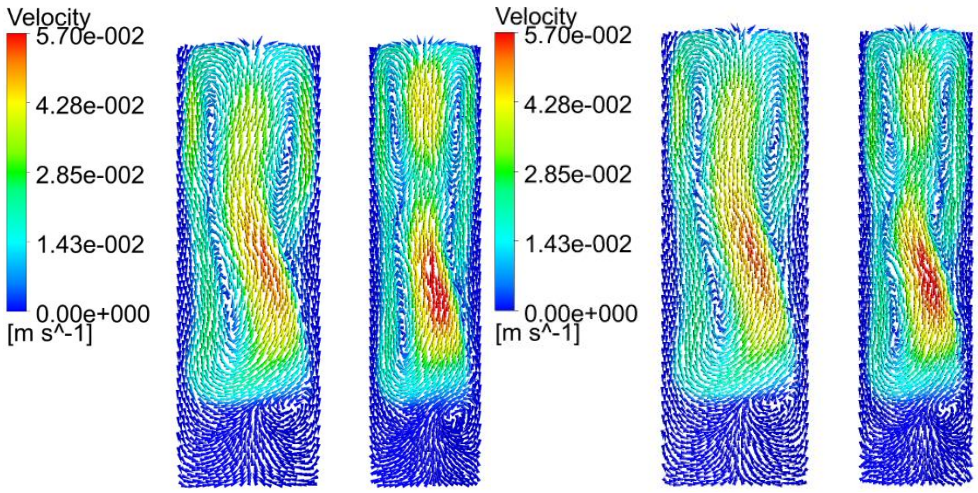

Figure 3-43: Comparison of RbCl targets YZ midplane velocity profiles for the average heat transfer coefficient model (L) and the refined cooling water domain model (R).

As the relative error between the two models is small, using an average heat transfer coefficient model for approximation of heat deposition in the target domains provides a reasonably accurate first-order picture of target behavior without the added computational expense. Due to the fine near-wall mesh resolution in the cooling water channels, the cooling water domain is the limiting factor on time step size and convergence. As a result, the average heat transfer coefficient model is able to run at least 18 times faster than the refined cooling water domain model and this factor increases the smaller the required time step for convergence in the cooling water domain.

Comparison of measured observable validation metrics determined with both the average heat transfer coefficient model and the refined cooling water domain model will allow for a quantitative determination of each model's predictive capabilities. It should be noted that indications of void development in the cooling water channels could in future limit the utility of the average heat transfer coefficient model. Void formation would significantly influence target heat removal through the cooling channels and the average heat transfer coefficient model would be unable to capture these physics.

CHAPTER 4. VALIDATION

Section 4.1. An Overview of Model Validation

When attempting to validate a model it is important to address whether the real-world behavior of the system is being modeled. To determine the degree to which a model is an adequate representation of the real world from the perspective of the intended uses of the model, accuracy of the model must be quantified. This is done via comparison of model responses with experimentally measured values, or measured observables.

Traditional methods of measuring the accuracy of computational results have been either qualitative or semi-qualitative. To measure the accuracy of computational results quantitatively, validation metrics are used. Validation metrics are measures of agreement between computational results and experimental measurements for system response quantities (SRQs) of interest. To evaluate a validation metric, one must first choose a SRQ of interest, then experimentally measure all input quantities needed for the model. In addition, the system response must be measured and uncertainties estimated. Using the input quantities obtained from the experiment, the SRQ can be calculated using the model. The difference between experimental measurements (typically the mean of the system response) and computational results may be calculated [42].

It is important to focus validation efforts on a specific application and quantity of interest (QoI). It is not possible to validate a model; it is only possible to validate the prediction of a particular quantity for a specific scenario using a model. While all physics occurring would be useful to validate, if they do not impact the specified QoI, then they are not of importance to the current validation study [42].

In this dissertation, a proton beam is incident upon a target material, RbCl. As previously discussed, phase and density changes in the target impact the incident proton beam's penetration, energy deposition, and production distribution. Therefore, accurately capturing both the independent and coupled behavior of the target becomes important. As it is not possible to directly observe this target during operation, computational modeling has proven a useful tool. The relevant QoIs are identified, calculated, and compared to measured

experimental values in the following sections to quantify the accuracy of the model predictions. Both separate and integral effects must be examined to identify sources of uncertainty that are present in the QoIs.

Section 4.2. Yield and Production Rate Calculations

Section 4.2.1. Predicted Yields

Target yields are directly measured in production targets and describe the net amount of a radioisotope of interest produced. Yields are a useful measured observable and validation metric as they may be determined computationally with given cross-section data. To provide a benchmark by which to compare computational results and experimental data, yields can be predicted in MCNP. Given a converged, steady state solution, it is possible to take the solution's density distribution and create a MCNP input deck that will provide yield information.

This has been implemented in the past to determine yields for gas targets [19] when taking into account the impact of convective currents on relocation of less dense fluids. For this model, comparison of yields obtained when allowing for density variation and a partially molten target against experimental production values will allow for validation of the present computational model and provide insight into potential discrepancies.

For this particular problem with high energy protons incident on RbCl targets, the cross-sections of the $^{nat}Rb(p,x)^{82}Sr$ reaction are of interest for yield calculations. The IAEA database [43] provides recommended cross-sections based on compiled and evaluated experimental data for the reaction of interest. This IAEA recommended fit and selected experimental data with associated error bars are shown in Figure 4-1. It can be seen that the threshold energy for the $^{nat}Rb(p,x)^{82}Sr$ reaction occurs at approximately 34 MeV, when the production probability falls to zero.

While numerical values of the fit given below in Figure 4-1 are provided at small energy intervals, unfortunately neither the functional form of the curve fit nor the standard deviation of the fit are provided by the IAEA database and therefore its quality is not quantifiable.

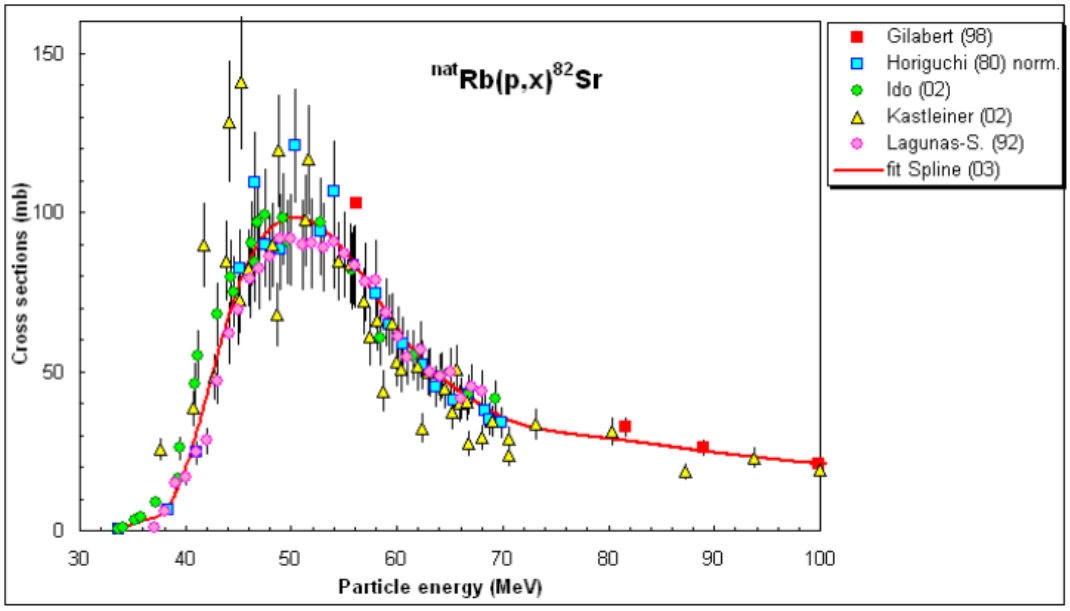

Figure 4-1: IAEA recommended cross-section fit and experimental data for $^{nat}Rb(p,x)^{82}Sr$ reaction.

A thick target yield curve provides a standardized set of values to compare with both predicted and experimental non-thick target yields. Both thick and non-thick target yields will be discussed in this section and are defined here. A thick target yield is the predicted yield assuming that all particles drop below the threshold energy for the reaction of interest before leaving the target [44]. Non-thick target yields are obtained when particles exit the target above the reaction threshold energy. Both thick and non-thick target yields may be determined using a thick target yield curve. This will be discussed in more detail later.

The thick target yields for RbCl can be calculated using numerical integration of stopping power obtained from SRIM [39] and integration of nuclear reaction rates using recommended cross-section data from the IAEA database [43].

Stopping power describes the energy loss of a particle per unit distance as a function of the particle type, energy, and the material composition of the medium through which it is traversing. Stopping power can be obtained as a function of energy in SRIM or by using another recognized stopping power correlation $dE/\rho dx$ in units of $\left[\frac{\text{MeV}\cdot\text{cm}^2}{\text{mg}}\right]$, also known as

mass stopping power [45]. Mass stopping power is density independent. By discretizing and summing over energy, saturation thick target yields may be determined as shown below.

The total reaction rate accounts for all products generated by the interaction of incident protons with the target material. As only the production of ^{82}Sr is of interest, the ^{nat}Rb(p,xn)^{82}Sr production cross-section is used, and the ^{82}Sr production – or reaction – rate may be obtained by integrating over energy as shown below.

$$R = A\varphi_0 \int_0^{\mathrm{E_{max}}} \frac{\Sigma(E)}{\rho}\left(\rho / \frac{dE}{dx}\right) dE \tag{4-1}$$

In Eq. (4-1), $\rho / \frac{dE}{dx}$ is the inverse of the mass stopping power, denoted by $1/SP$ from this point on. The beam intensity is $I_{beam} = A\varphi_0$, a product of the incident particle flux and the target area. $\Sigma(E)$ is the macroscopic ^{82}Sr production cross-section, discussed later, and ρ is the target material density. The resulting reaction rate is as shown below.

$$R = I_{beam} \int_0^{E_{max}} \frac{\Sigma(E)}{\rho}\left(\frac{1}{SP}\right) dE \tag{4-2}$$

To discretize Eq. (4-2), equally spaced points between the maximum and threshold energy for the reaction were taken as the mesh over which to numerically integrate. The form $\frac{\Sigma(E)}{\rho}$ can be reduced to:

$$\frac{\Sigma(E)}{\rho} = \frac{N \cdot \sigma(E)}{\rho} \tag{4-3}$$

Since the number density of the material $N = \frac{\rho \cdot N_A}{A}$ and A is the atomic mass, Eq. (4-3) reduces to:

$$\frac{\Sigma(E)}{\rho} = \frac{\rho \cdot N_A}{A} \cdot \frac{\sigma(E)}{\rho} = \frac{N_A \cdot \sigma(E)}{A} \tag{4-4}$$

In Eq. (4-4) the only material specific property is the atomic mass, and there is no dependency on density. The discretized form is as shown below in Eq. (4-5), and represents the number of reactions per second occurring in the target material per incident source particle. It may be expressed in units of Bq or [decays/s].

$$R = I_{beam} \sum_{i=1}^{N_E} \frac{N_A \cdot \sigma(E)}{A}\left(\frac{1}{SP}\right) \Delta E \tag{4-5}$$

Here N_E is the total number of points over the discretized energy mesh and ΔE is the size of each mesh element. To get this in terms of the reaction rate per unit current, or saturation

thick target yield, Eq. (4-5) is divided by 1 protons/s. As current can be expressed as 1 A = 1 C/s = 6.242×10^{18} protons/s, the saturation thick target yeild in Bq/μA is then as shown below.

$$\frac{R}{I_{beam}} = 6.242 \times 10^{18} \sum_{i=1}^{N_E} \frac{N_A \cdot \sigma(E)}{A} \left(\frac{1}{SP}\right) \Delta E$$

The saturation thick target yields of ^{82}Sr in RbCl as a function of energy are shown in Figure 4-2 in units of $\left[\frac{\text{GBq}}{\mu\text{A}}\right]$ and $\left[\frac{\text{mCi}}{\mu\text{A}}\right]$. These calculations were verified by comparing the saturation thick target yields of ^{82}Sr in Rb metal to the IAEA provided set of tabular values. The cumulative saturation yield values of ^{82}Sr in Rb metal given by the IAEA database are slightly higher than those predicted using the above method, but not significantly.

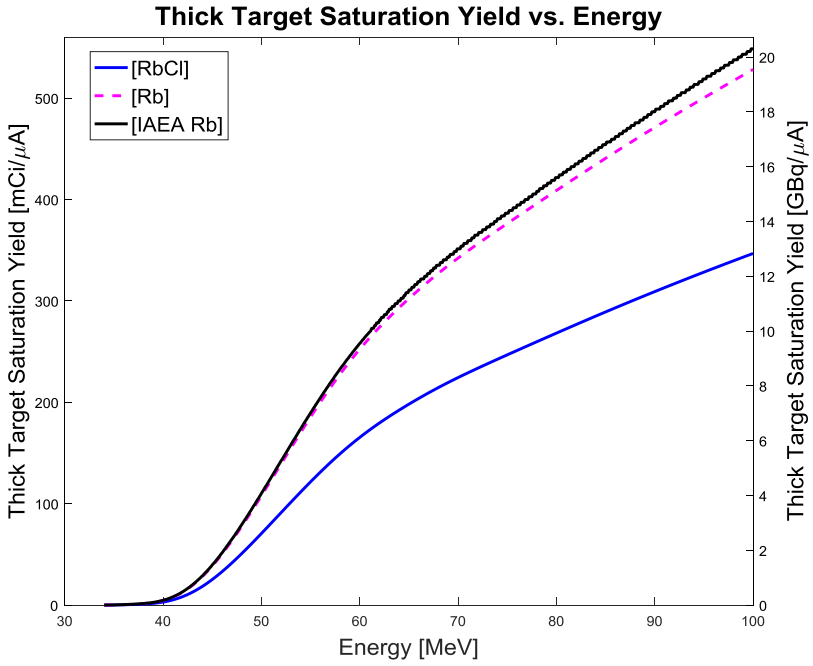

Figure 4-2: Saturation thick target yields in [GBq/μA] and [mCi/μA] as a function of incident proton energy for the ^{nat}Rb(p,xn)^{82}Sr reaction in RbCl.

The above saturation thick target yield curve may be used to determine both thick and non-thick target yields. The threshold energy is the location at which the production cross-section falls to zero, occurring at ~ 34 MeV for the ^{nat}Rb(p,xn)^{82}Sr reaction. Thick target yields assume that all particles entering the target drop below the threshold energy before exiting. Thus,

saturation thick target yields may be taken as the value of the above curve at the incident proton energy.

For non-thick targets that have particles streaming through above this threshold energy, their net yield may be calculated by subtracting the value of the saturation thick target yield curve at the exiting energy from the value of the saturation thick target yield curve at the incident energy. This calculation is shown in the equation below, where Y_{thick} is the value of the saturation thick target yield curve at the specified energy [44].

$$Y_{non\text{-}thick} = Y_{thick}(E_{in}) - Y_{thick}(E_{out}) \tag{4-6}$$

This will provide the total yield produced in the non-thick target, assuming all particles entering and exiting are travelling at approximately the same energy. As the A and B-slot RbCl targets experience protons both entering and exiting at energies well above the threshold energy, saturation non-thick target yields of this form are of interest for a first-order approximation.

However, if the particles are passing through a significant amount of material upstream before hitting the material of interest, the incident and exiting particle energies are no longer monoenergetic and are better described using a Gaussian energy distribution with some mean and standard deviation [5,46]. This concept will be described in further detail in Section 4.3.1.2. In addition, if the target experiences a significant density gradient – as is the case here for a ring-shaped beam– this average incident and exiting energy assumption is invalid.

As a result, it becomes important to capture the real-world activity production some other way. This may be done using particle energies computed by MCNP and corresponding cross-sections of the excitation function as recommended by the IAEA database.

It was assumed that the net yield was measured immediately after production and thus no decay after end-of-bombardment (EOB). Given the half-life of a radioisotope the radioactive decay constant is given below in Eq. (4-7).

$$\lambda = \frac{\ln(2)}{t_{1/2}} \tag{4-7}$$

The half-life of Sr-82 is 25.36 days. Thus,

$$\lambda = \frac{\ln(2)}{25.36\ \text{day}} = 0.02733\ \text{day}^{-1} \tag{4-8}$$

The saturation factor can be determined using the ordinary differential equation describing production and decay of radioisotopes. If it is assumed that there is initially no radioisotope present at the beginning of bombardment, i.e. an initial condition of $N(0) = 0$, and the only production term is as a result of bombardment, then [47,48]:

$$\frac{dN}{dt} = I_{beam}y - \lambda N(t) \tag{4-9}$$

Here I_{beam} is the number of beam particles per second incident on the target in [particles/sec], and y is the target product yield in [nuclei/μC], or [nuclei/μA·h]. This may also be converted to units of [MBq/μA] as [1 nuclei/μC] = [1 MBq/μA].

Eq. (4-9) can be solved using an integrating factor:

$$\frac{d}{dt}N(t)e^{\lambda t} = I_{beam}ye^{\lambda t} \tag{4-10}$$

When Eq. (4-10) is integrated it becomes Eq. (4-11).

$$\mathrm{N}(t) = \frac{I_{beam}y}{\lambda}\left(1\text{-}e^{-\lambda t}\right) \tag{4-11}$$

This may be simplified to provide the activity at time t.

$$A(t) = \lambda N(t) = I_{beam}y\left(1\text{-}e^{-\lambda t}\right) \tag{4-12}$$

For a long irradiation where $t \rightarrow \infty$,

$$\frac{A(t \rightarrow \infty)}{I_{beam}} = y = a_{sat}$$

This is called the saturation target yield and represents the activity produced per unit beam current when the production and decay rate of the product are in equilibrium (at $t = \infty$, or when $\lambda t \gg 1$). The saturation target yield is equal to the target product yield, and may be easily converted into its conventional units of activity per unit beam current as [1 nuclei/μC] = [1 MBq/μA]. Using the saturation factor $\left(1\text{-}e^{-\lambda t_{irr}}\right)$ and the beam current I_{beam}, the end-of-bombardment (EOB) target yield after a specified bombardment time may be calculated.

$$\mathrm{A}(t_{irr}) = a_{sat}\cdot\mathrm{I}_{beam}\cdot\left(1\text{-}e^{-\lambda t_{irr}}\right) \tag{4-13}$$

Another form of expressing yield is in the form of a physical target yield, which is the time derivative of the activity at $t = 0$ [48], with conventional units of [1 MBq/μA-h]. It can also

be thought of as the instantaneous production rate, and may be converted to an EOB target yield using the equation given below.

$$A(t_{irr}) = \frac{\alpha_{phys} \cdot I_{beam} \cdot \left(1 - e^{-\lambda t_{irr}}\right)}{\lambda} \tag{4-14}$$

The saturation and physical target yields may be converted easily between one another simply by multiplying or dividing by the decay constant of the radioisotope, as demonstrated below.

$$a_{sat} = \frac{\alpha_{phys}}{\lambda} \tag{4-15}$$

Both physical and saturation target yields may be used to determine EOB non-thick target yields. As stated previously, non-thick target yields are determined by subtracting the thick target yields at the average incident and exiting energies. For the purposes of simplicity, all target yields discussed from this point onward will be considered non-thick target yields unless specified otherwise.

In order to predict yields in MCNP, either a type 4 tally or a type 1 mesh tally with a flux specification may be used. A type four tally may be utilized when a target domain has one uniform density. However, once density variation is addressed in MCNP, a type 1 mesh tally with a flux specification must be utilized in order to divide the target domain into a number of cells corresponding to the specified MCNP density mesh.

This has been implemented in the past for gas targets [19] and has provided insight into yields obtained when relocation of less dense fluids as a result of convective currents is taken into account. Comparison of yields obtained when allowing for density variation and a partially molten target against experimental production values will allow for validation of the present computational model or provide insight into potential discrepancies. The pseudo steady state density distributions were used for all calculations. This is a valid simplification, as the pseudo steady state target behavior is achieved in less than one minute of irradiation time, and all targets are irradiated for significantly longer than this.

Formulation of the MCNP density mesh is addressed in Section 2.2.3 and it is important that the mesh tally used for production calculations aligns with the density mesh tally. As

material density plays an important role in determination of number density, the mesh resolution must be the same in order to assign the correct cell number density.

A type 1 mesh tally with a flux specification provides information for each cell in units of $\left[\frac{\text{reactions}}{\text{source-particle}\cdot\text{cm}^2}\right]$. Tabular data for the $^{\text{nat}}\text{Rb(p,xn)}^{82}\text{Sr}$ reaction was obtained from the IAEA database [43], and was read by MCNP using dose function (DE and DF cards).

The cross-sections used in the DF card are in barns and the energies used in the DE card are in MeV, thus the mesh tally modified with dose function cards will provide the flux in a cell in units of $\left[\frac{\text{protons}\cdot\text{barn}}{\text{source-particle}\cdot\text{cm}^2}\right]$.

A FORTRAN code is used to read the MCNP output, mesh resolution, and the corresponding density distributions in RbCl targets A and B. This FORTRAN code uses the cell center densities and dimensions to calculate cell number density and volume. The saturation yield for each cell is determined as demonstrated below.

$$\begin{aligned} \text{Saturation Yield}_i \left[\frac{mCi}{\mu A}\right] = Cell_i \left[\frac{\text{protons}\cdot\text{barn}}{\text{source-particle}\cdot\text{cm}^2}\right] \cdot N_{cell_i} \left[\frac{\text{atoms}}{\text{cm}^3}\right] \cdot V_{cell_i} \\ [cm^3] \cdot 10^{-24} \left[\frac{\text{cm}^2}{\text{barn}}\right] \cdot 6.24\cdot 10^{12} \left[\frac{\frac{\text{protons}}{\text{s}}}{\mu\text{A}}\right] \cdot 2.7\cdot 10^{-8} \left[\frac{\text{mCi}}{\frac{\text{protons}}{\text{s}}}\right] \end{aligned} \quad (4\text{-}16)$$

Each cell volume is calculated using the surface plane definition provided by the MCNP mesh.

$$V_{cell_i} = \pi \left[\frac{\left(D_{cell_i} - D_{cell_{i-1}}\right)}{2}\right]^2 \left[z_{cell_i} - z_{cell_{i-1}}\right] \quad (4\text{-}17)$$

The number density is determined by using the cell-specific density.

$$N_{cell_i} = \frac{\rho_{cell_i} N_A}{A_{RbCl}} \quad (4\text{-}18)$$

The total saturation yield for each target domain is calculated by summing over all the cells in the domain.

$$\text{Saturation Yield}_{domain} = \sum_{i=1}^{N_{domain}} \text{Saturation Yield}_i \quad (4\text{-}19)$$

This saturation yield may then be converted into an EOB yield using Eq. (4-13) and a given irradiation time and beam current. LANL production batch yields are only available in the

form of combined RbCl target A and B yields. Therefore all MCNP yield predictions for RbCl targets A and B were added together to compare with measured LANL values. As a point of comparison, all calculations were done with results from the final refined cooling water domain model and from the average heat transfer coefficient model with the correct beam distribution. A total of 30 million particle histories were used for these MCNP runs. Uncertainty propagation using the MCNP statistics for the refined cooling water domain model calculations will be performed later in Section 5.3.1.1 to quantify the statistical uncertainty in these predictions.

While this comparison provides some measure of confidence in the model's predictive capabilities, these production yields are very much an integral quantity – both because they are a comparison of the combined RbCl target A and B yields and because yields are a product of many combined physical effects. As a result they provide a limited degree of information about the model's accuracy.

Section 4.2.1.1. Refined Cooling Water Domain Model

To determine the accuracy of the MCNP predictions, five combined batch LANL production yield values were compared with the MCNP predicted numbers. As yield information of the LANL targets is proprietary, only a ratio of the MCNP predictions to the LANL production values is provided. All MCNP predictions were calculated using the final pseudo steady state density profiles for RbCl targets A and B.

The predicted EOB activity was determined using the actual irradiation history, which outlines a number of irradiation periods followed by a short break in between each irradiation. These gaps in irradiation are significantly shorter than both the half-life of ^{82}Sr and the individual irradiation periods and therefore should not significantly influence overall target behavior. As the production values were measured a certain number of days after irradiation, these MCNP predicted EOB activities were then decayed to the measurement date. A comparison of these values are presented in Table 4-1 below, with the EOB date and the date at which the activity of each production batch was measured. The measured production yields were not adjusted for chemical losses when processing, and the uncertainty in their measured activities was not provided.

Table 4-1: Combined production yield ratios of MCNP predicted to LANL measured production values for the refined cooling water domain model.

Batch EOB Date	Batch Measurement Date	Predicted to Production Yield Ratios: Y_{MCNP}/Y_{LANL}
12/20/2017	**1/12/2018**	0.9297
10/2/2017	**10/17/2017**	0.9369
1/30/2017	**2/14/2017**	0.9802
12/21/2016	**1/10/2017**	0.9515
12/6/2016	**12/20/2016**	1.0058

The ratio of the MCNP predicted and measured activities for these five LANL production batches are reasonably close to one, with MCNP predicting the combined RbCl target A and B yields within ~0.6% - ~7% of the production values

Sources of under or over prediction by MCNP could be due to an inaccurate pseudo steady state density profile prediction in RbCl targets A and B, or uncertainties in the cross-section fit provided by the IAEA. In addition, the average beam current for these production runs was approximately 220 μA, while a beam current of 230 μA was used to determine the pseudo steady state density profiles in the model. While it is not expected that the latter should make an appreciable difference in the predicted yields, it could be a contributing factor. In the case of over prediction by MCNP, there could be some chemistry losses during target processing.

Section 4.2.1.2. Average Heat Transfer Coefficient Model

Yield predictions using the density distribution obtained with the average heat transfer coefficient model were also compared with LANL production batch values.

Table 4-2: Combined production yield ratios of MCNP predicted to LANL production values for the average heat transfer coefficient model.

Batch EOB Date	Batch Measurement Date	Predicted to Production Yield Ratios: Y_{MCNP}/Y_{LANL}
12/20/2017	**1/12/2018**	0.9274
10/2/2017	**10/17/2017**	0.9346
1/30/2017	**2/14/2017**	0.9777
12/21/2016	**1/10/2017**	0.9491
12/6/2016	**12/20/2016**	1.0033

These MCNP combined yield predictions are reasonably close to the measured LANL production batch values. The predicted yields obtained with the average heat transfer coefficient model are within ~0.2% of the predicted yields obtained with the refined cooling water domain model. This indicates that that the average heat transfer coefficient model is a useful alternative for yield prediction as it provides values very close to those obtained with the refined cooling water domain model. However, if void development is occurring in the cooling water channels, incorporation of this into the refined cooling water domain model could significantly impact the cooling water near-wall heat transfer, beam penetration, and the transmitted energy distribution. This would then limit the predictive capabilities of the average heat transfer coefficient model.

Section 4.2.2. Volumetric Production Rates

While not possible to validate, it is useful to obtain information about the production rate distribution within the targets. Determining the volumetric production rate at different locations may provide insight into the areas of highest production within the target. MCNP was used to predict the saturation yield per unit volume. This may then be converted into a volumetric production rate, i.e. the instantaneous production rate per unit volume $\left[\frac{\text{mCi}}{\mu\text{A}\cdot\text{hr}\cdot\text{cm}^3}\right]$, for each specified MCNP mesh tally cell. This is done using a variation of Eq. (4-16) for cell saturation yield, and by using the relationship between instantaneous production rates and saturation yields given in Eq. (4-15).

$$Volumetric\ Production_i = \frac{Saturation\ Yield_i}{V_{cell_i}}\lambda \tag{4-20}$$

The volumetric production rate is provided in units of physical target yields, as described in Eq. (4-14). While this term and its associated units has caused confusion with experimentalists in the past, it is used to be consistent with standard production rate units.

Both the final refined cooling water domain model and the simplified average heat transfer coefficient model were run using the beam characteristics described in Section 2.2.2.2. Since the production rate distribution is an important design parameter, it is useful to see how much error there is in the average heat transfer coefficient model when doing scoping and parametric

studies. To highlight the regions of highest production in figures where production is not symmetric, the highest production area is circled in red.

Section 4.2.2.1. Refined Cooling Water Domain Model

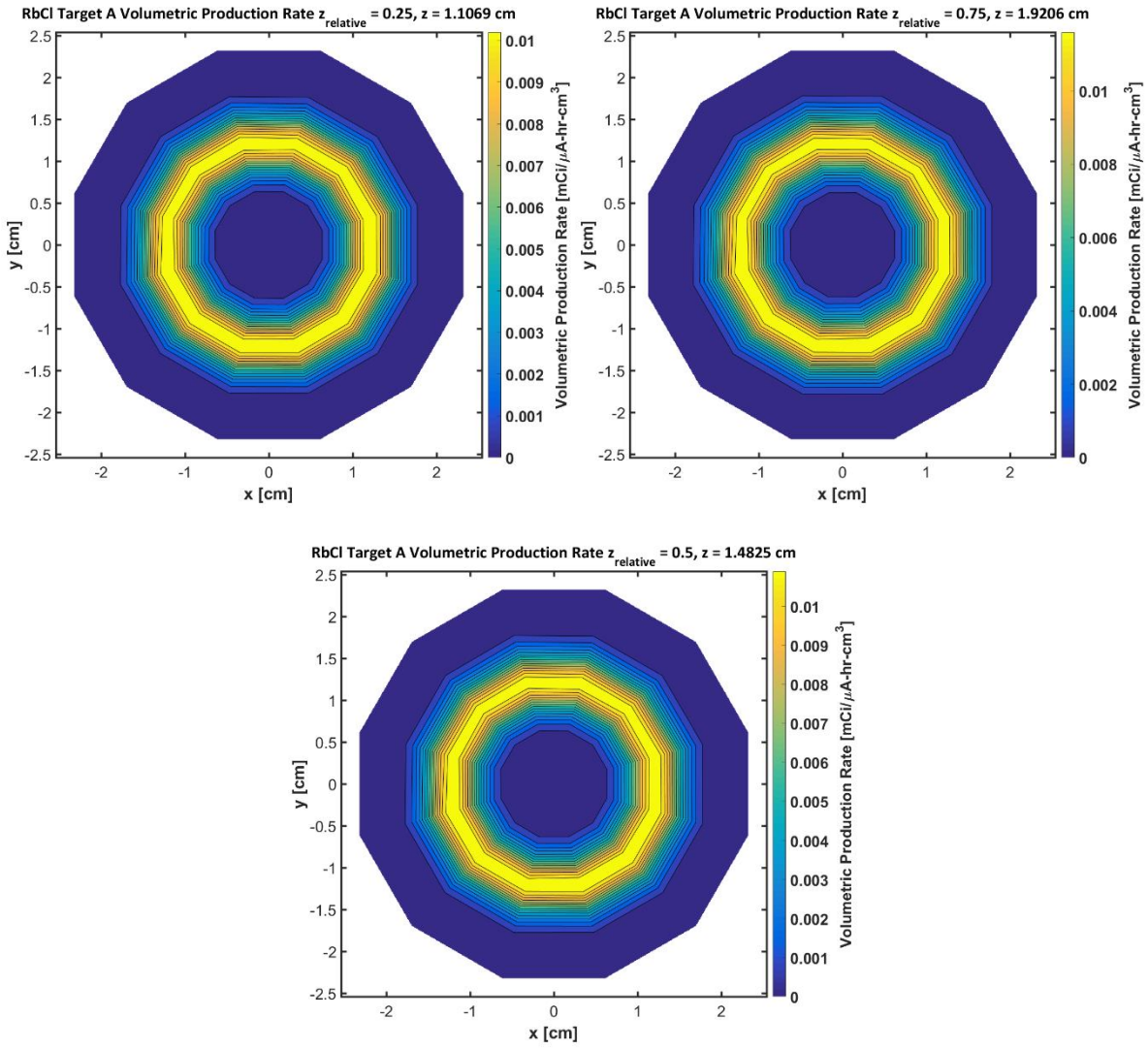

Figure 4-3: Contour plots of RbCl target A's volumetric production rate profiles in XY planes at axial positions 25%, 50%, and 75% of the way into the target for the refined cooling water domain model.

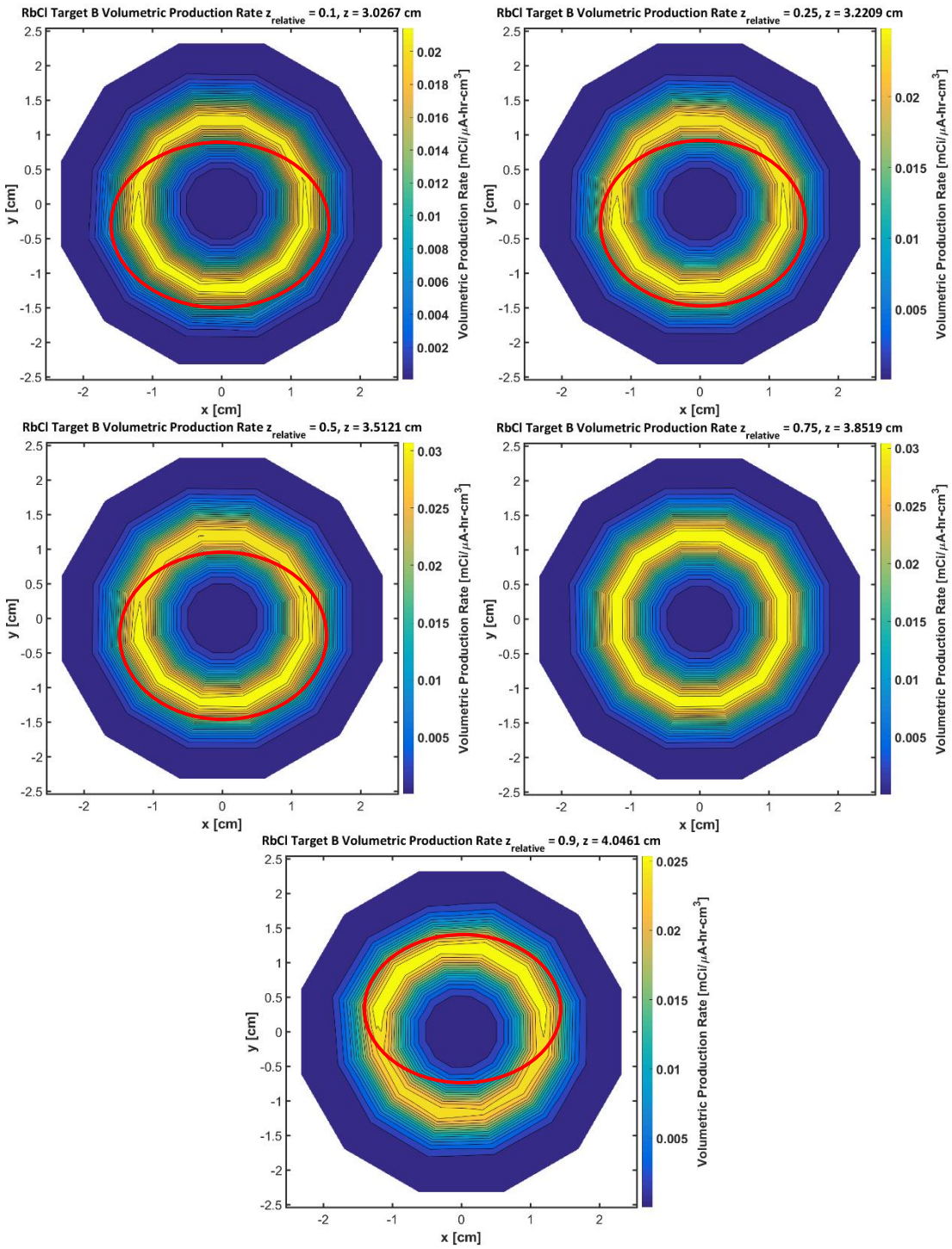

Figure 4-4: Contour plots of RbCl target B's volumetric production rate profiles in XY planes at axial positions 10%, 25%, 50%, 75%, and 90% of the way into the target for the refined cooling water domain model with regions of highest production circled in red.

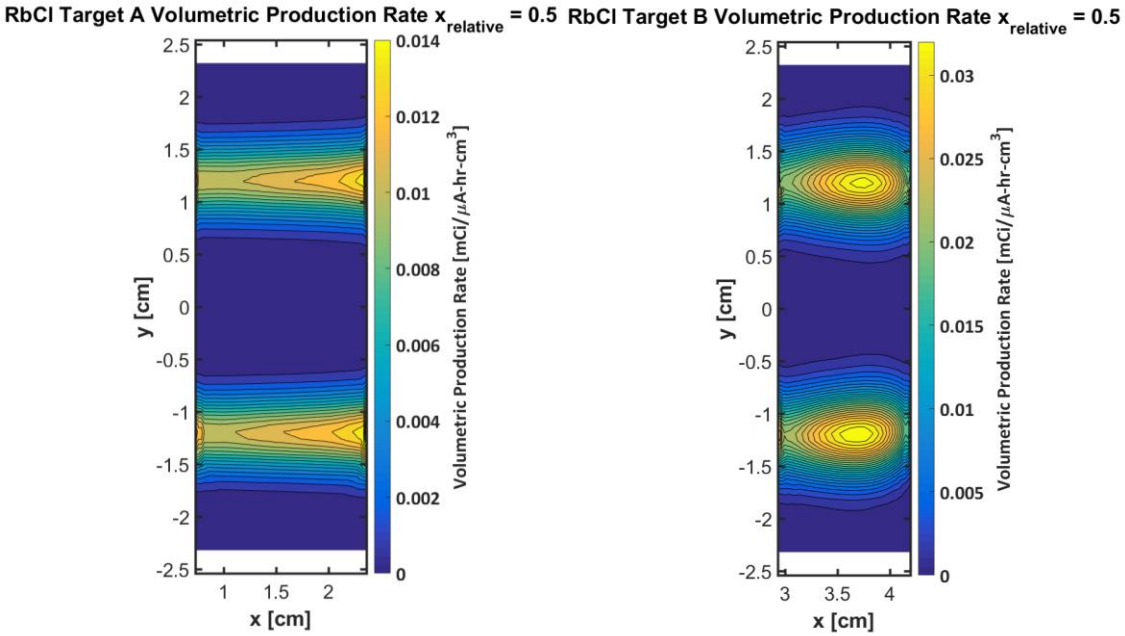

Figure 4-5: Contour plots of volumetric production rates in the YZ midplane of RbCl targets A and B for the refined cooling water domain model.

Figure 4-3, Figure 4-4, and Figure 4-5 provide a clear picture of the production in RbCl targets A and B. Figure 4-3 shows that the production rates in RbCl target A are relatively symmetric in the target. As the excitation function in RbCl Target A is more uniform over the energy range (see Figure 4-1), production rates are expected to be more similar at the top and bottom of the target. However, these images imply that production is slightly higher on the bottom of the target because of the more dense material. This density gradient is illustrated in the thermal hydraulic plots in Section 3.1.2. The difference in production at the top and bottom of RbCl target A is illustrated in further detail in Section 4.2.3.

This asymmetric production is more pronounced in RbCl target B due to the impact of compounded effects of upstream density gradients. It is clear when looking at Figure 4-4 that the location of peak production changes axially within the target. Upstream in the target, peak production is occurring at the bottom, as shown at positions 10%, 25%, and 50% of the way into the target. The production at a position 75% of the way into the target is fairly symmetric at the top and bottom of the target, but this asymmetry appears again downstream, 90% of the way into the target, when the peak production occurs at the top of the target.

This behavior is again explained by looking at the excitation function for the production of ^{82}Sr. More dense material at the bottom of both RbCl targets A and B causes particles to lose more energy as a function of axial distance travelled. As a result the peak energy of the excitation function is reached over a shorter distance. Conversely, less dense material at the top of RbCl targets A and B causes particles to lose less energy over a given distance travelled, reaching the peak of the excitation function energy deeper into RbCl target B. This will be more clearly illustrated in the linear production rate plots presented in Section 4.2.3, which further illustrates the same trends seen in the images above.

Section 4.2.2.2. Average Heat Transfer Coefficient Model

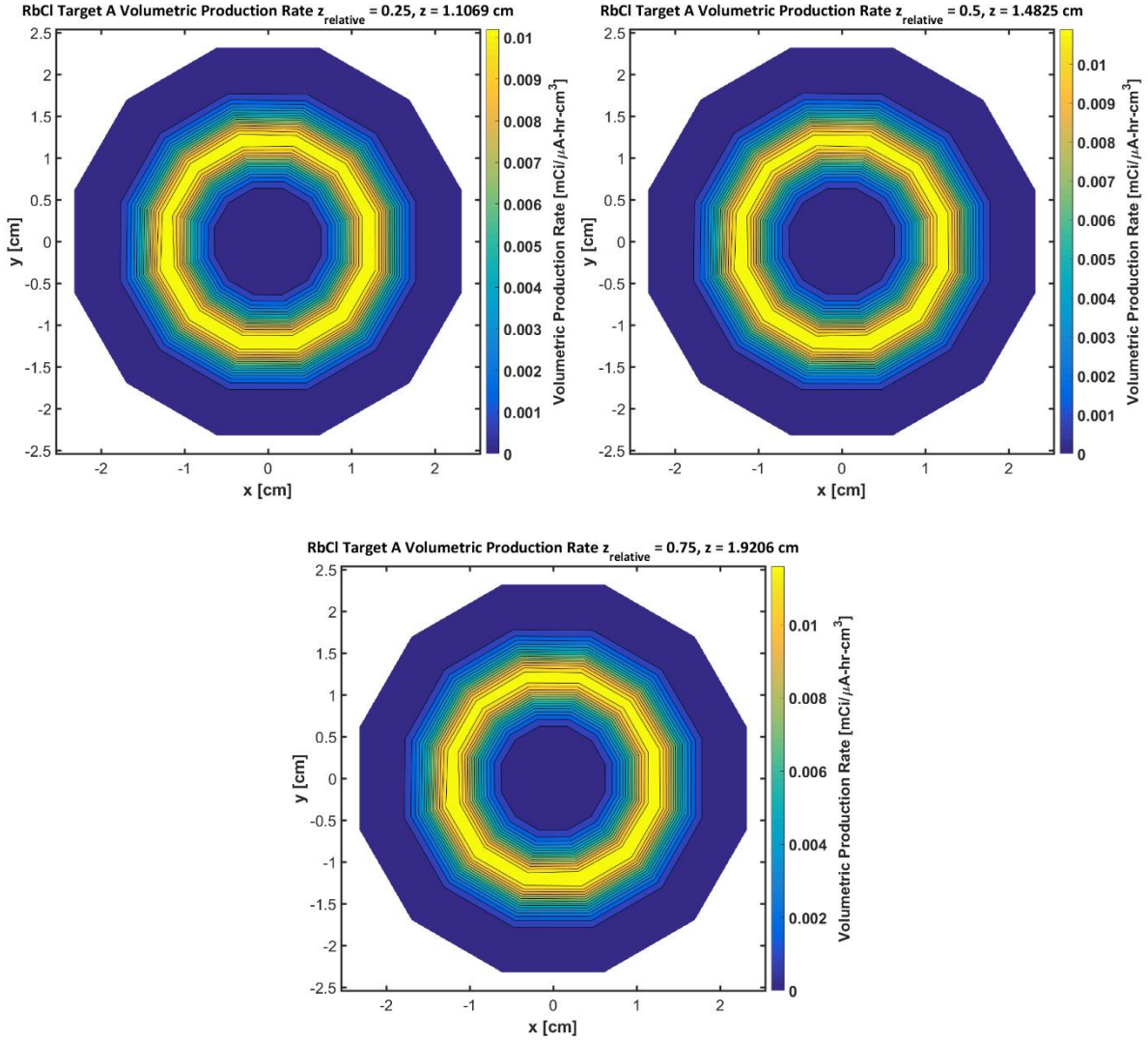

Figure 4-6: Contour plots of RbCl target A's volumetric production rate profiles in XY planes at axial positions 25%, 50%, and 75% of the way into the target for the average heat transfer coefficient model.

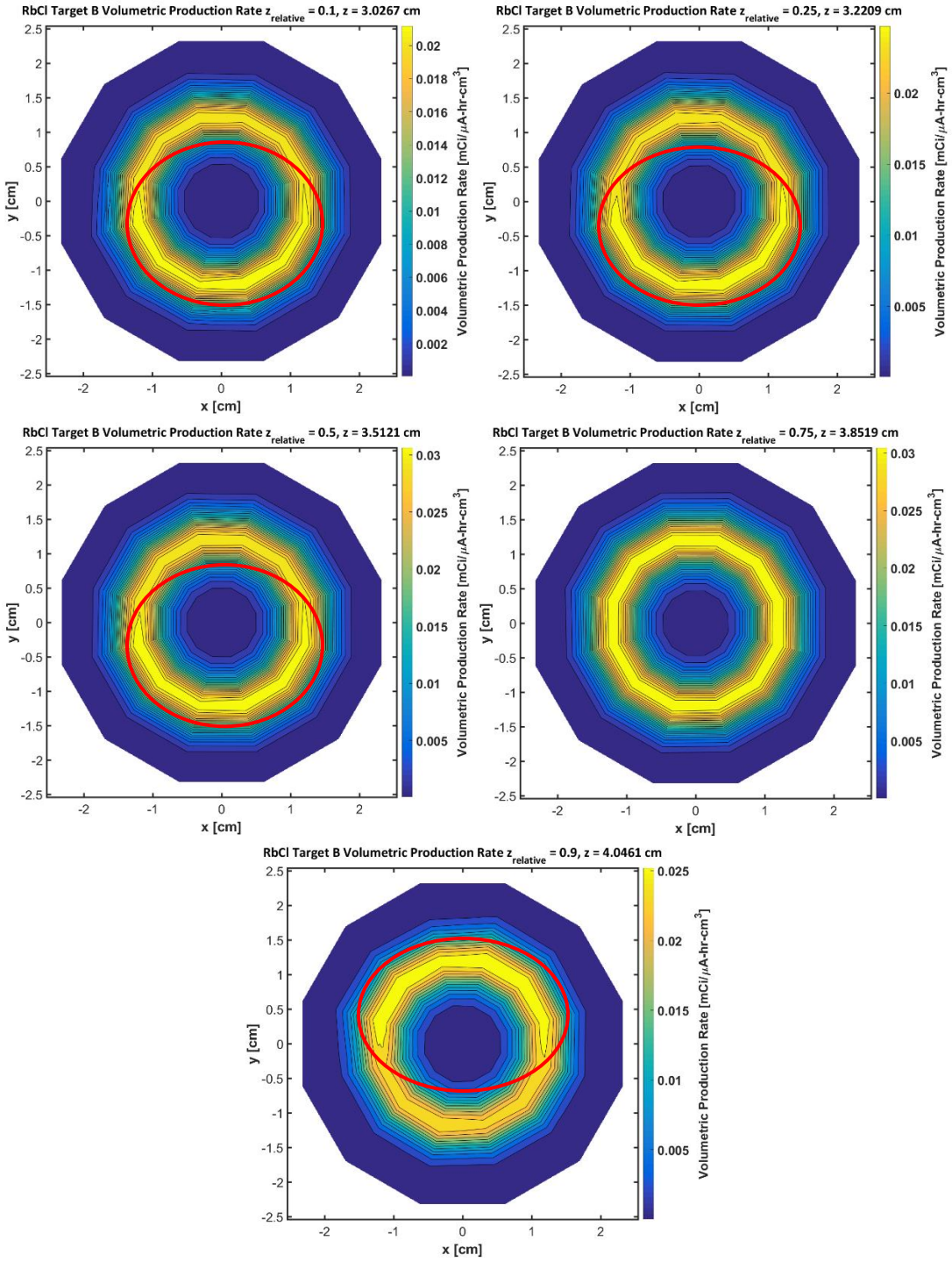

Figure 4-7: Contour plots of RbCl target B's volumetric production rate profiles in XY planes at axial positions 25%, 50%, and 75% of the way into the target for the average heat transfer coefficient model.

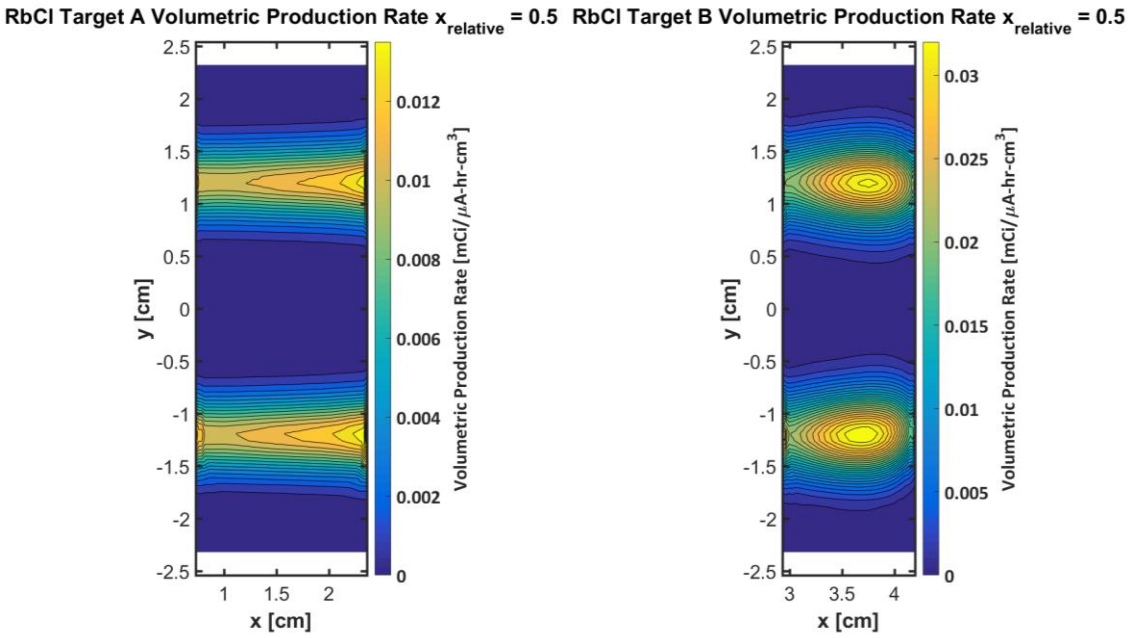

Figure 4-8: Contour plots of volumetric production rates in the YZ midplane of RbCl targets A and B for the average heat transfer coefficient model.

The volumetric production rates seen above in RbCl targets A and B are nearly identical to those obtained using the density distributions from the refined cooling water domain model in Section 4.2.2.1.

Section 4.2.3. Linear Production Rates

Linear production rates provide additional information about the locations of highest production within each target. Presented first are the total linear production rates, obtained by multiplying the volumetric production rate from 0 by the cell area and then integrating these values over each axial plane in the target.

$$Linear\ Production_i = \sum_{j=1}^{N_\theta}\sum_{k=1}^{N_r} VP_{i,j,k} A_{\theta r} = \sum_{j=1}^{N_\theta}\sum_{k=1}^{N_r} VP_{i,j,k} \frac{\theta_j r_k^2}{2} \qquad (4\text{-}21)$$

In the above formula, $VP_{i,j,k}$ is the total volumetric production rate in the cell denoted by angle θ_j, radius r_k, and axial position z_i, and N_θ and N_r are the total number of angular and radial planes. The total linear production rate at axial location z_i is then calculated by summing

over all cells at varying angular and radial locations at that axial position. These total linear production rate plots provide a more cumulative picture of target behavior.

However, following one point axially through the target provides additional information about differences in production at the top and bottom of the targets. These plots are obtained by tracking the linear production in a cell at the same radial and angular position axially through the target. This is done as shown below in Eq. (4-22).

$$Linear\ Production_{i,j,k} = VP_{i,j,k}\frac{\theta_j r_k^2}{2} \tag{4-22}$$

Both types of plots presented in the following section give an idea of production solely as a function of axial location, and can be used to further illustrate the behavior seen in the volumetric production rate plots in 0. Again, results were obtained using both the refined cooling water domain model and the simplified average heat transfer coefficient model for comparison.

Section 4.2.3.1. Refined Cooling Water Domain Model

The total linear production rate plots for RbCl targets A and B are presented below in Figure 4-9 and Figure 4-10.

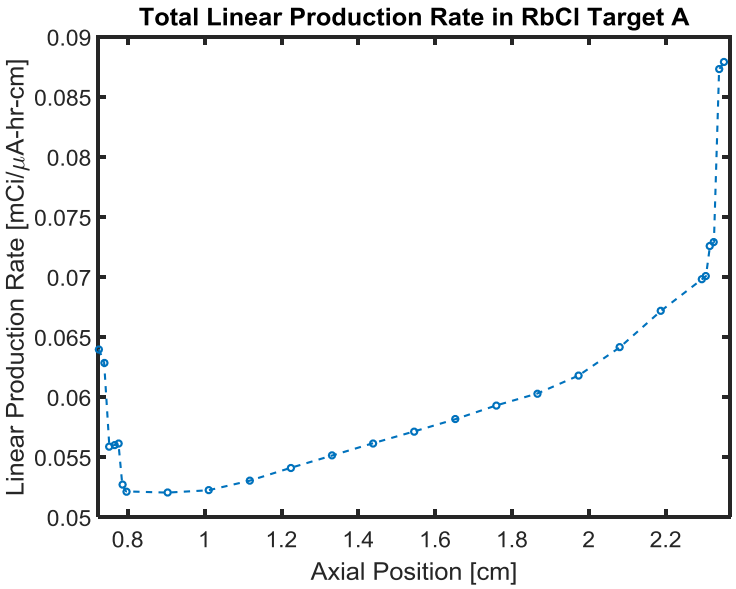

Figure 4-9: Total linear production rate integrated over each axial plane in RbCl target A for the refined cooling water domain model.

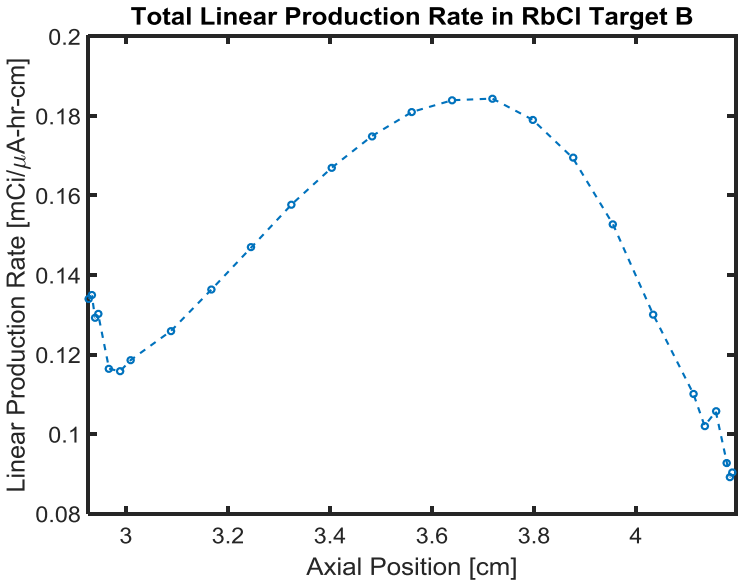

Figure 4-10: Total linear production rate integrated over each axial plane in RbCl target B for the refined cooling water domain model.

To provide more information about differing production rates at the top and bottom of RbCl targets A and B, the cell-specific linear production rates are also given in Figure 4-11 and Figure 4-12.

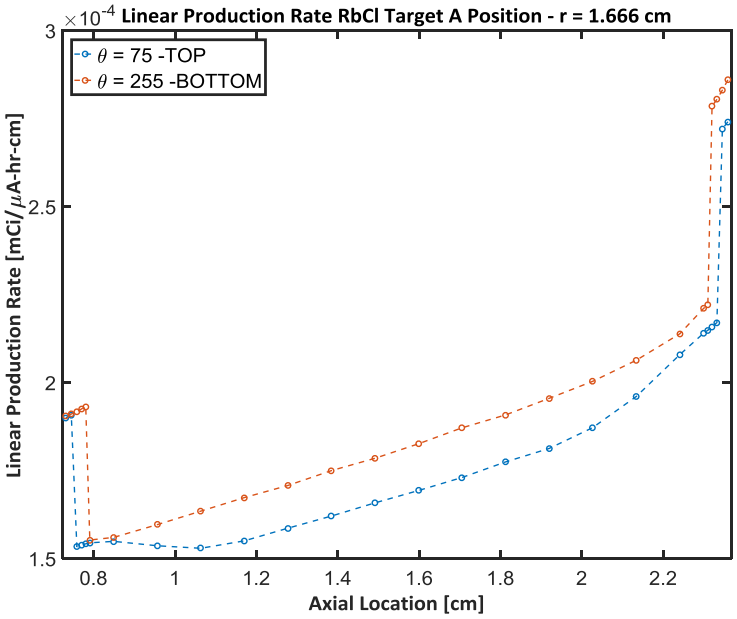

Figure 4-11: Comparison of production rates at the top and bottom of RbCl target A at r = 1.666 cm for the refined cooling water domain model.

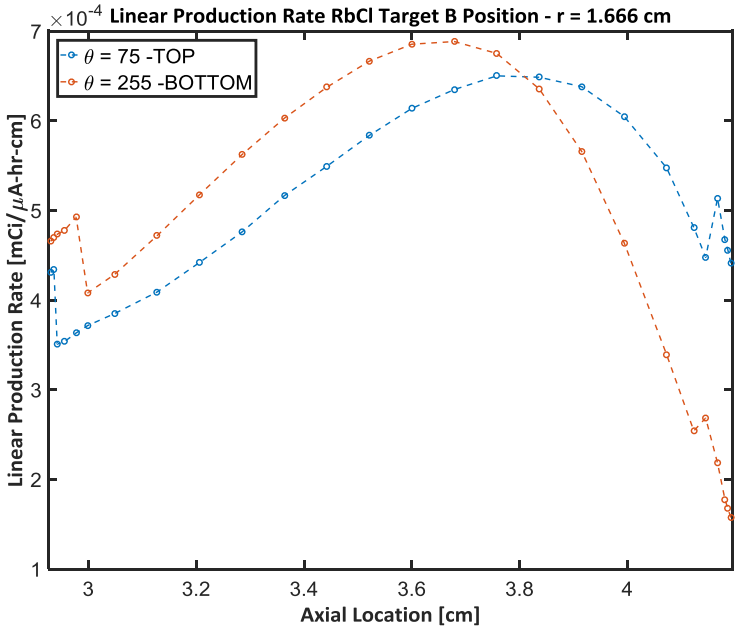

Figure 4-12: Comparison of production rates at the top and bottom of RbCl target B at r = 1.666 cm for the refined cooling water domain model.

The cell-specific linear production rate in RbCl target A is generally slightly higher at the bottom of the target. This is due to the denser or solid material at the bottom of the target leading to higher production and energy loss per unit distance travelled. In RbCl target B a shift in peak production is seen from the bottom to the top of the target as varying energies resulting from upstream density gradients shift the axial location of the excitation function. This was discussed in detail in Section 4.2.2.1.

Section 4.2.3.2. Average Heat Transfer Coefficient Model

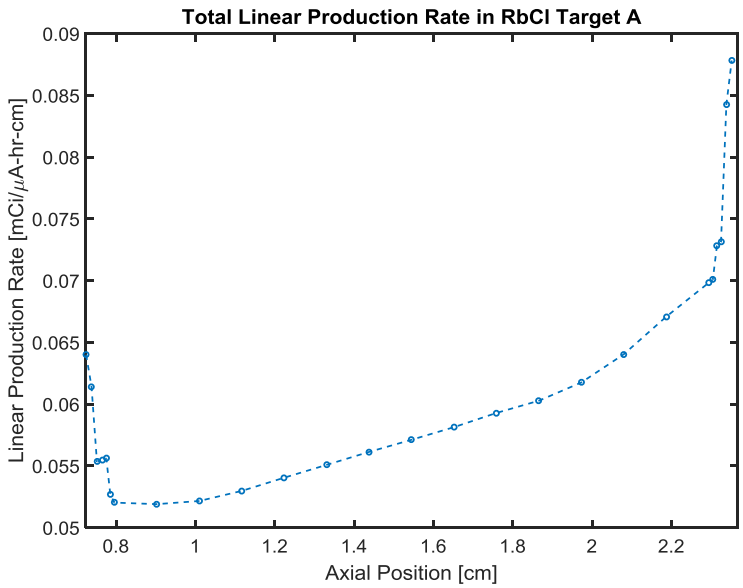

Figure 4-13: Total linear production rate integrated over each axial plane in RbCl target A for the average heat transfer coefficient model.

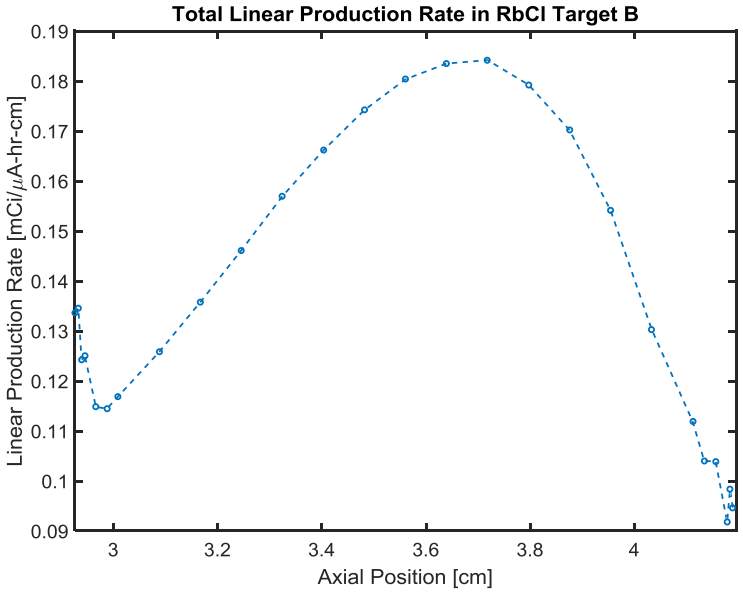

Figure 4-14: Total linear production rate integrated over each axial plane in RbCl target B for the average heat transfer coefficient model.

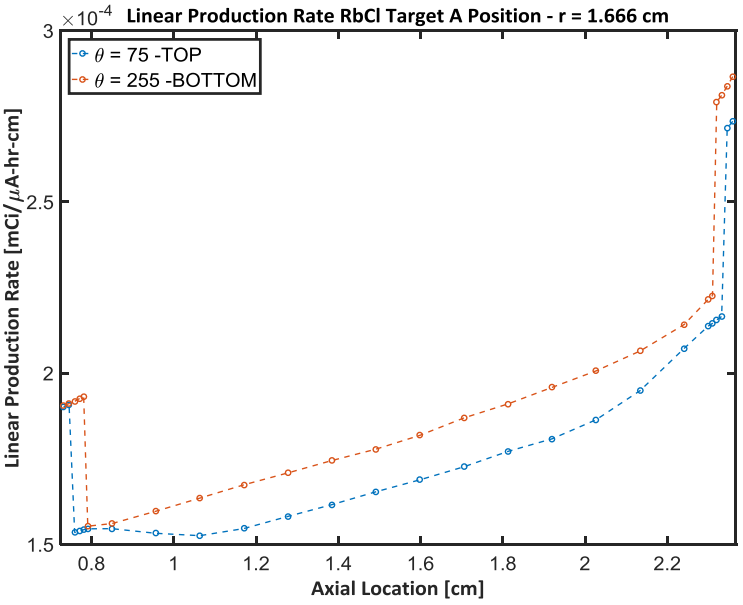

Figure 4-15: Comparison of production rates at the top and bottom of RbCl target A at r = 1.666 cm for the average heat transfer coefficient model.

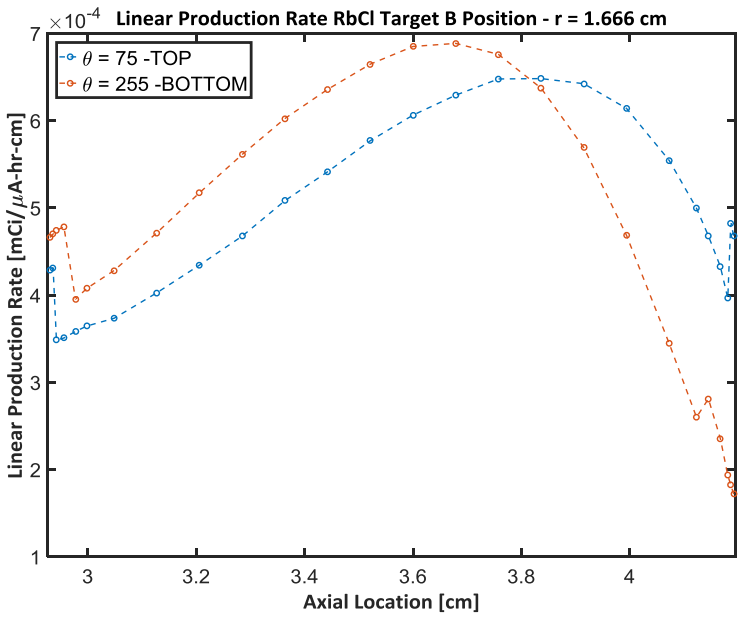

Figure 4-16: Comparison of production rates at the top and bottom of RbCl target B at r = 1.666 cm for the average heat transfer coefficient model.

The linear production rates seen above in RbCl targets A and B are very similar to those obtained using the density distributions from the refined cooling water domain model in Section 4.2.3.1.

Section 4.3. ^{58}Ni Foil Experiment

An experiment performed in 2014 by Jon Engle and Lauren Parker of Los Alamos National Laboratory aimed at determining the incident energy distribution in the C-slot involved measuring the activity of ^{56}Co and ^{57}Co produced using enriched ^{58}Ni foils in a bolt-together C-slot target with two RbCl targets upstream. Validation of computational results may be performed using MCNP to predict the activities of ^{56}Co and ^{57}Co using the pseudo steady state upstream density distribution for RbCl targets A and B and then comparing these results to the experiment. This will validate the model's predicted density and resulting energy distributions.

Section 4.3.1. Experiment Overview

A total of 31 nickel foils were placed inside an aluminum bolt-together target in the C-slot with two RbCl targets upstream. The incident protons pass through the front window of this

bolt-together target before hitting the foils. These foils present a sufficiently small area such that it may be assumed that protons incident on each foil are centered about some mean energy. As the production cross sections of ^{56}Co and ^{57}Co vary inversely over the proton energy range of interest, it is possible to use the ratios of these produced isotopes to ascertain the average energy incident on each foil.

The ratio of isotopes produced in each foil is directly dependent on the incident energy distribution as influenced by upstream target densities. Computational replication of this experiment will allow generation of isotopic ratios and average energies that are directly comparable to the experimentally obtained data.

Two such experiments were performed – one with a thinner front window and a second with a thicker front window. It is important to understand all experimental parameters so that the model created in MCNP matches the experimental conditions as closely as possible.

Significant experimental analyses were done specifically for this work in addition to calculations performed by the individuals who conducted the experiment. The analyses done by the experimenters versus the analyses done by the author of this work will be clearly delineated.

Section 4.3.1.1. Overview of Experiment Geometry

The CAD geometry matching the experimental parameters is given in Figure 4-17.

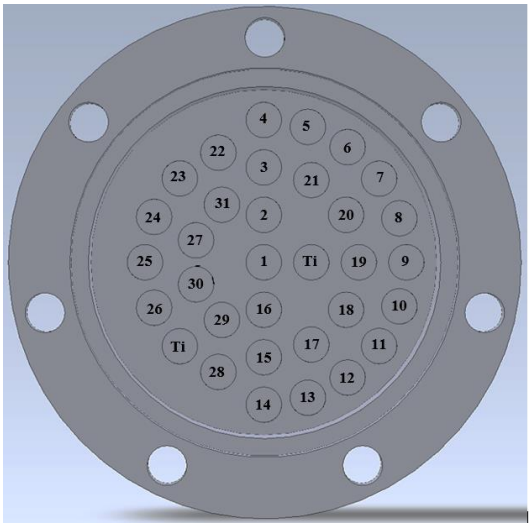

Figure 4-17: CAD geometry of experiment configuration with placement of numbered ^{58}Ni foils.

The foil isotopic composition is provided below.

Table 4-3: Isotopic composition of foils.

Isotopic Composition					
Isotope	**^{58}Ni**	**^{60}Ni**	**^{61}Ni**	**^{62}Ni**	**^{64}Ni**
Content [%]	99.48	0.505	0.005	0.005	0.005

The foils were place in an aluminum bolt-together target, with insets for each foil on the interior of the front face. The foil weights, dimensions, and positions are given in Appendix C. Each nickel foil disc was inset into the front window face by an average distance of 0.102 mm. Actual measurements of the aluminum windows with the grooved foil insets were taken. These values averaged 3.052 mm for the thick window and 1.5132 mm for the thin window with a series of five caliper measurements.

Section 4.3.1.2. Experimental Analysis

Experimental production cross-section data for the ^{58}Ni(p,x)^{56}Co and ^{58}Ni(p,x)^{57}Co reactions were used to generate fits. The experimental foil activities were measured approximately two months after the initial irradiation. Given this relatively long time frame between irradiation and measurement, cumulative cross-sections were used to account for decay of parent products into ^{56}Co and ^{57}Co. ^{56}Co is produced indirectly by the ^{58}Ni(p,3n)^{56}Cu and ^{58}Ni(p,p2n)^{56}Ni reactions. ^{57}Co may be produced directly via the ^{58}Ni(p,2p)^{57}Co reaction, but is also produced through the decay of ^{57}Ni and ^{57}Cu following the ^{58}Ni(p,2n)^{57}Cu and ^{58}Ni(p,pn)^{57}Ni reactions.

The experimental data shown in Figure 4-18 and Figure 4-19 were utilized for the cumulative production cross-sections of ^{56}Co and ^{57}Co from ^{58}Ni.

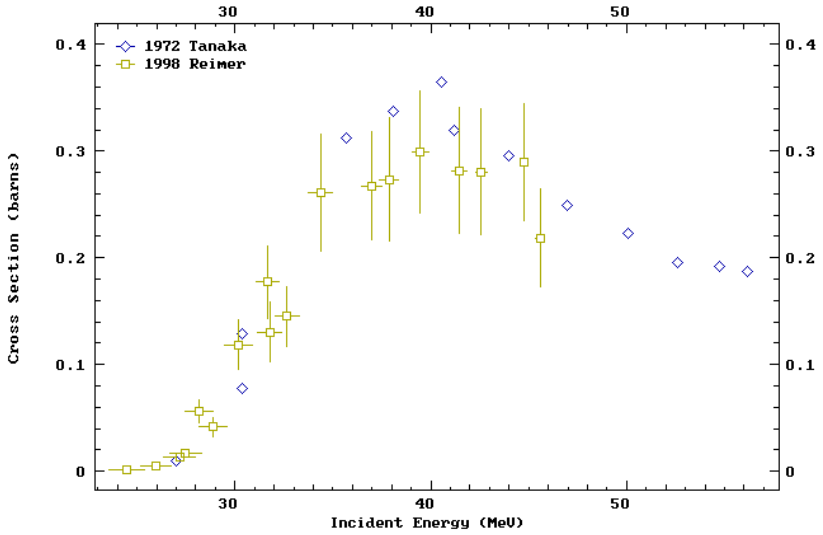

Figure 4-18: Measured cumulative nuclear formation cross-sections for the ^{58}Ni(p,x)^{56}Co reaction [49,50].

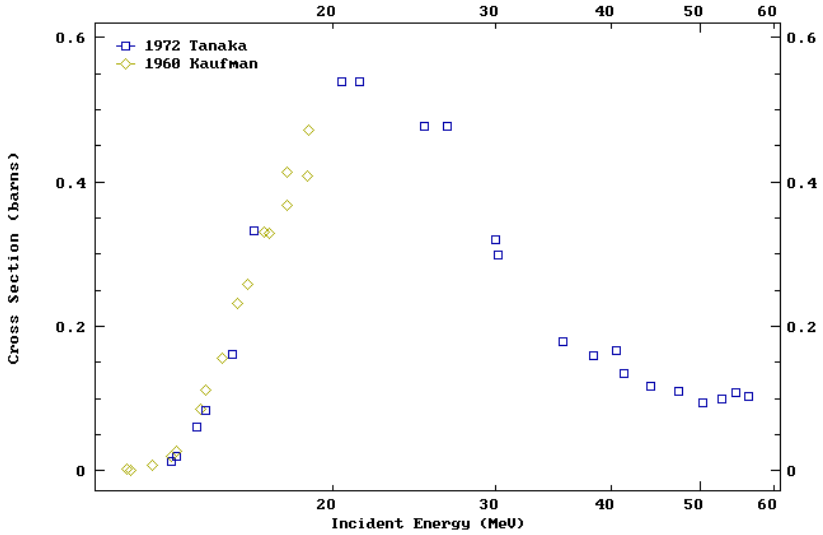

Figure 4-19: Measured cumulative nuclear formation cross-sections taken for the ^{58}Ni(p,x)^{57}Co reaction [49,51].

For the experimental data given in Figure 4-18 and Figure 4-19 the following fits were used, with σ as the microscopic cross-section in millibarns and E as incident proton energy in MeV. These fits were generated by the experimenters and utilized for this experimental

validation effort. They do not extend over the full experimental cross-section energy ranges as the energy range of interest is much narrower (see Figure 4-22).

A polynomial fit was used to fit the ^{56}Co cross-section data.

$$\sigma_{56_{Co}} = a \cdot E^3 + b \cdot E^2 + c \cdot E + d \tag{4-23}$$

Table 4-4: Coefficients for the ^{58}Ni(p, xn)^{56}Co excitation function fit.

Coefficient	Value
a	-0.169621
b	16.3867
c	-495.434
d	4788.05

This fit is plotted with the experimental data in Figure 4-20.

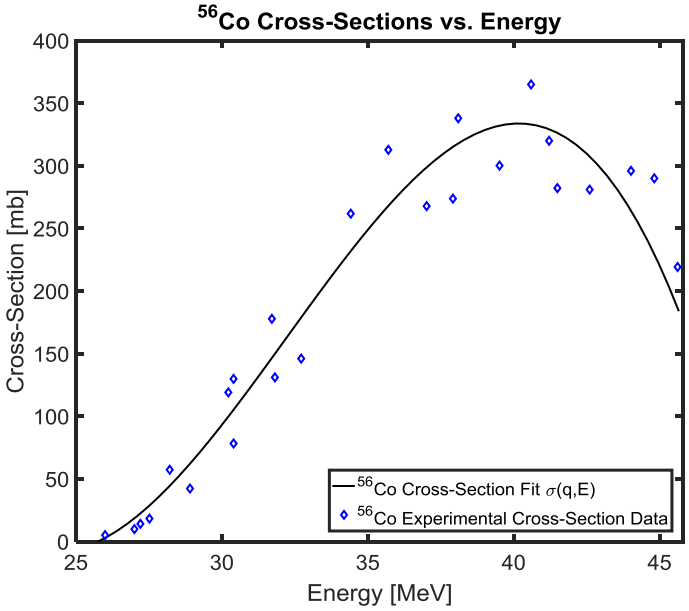

Figure 4-20: ^{56}Co cross-section fit and experimental data as a function of energy.

For the ^{57}Co production cross-sections a non-linear fit was used, with coefficients listed in Table 4-5.

$$\sigma_{57_{Co}} = 1000 \cdot \left\{ \frac{\left[A_5 + \frac{A_2}{[(A_4 - A_3 \cdot E)^2 + 1]} \right]}{\left[E \cdot exp\left(\frac{A_1}{\sqrt{E}} \right) - 1 \right]} \right\} \tag{4-24}$$

Table 4-5: Coefficients for the ^{58}Ni(p, 2p)^{57}Co excitation function fit.

Coefficient	Value
A_1	35.5206135
A_2	32287.0123
A_3	0.1891
A_4	3.63038358
A_5	0.0060008

This fit is plotted with the experimental data below in Figure 4-21.

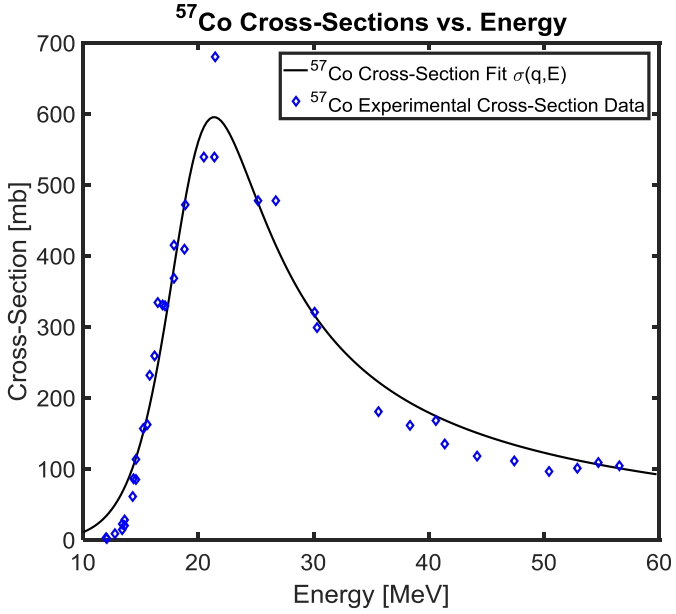

Figure 4-21: ^{57}Co cross-section fit and experimental data versus energy.

The 26 – 38 MeV energy range of interest is significantly narrower than the full energy range of the experimental data given in Figure 4-18 and Figure 4-19. This is partially due to the significantly lower energies incident on the nickel foils and partially due to the requirement that the cross-sections for each isotope are inversely varying over the energy range. Both these fits are plotted in Figure 4-22 along with experimental data over only the energy range of interest, illustrating that they are inversely varying over the energy ranges seen in this experiment.

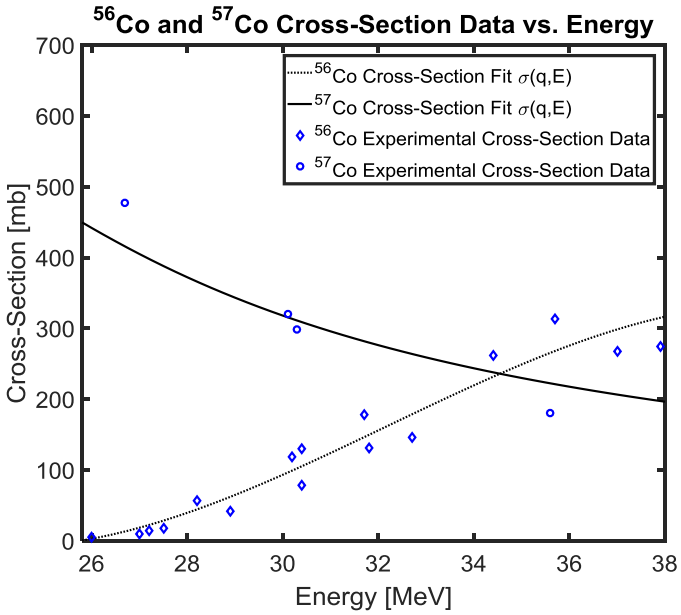

Figure 4-22: Fits of the cross-section excitation functions for the ^{58}Ni(p,x)^{56}Co and ^{58}Ni(p,x)^{57}Co reactions with experimental data.

For a given incident mono-energetic beam, the above cross-section curves may be used assuming that all particles are traveling at the same energy and thus have an equivalent probability of experiencing a specific interaction. However, assuming that particles slow down in a smooth and continuous fashion is no longer an accurate assumption. Small variations in energy loss leads to a variation around some mean particle energy that increases with the distance travelled by the particle. This is commonly called energy straggling. The theory of energy straggling dictates that as particles pass through material, the particle energy spreads around some mean value in the shape of a normal distribution [5,46,52].

A normal distribution may be described by Eq. (4-25).

$$f\left(E \mid \mu,\sigma^2\right) = \frac{1}{\sqrt{2\pi}\sigma} exp\left[- \frac{(E-\mu)^2}{2\sigma^2}\right] \tag{4-25}$$

In the above equation, σ is the assigned standard deviation of the normal distribution and μ is the associated mean, or center, of this distribution. For a normal distribution the average, mean, mode, and median are equivalent.

Applying the above theory to this experiment, particles incident on the nickel foils experience a substantial spread in beam energy as a result of passing through upstream RbCl

targets. In addition, the thermal results indicated that upstream RbCl targets experience a significant vertical density gradient that again impact the spread in beam energies incident upon the Ni^{58} foils. Because of this spread in particle energies, using one cross-section value at the mean incident energy is no longer accurate. Instead, effective cross-sections must be generated with a known standard deviation in the energy spread. While this was not taken into account by the individuals who originally performed the experiment, quantifying the impact of using effective cross-sections was considered essential. The procedure followed by the author of this work to determine the cumulative cross-sections is outlined below.

A conservative standard deviation of 2 MeV was chosen after plotting the energy distributions obtained in a number of MCNP runs with different average RbCl densities. Using an average energy mesh of size n with ΔE = 0.25 MeV, a probability density distribution was generated around each average energy, creating a $n \times n$ matrix. In this matrix, each row defines an array of values of the normal distribution about the diagonal energy entry.

$$\mathrm{p}df\left(E|\mu,\sigma^2\right)=\begin{bmatrix} pdf\left(E_1|\mu_1,\sigma_1^2\right) & pdf\left(E_2|\mu_1,\sigma_1^2\right) & \cdots & pdf\left(E_n|\mu_1,\sigma_1^2\right) \\ pdf\left(E_1|\mu_2,\sigma_2^2\right) & pdf\left(E_2|\mu_2,\sigma_2^2\right) & \cdots & pdf\left(E_n|\mu_2,\sigma_2^2\right) \\ \vdots & \vdots & \ddots & \vdots \\ pdf\left(E_1|\mu_n,\sigma_n^2\right) & pdf\left(E_2|\mu_n,\sigma_n^2\right) & \cdots & pdf\left(E_n|\mu_n,\sigma_n^2\right) \end{bmatrix}$$

The functional fits used to model the Co^{56} and Co^{57} cross-sections were applied to the energy mesh to generate a matrix of size $n \times 1$.

$$\sigma_{Co^{56}}(\mu)=[\sigma_{Co^{56}}(E_1) \quad \cdots \quad \sigma_{Co^{56}}(E_n)]^T$$
$$\sigma_{Co^{57}}(\mu)=[\sigma_{Co^{57}}(E_1) \quad \cdots \quad \sigma_{Co^{57}}(E_n)]^T$$

By multiplying the probability density function at each energy by the cross-section and energy spacing, ΔE, this effectively acts as a numeric integration of the curve and provides the total effective cross-section at the corresponding average energy of the normal distribution.

$$\mathrm{p}df\left(E|\mu,\sigma^2\right)\cdot\sigma_{Co^{56}}(\mu)\cdot\Delta E =$$
$$=\begin{bmatrix} \sigma_{Co^{56}}(E_1)\cdot pdf\left(E_1|\mu_1,\sigma_1^2\right)\cdot\Delta E+\ldots+\sigma_{Co^{56}}(E_n)\cdot pdf\left(E_n|\mu_1,\sigma_1^2\right) \\ \vdots \\ \sigma_{Co^{56}}(E_1)\cdot pdf\left(E_1|\mu_n,\sigma_n^2\right)\cdot\Delta E+\ldots+\sigma_{Co^{56}}(E_n)\cdot pdf\left(E_n|\mu_n,\sigma_n^2\right) \end{bmatrix}$$
$$=\begin{bmatrix} \sigma_{eff_{Co^{56}}}(E_1) \\ \vdots \\ \sigma_{eff_{Co^{56}}}(E_n) \end{bmatrix}$$

These effective cross-sections are plotted below in Figure 4-23 alongside the original cross-section curves to illustrate the differences. The original cross-section curves were determined assuming all particles were monoenergetic, while the effective cross-section curves were determined using a normal distribution of energies about some mean or average energy value.

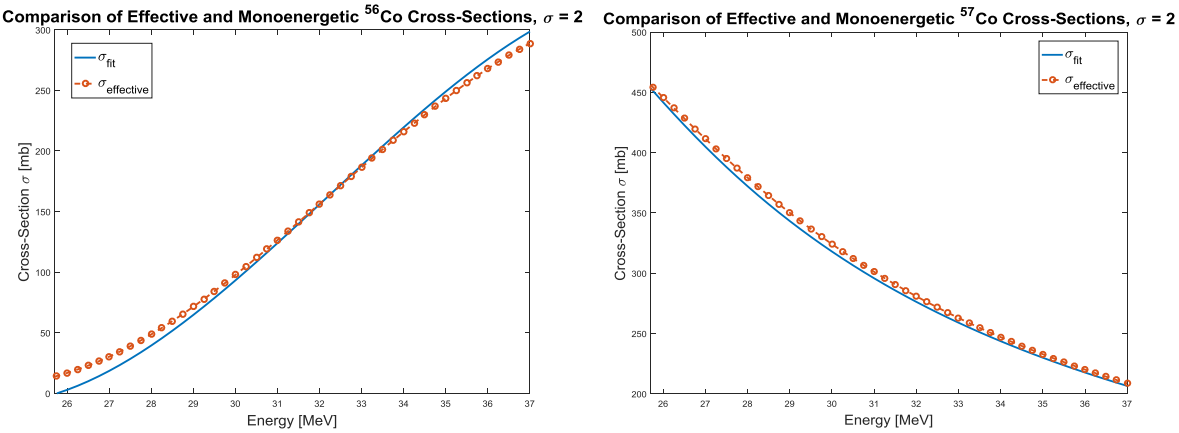

Figure 4-23: Comparison of effective and monoenergetic ^{56}Co (L) and ^{57}Co (R) cross-sections.

As the ^{56}Co cross-section falls to zero around 26 MeV, particles with an average energy close to this value have a portion of their normal distribution equal to zero. This proves problematic for activity measurement of foils with incident proton energies close to this value, as not all incident protons will contribute to the measured activity.

The half-lives and decay constants of ^{56}Co and ^{57}Co with associated uncertainties are given below in Table 4-6. The decay constant for each isotope is calculated as shown in Eq. (4-7) using the given half-life. These values were taken from the NNDC database [53,54].

Table 4-6: Half-lives, decay constants, and associated uncertainties for ^{56}Co and ^{57}Co.

Isotope	**Half-Life [days]**	$\sigma_{t_{1/2}}$ **[days]**	λ **[days^{-1}]**	σ_{λ} **[days^{-1}]**
^{56}Co	77.236	$\pm 2.6 \times 10^{-4}$	$\pm 8.974 \times 10^{-3}$	$\pm 3.0211 \times 10^{-8}$
^{57}Co	271.81	$\pm 4 \times 10^{-3}$	$\pm 2.55 \times 10^{-3}$	$\pm 3.7528 \times 10^{-8}$

The beginning irradiation time and EOB time was specified for both the thick and thin beam window experimental runs. The instantaneous current in μA was recorded at one minute

intervals. This instantaneous beam current was easily converted into beam intensity by multiplying by the following conversion factor.

$$1\ \mu A = 1 \times 10^{-6}\ \frac{C}{s} = 6.242 \times 10^{12}\ \frac{p}{s}$$

This conversion applies for any charged particle. The instantaneous beam current at each one minute irradiation interval is referred to here as *I*.

The incident fluxes were calculated using the time of irradiation as well as the time between EOB and the activity measurement. These values indicate the number of reactions per second occurring in the target after accounting for decay. Activity can be determined once the cross-section for the particular energy range and reaction of interest is applied. This is shown in Eq. (4-26) and was calculated for both ^{56}Co and ^{57}Co with the appropriate decay constants.

$$\Phi = I \cdot [1 - exp(-\lambda \cdot t_{irr})] \cdot exp[-\lambda \cdot (t_{EOB} - t)] \tag{4-26}$$

The sum of these values for the total irradiation time $\left(\int_{t_{irr}} \Phi\right)$ was used to obtain the total incident fluxes given in Table 4-7.

Table 4-7: Total incident proton fluxes on ^{58}Ni foils for the production of ^{56}Co and ^{57}Co.

Experiment	^{56}Co	^{57}Co
Thin Window Flux [p/s]	4.75×10^{11}	1.35×10^{11}
Thick Window Flux [p/s]	5.26×10^{11}	1.5×10^{11}

The gamma energies of interest, corresponding intensities, and associated uncertainties are provided in Table 4-8. These values were taken from the NNDC database [53,54].

Table 4-8: Photon intensities and associated uncertainties for ^{56}Co and ^{57}Co.

Isotope	γ Energy	γ Intensity (%)	σ_γ (%)
^{56}Co	846.8	99.9399	2.3×10^{-5}
	1238.3	66.46	1.2×10^{-3}
^{57}Co	122.07	85.60	1.7×10^{-3}
	136.48	10.68	8×10^{-3}

When observing a photo emission peak, the given real detector time in seconds and the percentage of dead time is utilized to determine the total live detector time during which counts were taken.

$$t_{live} = t_{real} \cdot (1 - f_{dead}) \tag{4-27}$$

For the majority of the foils measured from these experiments, a live count time of 40 minutes was used. The exception includes one 50 minute count taken for foil 9 from the thick window experiment and two 60 minute counts for foils 22 and 29 from the thin window experiment.

The count rate is determined by dividing the net number of counts by the total live counting time.

$$C = \frac{N}{t_{live}} \tag{4-28}$$

The actual number of photon emissions per unit time is then determined by dividing the recorded number of counts by the detector efficiency for that particular photon energy and detector geometry.

$$CR_{net} = C \cdot \frac{1}{\varepsilon_{detector}} \tag{4-29}$$

A high-purity germanium (HPGe) detector was used for all photon emission detection measurements. The detector efficiency is influenced by both the detector geometry and photon energy. Thus, the efficiency used for each count measurement is a function of the photon energy of interest. For the detector used here, the set of provided tabular efficiency values and uncertainties are given in Table 4-9 and graphically depicted in Figure 4-24 with 1σ error bars.

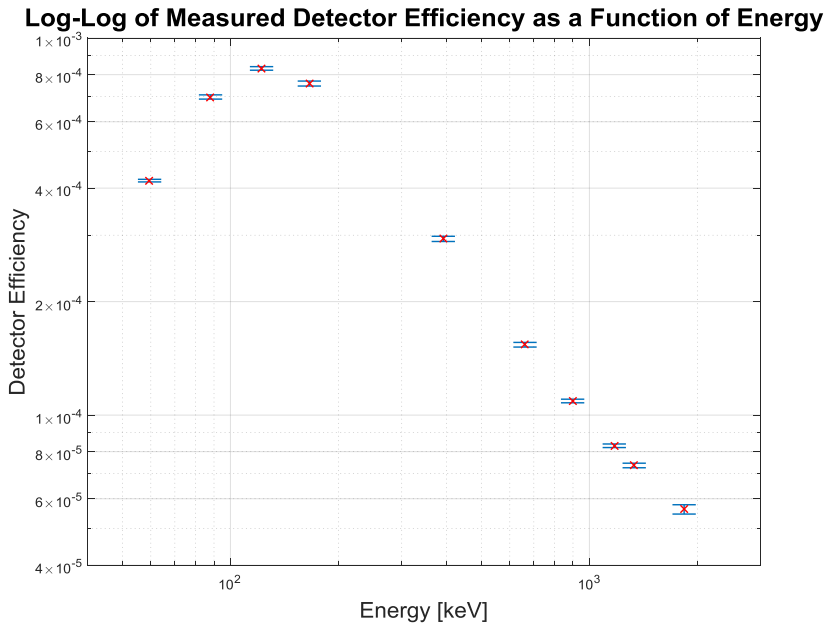

Figure 4-24: Log-log plot of measured detector efficiency and uncertainty as a function of energy.

Table 4-9: Tabular detector efficiencies and uncertainties as a function of energy.

Energy [keV]	Detector Efficiency ϵ	% Uncertainty	σ_ϵ
59.54	4.188×10^{-4}	0.7972	3.339×10^{-6}
88.03	6.98×10^{-4}	1.298	9.060×10^{-6}
122.10	8.31×10^{-4}	1.092	9.075×10^{-6}
165.90	7.577×10^{-4}	1.516	1.149×10^{-5}
391.7	2.934×10^{-4}	1.589	4.662×10^{-6}
661.6	1.537×10^{-4}	1.418	2.179×10^{-6}
898.0	1.09×10^{-4}	1.106	1.206×10^{-6}
1173.0	8.292×10^{-5}	1.091	9.047×10^{-7}
1333.0	7.352×10^{-5}	1.391	1.023×10^{-6}
1836.0	5.624×10^{-5}	2.846	1.601×10^{-6}

The efficiency fit as shown in Figure 4-25 was determined by linearly interpolating between the natural log of the measured efficiency and the natural log of the energy. This was calculated by the author of this work and was not done when the experiment was initially performed. This calculation is given in Eq. (4-30) and was repeated for calculation of the associated detector efficiency uncertainties.

$$\epsilon_\gamma = exp\left(\frac{ln(E_\gamma) - ln(E_i)}{ln(E_{i+1}) - ln(E_i)}(ln(\epsilon_{i+1}) - ln(\epsilon_i)) + ln(\epsilon_i)\right) \tag{4-30}$$

$$\sigma_{\epsilon_\gamma} = exp\left(\frac{ln(E_\gamma) - ln(E_i)}{ln(E_{i+1}) - ln(E_i)}\left(ln(\sigma_{\epsilon_{i+1}}) - ln(\sigma_{\epsilon_i})\right) + ln(\sigma_{\epsilon_i})\right) \quad (4\text{-}31)$$

In Figure 4-25 the interpolated fit is shown with ± 2σ bounds, while the measured data is shown with an error bar representing the error in the measured value ± 1σ.

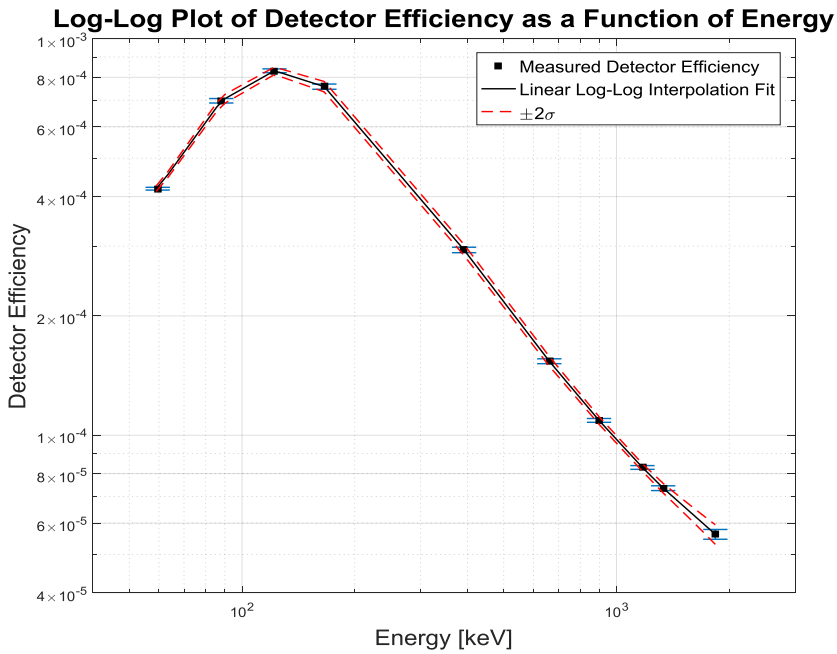

Figure 4-25: Log-log plot of measured and linearly interpolated detector efficiencies as a function of energy.

Using Eq. (4-32) and Eq. (4-33), the detector efficiencies and associated uncertainties may be calculated for the photon energies of interest. These values are given in Table 4-10.

Table 4-10: Efficiencies of photon energies of interest.

γ Energy [keV]	Detector Efficiency ϵ_γ	Uncertainty σ_{ϵ_γ}
122.06	8.3085×10^{-4}	9.0745×10^{-6}
136.47	8.0361×10^{-4}	9.8851×10^{-6}
846.77	1.1645×10^{-4}	1.3509×10^{-6}
1238.29	7.8800×10^{-5}	9.5289×10^{-7}

The calculated source gammas emitted per unit time was converted into activity in units of [mCi] as shown in Eq. (4-32).

$$\mathrm{A}\,[mCi\,] = \frac{\left[CR_{net}\left[\frac{\text{decay}}{\text{min}}\right]\cdot\frac{60\text{ s}}{1\text{ hr}}\cdot\left[\frac{1}{\gamma_{intensity}}\right]\cdot\left[\frac{1\text{ Bq}}{1\frac{\text{decay}}{\text{s}}}\right]\cdot\left[\frac{1\text{ Ci}}{3.7\times10^{10}\text{Bq}}\right]\right]}{\exp\left[-\lambda\left[\frac{1}{\text{s}}\right]\cdot(t_{EOB}-t)[\text{s}]\right]} \tag{4-32}$$

For each measured gamma emission, the activity ratio of ^{57}Co to ^{56}Co was taken.

In order to obtain a corresponding energy from this ratio, the ratio of the ^{56}Co and ^{57}Co production cross-sections as a function of energy must be mapped. The process by which this was done is explained below.

Stopping power and the thickness of each nickel foil were used to determine the midpoint energy. This midpoint energy was used in the functional form for the cross-section, correlating the cross-section to the loss of energy as a function of stopping power and distance travelled.

The given function for stopping power in ^{58}Ni with an incident energy of 40 MeV and minimum energy of 10 MeV is of the form shown in Eq. (4-33).

$$\frac{dE}{dx}\left[\frac{\text{MeV}}{\text{mg}\cdot\text{cm}}\right] = C_1\cdot E^5 + C_2\cdot E^4 + C_3\cdot E^3 + C_4\cdot E^2 + C_5\cdot E + C_6 \tag{4-33}$$

Table 4-11: Coefficients for the fit of proton stopping power in nickel.

Coefficient	Value
C_1	-1.5369×10^{-9}
C_2	-2.2731×10^{-7}
C_3	-1.3562×10^{-5}
C_4	4.1896×10^{-4}
C_5	-7.1731×10^{-3}
C_6	7.0193×10^{-3}

The change in energy was determined over every dx = 0.001 cm distance.

$$\mathrm{d}E\,[\text{MeV}] = \frac{dE}{dx}\left[\frac{\text{MeV}}{\text{mg}\cdot\text{cm}}\right]\cdot\left[1000\frac{\text{mg}}{\text{g}}\right]\cdot\rho\left[\frac{\text{g}}{\text{cm}^3}\right]\cdot dx[\text{cm}] \tag{4-34}$$

Nickel density was given as ρ = 8.19 g/cm^3. The midpoint energy at each of these 0.001 cm slices was determined using the arithmetic average.

$$E_{avg} = \frac{E_{in}+E_{out}}{2}$$

This midpoint energy was used to determine the cross-sections for the ^{58}Ni(p, xn)^{56}Co and ^{58}Ni(p, 2p)^{57}Co reactions using the appropriate fitting function such that $\sigma = \sigma(E_{avg})$.

The functional form of the activity ratio was determined using ratio of cross-sections and the incident flux values for each isotope as shown below. The number density for the nickel foils drops out as it appears on both the top and bottom of the ratio.

$$\frac{A_{57_{Co}}}{A_{56_{Co}}}(E) = \frac{N_{58_{Ni}}\sigma_{57_{Co}}(E)\Phi_{57_{Co}}}{N_{58_{Ni}}\sigma_{56_{Co}}(E)\Phi_{56_{Co}}} = \frac{\sigma_{57_{Co}}(E)\Phi_{57_{Co}}}{\sigma_{56_{Co}}(E)\Phi_{56_{Co}}} \tag{4-35}$$

This means that if given an activity ratio, $A_{57_{Co}}/A_{56_{Co}}$ and an energy-dependent distribution of activities $A_{57_{Co}}/A_{56_{Co}}(E)$ it is possible to determine the corresponding average energy E using Eq. (4-35).

An interpolation function was generated of the form given in Eq. (4-36). The values x_1 and x_2 correspond to the activity ratios bounding the activity ratio of interest - $A_{57_{Co}}/A_{56_{Co}}$. The values y_1 and y_2 correspond to the energies for each activity ratio.

$$\frac{\frac{A_{57_{Co}}}{A_{56_{Co}}} - x_1}{x_2 - x_1} = \frac{E - y_1}{y_2 - y_1} \tag{4-36}$$

Since four distinctive gammas are emitted, two each from ^{56}Co and ^{57}Co, there are four activity ratios. The average of activity ratio was calculated as shown below in Eq. (4-37).

$$\overline{R}_A = \frac{R_{A_1} + R_{A_2} + R_{A_3} + R_{A_4}}{4} \tag{4-37}$$

The minimum and maximum of these values determine the minimum and maximum energies incident on the foil and the average energy was found using the arithmetic average.

Full tables of maximum and minimum activity ratios of $A_{57_{Co}}/A_{56_{Co}}$ and E for both the thick and thin window experiments are given in Appendix C. The average activity ratio and incident energy are given in Section 4.3.1.3 in Table 4-14 and Table 4-15. The ^{58}Ni foils are considered thin targets in the sense that they are sufficiently thin such that the ΔE within the target may be ignored. Given this, the incident energy is equal to the energy predicted with the average activity ratio.

Section 4.3.1.3. Incident Average Energy and Activity Distribution

The average ^{56}Co and ^{56}Co activities are given in Table 4-12 and Table 4-13 and the predicted incident energies are given in Table 4-14 and Table 4-15. The average activities were calculated by the individuals who performed the experiment, but the incident energies were determined by the author of this work using the effective production cross-sections of ^{56}Co and ^{57}Co calculated above. It should be noted that of the four activity ratios taken for the thin window experiment, there was a very large spread in data (see Appendix C), leading to a decreased level of confidence in the final averaged results.

Table 4-12: Thin window experimental results for ^{56}Co and ^{57}Co activities.

Thin Window					
Foil Number	**^{56}Co Activity [mCi]**	**^{57}Co Activity [mCi]**	**Foil Number**	**^{56}Co Activity [mCi]**	**^{57}Co Activity [mCi]**
1	5.338E-04	8.875E-03	17	3.272E-04	1.238E-02
2	7.013E-03	2.005E-02	18	1.453E-03	2.037E-02
3	1.277E-02	1.929E-02	19	5.500E-03	2.649E-02
4	3.377E-03	5.078E-03	20	2.271E-02	2.945E-02
5	4.039E-03	5.807E-03	21	8.500E-04	8.585E-03
6	5.095E-03	9.093E-03	22	1.134E-02	1.123E-02
7	6.860E-03	1.243E-02	23	4.849E-03	1.226E-02
8	8.652E-03	1.689E-02	24	4.634E-03	1.464E-02
9	9.692E-03	2.305E-02	25	5.427E-03	2.077E-02
10	8.122E-03	2.819E-02	26	5.146E-03	2.706E-02
11	9.860E-03	3.478E-02	27	7.078E-03	2.869E-02
12	4.814E-03	3.677E-02	28	-	-
13	8.681E-04	3.325E-02	29	1.470E-03	1.613E-02
14	6.597E-04	3.411E-02	30	3.555E-03	2.694E-02
15	2.735E-04	1.476E-02	31	9.822E-03	2.630E-02
16	9.389E-05	3.872E-03		-	

Table 4-13: Thick window experimental results for ^{56}Co and ^{57}Co activities.

Thick Window					
Foil Number	**^{56}Co Activity [mCi]**	**^{57}Co Activity [mCi]**	**Foil Number**	**^{56}Co Activity [mCi]**	**^{57}Co Activity [mCi]**
1	1.148E-04	2.175E-03	17	1.466E-04	1.146E-02
2	1.604E-03	2.741E-02	18	1.224E-03	3.963E-02
3	6.794E-03	3.436E-02	19	1.967E-03	4.080E-02
4	2.389E-03	7.590E-03	20	3.336E-03	3.811E-02
5	3.118E-03	9.718E-03	21	1.757E-04	1.432E-02
6	2.535E-03	1.317E-02	22	2.526E-03	1.943E-02
7	2.674E-03	1.895E-02	23	1.398E-03	1.918E-02
8	3.041E-03	2.693E-02	24	1.031E-03	2.170E-02
9	2.011E-03	2.319E-02	25	1.024E-03	3.101E-02
10	1.595E-03	2.818E-02	26	6.656E-04	3.503E-02
11	8.374E-04	3.467E-02	27	1.071E-03	3.722E-02
12	3.123E-04	3.462E-02	28	1.966E-04	2.745E-02
13	1.528E-04	2.276E-02	29	1.569E-04	1.379E-02
14	1.246E-04	1.789E-02	30	4.377E-04	3.046E-02
15	1.337E-04	1.166E-02	31	2.343E-03	3.735E-02
16	1.170E-04	1.800E-03		-	

Table 4-14: Thin window experimental results for energies.

Thin Window			
Foil Number	**Incident Energy [MeV]**	**Foil Number**	**Incident Energy [MeV]**
1	26.207	17	25.908
2	27.581	18	26.095
3	28.522	19	26.988
4	28.852	20	29.517
5	28.871	21	26.377
6	28.464	22	30.211
7	28.272	23	27.793
8	28.113	24	27.473
9	27.824	25	27.229
10	27.352	26	26.899
11	27.496	27	27.174
12	26.368	28	-
13	25.903	29	26.207
14	25.867	30	26.569
15	25.864	31	27.672
16	25.929		-

Table 4-15: Thick window experimental results for energies.

Thick Window			
Foil Number	**Incident Energy [MeV]**	**Foil Number**	**Incident Energy [MeV]**
1	26.033	17	25.826
2	26.060	18	25.923
3	26.917	19	26.010
4	27.676	20	26.191
5	27.710	21	25.824
6	26.876	22	26.364
7	26.436	23	26.127
8	26.296	24	26.006
9	26.188	25	25.934
10	26.050	26	25.856
11	25.887	27	25.910
12	25.800	28	25.798
13	25.797	29	25.817
14	25.443	30	25.836
15	25.818	31	26.080
16	26.090		-

MATLAB was used to generate contour plots of the average energy distribution over the plane on which the ^{58}Ni foils were placed. These plots are shown in Figure 4-28 and Figure 4-29. Also shown are contour plots generated using the net average measured activity of ^{56}Co and ^{57}Co for each foil. These plots were generated by the author of this work.

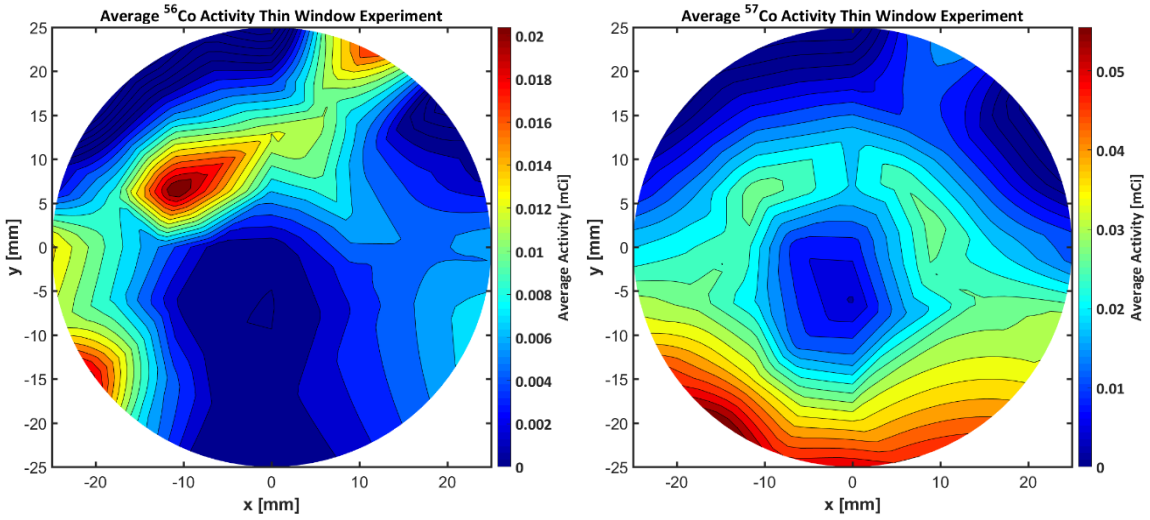

Figure 4-26: Contour plots of ^{56}Co and ^{57}Co activities produced in the thin window experiment.

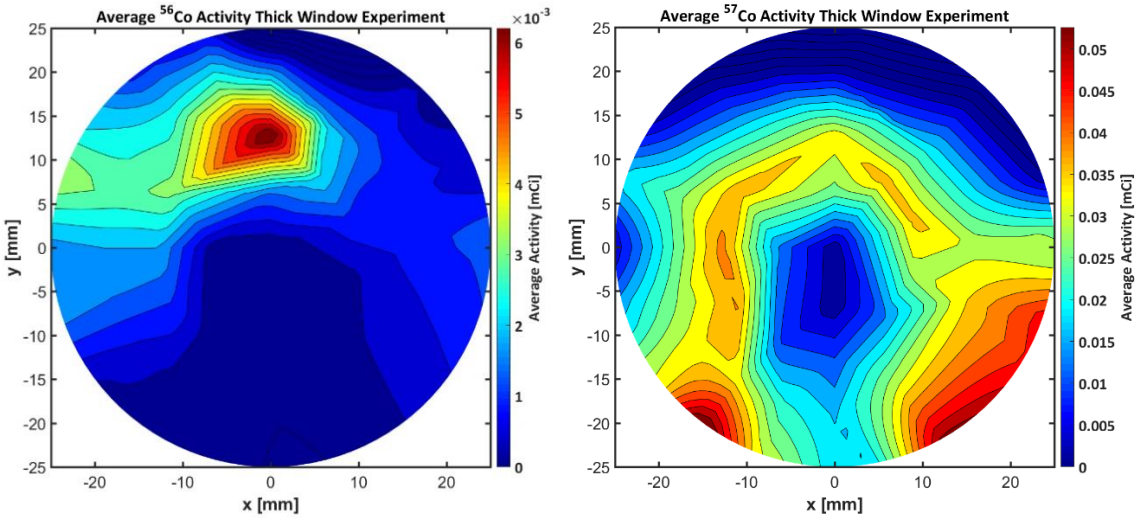

Figure 4-27: Contour plots of ^{56}Co and ^{57}Co activities produced in the thick window experiment.

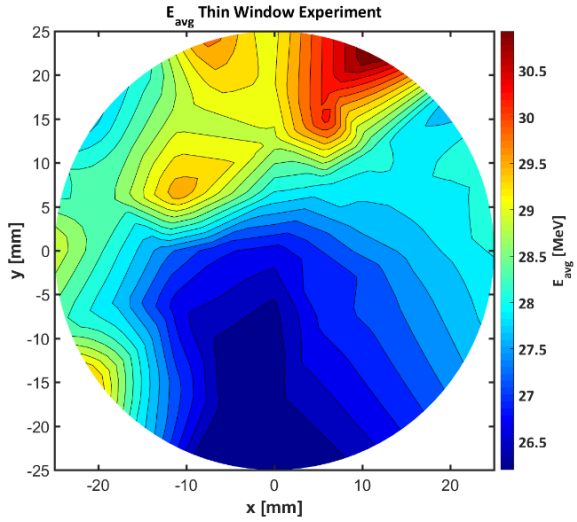

Figure 4-28: Contour plot of average energy incident on front face of ^{58}Ni foils in thin window experiment.

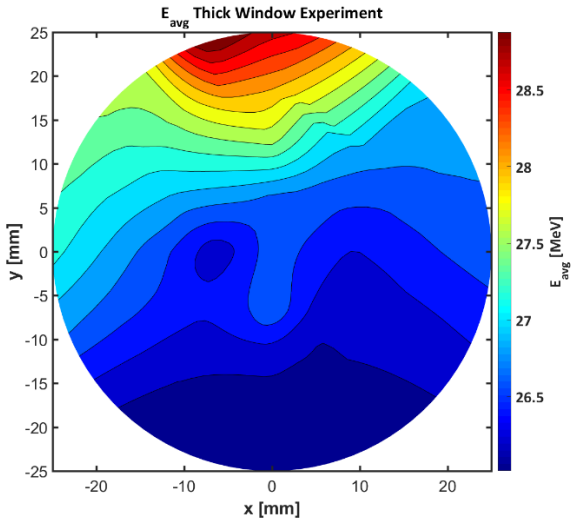

Figure 4-29: Contour plot of average energy incident on front face of ^{58}Ni foils in thick window experiment.

As the ^{56}Co production cross-section falls to zero around 26 MeV, particles with an average energy close to this threshold energy have a fraction of their Gaussian distribution with a probability of interaction equal to zero. As a result, these particles do not contribute to the activity of ^{56}Co produced in the foil and will thus skew the ratio of activities from which the average incident energy is extrapolated.

However, it is clear that the energy distributions given in Figure 4-28 and Figure 4-29 indicate that there is a noticeably higher incident energy distribution on the foils located at the top of the bolt-together target. This is indicative of the fact that the upstream RbCl targets are at least partially molten, causing the protons passing through the top of the target to lose less energy as a function of axial distance travelled.

Section 4.3.2. MCNP Replication of Experiment

The experimental geometry for both the thick and thin window experiments was recreated in MCNP. The thick window was assigned a thickness of 3.052 mm and the thin window was assigned a thickness of 1.5132 mm. All foil dimensions were taken from experimentally measured data, and all foils were inset into the front window by 0.102 mm. Activities of ^{56}Co and ^{57}Co were determined with the same cross-section fits used in the experiment in order to

be consistent. MCNP receives this cross-section information as a set of tabular values from which it can linearly interpolate. The RbCl target density distributions used are the pseudo steady state values after iterating to convergence. This is a valid simplification, as the pseudo steady state target behavior is achieved in less than one minute of irradiation time, and all targets are irradiated for significantly longer than this. The geometry as replicated by MCNP is shown in Figure 4-30. A total of 30 million particle histories were run in both the thick and thin window MCNP models.

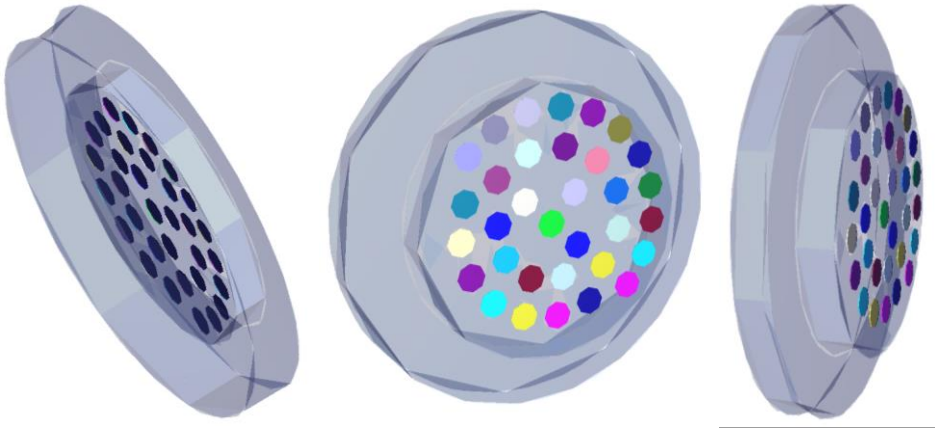

Figure 4-30: VISED [38] visualization of MCNP geometry replicating ^{58}Ni foil experiment.

A type four (F4) tally was used in MCNP for determination of the activities of ^{56}Co and ^{57}Co produced in each ^{58}Ni foil in MCNP. Two separate tallies and corresponding dose function cards must be used for each foil, one each for the production of ^{56}Co and ^{57}Co.

The cross-sections used in the DF card are in barns and the energies used in the DE card are in MeV, thus the F4 tally modified with dose function cards will provide the flux in a cell in units of $\left[\frac{\text{protons}\cdot\text{barn}}{\text{source-particle}\cdot\text{cm}^2}\right]$. As MCNP tracks the individual energy of each particle, the total and not the effective cross-sections may be used in the MCNP input deck. These total production cross-sections fits for ^{56}Co and ^{57}Co are provided in Eq. (4-23) and Eq. (4-24).

The tally results are then multiplied by conversion factors, cell volume, and number density in order to determine the saturation yield in $\left[\frac{\text{mCi}}{\mu\text{A}}\right]$. This is described below.

$$\text{Saturation Yield}\left[\frac{\text{mCi}}{\mu\text{A}}\right] = F4\left[\frac{\text{protons}\cdot\text{mbarn}}{\text{source-particle}\cdot\text{cm}^2}\right]\cdot N_{Ni^{58}}\left[\frac{\text{atoms}}{\text{cm}^3}\right]\cdot V_{Ni^{58}foil}$$

$$[\text{cm}^3]\cdot 10^{-27}\left[\frac{\text{cm}^2}{\text{mbarn}}\right]\cdot 6.24\cdot 10^{12}\left[\frac{\frac{\text{protons}}{\text{s}}}{\mu\text{A}}\right]\cdot 2.7\cdot 10^{-8}\left[\frac{\text{mCi}}{\frac{\text{protons}}{\text{s}}}\right] \quad (4\text{-}38)$$

The number density $N_{Ni^{58}}$ was calculated for each foil using the below equations. V_{foil} is the foil volume, determined by the foil diameter and thickness. The density of each foil, ρ_{foil}, is determined using the foil mass and volume. These parameters may then be used to determine the foil number density.

$$V_{foil} = \pi\cdot\left(\frac{D_{foil}}{2}\right)^2 \Delta z_{foil} \quad (4\text{-}39)$$

$$\rho_{foil} = \frac{m_{foil}}{V_{foil}} \quad (4\text{-}40)$$

$$N_{foil} = \frac{\rho_{foil} N_A}{A_{foil}} \quad (4\text{-}41)$$

Each foil tally will be multiplied by a constant, given below.

$$FM_{foil} = N_{Ni^{58}}\left[\frac{\text{atoms}}{\text{cm}^3}\right]\cdot V_{Ni^{58}foil}\left[\text{cm}^3\right]\cdot 10^{-27}\left[\frac{\text{cm}^2}{\text{mbarn}}\right]\cdot 6.24\cdot 10^{12}\left[\frac{\frac{\text{protons}}{\text{s}}}{\mu\text{A}}\right]\cdot 2.7\cdot 10^{-8}\left[\frac{\text{mCi}}{\frac{\text{protons}}{\text{s}}}\right]$$

The number densities and tally multiplier for each foil for the thick and thin window experiments are given in Appendix C.

Two sets of results are presented and discussed. They were obtained using the density profiles from both the final refined cooling water domain model and the average heat transfer coefficient model. The irradiation history for each experiment was used to obtain predicted EOB activities for each foil. The MCNP runs for both models were performed with 30 million particle histories. MCNP provides associated statistical uncertainties with all calculated activities. These uncertainties will be discussed for the refined cooling water domain model results in Section 5.3.2.3.

Section 4.3.2.1. Refined Cooling Water Domain Model Results

The activities and average incident energies obtained using MCNP are presented here. These results were generated with the pseudo steady state density profiles in RbCl targets A

and B of the refined cooling water domain model. The average ^{56}Co and ^{56}Co activities are given in Table 4-16 and Table 4-17.

Table 4-16: Thin window MCNP results for ^{56}Co and ^{57}Co activities.

Thin Window					
Foil Number	**^{56}Co Activity [mCi]**	**^{57}Co Activity [mCi]**	**Foil Number**	**^{56}Co Activity [mCi]**	**^{57}Co Activity [mCi]**
1	1.644E-06	1.779E-03	17	1.362E-03	6.327E-02
2	3.462E-04	1.766E-02	18	1.013E-03	6.519E-02
3	4.109E-03	5.850E-02	19	3.004E-03	6.177E-02
4	2.412E-04	9.912E-03	20	5.572E-03	5.939E-02
5	1.424E-05	9.957E-03	21	2.671E-04	1.790E-02
6	1.296E-04	1.087E-02	22	3.086E-03	3.387E-02
7	2.087E-04	1.077E-02	23	1.967E-03	3.423E-02
8	5.190E-04	9.815E-03	24	7.583E-04	3.588E-02
9	2.227E-04	8.700E-03	25	4.295E-04	3.725E-02
10	1.371E-06	7.052E-03	26	2.560E-04	3.565E-02
11	1.592E-06	7.830E-03	27	2.036E-03	4.647E-02
12	1.874E-06	7.976E-03	28	1.209E-04	3.493E-02
13	5.048E-06	8.490E-03	29	1.019E-03	4.686E-02
14	3.429E-06	7.915E-03	30	1.489E-03	4.742E-02
15	1.241E-03	6.470E-02	31	2.514E-03	4.550E-02
16	2.367E-04	1.887E-02		-	

Table 4-17: Thick window MCNP results for ^{56}Co and ^{57}Co activities.

Thick Window					
Foil Number	**^{56}Co Activity [mCi]**	**^{57}Co Activity [mCi]**	**Foil Number**	**^{56}Co Activity [mCi]**	**^{57}Co Activity [mCi]**
1	2.437E-07	1.848E-04	17	1.990E-08	2.382E-02
2	2.307E-07	6.928E-03	18	2.952E-07	2.071E-02
3	5.658E-07	3.764E-02	19	7.685E-07	3.057E-02
4	1.764E-07	3.507E-03	20	6.108E-07	4.190E-02
5	0.000E+00	1.325E-03	21	1.926E-07	6.530E-03
6	0.000E+00	3.342E-03	22	4.642E-07	2.379E-02
7	1.488E-09	3.855E-03	23	4.894E-07	2.012E-02
8	4.334E-07	6.026E-03	24	2.487E-07	1.251E-02
9	6.324E-09	2.981E-03	25	2.051E-08	1.015E-02
10	0.000E+00	4.505E-04	26	9.466E-08	8.069E-03
11	2.144E-08	4.966E-04	27	7.302E-08	2.461E-02
12	0.000E+00	5.483E-04	28	0.000E+00	5.803E-03
13	0.000E+00	7.701E-04	29	3.126E-07	1.803E-02
14	2.179E-07	5.914E-04	30	2.712E-08	2.158E-02
15	9.867E-09	2.302E-02	31	7.893E-07	2.686E-02
16	0.000E+00	6.057E-03		-	

The MCNP predicted incident energies are provided only for the thin window MCNP model, and are given in Table 4-18 along with the experimentally predicted energies. The extremely low ^{56}Co activities shown in Table 4-17 and Figure 4-32 indicate that the foils in the MCNP model of the thick window experiment experience incident energies below the threshold energy for the ^{58}Ni(p,x)^{56}Co reaction. Because of this, the activity ratios do not provide meaningful information and it was therefore not possible to use them to predict the energies incident on the ^{58}Ni foils. For this reason, the predicted incident energies are not provided for the thick window experiment.

Table 4-18: Thin window experimental and MCNP model results for energies.

Foil Number	Incident Energy [MeV]		Foil Number	Incident Energy [MeV]	
	MCNP Model	Experiment		MCNP Model	Experiment
1	25.7372	26.207	17	25.8734	25.908
2	25.8609	27.581	18	25.8407	26.095
3	26.1148	28.522	19	26.0122	26.988
4	25.8880	28.852	20	26.2184	29.517
5	25.7606	28.871	21	25.8381	26.377
6	25.8214	28.464	22	26.2063	30.211
7	25.8593	28.272	23	26.0542	27.793
8	26.0335	28.113	24	25.8710	27.473
9	25.8935	27.824	25	25.8186	27.229
10	25.6260	27.352	26	25.7978	26.899
11	25.6293	27.496	27	25.9886	27.174
12	25.6388	26.368	28	25.7878	-
13	25.7026	25.903	29	25.8747	26.207
14	25.6833	25.867	30	25.9257	26.569
15	25.8579	25.864	31	26.0440	27.672
16	25.8255	25.929		-	

MATLAB was used to generate contour plots of the net average measured activity of ^{56}Co and ^{57}Co for each foil for both the thick and thin window experiments. These contour plots are shown in Figure 4-31 and Figure 4-32. The average energy distribution for the thin window MCNP model is compared with the experimental energy distribution in Figure 4-33. This average energy distribution was obtained as described in Section 4.3.1.2.

It is clear from these images that the density distributions predicted by the iterative process between MCNP and ANSYS CFX are significantly higher than those seen in the physical

targets. This leads to lower predicted energies incident on the front face of the C-slot bolt-together target than expected, and therefore a lower incident energy on each foil. This is reflected in the MCNP predicted activities of ^{56}Co and ^{57}Co when compared to the experimentally predicted activities.

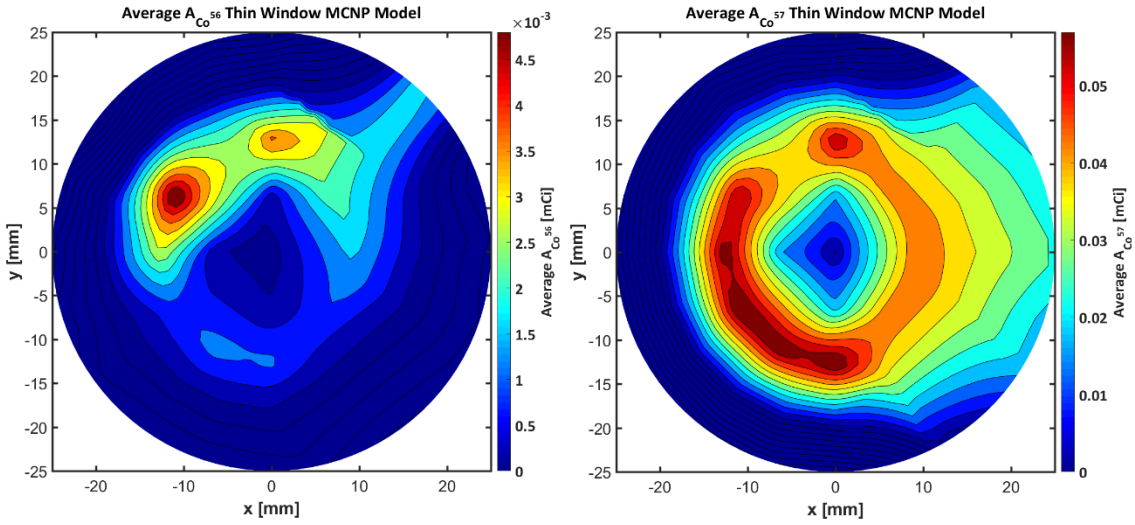

Figure 4-31: Contour plots of ^{56}Co and ^{57}Co activities produced in the MCNP replicated thin window experiment.

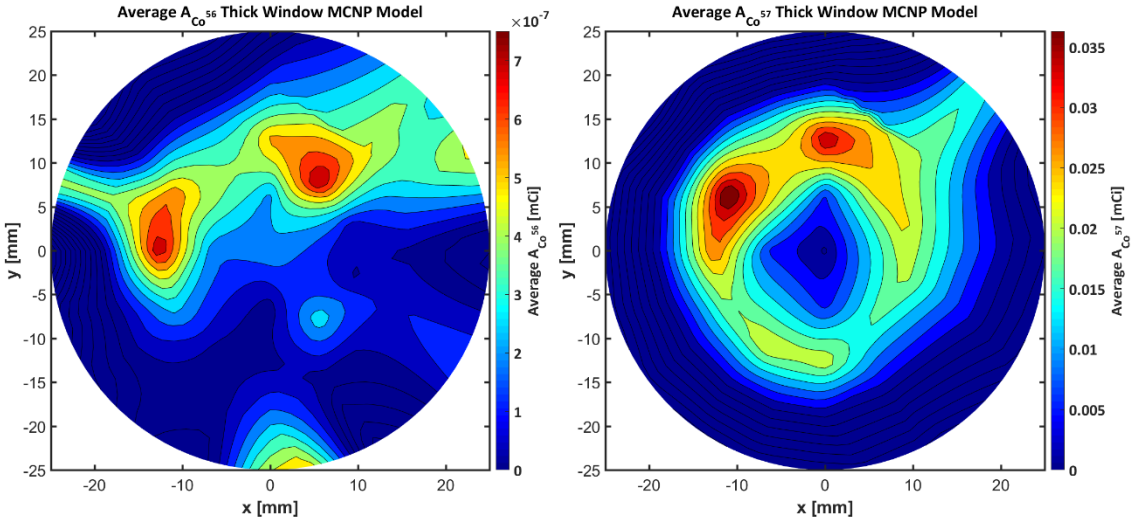

Figure 4-32: Contour plots of ^{56}Co and ^{57}Co activities produced in the MCNP replicated thick window experiment.

As the incident proton energies were above the threshold energy for the $^{58}Ni(p,x)^{56}Co$ reaction for the thin window MCNP model, it was possible to use the activity ratios of ^{56}Co and ^{57}Co to obtain an approximation of the energy distribution across the face containing the ^{58}Ni foils. Figure 4-33 shows that a much lower energy distribution was predicted by the MCNP thin window model in comparison to the thin window experimental results. However, similar trends are seen in the sense that higher energies are very clearly present at the top of the target than at the bottom of the target. This is expected due to the relocation of less dense molten RbCl to the top of the target as a result of convective flow patterns.

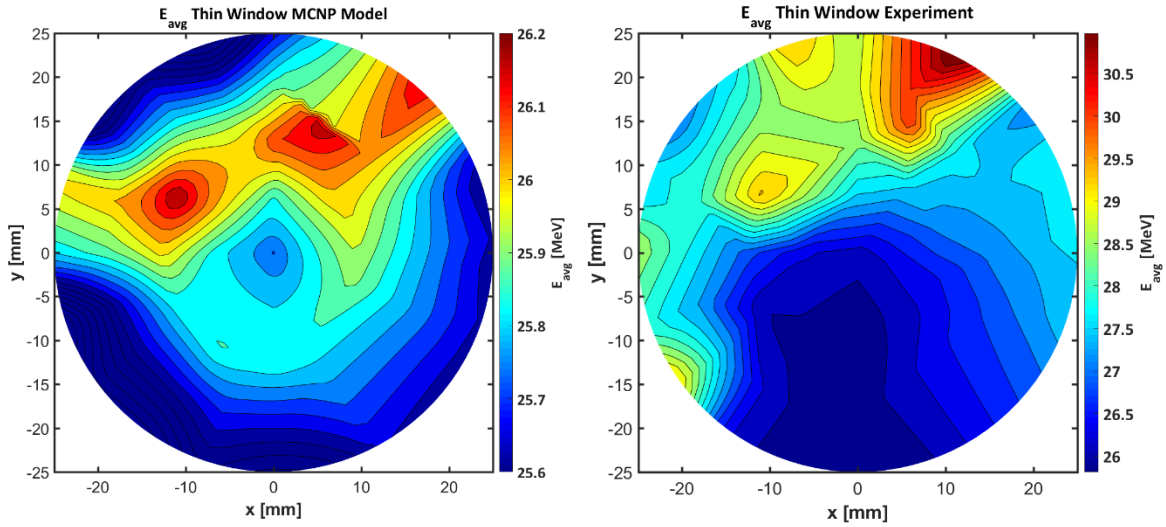

Figure 4-33: Contour plot of average energy incident on front face of ^{58}Ni foils in thin window MCNP model (L) and experiment (R).

These validation metrics provide clear evidence that the model is under predicting the peak target temperatures seen, leading to a lower incident energy distribution transmitted through to the C-slot target. To determine what densities (and corresponding temperatures) might be required by the MCNP model to obtain a transmitted energy of ~30-31 MeV – as seen in the thin window experimental transmitted energy distribution shown above – several MCNP thin window model runs were performed with an average RbCl target A and B density. Based on these average density MCNP runs, an average upstream density of 2.0 g/cm^3 is required in both targets to achieve an incident energy of ~31 MeV in the thin window experiment. This density

corresponds to a temperature of ~1269 K. When comparing this value to the ANSYS CFX temperature distribution obtained for RbCl targets A and B in Section 3.2, it is clear that the MCNP model is under predicting the peak temperatures seen in the experiment by ~100 K as suggested by the maximum energy incident on the ^{58}Ni foils.

As discussed in the modeling set-up section, several physical phenomena have been neglected or simplified as a result of computational limitations and it is not clear to what extent these influence the cumulative effects of upstream behavior leading to this transmitted energy distribution. One possible contributor could be insufficient modeling of the cooling water channels leading to an inaccurate and overly optimistic prediction of target heat removal, causing lower peak target temperatures and higher densities. A suggested approach to capture more details about the transmitted energy distribution and assist in further attempts at model validation is discussed in Section 6.3.

Section 4.3.2.2. Comparison with Average Heat Transfer Coefficient Model Results

The predicted activities and average incident energies were also calculated using the pseudo steady state density distribution profile in RbCl targets A and B obtained with the average heat transfer coefficient model and 30 million MCNP particle histories. This was done to compare the predictive capability of the average heat transfer coefficient model to the refined cooling water domain model. The average ^{56}Co and ^{56}Co activities are given in Table 4-19 and Table 4-20.

Table 4-19: Thin window MCNP results for ^{56}Co and ^{57}Co activities for the average heat transfer coefficient model.

Thin Window					
Foil Number	**^{56}Co Activity [mCi]**	**^{57}Co Activity [mCi]**	**Foil Number**	**^{56}Co Activity [mCi]**	**^{57}Co Activity [mCi]**
1	2.280E-06	1.851E-03	17	1.744E-03	6.273E-02
2	4.689E-04	1.740E-02	18	1.105E-03	6.500E-02
3	5.670E-03	5.688E-02	19	4.026E-03	6.069E-02
4	3.711E-04	9.784E-03	20	7.514E-03	5.758E-02
5	1.839E-05	1.015E-02	21	3.548E-04	1.770E-02
6	2.001E-04	1.079E-02	22	4.043E-03	3.291E-02
7	3.247E-04	1.055E-02	23	2.652E-03	3.338E-02
8	8.107E-04	9.473E-03	24	1.009E-03	3.557E-02
9	3.519E-04	8.778E-03	25	5.808E-04	3.714E-02
10	1.113E-06	7.564E-03	26	3.590E-04	3.563E-02
11	2.380E-06	8.305E-03	27	3.181E-03	4.499E-02
12	2.977E-06	8.446E-03	28	1.276E-04	3.476E-02
13	6.803E-06	8.668E-03	29	1.088E-03	4.678E-02
14	4.135E-06	8.275E-03	30	1.857E-03	4.685E-02
15	1.635E-03	6.397E-02	31	3.871E-03	4.388E-02
16	2.731E-04	1.882E-02		-	

Table 4-20: Thick window MCNP results for ^{56}Co and ^{57}Co activities for the average heat transfer coefficient model.

Thick Window					
Foil Number	**^{56}Co Activity [mCi]**	**^{57}Co Activity [mCi]**	**Foil Number**	**^{56}Co Activity [mCi]**	**^{57}Co Activity [mCi]**
1	2.437E-07	2.229E-04	17	3.507E-08	2.622E-02
2	3.373E-07	7.853E-03	18	3.600E-07	2.146E-02
3	1.387E-06	4.216E-02	19	1.238E-06	3.352E-02
4	2.054E-07	4.086E-03	20	1.520E-06	4.667E-02
5	0.000E+00	1.489E-03	21	5.549E-07	7.266E-03
6	2.600E-07	3.924E-03	22	8.930E-07	2.611E-02
7	1.269E-08	4.551E-03	23	8.638E-07	2.262E-02
8	5.424E-07	7.084E-03	24	2.857E-07	1.398E-02
9	4.013E-08	3.474E-03	25	2.636E-08	1.149E-02
10	0.000E+00	4.536E-04	26	2.308E-07	9.206E-03
11	2.579E-07	5.722E-04	27	3.053E-07	2.880E-02
12	0.000E+00	6.518E-04	28	2.831E-09	5.783E-03
13	0.000E+00	8.943E-04	29	9.365E-09	1.858E-02
14	2.179E-07	6.542E-04	30	6.763E-08	2.350E-02
15	3.533E-08	2.536E-02	31	1.166E-06	3.133E-02
16	5.070E-10	6.447E-03		-	

As in the case of the refined cooling water domain model, the extremely low ^{56}Co activities shown in Table 4-20 and Figure 4-35 indicate that the foils in the MCNP model of the thick window experiment experience incident energies below the threshold energy for the $^{58}Ni(p,x)^{56}Co$ reaction. For this reason, the predicted incident energies are not provided for the thick window experiment. The predicted average incident energies for the thin window MCNP model are given in Table 4-21 along with the experimentally predicted energies. These energies are also plotted spatially in Figure 4-36.

Table 4-21: Thin window experimental energies and MCNP predicted average incident energies for the average heat transfer coefficient model.

Foil Number	Incident Energy [MeV]		Foil Number	Incident Energy [MeV]	
	MCNP Model	Experiment		MCNP Model	Experiment
1	25.7532	26.207	17	25.9039	25.908
2	25.8989	27.581	18	25.8462	26.095
3	26.2425	28.522	19	26.0961	26.988
4	25.9578	28.852	20	26.3667	29.517
5	25.7704	28.871	21	25.8640	26.377
6	25.8530	28.464	22	26.3359	30.211
7	25.9222	28.272	23	26.1554	27.793
8	26.1832	28.113	24	25.9076	27.473
9	25.9701	27.824	25	25.8411	27.229
10	25.6024	27.352	26	25.8062	26.899
11	25.6497	27.496	27	26.1170	27.174
12	25.6681	26.368	28	25.7889	-
13	25.7261	25.903	29	25.8828	26.207
14	25.6921	25.867	30	25.9677	26.569
15	25.8934	25.864	31	26.1940	27.672
16	25.8362	25.929		-	

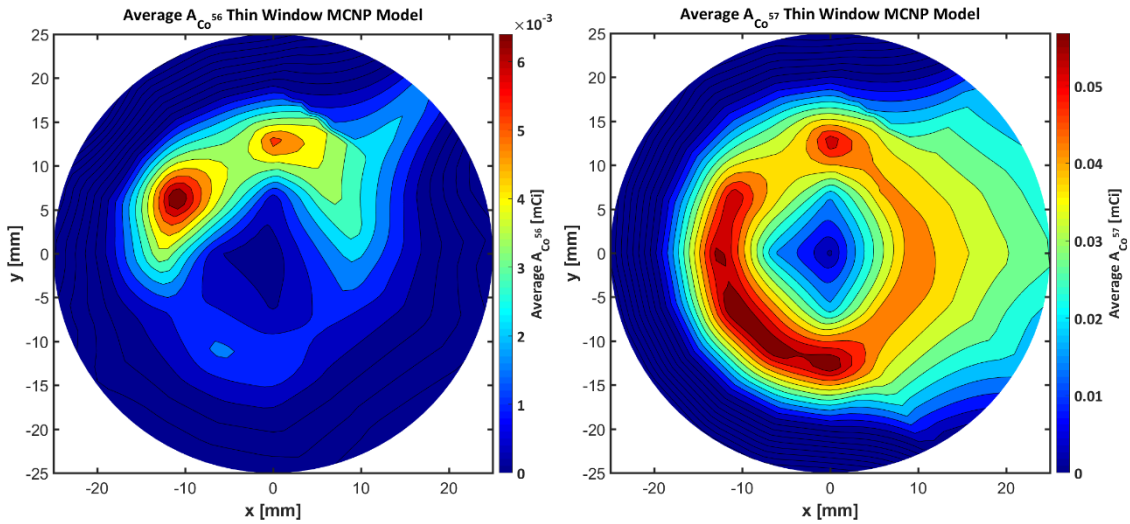

Figure 4-34: Contour plots of ^{56}Co and ^{57}Co activities produced in the MCNP replicated thin window experiment for the average heat transfer coefficient model.

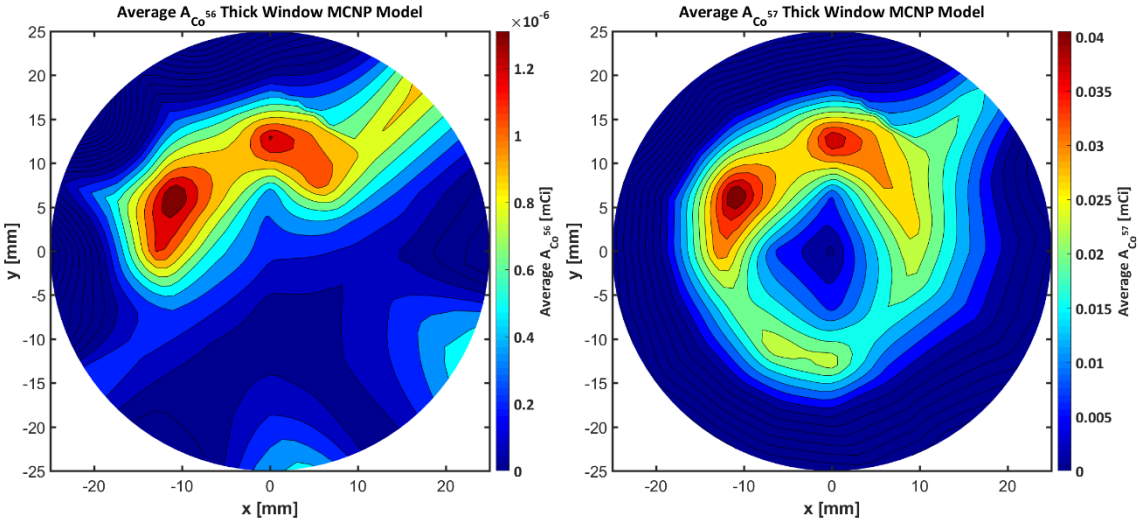

Figure 4-35: Contour plots of ^{56}Co and ^{57}Co activities produced in the MCNP replicated thick window experiment for the average heat transfer coefficient model.

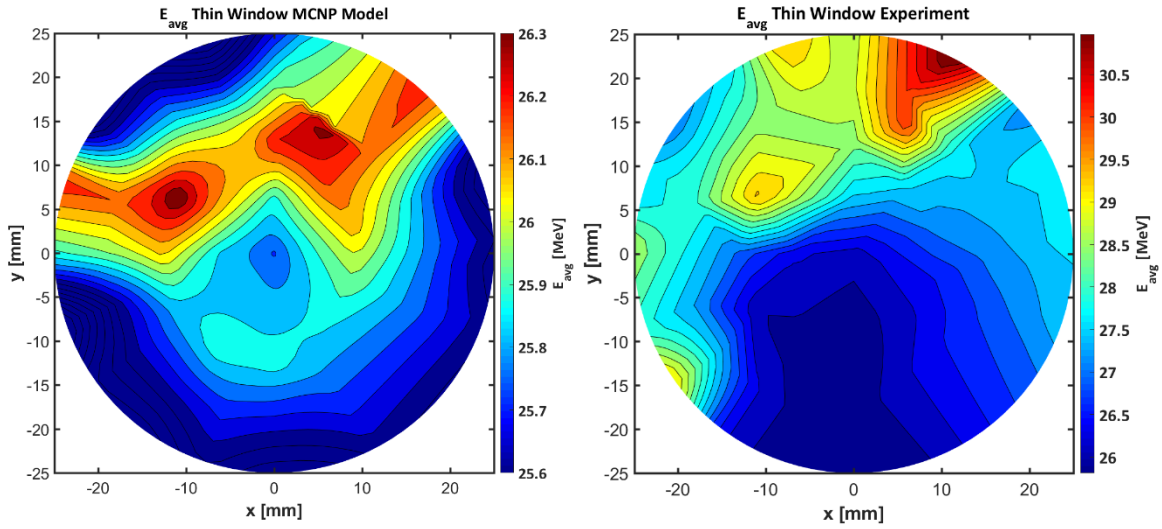

Figure 4-36: Contour plot of average energy incident on front face of ^{58}Ni foils in thin window MCNP average heat transfer coefficient model (L) and experiment (R).

It is again clear from these images that the density distributions predicted by the iterative process between MCNP and ANSYS CFX are significantly higher than those seen in the physical targets. This was also the case when using the refined cooling water domain model's pseudo steady state density distributions. This leads to lower predicted energies incident on the front face of the C-slot bolt-together target, and therefore a lower predicted incident energy on each foil.

The pseudo steady state results for the average heat transfer coefficient model presented in Section 3.2.1 show higher peak temperatures in RbCl targets A and B than those seen in the refined cooling water domain model. Therefore, although the predicted activities and energies follow the same trends, a slightly higher peak energy (by about 0.2 MeV) is seen in Table 4-21 and Figure 4-36 when compared to the predicted energies for the refined cooling water domain model in Table 4-18 and Figure 4-33.

It appears as though the average heat transfer coefficient model again yields results very close to those seen for the refined cooling water domain model. However, a stated previously, void development in the cooling water channels could significantly limit the predictive capabilities of this average heat transfer coefficient model.

CHAPTER 5. UNCERTAINTY QUANTIFICATION

Section 5.1. Overview

Uncertainty quantification is an important aspect of any model validation. Uncertainty quantification requires that physical processes essential to accurately modeling radioisotope targetry be addressed and validation metrics assigned.

Validation metrics provide some measure of agreement between computational and experimental results. A recommended characteristic of these quantities is estimation of the errors inherent in both the computational model and experimental data. This is a function of the assumptions made, the number of experimental replications formulated with a given quality, and the knowledge level of system phenomena. Thus, quantification of uncertainty can often prove difficult in complex systems [42].

Aleatory uncertainty is the inherent variation associated with a physical system or environment. This uncertainty is also classified as stochastic, or irreducible. Material properties, strength, and product dimensions may vary due to manufacturing processes and this contributes to aleatory uncertainties. Epistemic uncertainty is a deficiency in the modeling process due solely to lack of knowledge of a system parameter or phenomena. This is also classified as subjective, or reducible. Epistemic uncertainty is due to a poor understanding of the physical processes at play or material behavior under certain conditions. These sources of uncertainty require that a statistical confidence interval be given for experimental measurements.

To qualify all sources of uncertainty, validation metrics should be used to capture both integral and separate effects. For a complex system, many separate effects impact an integral effect. Therefore, individual behaviors must be examined separately to determine the degree to which they are understood, the uncertainties they contribute, and their overall impact on an integral effect and its associated uncertainty.

Uncertainty quantification is vital to determining the predictive capabilities of any model. To be able to use predictive capabilities of a model, a user must [42]:

1. Identify all relevant sources of uncertainty

2. Characterize each source of uncertainty
3. Estimate numerical solution error in the SRQ of interest (often assumed to be negligible compared to other sources of uncertainty)
4. Estimate uncertainty in the SRQs of interest
5. Update model
6. Conduct sensitivity analysis

Parameter inputs in any computational model have associated uncertainties. However, some input parameters based on experimentally measured values do not have associated confidence intervals or are not well characterized. For parameters with given uncertainties, it is important to understand how thoroughly uncertainties and sensitivities in validation metrics are characterized and propagated through the model. Where provided, uncertainties in input parameters for this model are propagated. This is done in Section 5.3.

Section 5.2. Separation of Problem Components

To address different potential sources of uncertainty and propagate them through the model, it is necessary to divide the problem into subcomponents and identify phenomena in each separate part of the system. This allows for separate effects tests to be performed that then influence the results of integral effects tests. The importance of decomposing phenomena is relevant for pinpointing where knowledge is lacking and where the most effort should be exerted to increase the knowledge base.

Phenomena and parameters important to modeling this system are listed below in Table 5-1 and Table 5-2. This list of relevant phenomena is used to decompose the system into smaller subsystems and problems.

Table 5-1: Relevant problem phenomena.

Relevant Phenomena	
Radiation transport of incident particle beam	Reaction rate Activity
Heat transfer	Conduction Convection Boiling heat transfer
Turbulence	Near-wall behavior Bubble-induced turbulence
Phase change	Porosity/Permeability Buoyancy Melting/Solidification
Phase interactions	Thermal interactions Interfacial tension Mechanical interactions Drag/Lift

Another phenomenon impacting production in radioisotope targetry is human error. Human errors or contaminants introduced will be dependent on the individual and the specific actions taken. These human errors impact nominal system operations as well as experimentally obtained results for validation metrics such as yield.

Table 5-2: Relevant problem parameters.

Relevant Parameters
System Geometry
Boundary Conditions
Initial Conditions
System Physics
Material Properties

The hierarchy given below in Figure 5-1 divides this complex engineering system into progressively simpler tiers. Generally, the top tier is a complete system, followed by subsystem cases, benchmark cases, and then unit problems. It should be noted that many of these subsystems are coupled, e.g. heat transfer is directly influenced by radiation transport and the effectiveness of the target cooling system, while radiation transport is influenced by heat transfer, phase change, and turbulence.

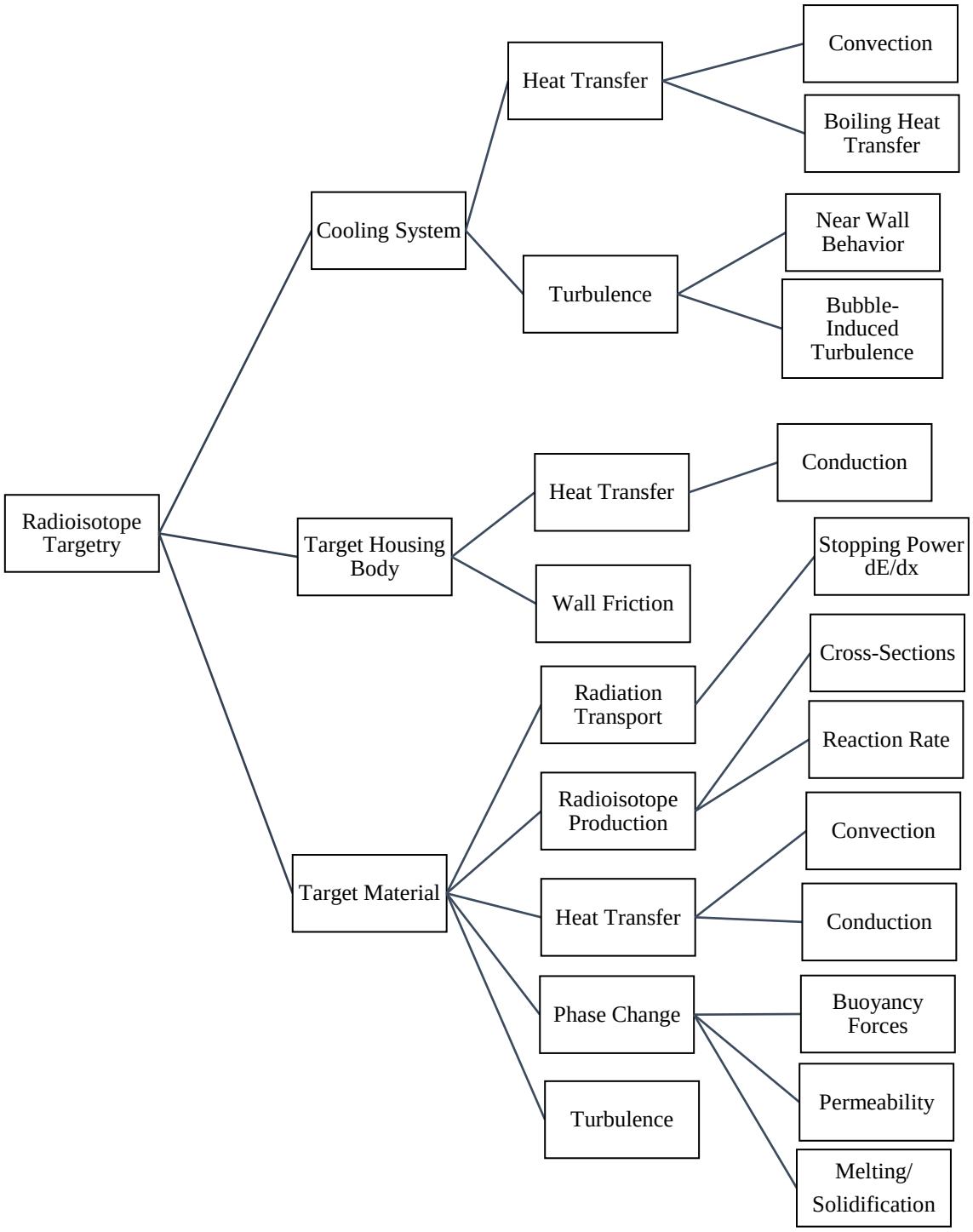

Figure 5-1: Component and phenomenon hierarchy for radioisotope targetry.

MCNP and ANSYS CFX provide independent uncertainty and variance estimates, and ANSYS CFD solutions are not considered converged without reaching a specified tolerance for all thermal hydraulic parameters of interest (velocity, temperature, etc.). To see a more in-depth discussion of the error types inherent in ANSYS CFX, refer to Section 2.1.7.

While each code provides separate uncertainty quantification, interpolation between meshes of the two codes introduces additional sources of uncertainty. It is not possible to create identical meshes as the mesh created in ANSYS is non-uniform and memory limitations in MCNP prevent the division of the target domain into increasingly fine resolutions. However, mesh sensitivity studies should be performed in both ANSYS and MCNP to determine if each mesh is sufficiently fine within the software limitations.

Many thermal properties used for this model have unknown uncertainties and the amount of data available for selection is very small. Accurate, temperature-dependent physical data for all materials are essential to correctly model system behavior. Lack of abundance of existing experimental data and unknown uncertainties leads to significant and unquantifiable errors in any simulation. Without conducting independent experimental measurements of all required data, it is not possible to quantify the associated uncertainty or the data quality. This encompasses thermal material properties such as thermal conductivity, density, and viscosity, as well as certain thermal or physical models that rely on specific material constants.

User-defined models introduce a source of uncertainty into any CFD simulation, particularly when assumptions or simplifications are made. Due to computational requirements a modified macroscale version of the Kozeny-Carman permeability model was used to simulate the transition from solid to molten RbCl (see Section 2.1.4.2). It is not clear to what extent the macroscale modifications impact the validity of the permeability model. In addition, current limitations of the CFD package required that certain physics (including solid rigid body motion) be neglected. These factors inevitably influence the uncertainty inherent in this model in a manner that is not quantifiable.

There are many physical processes at play that impact the solution, from models representing thermal hydraulic behavior to radiation transport. All models specified were

investigated on a unit problem basis where possible to ensure that the correct model was used and accurately captures the appropriate phenomena.

Section 5.3. Examination of Problem Uncertainties

In any experiment, statistical uncertainties exist in all performed measurements. Uncertainty is indicative of the accuracy of experimental values and without associated uncertainties, this data is difficult to interpret. When developing computational models to represent experimental data, uncertainty quantification assists in determining whether a computational model's prediction falls within a range that is reasonable for a given experiment. Without uncertainty, there is no means by which to know if a computational model predicts system behavior with any degree of accuracy.

In many cases, uncertainty can be described using standard deviation. Values of standard deviation indicate how the data is distributed about the mean. A large standard deviation relative to the mean indicates that there is a large spread in the measured data. When this occurs, the mean may not be an accurate representation of the data as a whole.

Several sources of uncertainty present in this model were identified and examined. Error propagation and uncertainty contribution to the overall system are discussed below for each subsystem.

Section 5.3.1. ^{82}Sr Production Uncertainties

In this section sources of uncertainty in the predicted production values are discussed and uncertainty quantification is performed where possible. Using MCNP provided statistics, the error in the MCNP predicted yields is determined via error propagation. Unknowns inherent in the production cross-sections are also discussed. In an attempt to quantify the uncertainty introduced by available production cross-sections, error propagation into cumulative yield data was performed using one set of experimentally measured ^{82}Sr production data.

Section 5.3.1.1. Statistical Uncertainties in MCNP Calculations

All values calculated in MCNP are assigned an associated relative uncertainty. These uncertainties are a measure of the statistical confidence in the results. It should be noted that while they provide a measure of the calculation's precision, they do not provide information

about the accuracy. Large relative uncertainties generally indicate that more particle histories are needed.

Thirty million particle histories were used when calculating the production yields. Error propagation was only performed for the results of the final refined cooling water domain model. It is expected that these uncertainties are representative of those seen for the average heat transfer coefficient model as well.

As shown in Eq. (4-19), MCNP uses a mesh tally to determine the saturation yield in each cell. Each cell also has an associated relative uncertainty provided by MCNP. The true uncertainty is then determined by multiplying the relative uncertainty by the saturation yield.

$$\sigma_{A_{cell_i}} = \sigma_{relative_{cell_i}} A_{cell_i}$$

The cell specific saturation yields are summed over the target domain to determine the net saturation yield. By performing the appropriate uncertainty propagation, the total uncertainty in the MCNP predicted yield may be determined as shown below in Eq. (5-1). Given the large number of cells (~17000) in the mesh tally, a FORTRAN code was utilized for error propagation.

$$A = \sum_{i=1}^{N} A_{cell_i}$$

$$\sigma = \sqrt{\sum_{i=1}^{N} \sigma_{A_{cell_i}}^2} \qquad (5\text{-}1)$$

For proprietary reasons only the relative percent uncertainties in the predicted yields are provided.

Table 5-3: Relative percent uncertainty in MCNP predicted RbCl target A and B yields.

Target	Relative Uncertainty [%]
RbCl Target A	4.46×10^{-3}
RbCl Target B	4.60×10^{-3}

It is clear from Table 5-3 that a sufficient number of particle histories was run when performing these predictions to provide a large degree of confidence in the precision of the results. Therefore statistical uncertainty due to insufficient particle histories is not a source of error in the MCNP predictions.

Section 5.3.1.2. Uncertainties in Production Cross-Sections

An inherent source of uncertainty is evident in the use of excitation functions for yield predictions. Excitation functions are determined via production cross-section measurements, which have associated uncertainties. These uncertainties impact the model-predicted yields, as there will be a range of yields falling within the propagated uncertainty present in the cross-sections. The following image shows a series of data taken for the production of ^{82}Sr using ^{nat}Rb radioisotope targetry.

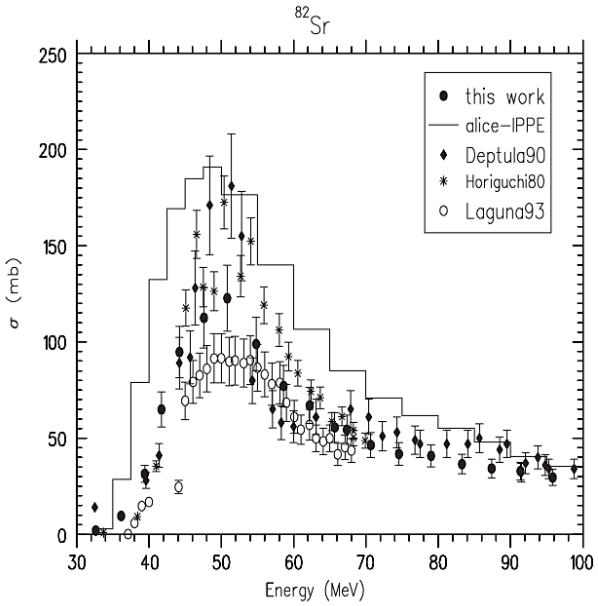

Figure 5-2: Cross-sections (mb) for the production of ^{82}Sr measured in [55] as a function of incident proton energy in MeV.

Also shown are the ALICE-IPPE calculations and other experimental cross-sections found in the literature. It is possible to use stopping power and cross-section data to determine a cumulative yield distribution for the production of ^{82}Sr via the ^{nat}Rb(p,xn)^{82}Sr reaction. The equation for the cumulative saturation yield as determined in Eq. (4-5) in Section 4.2.1 is given below.

$$\frac{R}{I}=\sum_{i=1}^{N_E}\frac{N_A\cdot\sigma(E)}{A}\Delta E$$

Experimentally obtained microscopic cross-sections for any reaction have associated uncertainties. These uncertainties must be propagated through the model. As the cumulative saturation yield is a summation, the rules for error propagation in functions involving addition are as follows.

$$f = Ax + By$$

The variance for a function of this form is:

$$\sigma_f^2 = A^2\sigma_x^2 + B^2\sigma_y^2 + 2AB\sigma_{xy}$$

The standard deviation, or uncertainty, is simply the square root of the variance.

$$\sigma_f = \sqrt{\sigma_f^2}$$

If it is assumed that there is no covariance and that the measured values are independent (uncorrelated), then the standard deviation may be simplified.

$$\sigma_f = \sqrt{A^2\sigma_x^2 + B^2\sigma_y^2}$$

For this specific problem, the uncertainty in the saturation yield may then be calculated as given below in Eq. (5-2).

$$\frac{\sigma_R}{I} = \sqrt{\sum_{i=1}^{N_E}\left[\frac{N_A}{A}\Delta E\sigma_{\sigma_i}\right]^2} = \sqrt{\sum_{i=1}^{N_E}\left[\frac{N_A}{A}\Delta E\right]^2\sigma_{\sigma_i}^2} \qquad (5\text{-}2)$$

In Eq. (5-2) σ_{σ_i} is the uncertainty in the cross-section at a specific energy point i, and $\sigma(E)$ is the microscopic cross-section at a specified energy.

Propagating the uncertainty in the cross-section data will give error bounds for the yield data. This error propagation was done using one set of cross-section data for the $Rb^{nat}(p,xn)Sr^{82}$ reaction given in Figure 5-2 [55] and is shown below in Figure 5-3.

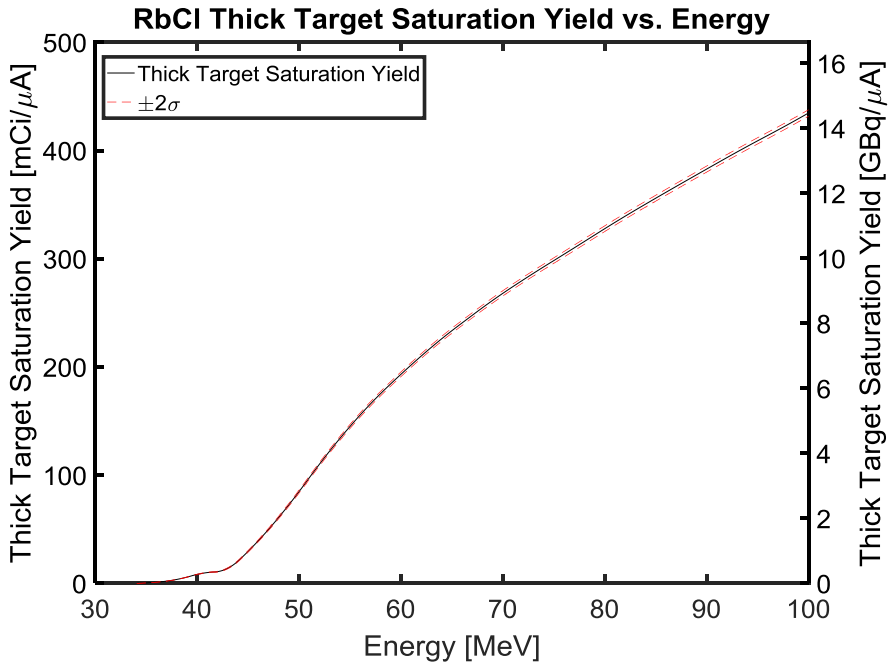

Figure 5-3: Cumulative yield data for the $^{nat}Rb(p,xn)^{82}Sr$ reaction as a function of energy and 2σ confidence interval.

Many sets of experimental data exist, see Figure 5-2 and Figure 4-1, with differing average values and associated errors. Unfortunately, neither the IAEA recommended curve fit from Figure 4-1 nor the standard deviation of the fit are provided by the IAEA database. As a result, the recommended fit quality and associated uncertainty is not quantifiable.

However, propagation of the uncertainties present in one set of experimental data as done here provides some bound by which to quantify the propagated error in the activities. Given the numerical errors introduced by the use of and translation between two different computational software codes, it is expected that the contribution of this uncertainty to the total error in the computational results will be relatively small.

Section 5.3.2. ^{58}Ni Experiment Uncertainties

Error propagation performed for activity measurements of the ^{58}Ni foil experiments is discussed here. In addition, a parameter analysis was performed for the functional fits used for the experimental ^{56}Co and ^{57}Co cross-section data. The analysis of the fit provides confidence intervals of the fit and parameter values as well as insight into parameter sensitivity.

The uncertainty in the cross-section fits was used to determine their impact on the uncertainty in the MCNP predicted $^{57}Co/^{56}Co$ activity ratios. The statistical uncertainties in the MCNP calculated ^{56}Co and ^{57}Co activities and the overall uncertainty in their activity ratios are also provided and compared with the uncertainties introduced by the cross-section fits.

Section 5.3.2.1. Radioactivity Uncertainty Quantification

When observing a given photo emission peak, the associated standard deviation may be calculated using the square root of the number of counts, *N* [52].

$$\sigma_N = \sqrt{N} \tag{5-3}$$

The count rate is determined by dividing the net number of counts by the total live counting time, as discussed in Section 4.3.1.2 and the associated standard deviation is shown below.

$$\sigma_C = \frac{\sigma_N}{t_{live}} = \frac{\sqrt{N}}{t_{live}} \tag{5-4}$$

The uncertainty in the calculated source count rate is determined via error propagation using Eq. (4-29) and the associated detector uncertainty given in Table 4-9.

$$\sigma_{CR_{net}} = CR_{net}\sqrt{\left(\frac{\sigma_C}{C}\right)^2 + \left(\frac{\sigma_{\epsilon_{detector}}}{\epsilon_{detector}}\right)^2} \tag{5-5}$$

The associated uncertainty in the measured activity of each isotope may then be determined. The activity as determined in Eq. (4-32) in Section 4.3.1.2 is shown again below to more clearly outline the error propagation process.

$$A = \frac{\left[CR_{net}\left[\frac{\text{decay}}{\text{min}}\right]\cdot\frac{1\text{ min}}{60\text{ s}}\cdot\left[\frac{1}{\gamma_{intensity}}\right]\cdot\left[\frac{1\text{ Bq}}{1\frac{\text{decay}}{\text{s}}}\right]\cdot\left[\frac{1\text{ Ci}}{3.7\times10^{10}\text{Bq}}\right]\right]}{exp\left[-\lambda\left[\frac{1}{\text{s}}\right]\cdot(t_{EOB}-t)[s]\right]}$$

The half-life of each radioisotope and its associated uncertainty is given in Table 4-6 in Section 4.3.1.2. In order to determine the uncertainty in the decay constants, error propagation must be performed. The equation for the decay constant defined in Eq. (4-7) is of the form shown below.

$$f = aY^b$$

The error for an equation of this form is then propagated as shown.

$$\sigma_f = \left| abY^{b-1}\sigma_Y \right| = \left| \frac{fb\sigma_Y}{Y} \right|$$

Given the equation for the decay constant of a radioisotope, b = -1 and a = ln(2), this becomes:

$$\sigma_\lambda = \left| \frac{\lambda\sigma_{t_{\frac{1}{2}}}}{t_{1/2}} \right| = \left| \frac{\frac{ln(2)}{t_{\frac{1}{2}}}\cdot\sigma_{t_{\frac{1}{2}}}}{t_{1/2}} \right| = \left| \frac{ln(2)\cdot\sigma_{t_{\frac{1}{2}}}}{\left(t_{\frac{1}{2}}\right)^2} \right| \quad (5\text{-}6)$$

The intensity of each emitted gamma also has a given uncertainty that must be taken into account. The gamma intensities and associated uncertainties are provided in Table 4-8 in Section 4.3.1.2.

The information shown in Table 4-6 and Table 4-8 was taken from the NNDC database [53,54]. In order to propagate the uncertainty in the activity, it is necessary to divide Eq. (4-32) up into smaller functions. For example, taking the denominator independently allows for definition of an individual function and propagation of the error associated with that form.

$$f_{bottom} = \exp\left(-\lambda\cdot(t_{EOB}-t)\right) \quad (5\text{-}7)$$

This can be described by the form:

$$f = a\cdot\exp(Yb)$$

The error for a function of this form is determined as shown below.

$$\sigma_f = |fb\sigma_Y|$$

When applying this to the equation of interest with a = 1, b = - (t_{EOB}-t), and $Y = \lambda$, the standard deviation is calculated as shown in Eq. (5-8).

$$\sigma_{f_{bottom}} = \left| exp\left(-\lambda(t_{EOB}-t)\right)\cdot-(t_{EOB}-t)\cdot\sigma_\lambda \right| \quad (5\text{-}8)$$

Another variable with associated uncertainty is the intensity of each gamma and the source strength, CR_{net}. By separating out the top of the fraction, it is possible to obtain another function and associated error.

$$f_{top} = \frac{aCR_{net}}{\gamma_{intensity}} \quad (5\text{-}9)$$

For a function of the ratio of two values with associated uncertainties as shown in Eq. (5-9), the standard deviation can be determined as given below.

$$f = \frac{aA}{B}$$

$$\sigma_f = |f| \sqrt{\left[\left(\frac{a\sigma_A}{aA}\right)^2 + \left(\frac{\sigma_B}{B}\right)^2 - \frac{2a\sigma_{AB}}{aAB}\right]}$$

Applying this to the function of interest and assuming no covariance, Eq. (5-10) may be formulated.

$$\sigma_{f_{top}} = \left|\frac{aCR_{net}}{\gamma_{intensity}}\right| \sqrt{\left[\left(\frac{a\sigma_{CR_{net}}}{aCR_{net}}\right)^2 + \left(\frac{\sigma_\gamma}{\gamma_{intensity}}\right)^2\right]} \tag{5-10}$$

These two functions may be utilized to obtain a simpler form of the activity equation.

$$A = \frac{f_{top}}{f_{bottom}} \tag{5-11}$$

Here the constant *a* is:

$$a = \left[\frac{1 \text{ min}}{60 \text{ s}}\right] \cdot \left[\frac{1 \text{ Bq}}{1\frac{\text{decay}}{\text{s}}}\right] \cdot \left[\frac{1 \text{ Ci}}{3.7\times10^{10}\text{Bq}}\right]$$

Using the appropriate form given previously for propagating error when dividing two terms, the standard deviation below is obtained.

$$\sigma_A = |A| \sqrt{\left(\frac{\sigma_{f_{top}}}{f_{top}}\right)^2 + \left(\frac{\sigma_{f_{bottom}}}{f_{bottom}}\right)^2}$$

$$\sigma_A = \frac{f_{top}}{f_{bottom}} \sqrt{\left(\frac{\sigma_{f_{top}}}{f_{top}}\right)^2 + \left(\frac{\sigma_{f_{bottom}}}{f_{bottom}}\right)^2} \tag{5-12}$$

These equations are then used in determining the uncertainty in the activity ratio. As there are four monitored photon emissions, two each from ^{56}Co and ^{57}Co, four activity ratios and uncertainties are calculated. The uncertainty in the activity ratios is determined by propagating the associated uncertainty in each measured activity.

$$R = \frac{A_{57_{Co}}}{A_{56_{Co}}}$$

$$\left(\frac{\sigma_R}{R}\right)^2 = \left(\frac{\sigma_{56_{Co}}}{A_{56_{Co}}}\right)^2 + \left(\frac{\sigma_{57_{Co}}}{A_{57_{Co}}}\right)^2 \tag{5-13}$$

$$\sigma_R = R\sqrt{\left(\frac{\sigma_{56_{Co}}}{A_{56_{Co}}}\right)^2 + \left(\frac{\sigma_{57_{Co}}}{A_{57_{Co}}}\right)^2} \tag{5-14}$$

The average activity ratio and associated standard deviation are given below and in Eq. (5-15).

$$\overline{R}_A = \frac{R_{A_1}+R_{A_2}+R_{A_3}+R_{A_4}}{4}$$

$$\sigma_{\overline{R}_A} = \frac{1}{4}\sqrt{\sigma^2_{R_{A_1}}+\sigma^2_{R_{A_2}}+\sigma^2_{R_{A_3}}+\sigma^2_{R_{A_4}}} \tag{5-15}$$

Calculations to determine the average predicted activity produced in each foil and standard deviation are shown below.

$$\overline{A} = \frac{A_1+A_2}{2} \tag{5-16}$$

$$\sigma_{\overline{A}} = \frac{1}{2}\sqrt{\sigma^2_{A_1}+\sigma^2_{A_2}} \tag{5-17}$$

The uncertainty in the mean could be determined by taking the standard deviation and dividing it by the square root of the number of samples.

$$u_{\overline{R}_A} = \frac{\sigma_{\overline{R}_A}}{\sqrt{4}} = \frac{\sigma_{\overline{R}_A}}{2} \tag{5-18}$$

$$u_{\overline{A}} = \frac{\sigma_{\overline{A}}}{\sqrt{2}} \tag{5-19}$$

The propagated standard deviation in each predicted average foil activity and activity ratio is given in Table 5-4 and Table 5-5 for the thin and thick window experiments, respectively. It was not possible to determine the uncertainty in the predicted incident energy, as this was done using interpolation between two non-linear excitation function fits.

Table 5-4: Average activities of ^{56}Co and ^{57}Co with associated standard deviations for the thin window experiment.

Thin Window Experiment				
Foil Number	$\bar{A}_{56_{Co}}$ **[mCi]**	$\sigma_{\bar{A}_{56_{Co}}}$ **[mCi]**	$\bar{A}_{57_{Co}}$ **[mCi]**	$\sigma_{\bar{A}_{57_{Co}}}$ **[mCi]**
1	5.3380E-04	5.6836E-06	8.8750E-03	7.3992E-05
2	7.0132E-03	7.4919E-05	2.0051E-02	1.6491E-04
3	1.2771E-02	1.3674E-04	1.9290E-02	1.5863E-04
4	3.3775E-03	3.6106E-05	5.0781E-03	4.1679E-05
5	4.0388E-03	4.3114E-05	5.8070E-03	4.7541E-05
6	5.0946E-03	5.4640E-05	9.0927E-03	7.4396E-05
7	6.8601E-03	7.3449E-05	1.2432E-02	1.0188E-04
8	8.6515E-03	9.2592E-05	1.6890E-02	1.3885E-04
9	9.6917E-03	1.0363E-04	2.3046E-02	1.8997E-04
10	8.1217E-03	8.6842E-05	2.8186E-02	2.3258E-04
11	9.8603E-03	8.2627E-05	3.4778E-02	2.8679E-04
12	4.8139E-03	4.0370E-05	3.6774E-02	3.0323E-04
13	8.6815E-04	9.2958E-06	3.3253E-02	2.7461E-04
14	6.5967E-04	7.0639E-06	3.4105E-02	2.8134E-04
15	2.7350E-04	2.9066E-06	1.4760E-02	1.2119E-04
16	9.3890E-05	1.0252E-06	3.8722E-03	3.2010E-05
17	3.2724E-04	3.5402E-06	1.2379E-02	1.0142E-04
18	1.4528E-03	1.5531E-05	2.0366E-02	1.6776E-04
19	5.5001E-03	5.8862E-05	2.6488E-02	2.1834E-04
20	2.2712E-02	1.9033E-04	2.9452E-02	2.4278E-04
21	8.4996E-04	9.0766E-06	8.5851E-03	7.0231E-05
22	1.1336E-02	9.4948E-05	1.1226E-02	9.2492E-05
23	4.8494E-03	5.1939E-05	1.2257E-02	1.0039E-04
24	4.6342E-03	4.9514E-05	1.4640E-02	1.2022E-04
25	5.4265E-03	5.8090E-05	2.0769E-02	1.7092E-04
26	5.1456E-03	5.4932E-05	2.7060E-02	2.2304E-04
27	7.0783E-03	7.5668E-05	2.8686E-02	2.3657E-04
28	-	-	-	-
29	1.4701E-03	1.2312E-05	1.6130E-02	1.3290E-04
30	3.5551E-03	3.8012E-05	2.6942E-02	2.2238E-04
31	9.8219E-03	1.0512E-04	2.6298E-02	2.1698E-04

Table 5-5: Average activities of ^{56}Co and ^{57}Co with associated standard deviations for the thick window experiment.

Thick Window Experiment				
Foil Number	$\bar{A}_{56_{Co}}$ **[mCi]**	$\sigma_{\bar{A}_{56_{Co}}}$ **[mCi]**	$\bar{A}_{57_{Co}}$ **[mCi]**	$\sigma_{\bar{A}_{57_{Co}}}$ **[mCi]**
1	1.1485E-04	9.6567E-07	2.1749E-03	1.7909E-05
2	1.6041E-03	1.3437E-05	2.7405E-02	2.2569E-04
3	6.7936E-03	5.6921E-05	3.4360E-02	2.8314E-04
4	2.3886E-03	2.0006E-05	7.5897E-03	6.2436E-05
5	3.1185E-03	2.6123E-05	9.7179E-03	7.9924E-05
6	2.5355E-03	2.1238E-05	1.3173E-02	1.0853E-04
7	2.6740E-03	2.2400E-05	1.8949E-02	1.5548E-04
8	3.0414E-03	2.5480E-05	2.6931E-02	2.2178E-04
9	2.0112E-03	1.6856E-05	2.3186E-02	1.9109E-04
10	1.5952E-03	1.3370E-05	2.8180E-02	2.3189E-04
11	8.3742E-04	7.0153E-06	3.4670E-02	2.8534E-04
12	3.1235E-04	2.6219E-06	3.4618E-02	2.8533E-04
13	1.5277E-04	1.2880E-06	2.2762E-02	1.8741E-04
14	1.2458E-04	1.0491E-06	1.7891E-02	1.4732E-04
15	1.3371E-04	1.1241E-06	1.1660E-02	9.5953E-05
16	1.1700E-04	9.8385E-07	1.7995E-03	1.4818E-05
17	1.4664E-04	1.2325E-06	1.1459E-02	9.4097E-05
18	1.2239E-03	1.0252E-05	3.9634E-02	3.2630E-04
19	1.9674E-03	1.6486E-05	4.0801E-02	3.3582E-04
20	3.3361E-03	2.7946E-05	3.8113E-02	3.1379E-04
21	1.7565E-04	1.4788E-06	1.4315E-02	1.1778E-04
22	2.5257E-03	2.1154E-05	1.9428E-02	1.6013E-04
23	1.3976E-03	1.1721E-05	1.9177E-02	1.5792E-04
24	1.0311E-03	8.6387E-06	2.1698E-02	1.7851E-04
25	1.0244E-03	8.5843E-06	3.1010E-02	2.5559E-04
26	6.6565E-04	5.5791E-06	3.5035E-02	2.8838E-04
27	1.0714E-03	8.9812E-06	3.7220E-02	3.0641E-04
28	1.9655E-04	1.6537E-06	2.7452E-02	2.2596E-04
29	1.5691E-04	1.3178E-06	1.3789E-02	1.1349E-04
30	4.3772E-04	3.6695E-06	3.0464E-02	2.5079E-04
31	2.3428E-03	1.9630E-05	3.7350E-02	3.0762E-04

Table 5-6: Average activity ratio, standard deviation, and percent uncertainty for the thick and thin window experiments.

Foil Number	Thin Window Experiment			Thick Window Experiment		
	$\bar{R}_A$	$\sigma_{\bar{R}_A}$	% Uncertainty	$\bar{R}_A$	$\sigma_{\bar{R}_A}$	% Uncertainty
1	52.3426	0.5906	1.128	18.9694	0.1582	0.834
2	9.3644	0.1023	1.092	17.0891	0.1421	0.832
3	5.0756	0.0556	1.095	5.0578	0.0420	0.830
4	4.9634	0.0548	1.104	3.1785	0.0264	0.831
5	4.6708	0.0513	1.098	3.1166	0.0259	0.831
6	6.1180	0.0674	1.102	5.1967	0.0432	0.831
7	6.0890	0.0666	1.094	7.0871	0.0588	0.830
8	6.5298	0.0714	1.093	8.8551	0.0736	0.831
9	7.8683	0.0861	1.094	11.5287	0.0958	0.831
10	11.4870	0.1258	1.095	17.6652	0.1467	0.830
11	3.5271	0.0293	0.831	41.4328	0.3445	0.831
12	7.6410	0.0635	0.831	110.8322	0.9218	0.832
13	128.5606	1.4137	1.100	149.2852	1.2421	0.832
14	173.5075	1.9084	1.100	143.6581	1.1955	0.832
15	165.9938	1.8150	1.093	87.6685	0.7327	0.836
16	175.5386	2.0647	1.176	15.3900	0.1282	0.833
17	143.6597	1.5996	1.113	78.6051	0.6565	0.835
18	46.2505	0.5065	1.095	32.3966	0.2693	0.831
19	16.0969	0.1764	1.096	20.7388	0.1723	0.831
20	1.2968	0.0108	0.833	11.4254	0.0949	0.831
21	32.8824	0.3595	1.093	81.5843	0.6783	0.831
22	0.9904	0.0082	0.828	7.6941	0.0640	0.832
23	8.5254	0.0933	1.094	13.7237	0.1140	0.831
24	10.3664	0.1132	1.092	21.0494	0.1749	0.831
25	12.8328	0.1405	1.095	30.2744	0.2517	0.831
26	17.0952	0.1868	1.093	52.6404	0.4375	0.831
27	13.3787	0.1464	1.094	34.7405	0.2886	0.831
28	-	-	-	139.7744	1.1621	0.831
29	10.9747	0.0912	0.831	88.0965	0.7346	0.834
30	25.0658	0.2746	1.096	69.6230	0.5790	0.832
31	8.9627	0.0982	1.096	15.9428	0.1325	0.831

These propagated uncertainties provide a range of acceptable activity values within which computational results may fall and be considered accurate. The uncertainties are no more than 2% of the predicted value, indicating that the range of acceptable activity ratios is reasonably small. However, these uncertainties do not take into account the cumulative cross-section curve and the fraction of particles that fall below the threshold energy for the production of ^{56}Co.

Section 5.3.2.2. Uncertainties in Cross-Section Fitting

Another uncertainty associated with this experiment is the approximation of cross-section data for ^{56}Co and ^{57}Co when using a fitting function. The fit of the cumulative cross-section data for the production of ^{56}Co and ^{57}Co has an associated error bounding the experimental data. The fits used for this experiment were developed by the individuals who performed the experiment, but no sensitivity analysis was done. Any fit used to describe experimental data has the form shown below.

$$Y_i = f(X_i, q) + \varepsilon_i$$

ε_i describes the error associated with the fit when computing the experimentally measured value.

^{56}Co Excitation Function

For the ^{56}Co cross-sections, a polynomial fit was used, given in Eq. (4-23).

$$\sigma_{56_{Co}} = a \cdot E^3 + b \cdot E^2 + c \cdot E + d$$

The nominal set of parameters for this fit are given below.

$$q = [\bar{a}, \bar{b}, \bar{c}, \bar{d}] = [-0.1696,\ 16.3867,\ -495.434,\ 4788.05]$$

When a fit's parameters are separable, as is the case for the ^{56}Co excitation function, it may be described using the following form [56].

$$Y = X \cdot q_0 + \varepsilon \tag{5-20}$$

Each component of this equation represents a matrix system of the form shown below.

$$Y = \begin{bmatrix} y_1 \\ \vdots \\ y_n \end{bmatrix} \quad ; \quad X = \begin{bmatrix} x_{11} & \cdots & x_{1p} \\ \vdots & \ddots & \vdots \\ x_{n1} & \cdots & x_{np} \end{bmatrix} \quad ; \quad q_0 = \begin{bmatrix} q_1 \\ \vdots \\ q_p \end{bmatrix} \quad ; \quad \varepsilon = \begin{bmatrix} \varepsilon_1 \\ \vdots \\ \varepsilon_n \end{bmatrix}$$

Here ϒ represents the experimental data set of size n, X is the dependent variable of the data set, q_0 is the parameter set of size p used to fit the experimental data, and ε is the associated error between the fit $X \cdot q_0$ and the experimental data ϒ. When fitting cross-section data as a function of energy, the above equation becomes:

$$\sigma = E \cdot q_0 + \varepsilon \tag{5-21}$$

$$\sigma = \begin{bmatrix} \sigma_1 \\ \vdots \\ \sigma_n \end{bmatrix} \quad ; \quad E = \begin{bmatrix} E_{11} & \dots & E_{1p} \\ \vdots & \ddots & \vdots \\ E_{n1} & \dots & E_{np} \end{bmatrix} \quad ; \quad q_0 = \begin{bmatrix} q_1 \\ \vdots \\ q_p \end{bmatrix} \quad ; \quad \varepsilon = \begin{bmatrix} \varepsilon_1 \\ \vdots \\ \varepsilon_n \end{bmatrix}$$

For Co^{56}, Eq. (5-21) can be described as shown below.

$$\sigma_{56_{Co}} = \begin{bmatrix} \sigma_{1_{56_{Co}}} \\ \vdots \\ \sigma_{n_{56_{Co}}} \end{bmatrix} \quad ; \quad E = \begin{bmatrix} E_1^3 & E_1^2 & E_1 & 1 \\ \vdots & \vdots & \vdots & \vdots \\ E_n^3 & E_n^2 & E_n^2 & 1 \end{bmatrix} \quad ; \quad q_{0_{56_{CFo}}} = \begin{bmatrix} a \\ b \\ c \\ d \end{bmatrix} \quad ; \quad \varepsilon_{56_{Co}} = \begin{bmatrix} \varepsilon_{1_{56_{Co}}} \\ \vdots \\ \varepsilon_{n_{56_{Co}}} \end{bmatrix}$$

This experimental cross-section data and corresponding fit is shown below in Figure 5-4.

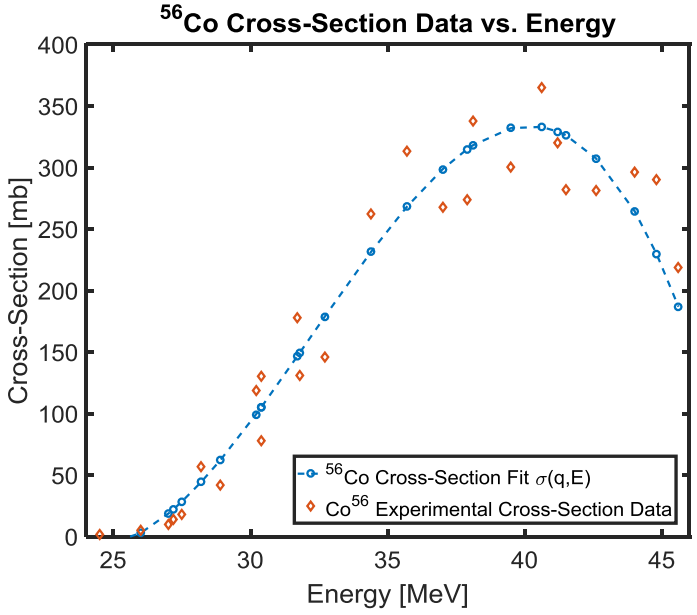

Figure 5-4: Cross-section fit for ^{56}Co plotted with experimental data.

The variance estimate of this fit is determined by the following equation [56]:

$$\sigma^2 = \frac{1}{n - p} R^T R \tag{5-22}$$

This is the equivalent of the form shown below in Eq. (5-23).

$$\sigma^2 = \frac{\sum_{i=1}^{n}\left(\sigma_{i_{56_{Co}}} - f_{\sigma_{56_{Co}}}(E_i)\right)}{n - p} \tag{5-23}$$

Here the residual $R_{56_{Co}} = \sigma_{56_{Co}} - E \cdot q_{0_{56_{Co}}} = \varepsilon_{56_{Co}}$. The residuals are plotted as a function of energy in Figure 5-5. The variance and standard deviation were found to be:

$$\sigma^2_{56_{Co}} = 975.5897$$

$$\sigma_{56_{Co}} = 31.2184$$

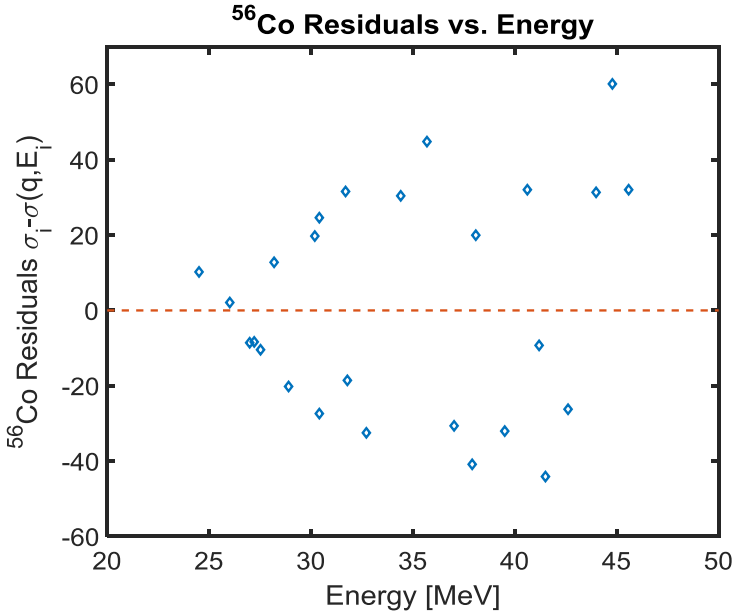

Figure 5-5: Residuals of ^{56}Co cross-section fit and experimental data in millibarns.

Confidence intervals indicated a range over which the observation value may fall 95% of the time. The confidence interval should align well with $\pm 2\sigma$ of the distribution, depending on the number of parameters and the sample size. For $n = 26$, $p = 4$, $n - p = 22$, and a two-tailed distribution with an $\alpha = 0.05$, confidence interval tables may be used to determine the appropriate value $t_{n-p,\frac{\alpha}{2}}$ [57].

$$t_{n-p,1-\frac{\alpha}{2}} = 2.0739$$

This yields a confidence interval very close to the 2σ that would encompass 95% of a Gaussian distribution. If the residuals from Figure 5-5 are plotted with a bound of

$t_{n\text{-}p,\frac{\alpha}{2}} \cdot \sigma_{56_{Co}} = 64.7438$, such that $\varepsilon_i = R_i \in \left[-2.0739\sigma_{56_{Co}}, 2.0739\sigma_{56_{Co}}\right]$, it can be seen that all residuals fall within the specified 95% confidence interval. This is demonstrated in Figure 5-6.

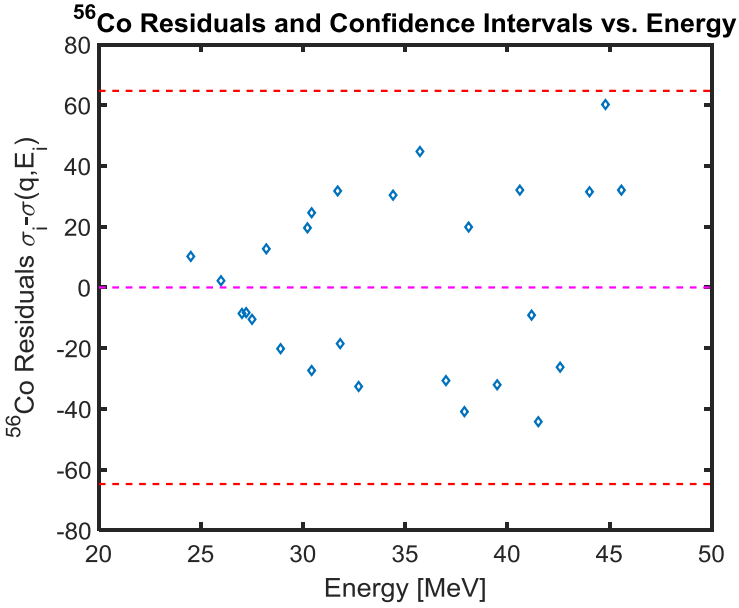

Figure 5-6: ^{56}Co residuals and 95% confidence intervals as a function of energy.

The 95% confidence intervals are plotted against both the function and the experimental data points in Figure 5-7.

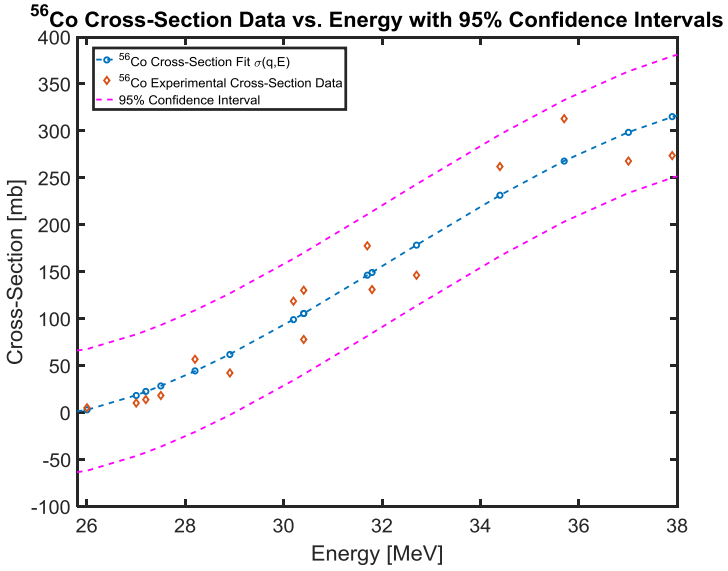

Figure 5-7: ^{56}Co 95% confidence intervals plotted with the fit and experimental data.

Given the system variance the covariance matrix may be calculated using known uncertainty quantification theory [56].

$$V_{56_{Co}} = \sigma_{56_{Co}} \left(E^T E\right)^{-1} \tag{5-24}$$

The covariance matrix for ^{56}Co was found to be:

$$V_{56_{Co}} = \begin{bmatrix} 9.4100\times10^{-4} & -0.0993 & -0.0993 & -38.6735 \\ -0.0993 & 10.5058 & -363.8403 & 4.1201\times10^{3} \\ 3.4265 & -363.8403 & 1.2644\times10^{4} & -1.4369\times10^{5} \\ -38.6735 & 4.1201\times10^{3} & -1.4369\times10^{5} & 1.6387\times10^{6} \end{bmatrix}$$

The variance and standard deviation for each parameter are taken from the diagonal entries in the covariance matrix.

$$\sigma_a^2 = 9.41\times10^{-4} \quad ; \quad \sigma_b^2 = 10.5058 \quad ; \quad \sigma_c^2 = 1.2644\times10^{4} \quad ; \quad \sigma_d^2 = 1.6387\times10^{6}$$

$$\sigma_a = 0.0307 \quad ; \quad \sigma_b = 3.2413 \quad ; \quad \sigma_c = 112.4455 \quad ; \quad \sigma_d = 1.2801\times10^{3}$$

If the same 95% percent confidence interval given above is utilized, confidence intervals for each parameter may be determined as shown below.

$$a \in [\bar{a} - 2.0739\cdot\sigma_a,\ \bar{a}+2.0739\cdot\sigma_a] = [-0.2333, -0.1059]$$

$$b \in [\bar{b} - 2.0739\cdot\sigma_b,\ \bar{b}+2.0739\cdot\sigma_b] = [9.6646, 23.1088]$$

$$c \in [\bar{c} - 2.0739\cdot\sigma_c,\ \bar{c}+2.0739\cdot\sigma_c] = [-728.6337, -262.2343]$$

$$d \in \left[\bar{d} - 2.0739 \cdot \sigma_d,\ \bar{d} + 2.0739 \cdot \sigma_d\right] = \left[2.1333 \times 10^3,\ 7.4428 \times 10^3\right]$$

To more clearly see the model's sensitivity to each parameter, the analytic derivative with respect to each parameter is determined.

$$\frac{\partial \sigma_{56_{Co}}}{\partial a} = E^3$$

$$\frac{\partial \sigma_{56_{Co}}}{\partial b} = E^2$$

$$\frac{\partial \sigma_{56_{Co}}}{\partial c} = E$$

$$\frac{\partial \sigma_{56_{Co}}}{\partial d} = 1$$

As expected, the function is progressively less sensitive to each parameter and clearly most sensitive to parameter *a*.

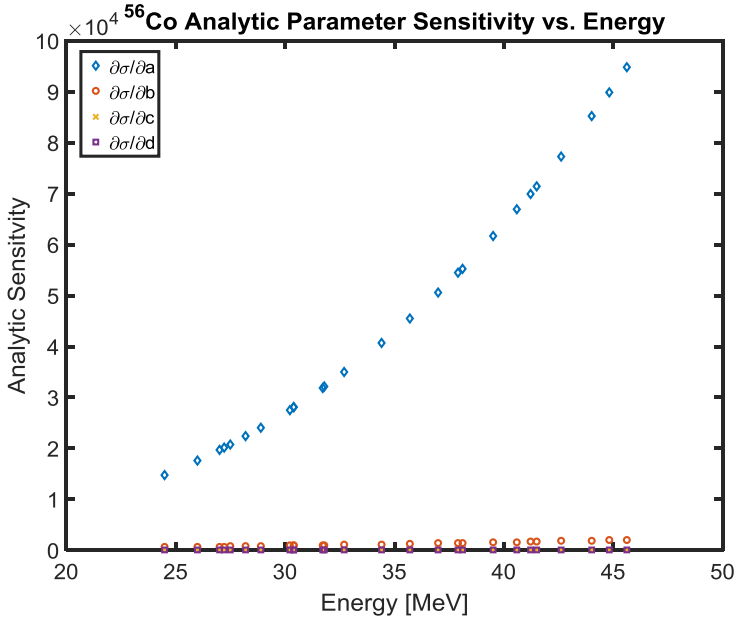

Figure 5-8: Analytic sensitivities of parameters for ^{56}Co fit.

^{57}Co Excitation Function

A non-linear fit was used to model experimental ^{57}Co cross-sections. The fit was defined in Eq. (4-24).

$$\sigma_{57_{Co}}(E) = 1000 \cdot \left\{ \frac{\left[A_5 + \frac{A_2}{[(A_4 - A_3 \cdot E)^2 + 1]} \right]}{\left[E \cdot exp\left(\frac{A_1}{\sqrt{E}} \right) - 1 \right]} \right\}$$

The set of nominal parameter values for this model are:

$$q = [\overline{A}_1, \overline{A}_3, \overline{A}_2, \overline{A}_4, \overline{A}_5] = [35.5206, 32287.0123, 0.1891, 3.6304, 0.0060]$$

This fit is shown with the experimental data in Figure 5-9.

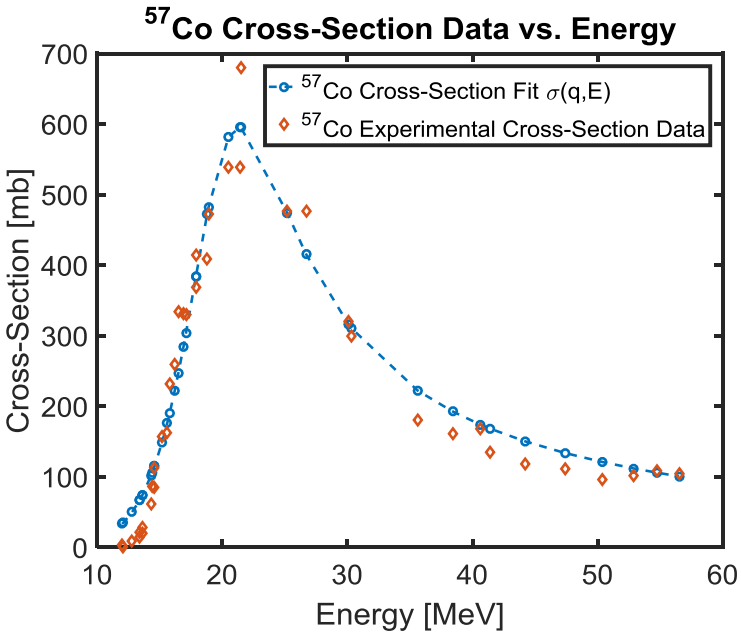

Figure 5-9: Cross-section fit for ^{57}Co plotted with experimental data.

When the dependent variables and parameters are not separable, as is the case for the ^{57}Co excitation function, the residual is calculated by:

$$R_{57_{Co}} = \sigma_{57_{Co}} - f_{57_{Co}}\left(E, q_{57_{Co}}\right) \tag{5-25}$$

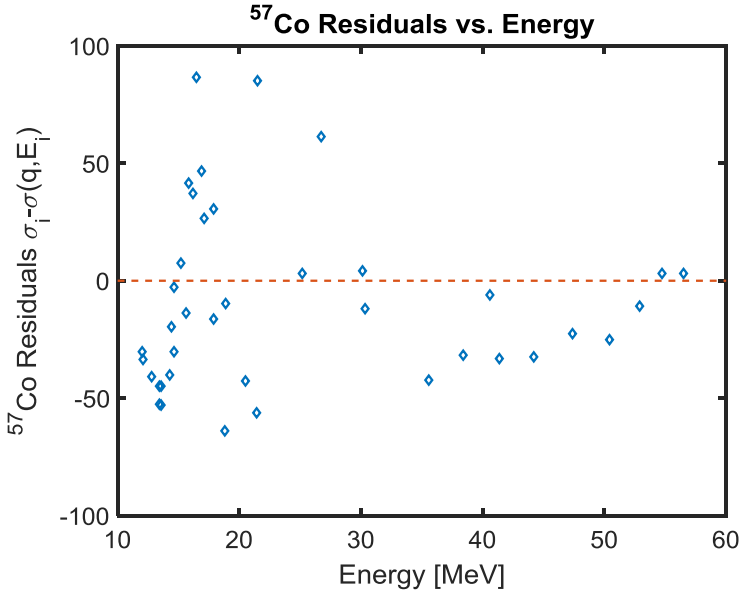

Figure 5-10: Residuals of ^{56}Co cross-section fit and experimental data in millibarns.

It can be seen from the residual plot of the errors ε_i in Figure 5-10 that the errors are not correlated. The system variance may be calculated using Eq. (5-22).

$$\sigma^2_{57_{Co}} = 1701.4098$$

$$\sigma_{57_{Co}} = 41.2481$$

For $n = 39$, $p = 5$, $n - p = 34$, and assuming a two-tailed distribution with an $\alpha = 0.05$, 95% confidence interval tables may be used to determine the appropriate value $t_{n\text{-}p,\frac{\alpha}{2}}$ [57].

$$t_{n\text{-}p,1\text{-}\frac{\alpha}{2}} = 2.0322$$

The residuals, or errors, may then be plotted with the appropriate confidence interval of $\pm\, t_{n\text{-}p,\,1\text{-}\frac{\alpha}{2}}\sigma_{57_{Co}} = 83.8244$. This is, again, very close to the $\pm\, 2\sigma_{57_{Co}} = 82.4962$.

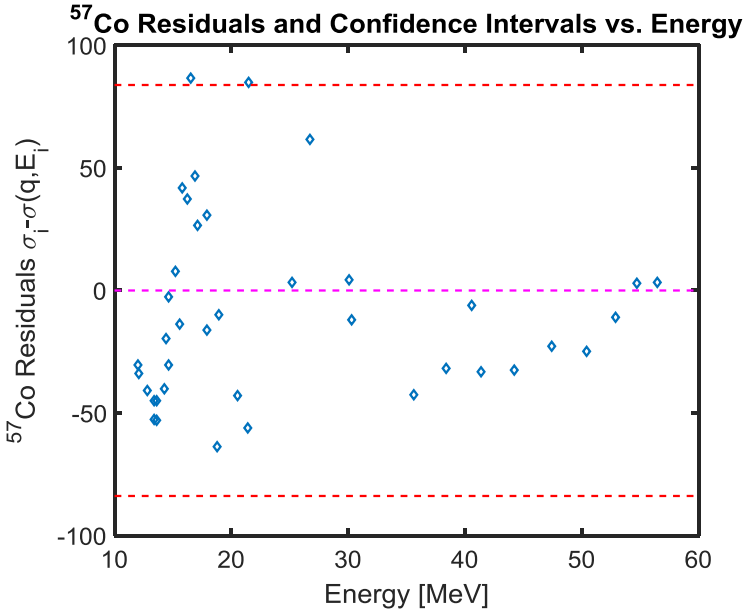

Figure 5-11: ^{57}Co residuals and 95% confidence intervals as a function of energy.

The fit and experimental data with the given 95% confidence interval is shown below in Figure 5-12.

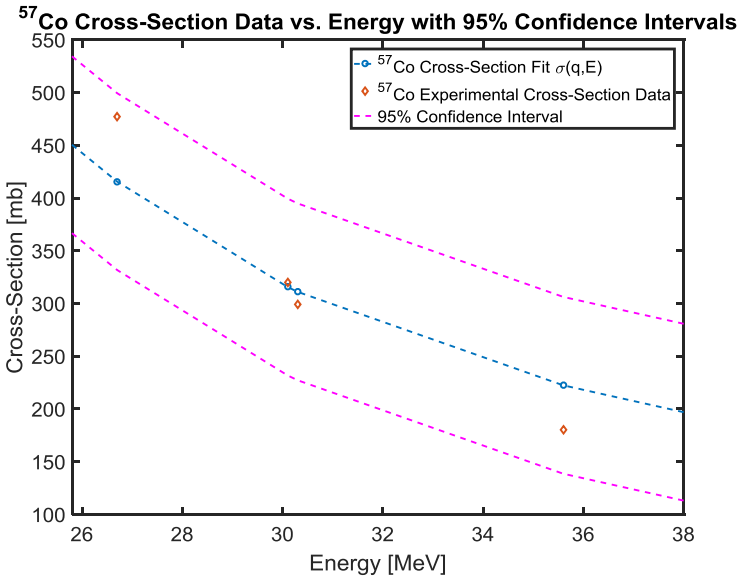

Figure 5-12: ^{57}Co 95% confidence intervals with fit and experimental data.

As the function is non-linear, a sensitivity matrix is required for the construction of the covariance matrix. The sensitivity matrix is determined by taking the derivative of the function with respect to each parameter.

$$\chi_{ik}(q) = \frac{\partial f_i(q)}{\partial q_k} \tag{5-26}$$

Here the parameters are $q = [A_1, A_2, A_3, A_4, A_5]$. The analytic derivative of the fitting function with respect to each parameter is given below.

$$\frac{\partial \sigma_{^{57}Co}}{\partial A_1}(E) = -\sqrt{E}\, exp\left(\frac{\overline{A}_1}{\sqrt{E}}\right) \cdot \frac{1000 \cdot \left[A_5 + \frac{\overline{A}_2}{(\overline{A}_4 - \overline{A}_3 E)^2 + 1}\right]}{\left(E \cdot exp\left(\frac{\overline{A}_1}{\sqrt{E}}\right) - 1\right)^2} \tag{5-27}$$

$$\frac{\partial \sigma_{^{57}Co}}{\partial A_2}(E) = \frac{1}{[(\overline{A}_4 - \overline{A}_3 E)^2 + 1]\left(E \cdot exp\left(\frac{\overline{A}_1}{\sqrt{E}}\right) - 1\right)} \tag{5-28}$$

$$\frac{\partial \sigma_{^{57}Co}}{\partial A_3}(E) = \frac{2000\overline{A}_2 E(\overline{A}_4 - \overline{A}_3 E)}{[(\overline{A}_4 - \overline{A}_3 E)^2 + 1]^2\left(E \cdot exp\left(\frac{\overline{A}_1}{\sqrt{E}}\right) - 1\right)} \tag{5-29}$$

$$\frac{\partial \sigma_{^{57}Co}}{\partial A_4}(E) = -\frac{1000\overline{A}_2(2\overline{A}_4 - 2\overline{A}_3 E)}{[(\overline{A}_4 - \overline{A}_3 E)^2 + 1]^2\left[E \cdot exp\left(\frac{\overline{A}_1}{\sqrt{E}}\right) - 1\right]} \tag{5-30}$$

$$\frac{\partial \sigma_{^{57}Co}}{\partial A_5}(E) = \frac{1000}{E \cdot exp\left(\frac{\overline{A}_1}{\sqrt{E}}\right) - 1} \tag{5-31}$$

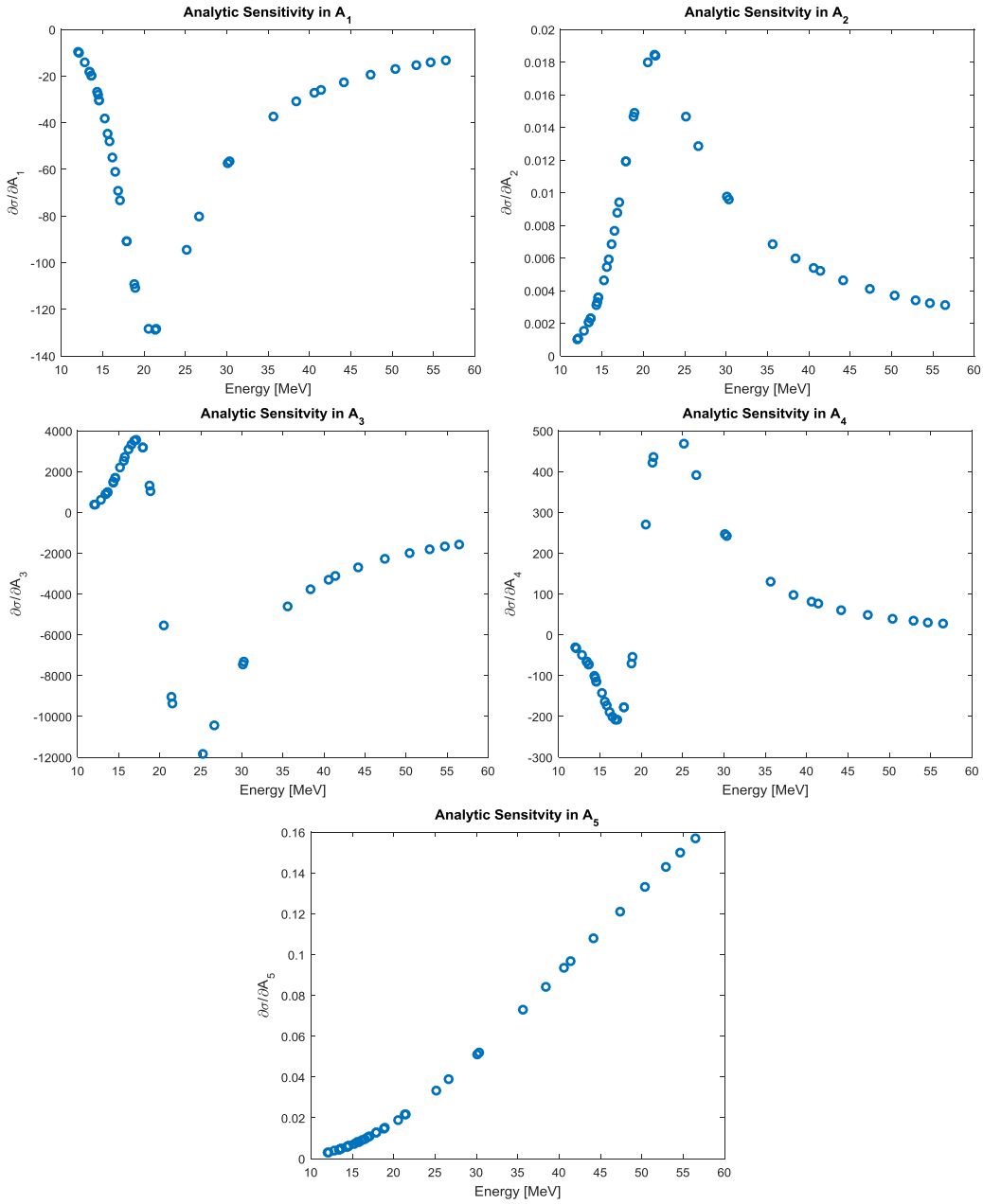

Figure 5-13: Analytic sensitivities of each parameter for ^{57}Co fit.

Thus the sensitivity matrix will be of the form:

$$\chi_{57_{Co}}(q) = \begin{bmatrix} \frac{\partial \sigma_{57_{Co}}}{\partial A_1}(E_1) & \frac{\partial \sigma_{57_{Co}}}{\partial A_2}(E_1) & \cdots & \frac{\partial \sigma_{57_{Co}}}{\partial A_3}(E_1) & \frac{\partial \sigma_{57_{Co}}}{\partial A_4}(E_1) & \frac{\partial \sigma_{57_{Co}}}{\partial A_5}(E_1) \\ \vdots & \vdots & & \vdots & \vdots & \vdots \\ \frac{\partial \sigma_{57_{Co}}}{\partial A_1}(E_n) & \frac{\partial \sigma_{57_{Co}}}{\partial A_2}(E_n) & \cdots & \frac{\partial \sigma_{57_{Co}}}{\partial A_3}(E_n) & \frac{\partial \sigma_{57_{Co}}}{\partial A_4}(E_n) & \frac{\partial \sigma_{57_{Co}}}{\partial A_5}(E_n) \end{bmatrix}$$

The covariance matrix may be calculated using this sensitivity matrix.

$$V_{57_{Co}} = \sigma^2_{Co^{57}}[\chi^T(q)\chi(q)]^{-1} \tag{5-32}$$

$$V_{57_{Co}} = \begin{bmatrix} 12.9065 & 9.7652\times10^{4} & 0.0280 & 0.2468 & -798.0934 \\ 9.7652\times10^{4} & 7.3995\times10^{8} & 217.5939 & 1.9806\times10^{3} & -6.0204\times10^{6} \\ 0.0289 & 217.5939 & 1.7106\times10^{-4} & 0.0028 & -0.6348 \\ 0.2468 & 1.9806\times10^{3} & 0.0028 & 0.0539 & 6.9347 \\ -798.0934 & -6.0204\times10^{6} & -0.6348 & 6.9347 & 7.4272\times10^{4} \end{bmatrix}$$

The variance for each parameter is:

$$\sigma^2_{A_1} = 12.9065\ ;\quad \sigma^2_{A_2} = 7.3995\times10^{8}\ ;\quad \sigma^2_{A_3} = 1.7106\times10^{-4}\ ;\quad \sigma^2_{A_4} = 0.0539\ ;\quad \sigma^2_{A_5} = 7.4272\times10^{4}$$

$$\sigma_{A_1} = 3.5926\ \ ;\quad \sigma_{A_2} = 2.7202\times10^{4}\ \ ;\quad \sigma_{A_3} = 0.0131\ \ ;\quad \sigma_{A_4} = 0.2322\ \ ;\quad \sigma_{A_5} = 272.5289$$

The confidence intervals for each parameter may be determined using the t-value establishing 95% confidence intervals.

$$A_1 \in \left[\overline{A}_1 - 2.0322\cdot\sigma_{A_1}, \overline{A}_1 + 2.0322\cdot\sigma_{A_1}\right] = [42.8215,\ 72.1850]$$

$$A_2 \in \left[\overline{A}_2 - 2.0322\cdot\sigma_{A_2}, \overline{A}_2 + 2.0322\cdot\sigma_{A_2}\right] = \left[-2.2993\times10^{4},\ 8.7567\times10^{4}\right]$$

$$A_3 \in \left[\overline{A}_3 - 2.0322\cdot\sigma_{A_3}, \overline{A}_3 + 2.0322\cdot\sigma_{A_3}\right] = [0.1625,\ 0.2157]$$

$$A_4 \in \left[\overline{A}_4 - 2.0322\cdot\sigma_{A_4}, \overline{A}_4 + 2.0322\cdot\sigma_{A_4}\right] = [2.9263,\ 4.3345]$$

$$A_5 \in \left[\overline{A}_5 - 2.0322\cdot\sigma_{A_5}, \overline{A}_5 + 2.0322\cdot\sigma_{A_5}\right] = [-553.8272,\ 553.8392]$$

It is clear that the function is most sensitive to parameters A_1, A_3, and A_4 and least sensitive to parameters A_2 and A_5.

As the parameters A_2 and A_5 have very large standard deviations in relation to their nominal parameter values, the function is not very sensitive to these parameters. This is also indicated in Eq. (5-28) and Eq. (5-31), where the parameter is not present in the functional derivative. Figure 5-13 graphically demonstrates this as well, as the sensitivity of parameters A_2 and A_5 over the specified energy range is extremely small.

The relatively small standard deviations for the other parameters indicate that the function is more sensitive to these values. This is again seen graphically in the plot of parameter sensitivity as a function of energy in Figure 5-13.

These analyses indicate that the provided fit of the experimental production cross-section data for ^{56}Co and ^{57}Co models the data reasonably well. The standard deviations of each fit are listed below.

$$\sigma_{\sigma_{56_{Co}}} = 31.2184 \text{ mb}$$

$$\sigma_{\sigma_{57_{Co}}} = 41.2481 \text{ mb}$$

As cross-section values supplied to MCNP were generated using these fits, the standard deviation of each fit may be propagated into the activities predicted with these cross-sections in MCNP. The relationship between calculated activities initially provided in Eq. (4-35) is given again below.

$$\frac{A_{57_{Co}}}{A_{56_{Co}}}(E) = \frac{N_{58_{Ni}}\sigma_{57_{Co}}(E)\Phi_{57_{Co}}}{N_{58_{Ni}}\sigma_{56_{Co}}(E)\Phi_{56_{Co}}} = \frac{\sigma_{57_{Co}}(E)\Phi_{57_{Co}}}{\sigma_{56_{Co}}(E)\Phi_{56_{Co}}}$$

Given the above relationship and assuming no uncertainties in the incident flux, it was assumed that the only source of uncertainty was that inherent in the cross-section fits. The uncertainty in each activity may then calculated as shown below.

$$\sigma_{A_{57_{Co}}} = N_{58_{Ni}}\Phi_{57_{Co}}\sigma_{\sigma_{57_{Co}}}$$

$$\sigma_{A_{56_{Co}}} = N_{58_{Ni}}\Phi_{56_{Co}}\sigma_{\sigma_{56_{Co}}}$$

In the equations above $\sigma_{\sigma_{56_{Co}}}$ and $\sigma_{\sigma_{57_{Co}}}$ are the standard deviation of the cross-section fits of ^{56}Co and ^{57}Co. The uncertainty in the MCNP calculated activity ratio may then be propagated as shown below.

$$R_A = \frac{A_{57_{Co}}}{A_{56_{Co}}}$$

$$\sigma_{R_A} = |R_A|\sqrt{\left(\frac{\sigma_{A_{57_{Co}}}}{A_{57_{Co}}}\right)^2 + \left(\frac{\sigma_{A_{56_{Co}}}}{A_{56_{Co}}}\right)^2} \tag{5-33}$$

Using the equations for the respective activities and associated uncertainties, Eq. (5-33) may be rewritten and simplified as given below in Eq. (5-34).

$$\sigma_{R_A} = |R_A|\sqrt{\left(\frac{\sigma_{\sigma_{57_{Co}}}}{\sigma_{57_{Co}}(E)}\right)^2 + \left(\frac{\sigma_{\sigma_{56_{Co}}}}{\sigma_{56_{Co}}(E)}\right)^2} \tag{5-34}$$

While the predicted energy is technically the effective energy incident on a foil determined by some Gaussian distribution, for the purposes of uncertainty quantification the total cross-section fit and associated standard deviation were used.

This uncertainty quantification was performed for all MCNP calculated foil activity ratios. As discussed in Section 4.3.2.1 it was only possible to calculate the activity ratios and predicted incident energies for the thin window experiment. As the predicted incident energy is required for the cross-section to be known, the uncertainty in the MCNP calculated activity ratios can only be determined for the thin window experiment. These uncertainties are presented below in Table 5-7.

Table 5-7: Predicted activity ratios, uncertainties, and relative errors for the thin window MCNP model.

Thin Window MCNP Model							
Foil Number	R_A	σ_{R_A}	**Relative Error [%]**	**Foil Number**	R_A	σ_{R_A}	**Relative Error [%]**
1	1081.615	156.092	14.91%	**17**	46.437	23.308	49.46%
2	51.015	25.214	50.17%	**18**	64.339	31.758	49.73%
3	14.238	7.084	49.68%	**19**	20.560	10.101	49.40%
4	41.096	20.649	49.37%	**20**	10.659	5.294	50.21%
5	699.278	337.891	51.15%	**21**	67.038	34.406	48.86%
6	83.854	44.368	50.31%	**22**	10.976	5.536	50.22%
7	51.610	25.824	50.48%	**23**	17.400	8.522	49.58%
8	18.911	9.356	49.34%	**24**	47.318	23.739	49.59%
9	39.065	20.137	49.54%	**25**	86.729	44.563	50.38%
10	5145.141	156.092	0.87%	**26**	139.257	64.336	47.67%
11	4919.865	156.092	3.13%	**27**	22.823	11.229	49.37%
12	4255.700	156.092	3.03%	**28**	288.858	84.481	29.27%
13	1681.799	156.092	8.40%	**29**	45.978	22.568	49.31%
14	2308.559	156.092	7.34%	**30**	31.848	15.986	49.26%
15	52.123	26.774	51.00%	**31**	18.100	8.987	49.54%
16	79.743	43.361	49.98%		-		

Some of the activity ratios shown in the table above present uncertainties ranging up to ~50%. These large uncertainties are predominantly due to the fact that as the ^{56}Co production cross-section approaches zero near the energy range of 25-26 MeV, the fixed value of the uncertainty in the fit causes a significantly larger percentage error. This large error is then propagated through to the associated error in the activity ratio. Another less significant potential source of error is that the associated fit uncertainty for the total cross-section fit is

used, while effective cross-sections are more applicable when looking at the total activity produced in a foil.

Based on the predicted incident energies presented in Section 4.3.1.3 and Section 4.3.2.1 for the thin window experiment and MCNP thin window model, it is already apparent that the MCNP model predicts much lower incident proton energies and therefore much higher $^{57}Co/^{56}Co$ activity ratios than the experiment. Based on the activity ratios and associated uncertainties for the thin window experiment given in Table 5-6, there could be potential overlap with the MCNP predicted activity ratios given the associated uncertainties shown above in Table 5-7. These uncertainties provide an idea of the errors inherent in the MCNP predicted activity ratios based on the quality of the cross-section fits used and the proximity to the threshold energy.

Section 5.3.2.3. Statistical Uncertainties in MCNP Calculations

Thirty million particle histories were used when calculating the activity produced in the ^{58}Ni foils for both the thin and thick window models. All MCNP calculated values are provided in Table 5-8 and Table 5-9 along with their absolute and relative uncertainties for each foil's calculated ^{56}Co and ^{57}Co activity.

Table 5-8: MCNP absolute and relative uncertainties for ^{56}Co and ^{57}Co activities in the thin window MCNP Model.

Thin Window MCNP Model						
Foil Number	$A_{56_{Co}}$ **[mCi]**	$\sigma_{A_{56_{Co}}}$ **[mCi]**	**Relative Uncertainty [%]**	$A_{57_{Co}}$ **[mCi]**	$\sigma_{A_{57_{Co}}}$ **[mCi]**	**Relative Uncertainty [%]**
1	1.644E-06	1.453E-07	8.834	1.779E-03	2.295E-04	0.713
2	3.462E-04	2.594E-06	0.749	1.766E-02	7.344E-05	0.228
3	4.109E-03	1.050E-05	0.255	5.850E-02	3.895E-05	0.121
4	2.412E-04	2.424E-06	1.005	9.912E-03	9.885E-05	0.307
5	1.424E-05	4.162E-07	2.923	9.957E-03	1.009E-04	0.313
6	1.296E-04	1.562E-06	1.205	1.087E-02	9.815E-05	0.305
7	2.087E-04	2.077E-06	0.996	1.077E-02	9.789E-05	0.304
8	5.190E-04	3.594E-06	0.693	9.815E-03	9.794E-05	0.304
9	2.227E-04	2.327E-06	1.045	8.700E-03	1.039E-04	0.323
10	1.371E-06	1.150E-07	8.387	7.052E-03	1.125E-04	0.35
11	1.592E-06	1.193E-07	7.498	7.830E-03	1.084E-04	0.337
12	1.874E-06	1.381E-07	7.368	7.976E-03	1.073E-04	0.334
13	5.048E-06	2.455E-07	4.864	8.490E-03	1.040E-04	0.323
14	3.429E-06	2.927E-07	8.536	7.915E-03	1.080E-04	0.336
15	1.241E-03	5.018E-06	0.404	6.470E-02	3.899E-05	0.121
16	2.367E-04	2.055E-06	0.868	1.887E-02	7.352E-05	0.228
17	1.362E-03	5.213E-06	0.383	6.327E-02	3.898E-05	0.121
18	1.013E-03	4.398E-06	0.434	6.519E-02	3.906E-05	0.121
19	3.004E-03	9.159E-06	0.305	6.177E-02	3.908E-05	0.121
20	5.572E-03	1.287E-05	0.231	5.939E-02	3.892E-05	0.121
21	2.671E-04	2.203E-06	0.825	1.790E-02	7.368E-05	0.229
22	3.086E-03	9.401E-06	0.305	3.387E-02	5.101E-05	0.159
23	1.967E-03	7.027E-06	0.357	3.423E-02	5.099E-05	0.158
24	7.583E-04	4.011E-06	0.529	3.588E-02	5.123E-05	0.159
25	4.295E-04	2.877E-06	0.670	3.725E-02	5.144E-05	0.160
26	2.560E-04	2.052E-06	0.801	3.565E-02	5.168E-05	0.161
27	2.036E-03	6.834E-06	0.336	4.647E-02	4.450E-05	0.138
28	1.209E-04	1.313E-06	1.086	3.493E-02	5.248E-05	0.163
29	1.019E-03	4.377E-06	0.429	4.686E-02	4.452E-05	0.138
30	1.489E-03	5.637E-06	0.379	4.742E-02	4.457E-05	0.139
31	2.514E-03	7.890E-06	0.314	4.550E-02	4.468E-05	0.139

Table 5-9: MCNP absolute and relative uncertainties for ^{56}Co and ^{57}Co activities in the thick window MCNP Model.

Thick Window MCNP Model						
Foil Number	$A_{56_{Co}}$ **[mCi]**	$\sigma_{A_{56_{Co}}}$ **[mCi]**	**Relative Uncertainty [%]**	$A_{57_{Co}}$ **[mCi]**	$\sigma_{A_{57_{Co}}}$ **[mCi]**	**Relative Uncertainty [%]**
1	2.437E-07	2.437E-07	100.000	1.848E-04	2.401E-06	1.299
2	2.307E-07	2.230E-07	96.671	6.928E-03	2.035E-05	0.294
3	5.658E-07	2.448E-07	43.254	3.764E-02	5.328E-05	0.142
4	1.764E-07	1.638E-07	92.830	3.507E-03	1.525E-05	0.435
5	0.000E+00	0.000E+00	0.000	1.325E-03	7.138E-06	0.539
6	0.000E+00	0.000E+00	0.000	3.342E-03	1.404E-05	0.420
7	1.488E-09	1.073E-09	72.137	3.855E-03	1.518E-05	0.394
8	4.334E-07	3.184E-07	73.476	6.026E-03	2.146E-05	0.356
9	6.324E-09	3.784E-09	59.842	2.981E-03	1.425E-05	0.478
10	0.000E+00	0.000E+00	0.000	4.505E-04	3.213E-06	0.713
11	2.144E-08	2.144E-08	100.000	4.966E-04	3.330E-06	0.671
12	0.000E+00	0.000E+00	0.000	5.483E-04	3.585E-06	0.654
13	0.000E+00	0.000E+00	0.000	7.701E-04	4.698E-06	0.610
14	2.179E-07	2.179E-07	100.000	5.914E-04	3.924E-06	0.663
15	9.867E-09	4.511E-09	45.715	2.302E-02	3.790E-05	0.165
16	0.000E+00	0.000E+00	0.000	6.057E-03	1.865E-05	0.308
17	1.990E-08	6.350E-09	31.912	2.382E-02	3.870E-05	0.162
18	2.952E-07	2.921E-07	98.941	2.071E-02	3.488E-05	0.168
19	7.685E-07	3.755E-07	48.869	3.057E-02	4.697E-05	0.154
20	6.108E-07	5.971E-08	9.775	4.190E-02	5.782E-05	0.138
21	1.926E-07	1.887E-07	98.005	6.530E-03	1.973E-05	0.302
22	4.642E-07	7.756E-08	16.707	2.379E-02	4.254E-05	0.179
23	4.894E-07	2.372E-07	48.470	2.012E-02	3.787E-05	0.188
24	2.487E-07	2.338E-07	94.001	1.251E-02	2.717E-05	0.217
25	2.051E-08	8.611E-09	41.983	1.015E-02	2.373E-05	0.234
26	9.466E-08	9.391E-08	99.212	8.069E-03	2.004E-05	0.248
27	7.302E-08	1.647E-08	22.555	2.461E-02	4.123E-05	0.168
28	0.000E+00	0.000E+00	0.000	5.803E-03	1.579E-05	0.272
29	3.126E-07	2.964E-07	94.840	1.803E-02	3.248E-05	0.180
30	2.712E-08	8.825E-09	32.541	2.158E-02	3.762E-05	0.174
31	7.893E-07	5.552E-07	70.339	2.686E-02	4.409E-05	0.164

The thin window MCNP model ^{56}Co and ^{57}Co activities presented in Table 5-8 in general show very small relative errors. In cases where the predicted ^{56}Co activity is very low, it is likely that a number of the protons hitting the foil are below the threshold energy for the ^{56}Co production reaction and are not tallied, thus reducing the total number of particle statistics and increasing the relative error. This is likely the case in foils 10 – 14.

The thick window MCNP model ^{56}Co activities presented in Table 5-9 show extremely large errors, in some cases up to 100% while the ^{57}Co activities show small relative errors similar to those seen in Table 5-8 for the thin window MCNP model. As evidenced by the extremely small (sometimes zero) ^{56}Co activities produced in the thick window MCNP model, a majority of the protons hitting the ^{58}Ni foils are below the threshold energy for the ^{56}Co production reaction and are not tallied. With so few particles to track for the ^{56}Co production tally, this significantly reduces the number of particle statistics and causes a huge rise in the relative error. Given this physical driver of poor ^{56}Co activity statistics, it is not likely that increasing the number of particles histories above 30 million will improve these statistics.

As discussed previously, the activity ratios for the thick window MCNP model are not meaningful because of the extremely low ^{56}Co activities. Therefore only the predicted activity ratios and associated uncertainties for the thin window MCNP model are presented. These uncertainties were calculated via uncertainty propagation as shown below using the uncertainties in the MCNP calculated ^{56}Co and ^{57}Co activities given in Table 5-8.

$$R_A = \frac{A_{57_{Co}}}{A_{56_{Co}}}$$

$$\sigma_{R_A} = |R_A| \sqrt{\left(\frac{\sigma_{A_{57_{Co}}}}{A_{57_{Co}}}\right)^2 + \left(\frac{\sigma_{56_{A_{Co}}}}{A_{56_{Co}}}\right)^2}$$

The activity ratios and associated absolute and relative uncertainties for the thin window MCNP model are presented in Table 5-10.

Table 5-10: Predicted activity ratios and absolute and relative uncertainties for the thin window MCNP model using MCNP statistics.

Thin Window MCNP Model							
Foil Number	R_A	σ_{R_A}	**Relative Uncertainty [%]**	**Foil Number**	R_A	σ_{R_A}	**Relative Uncertainty [%]**
1	1081.615	169.111	15.635%	**17**	46.437	0.180	0.388%
2	51.015	0.437	0.857%	**18**	64.339	0.282	0.438%
3	14.238	0.038	0.264%	**19**	20.560	0.064	0.311%
4	41.096	0.582	1.416%	**20**	10.659	0.026	0.240%
5	699.278	21.635	3.094%	**21**	67.038	0.618	0.922%
6	83.854	1.263	1.506%	**22**	10.976	0.037	0.340%
7	51.610	0.696	1.348%	**23**	17.400	0.067	0.387%
8	18.911	0.230	1.215%	**24**	47.318	0.259	0.548%
9	39.065	0.620	1.587%	**25**	86.729	0.593	0.684%
10	5145.141	439.266	8.537%	**26**	139.257	1.134	0.814%
11	4919.865	375.125	7.625%	**27**	22.823	0.080	0.349%
12	4255.700	318.738	7.490%	**28**	288.858	3.166	1.096%
13	1681.799	84.357	5.016%	**29**	45.978	0.202	0.440%
14	2308.559	199.563	8.644%	**30**	31.848	0.124	0.390%
15	52.123	0.213	0.409%	**31**	18.100	0.060	0.329%
16	79.743	0.759	0.952%			-	

The relative errors shown for the activity ratios above in Table 5-10 are very small, particularly in comparison to the large relative errors of up to 50% seen in Table 5-6 as a result of the uncertainty in the ^{56}Co cross-section fit near the threshold energy. Therefore it can be said that the number of particles histories run in MCNP provides sufficient confidence in the precision of the thin window model predictions.

CHAPTER 6. CONCLUSIONS

Section 6.1. Summary

The purpose of this work was to develop and attempt to validate a computational model representing the RbCl-RbCl-Ga target stack geometry at LANL's IPF with a quantifiable degree of accuracy. This was done with the intention of understanding system drivers contributing to overall system performance, ^{82}Sr radioisotope production, and simultaneous production of other isotopes of interest in the C slot target.

Multi-physics coupling was employed to capture both the proton beam transport within the target stack and the thermal response of the target. This iterative coupling process between MCNP and ANSYS CFX provided a picture of the transient thermal target behavior as well as a pseudo steady state solution.

Attempts at model validation through comparison with measured observables provided a measure of confidence in the model predictions of target behavior. These measured observables, or validation metrics, were measured ^{82}Sr production yields and isotope ratios produced with a distribution of ^{58}Ni foils in the C slot. Model predictions of these values were obtained using the pseudo steady state density distributions obtained for RbCl targets A and B.

Validation metrics for a simplified version of the full model with an applied average heat transfer coefficient were calculated in addition to those for the final refined model containing all target domains and cooling water channels. The results from these models were compared to determine the usefulness of the average heat transfer coefficient model for scoping and parametric studies. Sources of uncertainty and error were identified and uncertainty quantification was performed where possible.

Section 6.2. Conclusions

Attempts to validate this model through the use of measured observables and performed uncertainty quantification have provided some measure of confidence in the model and highlighted areas of needed improvement.

Five measured ^{82}Sr production yields were compared with model predictions obtained using their full irradiation history. The model-predicted ^{82}Sr yields were within ~0.6 – 7% of the measured values. Though this is a fairly accurate prediction, target yields are very much an integral quantity – both because they are a comparison of the combined RbCl target A and B yields and because they are a product of many combined physical effects. As a result, accurate prediction of this bulk integral quantity provides a limited degree of confidence in the model's overall accuracy when predicting target behavior.

The uncertainties in the MCNP predicted activities were propagated into the total predicted yields with a relative uncertainty of less than 0.005% for both RbCl targets A and B. As the IAEA recommended ^{82}Sr production cross-sections were not provided with any uncertainties, the uncertainty could not be propagated into the predicted yields. However, given the numerical errors introduced by the use of and translation between two different computational softwares, it was assumed the contribution of this uncertainty to the total error in the computational results is comparably small.

A measurement of the activity ratios of ^{56}Co and ^{57}Co produced in a number of ^{58}Ni foils distributed on a face in the C slot target downstream of two RbCl targets was used as a second measured observable. The activity ratios from two experiments (each with a different front window thickness) were measured in an attempt to provide more detailed information about the density and temperature distributions in the upstream targets. Error propagation of these activity measurements indicated very small uncertainties in these experimentally measured values.

Model predictions obtained through re-creation of the experiment geometries predicted significantly higher ^{57}Co/^{56}Co activity ratios than those seen in the experimental measurements. This corresponds to a much lower predicted transmitted spatial energy distribution than the experiment, indicating that the model is potentially under-predicting the peak upstream target temperatures. In order to obtain a lower isotope ratio and therefore higher transmitted energy on the foils located at the top of the target, upstream targets would need to experience higher peak target temperatures and less dense material.

Error propagation of the uncertainties in the ^{56}Co and ^{57}Co cross-section fits into the isotope ratios obtained for the model indicated extremely large errors of up to ~50%. This is due to the large uncertainty in the ^{56}Co fit and in the predicted ^{56}Co activity when near the threshold energy, and causes large error bounds on the calculated activity ratios. Relative uncertainties provided by MCNP were small, particularly in comparison with the uncertainty in the ^{56}Co excitation function near the threshold energy. While this validation metric indicates that the model predicts target thermal behavior with some relatively large degree of uncertainty, the predicted isotope ratios and transmitted spatial energy distribution display the same trends, with the highest transmitted proton energies present at the top of the target.

Several physical phenomena have been neglected or simplified as a result of computational limitations and it is not clear to what extent these influence the cumulative effects of upstream behavior leading to this transmitted energy distribution. Potential void development is indicated by the very high near-wall temperatures in the cooling water channels. If this is the case, insufficient modeling of the cooling water channels could be leading to an inaccurate and overly optimistic prediction of target heat removal, causing lower peak target temperatures and higher densities.

A comparison of the measured observables obtained using the solution of the refined cooling water domain model with values obtained using the solution of the average heat transfer coefficient model demonstrated little difference between them. While the average heat transfer coefficient model shows promise in its ability to predict target behavior, the indications of void development in the cooling water channels limit the utility of the average heat transfer coefficient model for more detailed studies.

It is clear that numerous sources of uncertainty – many unquantifiable – contribute to overall uncertainties in the predicted system behavior and increase the gap between predicted and measured observables. These sources of uncertainty call for additional investigation into avenues by which to increase the knowledge base and decrease this gap.

Although several sources of uncertainty exist in the computational model, this coupling methodology clearly demonstrates promise as a tool to understanding multiphase target behavior. While it has not been validated, it correctly predicted melting and redistribution of

less dense molten RbCl to the top of upstream targets, leading to a skewed energy distribution on the C slot target. This appears to match the intuitively expected real world target behavioral trends reflected in measured observables and calls for additional investigation into methods by which to increase the model's accuracy and supply additional validation metrics. This dissertation provides compelling evidence that these simulations provide a tool by which to improve target thermal performance and optimize ^{82}Sr radioisotope production in conjunction with simultaneous production of other radioisotopes of interest.

Section 6.3. Future Work

Results from this work will aid in making future decisions regarding predicted target behavior, experiment design, and operational tasks with a greater understanding of upstream target behavior. Several proposed avenues which should be investigated to improve the understanding of this system are discussed here.

While the heat input to the cooling water domain has been incorporated into the final model, the impact of void development on heat transfer and beam penetration has not been investigated. Each target puck is separated by water cooling channels. After the beam turns on the targets begin to heat up, increasing the temperature of the cooling water flowing along each target face. The results of the final refined cooling water domain model demonstrate near-wall cooling water temperatures well above the saturation temperature. Accounting for any subcooled nucleate boiling occurring along any target face could influence the transmitted energy distribution as void development significantly changes density. In addition, void development significantly alters near-wall turbulence and heat transfer profiles, potentially altering the target density and temperature distributions. Of particular concern is whether the surface is undergoing critical heat flux, which would cause a significant temperature excursion in this region. Quantifying void impact on heat transfer and beam transmittance could indicate whether the cooling mass flow rate is sufficient and identify the effect of any boiling on peak target temperatures and the transmitted beam distribution. In addition, directly monitoring the cooling channels during operation for void development or developing an experiment

mimicking these same conditions would be useful as a means of validating the computational results.

A comparative study of different coupling times between the radiation transport and thermal hydraulic calculations is also desirable, as it most likely influences transient target behavior in the first seconds of irradiation. Determining the optimum coupling time is desirable to closely match target behavior and failure risk in the initial stages of irradiation.

As many of the thermal properties used for this model have unknown associated uncertainties, a sensitivity study on the different thermal parameters could prove useful in determining the impact of widely varying thermal properties on the model's predictive capabilities. In addition, experiments could be performed where some of these thermal properties and their associated uncertainties could be directly measured. This would provide data that could be presented with a known degree of confidence.

While the ^{58}Ni foil experiment was a useful validation experiment, it was performed several years ago and tracking down all experimental parameters for a full uncertainty quantification study was difficult. In addition, it is reliant on cumulative effects from both the A and B slot upstream targets and the cooling water channels. Because of this, it would be desirable to perform a series of experiments with foils on the front face of the A, B, and C slot targets. This would provide additional validation metrics with which to compare computational results and a more in depth uncertainty analysis could be performed at the same time as the experiment.

Another validation experiment that should be performed involves individual processing of the A and B slot RbCl targets for activity quantification. This would allow for a more detailed comparison of predicted MCNP yields to individually measured target production yields, instead of comparing only the combined values. In addition, the uncertainty in the measured production activities should be determined for a more accurate comparison with model predictions.

While the thermal time response of the system is slow relative to the length of each beam pulse, these beam pulses may have unknown effects on the system. In addition, issues with the upstream beam could cause an inconsistent gate length between each pulse, altering both the average and transient target behavior. It is plausible that beam pulsing significantly impacts

system heat transfer by causing a rapid increase in near-wall void formation with each pulse. Trying to capture any effects of beam pulsing would be useful for determining its impact on the targets, capsules, and void development in the cooling channels. It may not be possible to fully capture the influence of beam pulsing on all system thermal hydraulic behaviors, but capturing some of these transient effects could prove informative for understanding certain aspects of target behavior, particularly heat transfer.

REFERENCES

[1] D.L. Bailey, D.W. Townsend, P.E. Valk, M.N. Maisey, Positron emission tomography, Springer-Verlag London Ltd, 2005.

[2] F. Daghighian, R. Sumida, M. Phelps, PET Imaging: An Overview and Instrumentation, J Nucl Med Technol. 18 (1990) 5–13.

[3] K. Duncan, Radiopharmaceuticals in PET Imaging, J Nucl Med Techno. 26 (1998) 228–234.

[4] F.M. Bengel, T. Higuchi, M.S. Javadi, R. Lautamäki, Cardiac Positron Emission Tomography, J. Am. Coll. Cardiol. 54 (2009) 1–15. doi:10.1016/j.jacc.2009.02.065.

[5] International Atomic Energy Agency, Cyclotron Produced Radionuclides: Principles and Practice, Vienna, 2008.

[6] International Atomic Energy Agency, Production of long lived parent radionuclides for generators, ^{68}Ge, ^{82}Sr, ^{90}Sr and ^{188}W., 2010. http://www-pub.iaea.org/books/IAEABooks/8268/Production-of-Long-Lived-Parent-Radionuclides-for-Generators-68Ge-82Sr-90Sr-and-188W.

[7] K. Yoshinaga, R. Klein, N. Tamaki, Generator-produced rubidium-82 positron emission tomography myocardial perfusion imaging-From basic aspects to clinical applications, J. Cardiol. 55 (2010) 163–173. doi:10.1016/j.jjcc.2010.01.001.

[8] J.K. Tuli, Nuclear Data Sheets for A = 82, Nucl. Data Sheets. 98 (2003) 209–334. doi:10.1006/ndsh.2003.0002.

[9] J.-F. Chatal, F. Rouzet, F. Haddad, C. Bourdeau, C. Mathieu, D. Le Guludec, Story of Rubidium-82 and Advantages for Myocardial Perfusion PET Imaging, Front. Med. 2 (2015) 1–7. doi:10.3389/fmed.2015.00065.

[10] F.M. Nortier, M. DeJohn, M.E. Fassbender, V.T. Hamilton, R.C. Heaton, D.J. Jamriska, J.J. Kitten, J.W. Lenz, C.E. Lowe, C.F. Moddrell, L.M. McCurdy, E.J. Peterson, L.R. Pitt, D.R. Phillips, L.L. Salazar, P.A. Smith, F.O. Valdez, Targetry at the LANL 100 MeV Isotope Production Facility: Lessons Learned from Facility Commissioning, in: Am. Nucl. Energy Symp., Miami Beach, Florida, 2004.

[11] F.M. Nortier, Isotope Production at LANL, in: Nation's Need Isot. Present Futur., Rockville, Maryland, 2008.

[12] T.A. Faugl, Modeling of Visualization Cyclotron Target with Coupling of Proton Range and Target Density, North Carolina State University, 2014.

[13] J.L. Peeples, M.H. Stokely, J. Michael Doster, Thermal performance of batch boiling water targets for 18F production, Appl. Radiat. Isot. 69 (2011) 1349–1354. doi:10.1016/j.apradiso.2011.06.015.

[14] F. Tárkányi, S. Takács, S.J. Heselius, O. Solin, J. Bergman, Static and dynamic effects in gas targets used for medical isotope production, Nucl. Instruments Methods Phys. Res. Sect. A Accel. Spectrometers, Detect. Assoc. Equip. 397 (1997) 119–124. doi:10.1016/S0168-9002(97)00736-5.

[15] S.J. Heselius, P. Lindblom, O. Solin, Optical studies of the influence of an intense ion beam on high-pressure gas targets, Int. J. Appl. Radiat. Isot. 33 (1982) 653–659. doi:10.1016/0020-708X(82)90065-5.

[16] S.J. Heselius, P. Malmborg, O. Solin, B. Långström, Studies of proton beam penetration in nitrogen-gas targets with respect to production and specific radioactivity of carbon-11, Int. J. Radiat. Appl. Instrumentation. Part. 38 (1987) 49–57. doi:10.1016/0883-2889(87)90236-X.

[17] J. Lenz, Gas target coupled density/proton heat load iterative CFD analysis for a Xe124 production target, Nucl. Instruments Methods Phys. Res. Sect. A Accel. Spectrometers, Detect. Assoc. Equip. 655 (2011) 111–117. doi:10.1016/j.nima.2011.06.033.

[18] E. O'Brien, M.H. Stokely, J.M. Doster, I.A. Bolotnov, Multi-Physics Coupling for Optimization of Cyclotron Targetry, in: Trans. Am. Nucl. Soc., Washington, D.C., 2015: pp. 1552–1555.

[19] J.L. Peeples, M. Magerl, E.M. O'Brien, J.M. Doster, I.A. Bolotnov, B.W. Wieland, M.H. Stokely, High Current C-11 Gas Target Design and Optimization Using Multi-Physics Coupling, in: 16th Proc. Work. Targety Target Chem., Santa Fe, NM, 2016.

[20] K. Gagnon, M. Jensen, H. Thisgaard, J. Publicover, S. Lapi, S.A. McQuarrie, T.J. Ruth, A new and simple calibration-independent method for measuring the beam energy of a cyclotron, Appl. Radiat. Isot. 69 (2011) 247–253. doi:10.1016/j.apradiso.2010.09.012.

[21] MCNP6.1.1, (2011).

[22] ANSYS CFX, Release 18.1, (2017).

[23] SolidWorks, (2016).

[24] F.W. Dittus, L.M.K. Boelter, Heat Transfer in Automobile Radiators of the Tubular Type, Univ. Calif. Publ. Eng. 2 (1930) 443–461. http://arc.aiaa.org/doi/10.2514/3.10922.

[25] Personal communication with Eric Olivas, (n.d.).

[26] M. Nallasamy, Turbulence Models and their Applications to the Prediction of Internal Flows: A Review, 15 (1987) 151–194.

[27] C.G. SPEZIALE, R. ABID, E.C. ANDERSON, Critical evaluation of two-equation models for near-wall turbulence, AIAA J. 30 (1992) 324–331. doi:10.2514/3.10922.

[28] F.R. Menter, Two-equation eddy-viscosity turbulence models for engineering applications, AIAA J. 32 (1994) 1598–1605. doi:10.2514/3.12149.

[29] D.C. Wilcox, Formulation of the k-w Turbulence Model Revisited, AIAA J. 46 (2008) 2823–2838. doi:10.2514/1.36541.

[30] D. a. Johnson, L.S. King, A mathematically simple turbulence closure model for attached and separated turbulent boundary layers, AIAA J. 23 (1985) 1684–1692. doi:10.2514/3.9152.

[31] F.R. MENTER, Performance of popular turbulence model for attached and separated adverse pressure gradient flows, AIAA J. 30 (1992) 2066–2072. doi:10.2514/3.11180.

[32] F.R. Menter, R. Langtry, S. Völker, P.G. Huang, Transition Modelling for General Purpose CFD Codes, Flow, Turbul. Combust. 77 (2006) 277–303. doi:10.1016/B978-008044544-1/50003-0.

[33] R.B. Langtry, F.R. Menter, Correlation-Based Transition Modeling for Unstructured Parallelized Computational Fluid Dynamics Codes, AIAA J. 47 (2009) 2894–2906. doi:10.2514/1.42362.

[34] J.W.K. van Boggelen, D.G. Eskin, L. Katgerman, Permeability of the mushy zone in aluminum alloys: Evaluation of different approaches, J. Light Met. (2003) 759–766.

[35] P.C. Carman, Fluid Flow Through Granular Beds, Trans. Chem. Eng. 15 (1937) S32–S48. doi:10.1016/S0263-8762(97)80003-2.

[36] M.W. Lee, J.C. Smith, P. Harriot, Unit Operations of Chemical Engineering, 4th ed., McGraw Hill, New York, 1985.

[37] F. White, Fluid Mechanics, 3rd ed., McGraw Hill, 1994.

[38] MCNPX Visual Editor Version 24E, (2011).

[39] J.F. Ziegler, SRIM: The Stopping Range of Ions in Matter, (2013).

[40] F.M. Nortier, Large-Scale Production of Isotopes at LANL, in: 30 MeV Cyclotr. Appl. Res. Facil. Symp., Jeongeup, Korea, 2010.

[41] MATLAB R2016a, (n.d.).

[42] W.L. Oberkampf, C.J. Roy, Verfication and Validation in Scientific Computing, Cambridge University Pres, 2010.

[43] S.M. Qaim, F.T. Tarkanyi, IAEA Charged-Particle Cross Section Database for Medical Radioisotope Production, (2003). https://www-nds.iaea.org/medical/rbp82sr0.html.

[44] K. Gul, A. Hermanne, M.G. Mustafa, F.M. Nortier, P. Oblozinsky, S.M. Qaim, B. Scholten, Y. Shubin, S. Takacs, F.T. Tarkanyi, Y. Zhuang, Charged particle cross-section database for medical radioisotope production: diagnostic radioisotopes and monitor reactions, 2001.

[45] J.E. Turner, Review Article, Health Phys. 88 (2005) 520–544. doi:10.1017/S0272263113000454.

[46] W.D. Newhauser, R. Zhang, The physics of proton therapy, Phys. Med. Biol. 60 (2015) R155–R209. doi:10.1088/0031-9155/60/8/R155.

[47] M.H. Stokely, Advanced Thermosyphon Targets for Production of the F-18 Radionuclide, 2007.

[48] N. Otuka, S. Takács, Definitions of radioisotope thick target yields, Radiochim. Acta. 103 (2015) 1–6. doi:10.1515/ract-2013-2234.

[49] S. Tanaka, M. Furukawa, M. Chiba, Nuclear Reactions of Nickel with Protons up to 56 MeV, 34 (1972) 2419–2426.

[50] P. Reimer, S.M. Qaim, Excitation Functions of Proton Induced Reactions of Highly Enriched Ni-58 with Special Relevance to the Production of Co-55 and Co-57, Radiochim. Acta. 80 (1998) 113–120.

[51] S. Kaufman, Reaction of Protons with Ni-58 and Ni-60, Phys. Rev. 117 (1960) 1532–1538.

[52] G.F. Knoll, Radiation Detection and Management, Fourth, John Wiley & Sons, Inc., 2010.

[53] H. Junde, H. Su, Y. Dong, Nuclear Data Sheets for A = 56, Nucl. Data Sheets. 112 (2011) 1513–1645. doi:10.1016/j.nds.2011.04.004.

[54] M.R. Bhat, Nuclear Data Sheets for A = 57, Nucl. Data Sheets. 85 (1998) 415. doi:10.1103/PhysRevB.74.024428.

[55] E.Z. Buthelezi, F.M. Nortier, I.W. Schroeder, Excitation functions for the production of

82Sr by proton bombardment of natRb at energies up to 100 MeV, Appl. Radiat. Isot. 64 (2006) 915–924. doi:10.1016/j.apradiso.2006.03.009.

[56] R.C. Smith, Uncertainty Quantification: Theory, Implementation, and Applications, Society for Industrial and Applied Mathematics, 2014.

[57] C. Dougherty, Introduction to Econometrics, 2nd ed., Oxford University Press, Oxford, 2002. doi:10.1002/bimj.201000076.

[58] Y. Nagasaka, N. Nakazawa, A. Nagashima, Experimental determination of the thermal diffusivity of molten alkali halides by the forced Rayleigh scattering method. I. Molten LiCl, NaCl, KCl, RbCl, and CsCl, Int. J. Thermophys. 13 (1992) 555–574. doi:10.1007/BF00501941.

[59] I.G. Murgulescu, S. Zuca, Die innere Reibung eininger geschmolzener Salze, Zeitschrift Fur Phys. Chemie. (1962) 300–304.

[60] M.G. Braunsfurth, a. C. Skeldon, A. Juel, T. Mullin, D.S. Riley, Free convection in liquid gallium, J. Fluid Mech. 342 (1997) 295–314. doi:10.1017/S0022112097005569.

[61] Special Metals Corporation, Inconel Alloy 625, (2013) 1–28. doi:SMC-066.

[62] Special Metals Corporation, Inconel 718 Alloy, (2007). doi:SMC-066.

[63] V.A. Kirillin, A.E. Sheindlin, V.Y. Chekovskoi, I.. Zhukova, Thermodynamic properties of niobium from 0 K to the melting point, 2740 K, in: Adv. Thermophys. Prop. Extrem. Temp. Press., American Society of Mechanical Engineers, New York, 1965: pp. 152–155.

[64] J.W. Arblaster, The Thermodynamic Properties of Niobium, J. Phase Equilibria Diffus. 38 (2017) 707–722. doi:10.1007/s11669-017-0557-4.

APPENDICES

Appendix A. RbCl Target Puck Casting Process

Figure A-1: RbCl in loose powder form.

Figure A-2: The RbCl is heated to above its melting point and poured into a cast.

Figure A-3: The molten RbCl is left to solidify into a solid target puck.

Figure A-4: The solid RbCl target puck is weighed and then ready to be encapsulated under vacuum.

Appendix B. Physical Properties of Problem Materials

Table B-1: RbCl material properties [58,59].

Rubidium Chloride				
Temperature [K]	**Density [kg m^{-3}]**	**Specific Heat [J kg^{-1} K^{-1}]**	**Thermal Conductivity [W m^{-1} K^{-1}]**	**Dynamic Viscosity [Pa s]**
293	2800	418	2.41	1.00E+08
400	2800	418	1.555	1.00E+08
989	2800	418	1.000099	1.00E+08
990	2246.732	607.6	0.249	1.37E-03
1000	2237.9	608.6	0.2479	1.33E-03
1010	2229.068	609.6	0.2468	1.29E-03
1020	2220.236	610.6	0.2457	1.25E-03
1030	2211.404	611.6	0.2446	1.21E-03
1040	2202.572	612.6	0.2435	1.18E-03
1050	2193.74	613.6	0.2424	1.15E-03
1060	2184.908	614.6	0.2413	1.12E-03
1070	2176.076	615.6	0.2402	1.09E-03
1080	2167.244	616.6	0.2391	1.06E-03
1090	2158.412	617.6	0.238	1.03E-03
1100	2149.58	618.6	0.2369	1.00E-03
1110	2140.748	619.6	0.2358	9.79E-04
1120	2131.916	620.6	0.2347	9.55E-04
1130	2123.084	621.6	0.2336	9.32E-04
1140	2114.252	622.6	0.2325	9.10E-04
1150	2105.42	623.6	0.2314	8.89E-04
1160	2096.588	624.6	0.2303	8.69E-04
1170	2087.756	625.6	0.2292	8.49E-04
1180	2078.924	626.6	0.2281	8.31E-04
1190	2070.092	627.6	0.227	8.13E-04
1200	2061.26	628.6	0.2259	7.95E-04
1210	2052.428	629.6	0.2248	7.79E-04
1220	2043.596	630.6	0.2237	7.63E-04
1230	2034.764	631.6	0.2226	7.47E-04
1240	2025.932	632.6	0.2215	7.32E-04
1250	2017.1	633.6	0.2204	7.18E-04
1260	2008.268	634.6	0.2193	7.04E-04
1280	1990.604	636.6	0.2171	6.78E-04
1290	1981.772	637.6	0.216	6.65E-04
1300	1972.94	638.6	0.2149	6.53E-04
1310	1964.108	639.6	0.2138	6.42E-04
1320	1955.276	640.6	0.2127	6.30E-04
1330	1946.444	641.6	0.2116	6.20E-04
1340	1937.612	642.6	0.2105	6.09E-04

Table B-1 (continued)

Rubidium Chloride				
Temperature [K]	**Density [kg m^{-3}]**	**Specific Heat [J kg^{-1} K^{-1}]**	**Thermal Conductivity [W m^{-1} K^{-1}]**	**Dynamic Viscosity [Pa s]**
1350	1928.78	643.6	0.2094	5.99E-04
1360	1919.948	644.6	0.2083	5.89E-04
1370	1911.116	645.6	0.2072	5.79E-04
1380	1902.284	646.6	0.2061	5.70E-04
1390	1893.452	647.6	0.205	5.61E-04
1400	1884.62	648.6	0.2039	5.52E-04
1410	1875.788	649.6	0.2028	5.43E-04
1420	1866.956	650.6	0.2017	5.35E-04
1430	1858.124	651.6	0.2006	5.27E-04
1440	1849.292	652.6	0.1995	5.19E-04
1450	1840.46	653.6	0.1984	5.12E-04
1460	1831.628	654.6	0.1973	5.04E-04
1470	1822.796	655.6	0.1962	4.97E-04
1480	1813.964	656.6	0.1951	4.90E-04
1490	1805.132	657.6	0.194	4.83E-04
1500	1796.3	658.6	0.1929	4.77E-04
1510	1787.468	659.6	0.1918	4.70E-04
1520	1778.636	660.6	0.1907	4.64E-04
1530	1769.804	661.6	0.1896	4.58E-04

Table B-2: Ga material properties [60].

Gallium				
Temperature [K]	**Density [kg m^{-3}]**	**Specific Heat [J kg^{-1} K^{-1}]**	**Thermal Conductivity [W m^{-1} K^{-1}]**	**Dynamic Viscosity [Pa s]**
293	5907	370.77	40.6	1.000E+06
302	5907	370.77	40.6	1.000E+06
303	6078	408.64	28.2	2.000E-04
350	6050	397.29	31.2	1.741E-04
400	6019	389.46	34.4	1.483E-04
450	5989	385.05	37.5	1.305E-04
500	5959	383.12	40.5	1.175E-04
550	5929	382.71	43.5	1.075E-04
600	5899	382.86	46.3	9.996E-05
650	5869	382.63	49.1	9.325E-05
700	5838	381.06	51.8	8.798E-05

Table B-3: In625 material properties [61].

Inconel 625			
Temperature [K]	**Density [kg m^{-3}]**	**Specific Heat [J kg^{-1} K^{-1}]**	**Thermal Conductivity [W m^{-1} K^{-1}]**
295	8440	410	9.8
366	8440	427	10.8
477	8440	456	12.5
588	8440	481	14.1
700	8440	511	15.7
811	8440	536	17.5
922	8440	565	19.0

Table B-4: In718 material properties [62].

Inconel 718			
Temperature [F]	**Density [lb in^{-3}]**	**Specific Heat [Btu lb^{-1} °F^{-1}]**	**Thermal Conductivity [BTU in ft^{-2} hr^{-1} °F^{-1}]**
70	0.296	0.104	77
200	0.296	0.104	86
400	0.296	0.104	98
600	0.296	0.104	111
800	0.296	0.104	123
1000	0.296	0.104	135
1200	0.296	0.104	147
1400	0.296	0.104	160
1600	0.296	0.104	173
1800	0.296	0.104	185
2000	0.296	0.104	196

Table B-5: Nb material properties [63,64].

Niobium			
Temperature [K]	**Density [kg m^{-3}]**	**Specific Heat [J kg^{-1} K^{-1}]**	**Thermal Conductivity [W m^{-1} K^{-1}]**
293	8570	24.6	53.6
350	8570	25.2	54.4
400	8570	25.5	55.1
450	8570	25.7	55.8
500	8570	25.9	56.6

Appendix C. Experimental ^{58}Ni Foil Data

Table C-1: Position of each nickel foil – equivalent for both the thick and thin window experiments.

Position of Ni Foil Discs							
Disc	**Position [mm]**			**Disc**	**Position**		
	x	**y**	**z**		**x**	**y**	**z**
1	0	0	6.221	**18**	-10.999	-6.35	6.221
2	0	6.35	6.221	**19**	-12.7	0	6.221
3	0	12.7	6.221	**20**	-10.999	6.35	6.221
4	0	19.05	6.221	**21**	-6.35	0	6.221
5	-5.887	18.118	6.221	**22**	6.075	14.667	6.221
6	-11.197	15.412	6.221	**23**	11.225	11.225	6.221
7	-15.412	11.197	6.221	**24**	14.667	6.075	6.221
8	-18.118	5.887	6.221	**25**	15.875	0	6.221
9	-19.05	0	6.221	**26**	14.667	-6.075	6.221
10	-18.118	-5.887	6.221	**27**	9.059	2.943	6.221
11	-15.412	-11.197	6.221	**28**	6.075	-14.667	6.221
12	-11.197	-15.412	6.221	**29**	5.599	-7.706	6.221
13	-5.887	-18.118	6.221	**30**	9.059	-2.943	6.221
14	0	-19.05	6.221	**31**	5.599	7.706	6.221
15	0	-12.7	6.221	**Titanium 1**	-6.35	10.999	6.221
16	0	-6.35	6.221	**Titanium 2**	11.225	-11.225	6.221
17	-6.35	-10.999	6.221		-		

Table C-2: Information on nickel foil discs used for thin window experiment.

Thin Window Disc Data							
Disc	**Weight [mg]**	**Thickness [mm]**	**Diameter [mm]**	**Disc**	**Weight [mg]**	**Thickness [mm]**	**Diameter [mm]**
1	16.9	0.133	4.763	**18**	17.6	0.15	4.762
2	16.6	0.146	4.762	**19**	17.4	0.15	4.763
3	16.9	0.15	4.762	**20**	17.6	0.15	4.762
4	17.2	0.16	4.762	**21**	16.8	0.14	4.762
5	17.7	0.16	4.763	**22**	17.0	0.15	4.762
6	18.1	0.17	4.763	**23**	16.5	0.15	4.762
7	17.9	0.15	4.762	**24**	16.6	0.15	4.762
8	17.2	0.16	4.763	**25**	17.2	0.16	4.763
9	17.4	0.16	4.762	**26**	16.6	0.16	4.763
10	17.7	0.16	4.762	**27**	16.9	0.16	4.763
11	17.6	0.15	4.763	**28**	16.9	0.16	4.762
12	17.3	0.15	4.763	**29**	16.5	0.15	4.762
13	16.7	0.15	4.763	**30**	17.0	0.15	4.763
14	17.4	0.15	4.763	**31**	16.9	0.16	4.763
15	17.5	0.15	4.762	**Titanium 1**	9.6	0.16	4.762
16	17.6	0.16	4.762	**Titanium 2**	9.5	0.16	4.763
17	17.2	0.16	4.763	-			

Table C-3: Information on nickel foil discs used for thick window experiment.

Thick Window Disc Data							
Disc	**Weight [mg]**	**Thickness [mm]**	**Diameter [mm]**	**Disc**	**Weight [mg]**	**Thickness [mm]**	**Diameter [mm]**
1	16.8	0.14	4.763	**18**	17.4	0.15	4.762
2	16.8	0.15	4.762	**19**	17.4	0.15	4.763
3	16.8	0.13	4.762	**20**	17.5	0.16	4.762
4	17.5	0.16	4.762	**21**	17.4	0.14	4.762
5	18.2	0.16	4.763	**22**	16.3	0.14	4.762
6	17.7	0.15	4.763	**23**	16.6	0.15	4.762
7	17.1	0.17	4.762	**24**	16.2	0.15	4.762
8	17.9	0.16	4.763	**25**	17.0	0.15	4.763
9	17.4	0.16	4.762	**26**	17.0	0.16	4.763
10	17.6	0.15	4.762	**27**	17.0	0.16	4.763
11	17.3	0.15	4.763	**28**	17.1	0.16	4.762
12	17.1	0.15	4.763	**29**	16.3	0.15	4.762
13	17.0	0.15	4.763	**30**	17.3	0.16	4.763
14	16.9	0.15	4.763	**31**	16.9	0.15	4.763
15	17.8	0.15	4.762	**Titanium 3**	9.5	0.16	4.762
16	17.7	0.16	4.762	**Titanium 4**	9.4	0.16	4.763
17	17.6	0.16	4.763	-			

Table C-4: Thin window experimental results for activity ratios and energies.

Thin Window					
Foil Number	$A_{Co^{57}}/A_{Co^{56}}$		**Corresponding Energy [MeV]**	E_{avg} **[MeV]**	**Average** $A_{Co^{57}}/A_{Co^{56}}$
1	**Max**	126.119	25.80	26.2070	66.158
	Min	6.196	26.62		
2	**Max**	17.330	26.06	27.5810	9.437
	Min	1.545	29.11		
3	**Max**	9.431	26.27	28.5224	5.122
	Min	0.813	30.78		
4	**Max**	11.021	26.20	28.8515	5.834
	Min	0.647	31.50		
5	**Max**	10.059	26.24	28.8705	5.353
	Min	0.647	31.50		
6	**Max**	13.115	26.14	28.4636	6.963
	Min	0.810	30.79		
7	**Max**	11.741	26.18	28.2718	6.339
	Min	0.938	30.36		
8	**Max**	12.157	26.17	28.1127	6.603
	Min	1.048	30.06		
9	**Max**	14.572	26.11	27.8238	7.928
	Min	1.284	29.54		
10	**Max**	21.446	26.00	27.3522	11.652
	Min	1.858	28.70		
11	**Max**	3.578	27.47	27.4962	3.527
	Min	3.477	27.52		
12	**Max**	7.852	26.35	26.3682	7.642
	Min	7.432	26.38		
13	**Max**	241.642	25.79	25.9028	131.005
	Min	20.368	26.01		
14	**Max**	323.632	25.79	25.8666	175.672
	Min	27.712	25.95		
15	**Max**	310.237	25.79	25.8640	169.546
	Min	28.856	25.94		
16	**Max**	417.902	25.78	25.9288	216.982
	Min	16.062	26.08		
17	**Max**	280.905	25.79	25.9085	150.099
	Min	19.293	26.03		
18	**Max**	85.176	25.82	26.0952	46.394
	Min	7.612	26.37		
19	**Max**	29.851	25.94	26.9884	16.224
	Min	2.597	28.04		
20	**Max**	1.314	29.49	29.5166	1.297
	Min	1.280	29.55		

Table C-4 (continued)

Thin Window					
Foil Number	$A_{Co^{57}}/A_{Co^{56}}$		**Corresponding Energy [MeV]**	E_{avg} **[MeV]**	**Average** $A_{Co^{57}}/A_{Co^{56}}$
21	**Max**	65.098	25.84	26.3767	35.083
	Min	5.069	26.91		
22	**Max**	1.005	30.17	30.2106	0.990
	Min	0.976	30.25		
23	**Max**	16.565	26.07	27.7930	3.931
	Min	1.297	29.52		
24	**Max**	19.472	26.03	27.4726	10.576
	Min	1.681	28.92		
25	**Max**	23.672	25.98	27.2288	12.873
	Min	2.075	28.48		
26	**Max**	31.584	25.93	26.8994	17.215
	Min	2.846	27.87		
27	**Max**	24.863	25.97	27.1739	13.522
	Min	2.180	28.38		
28	**Max**	-	-	-	-
	Min	-	-		
29	**Max**	11.208	26.20	26.2065	10.976
	Min	10.743	26.22		
30	**Max**	46.883	25.87	26.5694	25.466
	Min	4.050	27.27		
31	**Max**	16.737	26.07	27.6722	9.085
	Min	1.433	29.28		

Table C-5: Thick window experimental results for activity ratios and energies.

Thick Window					
Foil Number	$A_{Co^{57}}/A_{Co^{56}}$		**Corresponding Energy [MeV]**	E_{avg} **[MeV]**	**Average** $A_{Co^{57}}/A_{Co^{5}}$
1	**Max**	19.745	26.02	26.0328	18.97
	Min	18.194	26.04		
2	**Max**	17.394	26.05	26.0598	17.09
	Min	16.785	26.07		
3	**Max**	5.102	26.90	26.9169	5.06
	Min	5.014	26.93		
4	**Max**	3.261	27.63	27.6757	3.18
	Min	3.097	27.72		
5	**Max**	3.178	27.68	27.7099	3.12
	Min	3.055	27.74		
6	**Max**	5.294	26.85	26.8758	5.20
	Min	5.100	26.90		
7	**Max**	7.400	26.39	26.4363	7.09
	Min	6.780	26.49		
8	**Max**	8.927	26.29	26.2962	8.86
	Min	8.783	26.30		
9	**Max**	11.662	26.18	26.1880	11.53
	Min	11.396	26.19		
10	**Max**	17.751	26.05	26.0498	17.67
	Min	17.580	26.05		
11	**Max**	42.723	25.88	25.8871	41.44
	Min	40.150	25.89		
12	**Max**	112.201	25.80	25.7996	110.84
	Min	109.470	25.80		
13	**Max**	155.887	25.80	25.7971	149.29
	Min	142.684	25.80		
14	**Max**	146.348	25.09	25.4428	143.66
	Min	140.973	25.80		
15	**Max**	94.485	25.81	25.8176	87.70
	Min	80.907	25.82		
16	**Max**	15.762	26.08	26.0904	15.39
	Min	15.019	26.10		
17	**Max**	86.718	25.82	25.8265	78.75
	Min	70.790	25.83		
18	**Max**	33.058	25.92	25.9228	32.40
	Min	31.736	25.93		
19	**Max**	20.859	26.01	26.0099	20.74
	Min	20.619	26.01		
20	**Max**	11.545	26.19	26.1912	11.43
	Min	11.306	26.19		

Table C-5 (continued)

Thick Window					
Foil Number	$A_{Co^{57}}/A_{Co^{56}}$		**Corresponding Energy [MeV]**	E_{avg} **[MeV]**	**Average** $A_{Co^{57}}/A_{Co^{5}}$
21	**Max**	84.746	25.82	25.8236	81.60
	Min	78.456	25.83		
22	**Max**	7.893	26.35	26.3643	7.70
	Min	7.498	26.38		
23	**Max**	13.911	26.12	26.1271	13.72
	Min	13.537	26.13		
24	**Max**	21.570	26.00	26.0060	21.05
	Min	20.534	26.01		
25	**Max**	30.799	25.93	25.9340	30.28
	Min	29.754	25.94		
26	**Max**	53.413	25.85	25.8564	52.64
	Min	51.871	25.86		
27	**Max**	34.797	25.91	25.9104	34.74
	Min	34.684	25.91		
28	**Max**	143.992	25.80	25.7977	139.78
	Min	135.577	25.80		
29	**Max**	92.749	25.81	25.8172	88.11
	Min	83.474	25.82		
30	**Max**	71.054	25.83	25.8355	69.62
	Min	68.194	25.84		
31	**Max**	16.069	26.08	26.0804	15.94
	Min	15.817	26.08		

Table C-6: Thin window experimental foil information and tally multiplier value in order to obtain tally information from MCNP in units of $\left[\frac{\text{mCi}}{\mu\text{A}}\right]$.

Thin Window Disc Data				
Disc	**Volume** $[\text{mm}^3]$	**Density** $\left[\frac{\text{g}}{\text{cm}^3}\right]$	**Number Density** $\left[\frac{\text{atoms}}{\text{cm}^3}\right]$	FM_{foil}
1	2.3698	7.1316	7.4130E+22	0.029597
2	2.6003	6.3839	6.6358E+22	0.029071
3	2.6715	6.3260	6.5756E+22	0.029597
4	2.8496	6.0359	6.2740E+22	0.030122
5	2.8508	6.2087	6.4537E+22	0.030998
6	3.0290	5.9756	6.2114E+22	0.031698
7	2.6715	6.7003	6.9647E+22	0.031348
8	2.8508	6.0333	6.2714E+22	0.030122
9	2.8496	6.1061	6.3470E+22	0.030472
10	2.8496	6.2113	6.4564E+22	0.030998
11	2.6727	6.5852	6.8451E+22	0.030823
12	2.6727	6.4730	6.7284E+22	0.030297
13	2.6727	6.2485	6.4950E+22	0.029246
14	2.6727	6.5104	6.7673E+22	0.030472
15	2.6715	6.5506	6.8090E+22	0.030647
16	2.8496	6.1762	6.4200E+22	0.030823
17	2.8508	6.0333	6.2714E+22	0.030122
18	2.6715	6.5880	6.8479E+22	0.030823
19	2.6727	6.5104	6.7673E+22	0.030472
20	2.6715	6.5880	6.8479E+22	0.030823
21	2.4934	6.7377	7.0036E+22	0.029422
22	2.6715	6.3634	6.6145E+22	0.029772
23	2.6715	6.1762	6.4200E+22	0.028896
24	2.6715	6.2137	6.4589E+22	0.029071
25	2.8508	6.0333	6.2714E+22	0.030122
26	2.8508	5.8229	6.0526E+22	0.029071
27	2.8508	5.9281	6.1620E+22	0.029597
28	2.8496	5.9306	6.1646E+22	0.029597
29	2.6715	6.1762	6.4200E+22	0.028896
30	2.6727	6.3607	6.6117E+22	0.029772
31	2.8508	5.9281	6.1620E+22	0.029597
Titanium 1	2.8496	3.3689	4.2384E+22	0.020349
Titanium 2	2.8508	3.3324	4.1924E+22	0.020137

Table C-7: Thin window experimental foil information and tally multiplier value in order to obtain tally information from MCNP in units of $\left[\frac{\text{mCi}}{\mu\text{A}}\right]$.

Thick Window Disc Data				
Disc	**Volume** $[\text{mm}^3]$	**Density** $\left[\frac{\text{g}}{\text{cm}^3}\right]$	**Number Density** $\left[\frac{\text{atoms}}{\text{cm}^3}\right]$	FM_{foil}
1	2.4945	6.7349	7.0006E+22	0.029422
2	2.6715	6.2885	6.5367E+22	0.029422
3	2.3153	7.2560	7.5423E+22	0.029422
4	2.8496	6.1411	6.3835E+22	0.030647
5	2.8508	6.3841	6.6360E+22	0.031873
6	2.6727	6.6226	6.8840E+22	0.030998
7	3.0277	5.6478	5.8706E+22	0.029947
8	2.8508	6.2789	6.5266E+22	0.031348
9	2.8496	6.1061	6.3470E+22	0.030472
10	2.6715	6.5880	6.8479E+22	0.030823
11	2.6727	6.4730	6.7284E+22	0.030297
12	2.6727	6.3981	6.6506E+22	0.029947
13	2.6727	6.3607	6.6117E+22	0.029772
14	2.6727	6.3233	6.5728E+22	0.029597
15	2.6715	6.6629	6.9258E+22	0.031173
16	2.8496	6.2113	6.4564E+22	0.030998
17	2.8508	6.1736	6.4173E+22	0.030823
18	2.6715	6.5131	6.7701E+22	0.030472
19	2.6727	6.5104	6.7673E+22	0.030472
20	2.8496	6.1411	6.3835E+22	0.030647
21	2.4934	6.9783	7.2537E+22	0.030472
22	2.4934	6.5372	6.7951E+22	0.028546
23	2.6715	6.2137	6.4589E+22	0.029071
24	2.6715	6.0639	6.3032E+22	0.028371
25	2.6727	6.3607	6.6117E+22	0.029772
26	2.8508	5.9632	6.1985E+22	0.029772
27	2.8508	5.9632	6.1985E+22	0.029772
28	2.8496	6.0008	6.2376E+22	0.029947
29	2.6715	6.1014	6.3421E+22	0.028546
30	2.8508	6.0684	6.3079E+22	0.030297
31	2.6727	6.3233	6.5728E+22	0.029597
Titanium 1	2.8496	3.3338	4.1942E+22	0.020137
Titanium 2	2.8508	3.2973	4.1483E+22	0.019925